Grant Agreement Number 608553

IMAGE
Integrated Methods for Advanced Geothermal Exploration

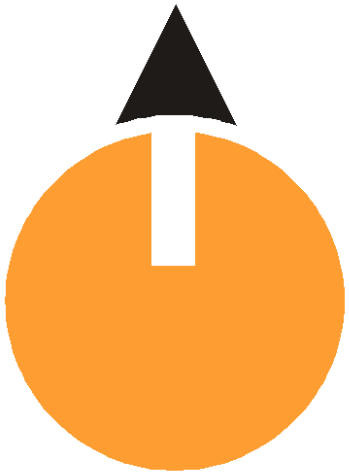

IMAGE-D3.2

Final report on:
Rock/fluid interactions at supercritical conditions

Responsible author	Giovanni Ruggieri (IGG-CNR)
Responsible WP-leader Responsible SP-leader	Domenico Liotta (UNIBARI) Gylfi Páll Hersir (ISOR)
Contributions by:	Francesco Capecchiacci, Laura Chiarantini, Giordano Montegrossi, Isabella Nardini, Valentina Rimondi, Giovanni Ruggieri, Andrea Orlando (IGG-CNR) Andrea Brogi, Domenico Liotta (UniBari) Tobias Björn Weisenberger, Helga Margrét Helgadóttir (ISOR)

Introduction & summary

This report describes rock/fluid interactions at super-critical[1] conditions building concepts for deep fluid circulation and validation from lab results (Deliverable D3.2 Rock/fluid interactions at supercritical conditions, pag. 14-15 of the DoW).
In particular we report:

- the results of fluid-rock interaction experiments by using a cold seal pressure vessel apparatus between aqueous solutions and crystalline solids in which several parameters were taken into account, such as type of solid, fluid composition and its salinity, solid/fluid ratio, P-T conditions. Fluids and solids were characterized before and after experiments.
- Fluid-rock interaction modelling by using the modified code-packages upgraded up to supercritical conditions.
- Collection and geochemical/isotopic analyses of fluid samples from geothermal systems in Iceland.
- Validation of fluid-rock interaction modelling by comparing the results with the data of fluid from active geothermal fields.
- Data interpretation and assessment of the mineralogical and chemical changes of the rocks and fluids by fluid-rock interaction of magmatic hydrothermal system around cooling intrusions at supercritical conditions as a function of temperature, pressure and fluid composition.

The objectives of this task is the investigation of fluid-rock interaction processes that can occur in super-hot geothermal reservoirs. The deliverable will provide information on: 1) the mineralogical and chemical changes related to water-rock interactions processes at super-hot conditions, and 2) the interaction between magmatic - geothermal systems during the development of hydrothermal systems around cooling magma intrusions. The results will build concepts for deep fluid circulation within super-hot geothermal reservoirs (at temperature up to 600°C and pressure up to 1.3 Kbar).
The approach of the IMAGE project to WP3 is to obtain information on super-hot geothermal systems from the study of exhumed geothermal systems considered to represent proxies of different active geothermal areas (see report Task 3.1 of WP3). In particular, two different types of super-hot exhumed geothermal systems have been considered in WP3: 1) the Eastern Elba Island (Italy) hydrothermal system, characterized by quartz-tourmaline veins and masses within Mt. Calamita micaschists and 2) the Geitafell (Iceland) basaltic hydrothermal system, characterized by a contact-metamorphic event overprinted by a lower-temperature hydrothermal stage (see report Task 3.1). The first is assumed to represent a proxy of a super-hot

[1] A supercritical fluid is any substance at a temperature and pressure above its critical point, where distinct liquid and gas phases do not exist. In the case of pure water the critical point is at 221 bars and 374.2°C. However, the critical point of aqueous saline solution is modified depending on the type of dissolved salts and its concentration. For example the presence of dissolved NaCl in the fluid will move the critical point of pure water to higher P-T values (Knight and Bodnar, 1989). As part of the experiments and geochemical modeling carried out in this task have been made by using aqueous saline solutions that would not be super-critical fluids at the considered P-T conditions, in this report we always will use the terms super-hot fluids or super-hot conditions meaning that the fluids are at temperature >400°C without any consideration if the fluid was at super-critical conditions or not.

reservoir present below the exploited Larderello geothermal reservoir, whereas the second is considered to resemble the supercritical reservoir that might be present below exploited Icelandic geothermal reservoirs and in particular below the Krafla geothermal system.
The investigation, performed both with experimental (by using hydrothermal autoclave apparatus) and computational methods (by thermodynamic numerical modelling), aims to reproduce fluid-rock interaction that likely occur in these two reservoirs characterized by different host rocks (i.e. micaschists at Elba Island and basalt at Geitafell) and to assess the chemical evolution of solids and fluids after the interaction took place. The chemical and mineralogical changes resulting from fluid-rock interaction may give crucial indications about parameters (such as temperature, fluid salinity, concentration of some chemical species) controlling the considered geothermal systems. This information may help to design and develop proper exploration and exploitation methods in these extreme environments.
In particular, the aim of the fluid-rock interaction on Mt. Calamita micaschist from Elba Island was to reproduce the reactions that occurred in a super-hot geothermal reservoir yielding the observed tourmaline-rich hydrothermal rocks (see task 3.1). And in particular to verify if a B-rich, NaCl-rich hot fluids of magmatic derivation can actively react with biotite, producing tourmaline, can effectively generates the significant Fe enrichment in the fluid found in fluid inclusions (see report task 3.1). The results of thermodynamic modelling were validated by comparing these results with the available composition of tourmaline from the Larderello geothermal field.
The aim of our fluid-rock interaction studies on Icelandic basalt was to reproduce the mineralogical and fluid changes that occurred in the fossil hydrothermal system of Geitafell when an aqueous fluid reacted with the reservoir rock at super-critical condition or at super-hot temperature. The results of this study, integrated with result of task 3.1, could help to better understand the geological processes and to constrain some physical-chemical features which characterize a possible super-hot geothermal reservoir present below the exploited reservoirs of "Karfla-like" systems of Iceland (i.e. geothermal systems characterized by low-salinity fluid of meteoric derivation). Numerical modelling of fluid-rock interaction processes was also extended to "Reykjanes-like" geothermal fields (i.e. geothermal systems characterized by relatively high-salinity fluid of seawater dominated origin) . The results of thermodynamic modelling were validated by comparing these results with fluid composition of active magmatic geothermal fields of Iceland (Krafla and Reykjanes). To this purpose, fluid from some geothermal wells of these two fields were sampled and analysed, and the result integrated with the data furnished by ISOR. In addition, fumaroles were also sampled for gas compositions. The fluid collected during this project were also analysed to determine the Volatile Organic Compounds (VOCs) with the aim to contribute to the study of indicators that can reveal the presence of fluid in supercritical conditions.

The main results of fluid-rock interaction in micaschist of Elba Island (Italy):

1) The interaction between a B-rich, saline, fluid (of magmatic derivation) with micaschist from Mt. Calamita at T= 500-600°C and P= 1000-1300 bars lead to the formation of tourmaline and reproduce the process that likely occurred in the natural hydrothermal system. Thermodynamic modelling showed that tourmaline can also form at lower temperature if the pH is sufficiently low.

2) The interaction process caused fluid enrichment in K and Fe (when using saline solution), if this Fe-rich fluid upraise at shallower level it readily precipitate magnetite as soon as the mixing with oxidizing water provide enough dissolved oxygen to allow magnetite precipitation, and the fluid is cooled down as well. This process likely explain the occurrence of the Fe deposits present in Elba Island.
3) Deep exploration/exploitation of the super-hot geothermal reservoir in the Larderello geothermal area should find tourmaline-rich rocks and a deep reservoir fluid characterized by low-pH and significant content of B, Fe, K, in addition to Na and Cl. If such fluid become in contact with an oxidizing environment and/or is cooled it is expected that precipitated iron oxides.

The main results of fluid-rock interaction in basalt of Iceland:

1) The formation of secondary minerals during autoclave experiment was modest possibly because of kinetic effect. The presence of CO_2, HCl and H_2SO_4 appears to enhance fluid-rock interaction.
2) The scarce secondary phases, formed in the range of 400-600°C, are: plagioclase (labradorite/andesine), a Ca-phase (presumably epidote), amphiboles, scapolite and anhydrite+hematite+quartz (when H_2SO_4 is present in reacting fluid).
3) The presence of H_2SO_4 in the reacting fluid mobilized Ca^{2+}.
4) During deep exploration/exploitation of the super-critical geothermal reservoir, the recognition of an anhydrite+hematite+quartz alteration assemblage can be indicative of a leaching process related to the presence of SO_2, likely introduced by a nearby magmatic source. Whereas the finding of secondary amphibole and/or scapolite can be indicative that the system reached relatively high-temperature typical of supercritical conditions for pure water.

TABLE OF CONTENT

1. Fluid-rock interaction in micaschist of Elba Island (Italy)

Main features of the Elba Island fossil hydrothermal system

At Elba Island In the Mt. Calamita Promontory biotite-rich Calamita Schists were massively tourmalinized and crossed by tourmaline-quartz veins and breccias particularly (but not only) at the contact with and around the leucogranite sills and dykes. The development of these veins and masses are related to a large super-hot hydrothermal system, dominated by boron-rich and saline fluid of magmatic derivation related to the emplacement of numerous intrusions of tourmaline bearing leucogranites (see report task 3.1). The metasomatic B-rich fluids selectively replaced the biotite-rich layers of the Calamita Schists producing tourmaline with a dominantly dravitic composition (Dini et al., 2008). Fluid inclusion studies (see report task 3.1) indicate that the fluid that circulated within quartz-tourmaline veins related to tourmaline deposition (i.e. L and V inclusions) were characterized by: temperatures of 420-650°C, pressure of 740-1600 bars and salinity of 16-30 wt. % NaCl eq.. Moreover, this fluid contain significant amount of K, Fe, B in addition to Na.

The normal trends of fractionation of acidic peraluminous magmas (like most of Elba Island granites) reduce the Fe and Mg contents of melts (mainly by early crystallization of biotite) before the concentration of B reaches values sufficient to stabilize tourmaline (London, 2008 and references therein). Therefore, once magmas contain enough boron to crystallize tourmaline, they most likely lack the necessary Fe and Mg. In tourmaline bearing leucogranites from Calamita area biotite is rarely observed and, in spite of the overall low Fe and Mg contents, the conditions for tourmaline crystallization were frequently reached. However, the boron content of the magma feeding the Calamita leucogranite dykes/sills largely exceeded the Fe and Mg contents, in fact after the magmatic Fe and Mg were incorporated in magmatic tourmaline significant amounts of B-rich fluids were released to the host rocks. Iron, therefore, would be included in B-rich fluid circulating in quartz-tourmaline veins after its release from the crystallizing magma.

Elba Island quartz-tourmaline veins represent a proxy of a super-hot reservoir present below the exploited Larderello geothermal reservoir, whereas the fossil hydrothermal systems that generated the Fe deposits of Elba Island of Terranera Valle Giove, Bacino and Topinetti can represent shallower reservoirs similar to those presently exploited at Larderello (see report task 3.1). Therefore, the results of the experiments and thermodynamic modeling will provide information on the solid and fluid phases that would occur in the super-hot reservoir at Larderello.

Main features of the Larderello geothermal system

A super-hot reservoir (>420°C) with pressurized fluids was likely found in the Larderello geothermal field by the San Pompeo 2 well which blew-out on reaching a depth roughly corresponding to the so-called K-horizon seismic in the reflector (Dini et al., 2008). During the blow-out quartz-tourmaline fragments were ejected at surface by well. The K-horizon is an intense and continuous seismic reflector exhibiting local "bright spot" features inside the Palaeozoic crystalline basement (Batini et al., 1983; Gianelli et al., 1997; Brogi et al., 2005). Its depth varies between 3-4 km in the western zone and 8-10 km in the Travale geothermal area (Bertini et al., 2006). This seismic facies is characterized by a lozenge-shape geometry whose thickness is estimated in about 2 km. The "bright spot" nature of the K-horizon can be likely

related to the presence of micro-cracks and micro-fractures filled locally by fluids (Marini & Manzella, 2005). However, information on the characteristics of the fluids (likely of magmatic derivation) stored in the K-horizon are limited as such fluids apparently did not significantly contribute to the fluid presently discharged the exploited reservoirs. The latter are: 1) a shallow steam-dominated reservoir, hosted at 500-1500 m depth in sedimentary rocks, is characterized by medium-high permeability, present-day temperatures of about 220-250°C and a pressure of about 20 bar at 1000 m depth; 2) a deep superheated steam reservoir, in vapor-static equilibrium with the shallow one, hosted in fractured metamorphic basement and thermo-metamorphic rocks at depths ranging between 2000 and 4500 m, is characterised by temperatures ranging between 300-350°C and a reservoir pressure of 70 bar at 3000 m depth (Batini et al., 2003). The two reservoirs are interconnected by fractures and currently show vertical hydraulic continuity, but this does not imply uniform characteristics of the geothermal fluid delivered.
Most geothermal wells deliver superheated dry steam with 2–10% by weight of non-condensable gases, mostly consisting of CO_2 (90–98%). Methane accounts for about 1–2% of the dry gas, and detectable amounts of higher hydrocarbons (ethane to hexane) are also present (Tassi et al., 2010; Capecchiacci et al., 2012; Scandiffio et al., 1995). Stable isotope data on H_2O (before re-injection) indicate meteoric water as the main source of the vapor (Craig, 1963; Ferrara et al., 1965). A simple mixing between two end-members could explain the isotopic composition of the steam produced in the field (Panichi et al., 1995; Scandiffio et al., 1995). Moreover, magmatic gases (SO_2, HCl and HF) are not detected. (e.g. D'Amore & Truesdell, 1979; D'Amore & Panichi, 1980; D'Amore & Celati, 1983; Bertrami et al., 1985; D'Amore & Pruess, 1986; Minissale, 1991; Duchi & Minissale, 1993; Gherardi et al., 2005; Capecchiacci et al., 2012). The only exceptions for a deep inputs among vapour dominated fluids of the present day Larderello geothermal system, can be inferred from both CO_2 isotope composition ($\delta^{13}C$ from −1.4 to −7.1‰ versus V-PDB) which is considered to derive from mixing of crustal and mantle fluids, and helium isotope ratios (R/R_A from 1.4 to 3), indicating an important mantle He contribution that may constitute up to 50% of the total He (Pennisi et al., 2001). Furthermore, Bernard-Romero et al., (2010) evidenced that B isotopes and Cl/B ratio of Larderello system indicate that a Cl and B- rich magmatic fluid is mixed with a Cl-free B-rich vapor derived from (superficial) sedimentary source.

1.1 Water-rock experiments by hydrothermal autoclave

These experiments were projected in order to reproduce the reactions between a B-rich, NaCl-rich hot fluid of magmatic derivation and the Calamita Schist (in particular with the biotite of the schist) that would yield the tourmaline observed in the tourmaline-rich hydrothermal rocks of Elba Island (see task 3.1).
The analytical methods used for laboratory experiments are described in Appendix I

1.1.1 Starting material

Solids

As solid staring material for the synthesis of tourmaline, a rock sample (GN1B) from Calamita Schist Formation outcropping in the Calamita Promontory (Elba Island) was selected. The rock is classified as a biotite–andalusite–feldspar bearing hornfels.
Since geologic evidences suggest that biotite represents the major supplier to the crystallisation of tourmaline a biotite rich separate from the whole rock (GN1B sep.) was prepared enriching biotite crystals by means of Franz isodynamic magnetic separator and the 60-120 μm granulometric fraction was selected for the experiments.
Both GN1B whole rock and GN1B sep. were characterised through X-ray diffraction (XRD). The diffractogram GN1B sep (Figure 1.1.1) indicates the presence of minor amounts of plagioclase, quartz and chlorite (chamosite). The wt% contents of minerals detected in the two starting materials made by Rietveld refinement are indicated in Figure 1.2.2a,b.
Moreover, in order to eliminate chlorite from the starting material, biotite separate was calcined at 600°C for 120 hours. The chlorite content was probably reduced below 1 wt% since its presence was not detected in the diffraction pattern, the recalculated modal mineralogy is then represented in Figure 1.1.2c. It is also remarkable the presence of andalusite in this starting material, probably as a result of passive enrichment of this phase after heat treatment.
A portion of GN1B was also analysed by means of the electron microprobe in order to characterize each mineralogical phases. Representative analyses of minerals in the starting material rock are reported in the Table 1.1.1.
As mentioned before the chlorite phase is mostly a Fe-chlorite (chamosite) and the analysed biotite are generally annite-siderophillite terms with XFe (Fe/(Fe+Mg)) in the range of 0.64-0.72. Plagioclase are mostly albitic and minor cordierite and ilmenite crystals have been also detected (not identified by XRD).
Boric acid (H_3BO_3) was chosen as B source in experiments and aqueous solution was selected as fluid reactant. With increasing temperature H_3BO_3 dehydrates in few steps and the overall reaction can be summed up as follows:

$$4H_3BO_3 = 2B_2O_3 + 6H_2O$$

Al_2O_3 was added in one experiment, just to check if tourmaline crystallization can be favoured with an addition of this chemical component.
Thus, the following starting materials were used in the experiments:

1. GN1B sep. + H_3BO_3 (4:1 in weight);
2. GN1B sep. + H_3BO_3 + Al_2O_3 (4:1:1 in weight)
3. GN1B whole rock
4. GN1B sep.
5. GN1B sep. cal.

The GN1B sep./H_3BO_3 chosen ratio should ensure a more than enough B availability in the system to theoretically transform completely biotite to tourmaline.

Fluids

Aqueous solutions with variable H_3BO_3 concentrations were selected as fluid reactant. 20 wt% NaCl were added to the starting fluid in a number of experiments. This concentration was chosen considering the results of fluid inclusion data on L type inclusions (see task 3.1). Moreover, some experiments have been carried without NaCl with the aim to verify the effect of NaCl in the reaction.

Thus, the following types of solutions were chosen in the experiments:
20wt%NaCl: 20wt% NaCl aqueous solution was prepared using suprapur NaCl and milliQ water;
0.1M: 20wt% NaCl + 0.1M H_3BO_3;
0.01M: 20wt%NaClbis + 0.01M H_3BO_3;
pure H_2O: milliQ water;
pure 0.1M: milliQ water + 0.1M H_3BO_3.
The list of experiments performed and relative conditions are reported in Table 1.1.2.

1.1.2. P-T conditions of experiments

Experiments within hydrothermal autoclave were performed using P-T conditions in the range 1000-1300 bar and 500-600°C, respectively. These conditions are considered to be realistic for tourmaline formation on the basis fluid inclusion data obtained on quartz-tourmaline veins (see report task 3.1).

1.1.3. Results

The experiments were performed varying the following parameters: T, P, starting materials, solid/fluid ratio, H_3BO_3 concentration and amount of starting material and fluid (Table 1.1.2.). The duration of each experiment was 1 week (168 hours) and after cooling, experimental products were usually washed in milliQ water to remove any salts formed.
Experiments 2-4-5 were run employing GN1B sep. and *20wt%NaCl* in "short" Au capsules (length 17-19 mm) since the aim was to assess the phase equilibria within the solid; on the contrary, experiments 6 and 7 were accomplished using the same starting materials but "long" capsules with the additional purpose of recording chemistry variations within the fluid phase.
Differently, in the experiments 8-13 the GN1B whole rock was used, together with pure water or saline solutions with decreasing boric acid concentrations (see details reported in Table 1.1.2.), employing "short" Au capsules.
Experiments 14 and 15 were run considering the GN1B sep. but using lower H_3BO_3 concentrations (0.1 and 0.01M) in comparison to experiments 2-5.
In Experiment 16 the GN1B sep cal. (calcined at 600°C for 120 hours) reacted with saline fluid (20wt%NaCl).
One experiment (Experiment 17) was planned in similar condition of Experiment 6 but with lower temperature (500°C) and a long capsule in order to recover the fluid.
Finally, Experiments 18 and 19 were run adding graphite to the starting materials (GN1B sep. or GN1B rock), just to buffer oxygen fugacity to the C-CO-CO_2 buffer.
Most of the runs were considered technically successful since the weight of capsules did not change after the experiments; on the contrary, other runs (7 and 12-14) were discarded since capsules changed their weights after the experiments.
These different sets of experiments will be distinctly discussed.

Experiments 2-4-5

Experimental products were firstly observed and analysed using SEM-EDS (scanning electron microscope – energy dispersive spectroscopy). Acicular tourmaline crystals ranging up to 20 μm were dispersed in all the three experiments, as shown in Figure 1.1.3. Biotite, chlorite and plagioclase were also observed.
Preliminary analyses on neo formed tourmaline were performed by SEM-EDS and are reported in Table 1.1.3. and represented in Figure 1.1.4. Analyses are semi-quantitative and should therefore be considered with caution.
For comparison electron probe micro analysis (EPMA)of tourmaline from Stagnone (see report task 3.1) have been reported in Figure 1.1.4.
It should be remembered that experiment 4 was executed with an Al_2O_3-doped starting material and Experiment 2 and 5 were performed with different solid/fluid ratios, respectively 0.5 and 1. Tourmaline has a wide chemical variability, also within a single experiment. This can be imputable to experimental conditions far from equilibrium or can be an artefact caused by analytical conditions (e.g. contribute of coexisting phases to the analyses).
Tourmaline in experiment 4 is richer in Al_2O_3 and poorer in SiO_2 and MgO respect to those from experiment 2 and 5 (Figure 1.1.4.) since the starting material used was Al_2O_3 doped. The SiO_2 depletion could be a consequence of Si/Al substitution in one tetrahedrally coordinated site, labelled *T*, which is predominantly occupied by Si but also can contain Al. Similarly, Mg/Al substitution in the two octahedrally coordinated sites (Y and Z) could account for MgO depletion. Tourmaline in experiment 5 have generally higher FeO contents and smaller Al_2O_3 contents respect to tourmaline in experiment 2. These variations are likely caused by the different solid/fluid ratios utilised in the experiments, this parameter being the only variable between these two experiments. Possibly, the high solid/fluid ratio in experiment 5 could have favoured the biotite dissolution (respect to experiment 2), thus favouring crystallisation of high Fe (and low Al) tourmaline. Natural tourmaline from Stagnone have similar compositions to some crystals from experiment 2, even if their MgO contents is the highest among all analyses (Figure 1.1.4.). In order to have a better mineralogical characterisation of both tourmalines and other phases found after the experiments, EPMA were performed on representative batches of powders (preparation is described in appendix I) of experiments 2,5 which are reported in Table 1.1.4.

Experiments 6-7

Experiment 6 was technically a successful run since the weight of the capsule after the run was unchanged respect to its weight before the run. On the contrary, experiment 7 is considered a failed run because weight of the capsule decreased after the run indicating that experiment was not run taking into account a closed system. Anyway, it was possible that opening of the capsule occurred during the unloading of P and T, at the end of the run. In this case information got from the solid phase could be valuable too but determination of the chemistry of the fluid phase is impractical.
Thus, extraction of the fluid phase from the capsule was limited to experiment 6. The procedure is described in appendix I The calculated dilution is 1:92.91, moreover considering also the H_2O derived from the H_3BO_3 dehydration dilution shifts to 1:92.97.
Solid phases of experiments 6 and 7 were investigated through XRD. The spectra, compared with that of GN1B sep. are reported in Figure 1.1.5.

In order to better compare mineralogy of starting material (GN1b sep.) with products of experiment 6 Rietveld refinement from powder diffraction data were performed and wt% contents of minerals in the two samples are reported in Figure 1.1.6.
Some evidences can be highlighted:

1) chlorite (chamosite) is not found in experiments 6 and 7. The experiments should have performed in a P-T area in which this phase is not stable;
2) tourmaline crystallised in experiment 6 only (25 wt%), suggesting that failure of experiment 7 occurred before P-T unloading. In particular, EPMA reveal that most tourmaline is dravite, an end-member belonging to the alkali group (as illustrated in Figure 1.1.7.);
3) Na-plagioclase increase from 44.3 to 49.0 wt%;
4) quartz amount seems to be greatly decreased in experiments respect to the starting material (4.0 to 2.0 wt%) due possibly to the increasing quartz solubility with T. Dissolved SiO_2 is thus expected to be found in the fluid phase;
5) a small amount of neo-formed K-feldspar (microcline, 1.7 wt%) appears in the experiment 6. No significant K-feldspar crystals have been found and analysed during EPMA investigation.

Moreover, investigations using backscattered electrons allowed to find Fe--oxides in experiments 6 (Figure 1.1.8.) and their analyses are reported in Table 1.1.4. They seems to be referred at both magnetite and hematite. However, the relatively high contents of SiO_2, TiO_2, Al_2O_3, MnO, MgO and Na_2O detected in these phases could suggest the presence of not-fully crystalline phases (like amorphous oxyhydroxides) and this could explain why Fe-oxides were not detected through XRD investigation (if they are more than 5 wt% in the experimental product).
Chemical composition of starting solution NaCl 20% and fluid extracted at the end of experiment 6 (solution 6) analysed by Liquid Chromatography are reported in Table 1.1.5.
The data indicate notable K contents and minor amounts of other cations and anions in solution 6. This was expected since the partial biotite transformation to tourmaline should have led a K enrichment in the fluid. Furthermore, the low difference (in meq/l) between the sums of anions and cations (expressible by an error equal to 0.62) suggest that other cations may be present in very low concentrations (ppm order).
In order to calculate the composition of the fluid found in the experiment 6, we followed two approaches (data in red in Table 1.1.5):

1) considering that fluid in capsule was diluted 1:93, we accordingly recalculated it. This recalculation evidenced a Cl depletion that could be explained by the precipitation of (a) Cl-bearing phase(s);
2) Cl was assumed to be a conservative element. Its use as a tracer indicate that dilution should have been 1:109 instead of 1:93. This was possible if about 0.100 g of the fluid into capsule 6 (total fluid= 0.659 g) was not extracted but this is considered improbable since during the fluid extraction care was taken in order to recover the entire fluid. Note that the contribute of chlorite dehydration to the H_2O budget we are considering is negligible; in addition biotite and tourmaline retain about the same H_2O contents and the tourmaline crystallisation does not consequently affect significantly the water budget.

The analyses, besides to indicate a K (and secondarily Ca, Mg and Li) enrichment in the fluid as a result of fluid rock interaction during the experiment, evidence a Na depletion expectable since it was incorporated into tourmaline. Nevertheless, this

depletion is more than expected, if mass balance calculations are performed considering that all the lacking Na entered into the tourmaline structure. In fact the amount of tourmaline required in order to account for Na depletion is 178% (approach 1) and 96% (approach 2) of the starting material used in the experiment and this is clearly impossible.
From the consideration above expressed it is likely that Cl and Na deficits in capsule of experiment 6 were caused by a precipitation of Cl and Na-bearing phase. The XRD spectrum of the solid recovered by experiment 6 (Figure 1.1.5.) even if showing some minor un-attributable peaks (e.g. d=3.75 Å), does not reveal the presence of other major phases besides those identified. Na- and Cl- bearing phases as sodalite were considered in mass balance calculations but the presence of this phase in minor amounts (in XRD there are no peaks attributable to this phase) can be excluded, since its Cl and Na contents would not justify the measured depletion of these elements in the fluid. On the contrary, halite precipitation in small amounts deplete significantly the fluid in Na and Cl. Calculations indicate that the precipitation of about 20 mg of halite (about 5 wt% of the starting material) could explain the recorded Cl deficit in experiment 6. This phase should not have dissolved in the milliQ added during the fluid extraction and this is anomalous; nevertheless, small amount of solids were trapped into the capsule despite the great majority of solids escaped from the capsule during the ultrasonic bath treatment (Figure A1.2c). It is possible that halite in solid trapped into the capsule could not have completely dissolved. The subsequent washing of the solid and filtering of solution produced could have completely dissolved halite. This could explain the lack of NaCl peaks in XRD spectrum; nonetheless even if it was not (completely) dissolved, its detection through XRD would be difficult due to its small concentration. The halite precipitation could in part resolve the Na budget as well, since tourmaline crystallisation cannot entirely account for Na depletion in fluid, as stated before. Nonetheless, the precipitation of halite (about 20 mg) and tourmaline do not explain the wholly Na depletion in the fluid after the experiment. It is therefore possible that other neo formed phases during the experiment can host some Na such as alkali feldspars (1.7 wt%) quantified by Rietveld refinement (Figure 1.1.6.).
In conclusion, we prefer to consider analyses recalculated according the first approach, e.g. using the actual dilution utilised to recover fluid from the capsule. The analyses so recalculated is compared with data got from ICP-OES and from analyses of fluid recovered from capsule relative to experiment 17 (see after, Table 1.1.6). The data of these 2 experiments will be discussed after the presentation of results relative to experiment 17.
Considering the K budget, if it is considered that K in fluid derives from biotite dissolution, it is necessary to dissolve 95 mg of this phase. This imply that about 24-25 wt% of the starting material dissolved during the experiment (forming mainly tourmaline). This value is clearly in agreement with the amount of biotite remained after the experiment 6 (22 wt%) calculated by Rietveld refinement. Moreover, biotite dissolution can explain the fluorine content in the fluid recovered. Assuming that 24 wt% of mica dissolved, this value can be obtained if F is about 0.02 atoms per formula unit in biotite. It is remarkable the considerable Li content in the fluid extracted which can be derived from biotite as well. In fact Li can be hosted in the octahedral site of the mica in significant amounts and lepidolite is the Li end-member of trioctahedral micas. Thus, mica dissolution beyond to enrich fluid in Li can also contribute to the formation of Li end-member (elbaite, Figure 1.1.7.) of the tourmaline.

Experiments 8-13

As regards experiments 8-13, which employed GN1B whole rock and pure water or saline solutions with decreasing boric acid concentrations, tourmaline was detected only in experiment 8 as evidenced in Figure 1.1.9. where XRD of experimental products are compared with XRD of the starting material.

Thus, it is relevant to note the crystallisation of tourmaline when using rock powder as starting material + H_3BO_3 and pure H_2O (MilliQ) as fluid reactant (experiment 8).

Note that chlorite is present only in the starting material GN1B (black spectra) and it disappears in all the experiments.

In the experiments 9-13 the low amount of H_3BO_3 (Table 1.1.2.) probably hindered tourmaline crystallisation; furthermore, this assumption could be not valid for Experiments 12-13 since they were not considered technically successfully.

Rietveld refinement from powder diffraction data helped to quantify mineralogical phases found in experiment 8 and wt% contents of minerals are compared with starting material (GN1B) in Figure 1.1.10. where some evidences can be highlighted:

1) chlorite, muscovite and andalusite are not present anymore;
2) a large amount of tourmaline (43 wt%) crystallised;
3) Na-plagioclase drastically decreased from 41 to 29 wt%;
4) quartz greatly decreased (from 25 to 8 wt%);
5) K-feldspar (microcline) crystallised (17 wt%).

SEM investigations allowed to observe in experiment 8 tourmaline acicular crystals with the larger size ranging up to 20 μm and the smaller one generally smaller than 2 μm. Sometimes crystals coalesce in aggregates of tens of individuals (see pictures taken in Secondary Electrons mode in Figure 1.1.11 a,b). Accurate investigations of the powders relative to experiments 9-15 was performed in order to find possible tourmaline crystals (remember that XRD does not detect a phase < 5 wt%) but the results were negative. In the other two images of Figure 1.1.11. (Secondary Electrons relative to experiment 10-11) only plagioclase and biotite crystals can be observed.

EPM analyses of mineralogical phases of experiment 8 are reported in Table 1.1.4. Tourmaline is all schorl, showing FeO contents in the range of 9-9.8 wt%, definitely higher of those detected in dravite found in experiment 6 (2.2-4.1 wt%).

In agreement with Rietveld refinement, abundant K-feldspars were found among products of the experiment 8 where they mainly surround plagioclase relicts of the starting material (Figure 1.1.12 b,c). Their composition is $An_{0-3}Ab_{21-28}Or_{65-77}$ (Table 1.1.4.).

EPMA investigations using backscattered electrons allowed to identify small Fe--oxides in experiment 8 associated to biotite and tourmaline (Figure 1.1.12 a); they are less abundant than in experiment 6 and, analogously to crystals from this latter experiment, they are probably not-fully crystalline phases (like amorphous oxyhydroxides), since they were not detected through XRD investigation.

Experiments 14 -15-16

In the next graph XRD spectra of experiments 14 and 15 are compared with experiments 6 and 7 and with the starting material (GN1B sep). Figure 1.1.13. reveals that tourmaline did not crystallised in both the experiments 14-15 where low H_3BO_3 concentrations in the reactant fluid (respectively 0.1M H_3BO_3 and 0.01M H_3BO_3) were employed.

Differently, considering the experiment performed using as starting material the calcined powder of biotite-enriched separate (Experiment 16), XRD spectrum revealed that tourmaline crystallised (Figure 1.1.14.). Thus, tourmaline crystallisation occurs when the starting material is devoid of chlorite since heating treatment at 600°C at atmospheric pressure destroyed most of this phase probably through a dehydroxylation process (see Figure 1.1.2 c). These results show that the role of chlorite in the tourmaline formation is limited and probably negligible.

Experiment 18-19

XRD spectra of experiments 18-19 (in which graphite was inserted into the capsule just to buffer oxygen fugacity) are reported in Figure 1.1.15. Note that product of experiment 18, after washing with deionised water to remove NaCl, was low in quantity and the relative spectrum has low intensities. Tourmaline peaks are present in experiment 19 spectrum and probably also in experiment 18. There are no other peaks ascribable to phases other than biotite, plagioclase and tourmaline. The introduction of graphite in capsule should have buffered oxygen fugacity close to C-CO-CO_2 buffer and these could have had an effect to the chemistry of tourmaline. The spectra give no information about this issue since peaks attributable to tourmaline do not show significant shifts from peaks resulted from un-buffered experiments. EPM analyses (still to do) would be diriment to check a possible change in chemistry (respect to tourmaline synthesised in un-buffered experiments). Rietveld refinements show that tourmaline extensively crystallised (about 93 wt% and 79 wt% in experiment 18 and 19, respectively) at expenses of biotite (<2 wt% in both runs). Albite is estimated to be 6 wt% (experiment 18) and 14 wt% (experiment 19) and quartz (4 wt%) is found only in experiment 19.

Experiment 17

Rietveld refinement of experiment 17 is sketched in Figure 1.1.16. The results of this experiment can be compared to those from experiment 6 (Figure 1.1.6.). In fact these two experiments were performed using the same starting material (GN1B), fluid (20 wt% NaCl), solid/fluid ratio (0.6), pressure (1000 bar) and similar H_3BO_3 concentrations (1.6-1.9M) but they were run at two different temperatures: 600°C (experiment 6) and 500°C (experiment 17). Rietveld refinements seems not to be congruent each other, since dissolution of biotite is greater in experiment 17 respect to experiment 6, but tourmaline crystallisation follow an opposite trend. Nevertheless, note the greater amount of feldspars (plagioclase and K-feldspar) in experiment 17 respect to experiment 6 suggesting that these phases could have been more stable at 500°C than at 600°C.

Fluid was extracted from experiment 17 following the same procedure and using the same analytical equipment used for experiment 6. The analyses of both solutions, performed using an ICP-OES and Liquid Chromatography, are reported in Table 1.1.6. and they are represented in Figure 1.1.17. where they are compared with the starting solution (20 wt%NaCl).

Apart from considerations just stated for experiment 6, it is noteworthy the high concentrations of Fe and K in the extracted fluids, likely derived from biotite dissolution, and a depletion of Na (respect to the starting solution) as a consequence of tourmaline crystallisation. However, K in experiment 17 is about the half of the value of experiment 6 and this cannot be due to a less efficient dissolution of biotite at 500°C respect to 600°C (see the results of Rietveld refinements, Figures 1.1.6. and

1.1.16.) but to a greater stabilization of a K-feldspars at the lowest investigated temperature. Concordantly, the greater dissolution of biotite at 500°C (respect to 600°C) suggested by Rietveld refinements is reflected by the Fe content measured in fluids which is greater at 500°C respect to 600°C (Figure 1.1.17.).

Experiment 20

Tourmaline was found among experimental products, as expected. Rietveld refinement (tourmaline= 29 wt%, albite= 47 wt%, biotite= 21 wt%, quartz= 4 wt%) gives results similar to those found in experiment 6; this suggests that fluid salinity is an irrelevant parameter in controlling the extent of biotite dissolution. Nevertheless, K-feldspar was not found in the refinement, inversely from experiment 6.
This (long-capsule) experiment was planned in order to analyze the fluid produced after the interaction between biotite-enriched separate and pure water. The results, shown in Table 1.1.6, indicates that K and Fe contents in the extracted fluid are one order of magnitude less than in fluids produced starting from saline solutions (experiments 6 and 17, Table 1.1.6). Furthermore, Mn is two order of magnitude less than in fluids from experiments 6 and 17. On the contrary, Si is about seven times more than in experiment 17. It is likely that the paucity of K in solution hinders K-feldspars crystallisation, differently from experiments performed with saline solutions in which Si was consequently depleted in fluids.

1.1.4 Outline of experimental results

Fluid-rock interaction experiments undoubtedly show that biotite dissolution is the major supplier for tourmaline crystallisation. They allowed to establish that tourmaline (mainly dravite and schorl) crystallisation in the experiments occurred in a short time (1 week) when each one of the following conditions are verified:
1) micaschist or biotite-enriched separate are used as solid reactant;
2) H_2O or H_2O+NaCl are used as fluid reactant;
3) H_3BO_3 concentration is greater than a threshold, which can be roughly indicated as 1.5 M.

Lithium may be present in tourmaline, possibly shifting some of them to elbaite compositions, but this element was not analysed due to analytical constraints.
The presence of feldspars in the starting material is important when pure water is used since it supplies Na, necessary for tourmaline formation. Iorn oxides and K-feldspars were also detected among neo-formed phases, the former being more abundant when saline fluid was utilised, the latter mostly rounding albite relicts in runs performed with pure water. Other minor phases originally in the starting material (e.g. chlorite, muscovite, andalusite) were not detected among experimental products.
At the end of experiments in which saline aqueous solution was employed, biotite dissolution and tourmaline crystallisation caused enrichment in K and Fe and depletion in Na in the recovered fluid. Such Fe enrichment can have key metallogenic implications in SE Elba where Fe ore deposits are known from ancient times. Nevertheless, fluid salinity appears to be an irrelevant parameter in controlling biotite dissolution.

1.2 Thermodynamic modelling

Thermodynamic modelling of fluid rock interaction processes possibly developed in Elba geothermal system, was performed using SUPCRT92, TOUGHREACT PITZER 1.21 and PHREEQC 3.2 EOS 2 packages, compiling apposite thermodynamic databases (for both solid phases and gases) as reported and discussed in Appendix 1.

1.2.1 Results

The effectiveness of the process tested by means of laboratory experiments (chapter 1.1) is modelled as described below.
At first, we used the new acquired data to assess the tourmaline stability field, referring as precipitation of tourmaline from ions in solution. This reaction could be summed up with the dissolution of biotite, and written as a whole process distinguished by its two endmembers (Fe and Mg endmembers) with respect to oxides and aqueous ions:

Fe endmembers:

$NaOH + 3\ B(OH)_3 + 6$ **Annite** ⇔ **Schorl** $+ 15\ FeO + 6\ H_2O + 6\ KOH + 12\ SiO_2$
(1)

In aqueous phase:
$5H^+ + Na^+ + 3\ B(OH)_3 + 6$ **Annite** ⇔ **Schorl** $+ 15\ FeO + 11\ H_2O + 6\ K^+ + 12\ SiO_2$
(2)

Mg endmembers:

$NaOH + 3B(OH)_3 + 6$ **Phlogopite** ⇔ **Dravite** $+ 15\ FeO + 6\ H_2O + 6\ KOH + 12\ SiO_2$
(3)

In aqueous phase:
$5H^+ + Na^+ + 3\ B(OH)_3 + 6$ **Phlogopite** ⇔ **Dravite** $+ 15\ FeO + 11\ H_2O + 6\ K^+ + 12\ SiO_2$
(4)

Schorl – Dravite solid solution:

$3\ Mg^{2+}$ + **Schorl** ⇔ $3\ Fe^{2+}$ + **Dravite**
(5)

This set of reactions is enough to describe the process of biotite dissolution and tourmaline formation and we could compute the stability field of tourmaline. As an example, in Figure 1.2.1. we report the Saturation Index (SI) of tourmaline, versus pressure and temperature, in case of NaCl 20 wt% salinity (from fluid inclusions), pH 3, and activities set equal to 1 except for $B(OH)_3$. In details, Figure 1.2.2a shows the little dependence of tourmaline SI with Pressure and in Figure 1.2.2b is illustrated the SI dependence with temperature considering different Boron activities in the fluid.

According to the fluid inclusions data, the fluid at Elba Island should have a temperature in the range of 500°C or higher, and a salinity as NaCl near 20 wt%. We can see in Figure 1.2.2 b that tourmaline could be formed also at lower temperature, given a high enough boron concentration.
Furthermore, we should investigate the biotite stability with respect to pH. Boric acid in fact is a weak acid, and related solutions could reach a pH low enough for dissolving biotite only for high boric acid concentration, or at high temperature where biotite stability is lower.
In Figure 1.2.3 we could observe biotite stability as function of pH (obtained titrating with HCl) at 250 (Figure 1.2.3 a) and 500°C (Figure 1.2.3 b). As illustrated in Figure 1.2.3. the pH needed to have significant biotite dissolution, increases with temperature. Therefore, a high concentration of boron is able by itself to provide biotite dissolution and tourmaline precipitation at low temperature (e.g. lower than 400°C) and tourmaline could precipitate at lower temperature given other acidic component able to provide the biotite dissolution.
As illustrated in Figure 1.2.4., where temperature versus pH is shown for two different boric acid concentrations, biotite dissolution does not occur at low temperatures for boric acid concentration ≤ 1. In this thermodynamic framework it is clear that in the experiments tourmaline is formed only at high temperature or when acid boric contents are extremely high.
Several experiments (see Table 1.1.2.), in which tourmaline was successfully formed, were carried out considering biotite enriched starting material (GN1B sep.) at 500°C, 1000 bar, 20 wt% of NaCl. Some modelling of these series of experiments were performed in order to verify the conditions for tourmaline crystallisations.
Since high temperature and pressure are not available in the standard code, thus the first step was to assess the physical state of water phase according to the phase diagram reported in Figure A2.1.
The diagram (IAPWS-95 and IF97) shows that at the considered conditions water is still a liquid. There are papers (e.g. Driesner, 2007 and reference therein) that review the water phase diagrams, with similar results. In this case, the adopted solutions were to insert the correct values of physical and thermodynamic properties of water, and use the TOUGHREACT software package in batch reaction mode. Following the modelling, results evidenced that, as long as the reaction proceed, biotite (annite 60 wt%, phlogopite 40 wt%, as obtained from GN1B biotite analyses and literature data, Dini et al., 2008; Cavarretta and Puxeddu, 1990) was consumed and tourmaline formed.
The concentration variation of some of the major dissolved species (i.e. Fe, Mg, Al, K and SiO_2) in the fluid at various temperature corresponding to the tourmaline-biotite equilibrium were also modelled (Figure 1.2.5.). In this model we consider a NaCl concentration of 20 wt% and a $B(OH)_3$ concentration of 2M, that is enough acid to lead to the simultaneous equilibrium of annite, phlogopite, schorl and dravite. The concentration of magnesium is controlled by dravite-phlogopite equilibrium, as well the concentration of Iron(II) is controlled by annite-Schorl equilibrium at Eh=1.04 (Volt SHE).
The model shows a decrease of Fe, Mg and Al with temperature up to 425°C, then these species increase up to 550°C. SiO_2 remain more or less constant whereas K is relatively constant up to 500°C and then decrease. As shown in Fig. 1.2.5 the concentration of Mg in the fluid is higher than that of Fe. This contrasts with the results of laboratory experiments which always shows that Fe occur in higher

concentrations with respect Mg, in particular in the saline fluid (Tab. 1.1.6). This discrepancy can be likely related to the occurrence of Fe-chloride complex in the saline solution which greatly increase Fe solubility in aqueous solutions (Seward & Barnes, 1997). In the thermodynamic models, in fact, the effect of Fe complexation due Cl cannot be considered. Moreover, it is noteworthy to point out that the water pH due to boric acid is nearly 3, but once the biotite is dissolved and the simultaneous equilibrium between biotite and tourmaline is achieved, pH will rise up to 7 at 425°C (Figure 1.2.6.), then pH gently drop at higher temperature because of the increased instability of biotite with respect to tourmaline.

1.2.2 Model validation against literature and experimental data

The validation of the thermodynamic model was attempted on the basis of the evolution of Fe/Mg partition in tourmaline during progressive biotite dissolution, by comparing published data on natural tourmaline, from Larderello geothermal field (Cavarretta & Puxeddu, 1990) and quartz-tourmaline veins of Elba Island (Dini et al., 2008), and on tourmaline obtained from the experiments with our theoretical batch reaction model. In the model, an useful immediately available parameter is the reaction progress, while in the literature data this parameter is obviously hardly deduced.
In Cavarretta & Puxeddu (1990) an information on the ongoing reaction can be obtained by the core-rim chemical variability in tourmaline crystals. In this paper the authors describe the evolution of tourmaline found in Larderello San Pompeo and VC11 wells, with the latter being particularly suitable for this purpose.
In Dini et al. (2008) a chemical variation in tourmaline is established based on both structural and petrological inferences, so that a reaction process could be approached. As a consequence an early and a late stages of tourmaline formations are hypothesized.
The results of the comparison between modelling and natural samples from Cavarretta & Puxeddu (1990) and Dini et al. (2008) are shown in Figure 1.2.7., where true (for model) and inferred (for natural samples) reaction progress is plotted vs XFeO (FeO/(FeO+MgO). The agreement between modelled and natural data is quite good.
Modeling of the experimental data were carried out taking into account the different experimental conditions (Table 1.1.2.) and the Fe(II) – water buffer for redox condition. From a theoretical point of view, and following the model of biotite dissolution and tourmaline formation, we could have two end-members: 1) the tourmaline at early stage of formation (very beginning of modelled reaction) having around 0.9 XFeO; 2) the tourmaline at the late stage of reaction having (from theoretical model) 0.65 XFeO, as reported in Table 1.2.1. The equilibrium composition have an error due to the uncertainty in the experimental condition, that are 500°C, NaCl 20%, Biotite GN1B-H3BO3 4:1.
The experimental and modeled data compare relatively well (Table 1.2.1.), and we believe that the low XFeO found in the experiment 2 is due to the poor control of oxygen fugacity, that may have led to Fe(III) oxy-hydroxides formation.

1.2.3. Model of Tourmaline and Ore deposit formation

The knowledge of mineral dissolution and self-sealing processes and their spatial-temporal evolution is critical in order to understand the dynamic evolution of

geothermal reservoirs. The hydrothermal systems of Elba Island, recorded by the quartz-tourmaline veins within the Mt. Calamita schist, represent a deep geothermal reservoir similar to a super-hot reservoir occurring below the exploited Larderello geothermal reservoir. On the other hand, the Fe deposits of Elba Island examined in task 3.1 are fossil hydrothermal systems that can represent shallower reservoirs similar to those presently exploited at Larderello (see report task 3.1). Assuming that these two geothermal reservoirs were interconnected we can suppose that the fluid which reacted with biotite in the deep reservoir producing tourmaline and a Fe-enriched fluid raised up within the shallower reservoir where precipitated Fe as iron-oxides.

In this paragraph, we present a theoretical model that simulates this fluid evolution. In particular, we consider a hydrothermal event in which a micaschist block reacted with a B-rich hot fluid in order to simulate how and where within the rock block, biotite dissolution, tourmaline crystallization and iron oxides deposition took place.

Fluid inclusion studies showed that fluid-rock interaction in quartz-tourmaline veins should have occurred at relatively high temperature (e.g. 420-650°C) in the presence of a boron-rich saline fluids. Our model, however, was limited by the up-to date maximum temperature available with TOUGHREACT-EOS2 which is about 350°C. Nevertheless, the latter temperature is comparable with the temperature range indicated by fluid inclusions for the deposition of the Fe deposits (see report task 3.1).

In order to be within the validity range of TOUGHREACT equation of state, we choose a B content in the fluid, so that the biotite-tourmaline reaction could take place at temperature lower than 350°C. To model the tourmaline formation from micaschist due to an 'hydrothermal event', we assumed as initial steady state a column 1x1 km with 5 km height, in its hydrostatic (from 1 bar to nearly 433 bar) pressure with a normal thermal gradient (from 20 to nearly 200°C). For simplicity the mineralogy of the column is modelled similar of biotite separate (GN1B sep.) and is reported in Table 1.2.2.; it is assumed uniform in the model.

The fractures within the column are modeled using 5 elements, the central one having high permeability ($1E^{-13}$ m^2, mesh size 4 cm) and the 2 elements at each side with lower permeability ($1E^{-15}$ m^2, mesh size 3 cm), while whole rock column have $1E^{-17}$ m^2.

The hydrothermal event was modeled using an inflow of hot water (330°C) with high boron concentration (2mol/kg), with 1 kg/s constant inflow in the fracture at the bottom center of the column for 50 years. We also assume that the uprising fluid mixed at shallower level with oxidizing formation water. Such water may be meteoric fluid similar to those recorded by the low-salinity fluid inclusions present within quartz crystals of most of the Fe deposits (see report task 3.1).

In the simulation, the most extended effect, after 50 years, is the pH variation; the hydrolysis pH for the given rock composition is 11.15, but it is easily re-buffered at a pH nearly 7.2, while the hot, boron-rich fluid reach a buffer at a pH of 4.53 at the fracture bottom, causing biotite dissolution. In Figure 1.2.8. we could observe the annite (biotite) dissolution at the bottom of block according to the dissolution reaction before mentioned. In a zone slightly below (Figure 1.2.8 b), the hot boron-rich fluid allow the schorl precipitation, while the iron excess present in the uprising fluid is readily precipitated as magnetite in an upper zone, i.e. as soon as the mixing with formation water provide enough dissolved oxygen to allow magnetite precipitation, and the fluid is cooled down as well.

To have an idea of the model sensitivity respect to permeability, we carried out a second model where the fracture is modeled using the same 5 elements the central one having high permeability ($1E^{-13}$ m^2, mesh size 4 cm) and 2 elements at each side and granite having higher permeability (respectively $1E^{-14}m^2$, mesh size 3 cm; and $1E^{-15}$ m^2) respect to the previous simulation.
The hydrothermal event was modeled using the same inflow of hot water (330°C) with high boron concentration (2mol/kg), with 1 kg/s constant inflow in the fracture at bottom center for 50 years.
The results are exactly the same of previous simulation, with after 50 years, there is the pH variations; the hydrolysis pH for the given rock composition is 11.15, but it is easily re-buffered at a pH nearly 7.2, while the hot boron rich fluid reach a buffer at a pH of 4.53 at the fracture bottom, causing biotite dissolution.
Differently from the previous case (Figure 1.2.9.), due to the higher permeability, the hot, boron-rich fluid allow more diffuse annite dissolution and schorl precipitation, while the iron excess present in the uprising fluid is readily precipitated as magnetite in an upper zone, i.e. as soon as the mixing with formation water provide enough dissolved oxygen to allow magnetite precipitation, and the fluid is cooled down as well. At shallower level the formation fluid can contain enough oxygen that would form a Fe^{+3} deposits (e.g. hematite).
In order to test the model sensitivity to fluid flow rate we changed the fluid flow, with respect to the reference case, increasing from 1 to 5 Kg/s. This change could also be related to the change in porosity, because the upraising fluid velocity is proportional to fluid flow divided by porosity. On a thermodynamic point of view, no significant changes can be observed, and both the alteration zone (biotite dissolution and tourmaline formation) and magnetite deposition (within the fracture and aside on top of the structure) keep standing still as reported for reference case. But, being this a kinetic model, higher velocity means lower contact time for both dissolution and precipitation, thus the resulting liquid phase have a lower ions content. The lower ions content reflect in a slightly enhanced dissolution of the rock forming minerals, but on the other hand the amount of deposited minerals (secondary phases) is lower, as shown in Figure 1.2.10.
The results of the sensitivity show that, since magnetite precipitate during the fluid cooling, the magnetite ore deposit will be formed at a longer distance from the model bottom. The iron rich fluid are responsible for the ore deposit, but as the process stop they remain as vein filler, depositing Iron oxides during the cooling stage. These considerations support the hypothesis that partial dissolution of the biotite-rich rocks (e.g. micaschists) could have provided the Fe necessary to form iron ores, besides to allow the crystallization of tourmaline.

1.3 Discussion

1.3.1 Synthesis of tourmaline and their comparison with natural crystals

Synthetic tourmaline is acicular (with the longest size ranging up to 20 μm). As comparison, natural tourmaline in veins crosscutting Mt. Calamita micaschist in SE Elba are acicular as well, even if their longest size can exceed 100 μm. Crystal chemistry shows that synthetic tourmaline belong to the alkali group, being mainly

dravite with secondarily schorl (Table 1.1.4.), like natural crystals found in Elba Island (e.g. Dini et al., 2008). Thus, natural and synthetic tourmaline have both similar textural and compositional features. In particular, as regards this latter feature, the variation of some important major oxides in natural and synthetic tourmaline are shown in Figure 1.3.1. Synthetic crystals were split in two groups: crystals formed by reacting the biotite-enriched separate (GN1b sep.) with saline fluid (Group 1) and those formed by reacting whole rock (GN1B) with pure water (Group 2, Experiment 8). These latter tourmaline have Na_2O values similar to natural crystals and generally lower than tourmaline from Group 1. On the contrary, CaO values of Group 2 tourmaline is higher than contents in Group 1 and both are within the range of natural crystals. FeO and MgO contents of Group 2 tourmaline is respectively higher and lower respect to those from Group 1 and overlap values of natural crystals. Group 1 tourmaline has lower FeO contents respect to natural tourmaline at constant MgO and this can be an effect of the different oxygen fugacity conditions under which crystals formed.
The first experiments were run using saline fluid as reactant (Table 1.1.2.) since the introduction of Na was thought to be crucial in order to get tourmaline crystallisation. Nevertheless, experiments show that tourmaline also forms when pure water is utilised, so that Na necessary for their crystallisation derives from plagioclase dissolution. Furthermore, the utilisation of saline fluid caused the crystallisation of Mg-rich tourmaline (dravite) whereas when pure water was used, Fe-rich tourmaline (schorls) formed. This indicates that fluid salinity is a crucial parameter in controlling the chemistry of tourmaline, since the complexing role of Cl controls Fe content in solution (from the dissolution of biotite, as will be after discussed) and, as a consequence, in neo-formed phases. In fact, the high Fe contents found in fluids at 500-600°C when saline fluid was employed in experiments (Figure 1.1.17.) are imputable to the complexing agent of Cl, causing $FeCl_4^{2-}$ to be the Fe main species in solution, as results from PHREEQC simulation. This implies an important role of Fe-Cl complexing on Fe solubility at hydrothermal conditions, as also known from literature (e.g. Ding & Seyfried, 1992).
In this context the composition of tourmaline could be considered as a proxy of the salinity of the fluid from which they crystallised. In addition, Mg/Fe variation of tourmaline can be imputed to the reaction progress of biotite dissolution as well, as modellised and shown in Figure 1.2.7. Tourmaline could have registered different steps in the reaction completion, thus denoting a not equilibrium conditions in experiments. Besides Fe, Cl can be a complexing agent for K (available from biotite dissolution, as well). This is indicated by K analyses in solutions extracted when saline solutions were used (Figure 1.1.17.) and by the comparison of Rietveld refinements of experimental products obtained when saline solution (Figure 1.1.6.) or pure water (Figure 1.1.10.) were employed. Analogously to Fe behaviour, K remains preferentially in solution if Cl is here available; on the contrary, K enters in neo-formed feldspar (Figure 1.1.12.) if pure water is used as fluid reactant.
Tourmaline was not synthesized when H_3BO_3 concentration was low (indicatively less than 1.5M). In fact, in such experiments pH was probably not low enough in order to have a significant biotite dissolution. pH must be lower than a threshold to dissolve entirely biotite, as shown in Figure 1.2.3. (at T= 500°C); such low pH values can be achieved increasing H_3BO_3 concentration (see e.g. Figure 1.2.4).

1.3.2 Fluid-solid interaction, mass balance and metallogenic implications

Results of experiments indicate that biotite is the major supplier for tourmaline formation; anyway, the use of biotite-enriched separate (instead of the whole rock) as starting material did not enhance significantly tourmaline formation. This dissolution mainly caused K and Fe mobilization in the resulting fluid and part of this Fe is certainly responsible for Fe--oxides formation observed among residual phases after the experiment, as well in fluid inclusions in natural samples (report of Task 3.1, paragraph 1.5.1)
A possible reaction reporting equilibrium of biotite and tourmaline with the corresponding aqueous solution, obtained by the findings of theoretical modelling (reaction 2 and 4, chapter 1.2), is hereafter reported. We preferred to report two reactions considering either Fe- (annite - schorl, reaction 6) and Mg- (phlogopite - dravite, reaction 7) end-members.

Fe end-members:
6**Annite** + $5H^+$ + Na^+ + $3B(OH)_3$ ↔ **Schorl** + $15FeO$ + $11H_2O$ + $6K^+$ + $12SiO_2$ (2)

Mg end-members:
6**Phlogopite** + $5H^+$ + Na^+ + $3B(OH)_3$ ↔ **Dravite** + $15MgO$ + $11H_2O$ + $6K^+$ + $12SiO_2$ (4)

In particular, considering the actual mineral chemistry detected among starting materials and experimental products, the following reactions could be proposed when using saline aqueous solution (20 wt% NaCl, reaction 6) or pure water (reaction 7) as fluid reactant:

Using saline aqueous solution:
$6KFe_{2.1}Mg_{0.9}AlSi_3O_{10}(OH)_2$ + $5H^+$ + Na^+ + $3B(OH)_3$ ↔ $NaFe_{0.5}Mg_{2.5}Al_6(BO_3)_3Si_6O_{18}(OH)_4$ + $2.9MgO$ + $12.1FeO$ + $11H_2O$ + $6K^+$ + $12SiO_2$ (6)

Using pure water:
$6KFe_{2.1}Mg_{0.9}AlSi_3O_{10}(OH)_2$ + $5H^+$ + Na^+ + $3B(OH)_3$ ↔ $NaFe_{1.8}Mg_{1.2}Al_6(BO_3)_3Si_6O_{18}(OH)_4$ + $4.2MgO$ + $10.8FeO$ + $11H_2O$ + $6K^+$ + $12SiO_2$ (7)

Mass balance calculation following reaction (2) indicates that about 17 wt% of the Fe produced by annite dissolution enters in schorl and the remnant is available is available to enter in other neo-formed phases and/or dissolved in solution. Fe mass-balance calculations performed in experimental products are compatible to the accomplishment of such reaction. For example, if experiment 6 is taken into account (considering its real chemistry of minerals, reaction 6, Table 1.1.4.), the Fe produced by the modal amount of biotite actually dissolved (Figure 1.1.6.), is partitioned as follows: 18.7 wt% in tourmaline, 8.2 wt% in the recovered fluid (Table 1.1.6), the remnant (73.1 wt%) being mostly incorporated in neo-formed Fe--oxides (Figure 1.1.8.) corresponding to a modal amount of Fe-oxides of 4.7 wt%. The presence of newly formed Fe-oxides was, in fact, by SEM observations. However, these phases were probably not-fully crystalline (like amorphous oxyhydroxides) and this could

explain why Fe-oxides were not detected through XRD investigation. It is likely that Fe-oxides formed during the cooling at the end of experiments, since the stability of Fe-Cl species generally decreases with falling temperature (Ding & Seyfried, 1992). If water is used as fluid reactant (e.g. experiment 8, reaction 7) the Fe sequestered in tourmaline is much higher than before (70.0 wt% of the Fe produced by biotite dissolution), due to its schorlitic composition (Table 1.1.4.) and to its greater amount of crystallisation (Figure 1.1.10.). This explains why Fe--oxides were scarcely found among experimental products of experiment 8.
In the complex, these data highlight the high Fe availability as a consequence of biotite dissolution in the presence of saline fluids and they may have important metallogenic implications in an area where Fe deposits have been known and exploited from ancient times. These consequences have been simulated using TOUGHREACT equation of state in chapter 1.2, although at temperature lower than 350°C. The theoretical model showed that biotite dissolution due to a boron-rich fluid could lead to the precipitation of tourmaline at relatively low temperature, with a related iron oxide deposition into a zone located at longer distance from the model bottom similarly to what we can observe in the fossil hydrothermal systems of Elba Island.

The same concordance between calculus on experimental observations and on reaction (7) can be obtained using K. On the other hand, mass balance calculation based on Na suggests that other Na-bearing phases crystallize during experiments, apart tourmaline. A valuable process should be the albitisation of muscovite, according to the following reaction:

$$3Na^{+} + KAl_2(AlSi_3)O_{10}(OH)_2 + 6SiO_2\ (aq) = 3NaAlSi_30_8 + 2H^{+} + K^{+}$$
(8)

This reaction is favoured by the availability of SiO_2 (during the experiments) produced by reactions 2, 4, 6, 7 - and should explain the disappearance of muscovite, the increase of plagioclase and the appearance of K-feldspar in the experimental products respect to the starting material. This reaction was proposed to occur during the metasomatism processes in the Mt. Calamita area by Puxeddu et al. (1984) (see pag. 102).
Biotite is the major supplier of tourmaline, as above emphasised, and it undoubtedly dissolves in significant amounts. On the contrary, the fate of plagioclase during the experiments is less evident. It is not dissolved in experiments in which saline solution was used (e.g. Figures 1.1.6. and 1.1.16.) but the opposite occurs if pure water was utilised in runs (e.g. Figure 1.1.10.). Thus, if Na is available in solution, tourmaline crystallises without requiring plagioclase dissolution. Differently, tourmaline crystallisation necessarily involves plagioclase dissolution if Na is not present from the start in solution.

1.3.3 Comparison with the Larderello geothermal fluid

One of the aim of this task is to validate the result of water-rock interaction experiments and modelling with the data of the fluids of active geothermal system. As stated in the introduction, the quartz-tourmaline veins of Elba Island are considered a proxy of a super-hot reservoir present below the exploited Larderello geothermal

reservoirs which was likely reached by the San Pompeo well at the depth of the K-horizon. Such super-hot reservoir could represent a hydrothermal circuit confined at the top of a recent granite intrusion (Bertini et al., 2006), not directly connected with the overlying fluid reservoirs mostly dominated by meteoric recharge, that are currently exploited for geothermal fluids. In fact, despite upper temperatures (>300°C cf. Barelli et al., 2000) are registered for geothermal steam currently deriving from lower permeable horizons of metamorphic basement, a clear magmatic contribution in such fluids does not result except for He, CO_2 and B (see chapter 1 and reference therein).
Since reliable data on the fluid stored in this reservoir are lacking the validation of our result by comparing the compositions of geothermal fluids with those obtained from laboratory experiments and/or thermodynamic modelling was nearly hindered. However, a validation of the thermodynamic models was performed by comparing the tourmaline compositions of the models with those reported by Cavarretta & Puxeddu (1990) for the tourmaline of the Larderello geothermal field (see paragraph 1.2.2.). Moreover, we can also observe that at Larderello the occurrence of magmatic B is at least suggested by B isotopes and Cl/B ratio indicating that a Cl and B- rich magmatic fluid is mixed with a Cl-free B-rich vapor derived from (superficial) sedimentary source Bernard-Romero et al. (2010).

1.4 Final remarks

The results of experimental data and thermodynamic modelling of fluid-rock interaction in the fossil super-hot reservoir of Elba Island highlight the following conclusions:
The formation of tourmaline veins in Eastern Elba is compatible with the interaction between a B-rich fluid with micaschist from Mt. Calamita at T= 500-600°C and P= 1000-1300 bars. Thermodynamic modelling showed that tourmaline can also form at lower temperature if the pH is sufficiently low. A low pH is in fact necessary for biotite dissolution. The acidity of the fluid can be provided by H_3BO_3 if it occurs in high concentrations or by additional acidic species (i.e. HCl, H_2SO_4).
Synthetized tourmaline is mainly dravite and minor schorl and show a good compositional overlapping with natural crystals. The presence of NaCl strongly influence tourmaline compositions.
The interaction process caused fluid enrichment in K and Fe (when using saline solution). Thermodynamic modelling showed that if this Fe-rich fluid upraise at shallower level it readily precipitate magnetite as soon as the mixing with oxidizing water provide enough dissolved oxygen to allow magnetite precipitation, and the fluid is cooled down as well. This process likely explain the occurrence of the Fe deposits present in Elba Island.
An important consequence of the above points concern the possible exploration/exploitation of the super-hot geothermal reservoir that likely occur at the depth of the K-horizon in the Larderello geothermal area. If this horizon will be reached by deep geothermal wells it is expected to find tourmaline-rich rocks. Moreover, the deep reservoir fluid would be characterised by low-pH and significant content of B, Fe, K, in addition to Na and Cl. If such fluid become in contact with an oxidizing environment and/or is cooled it is expected that precipitated iron oxides.

References

Barelli A., Bertini G., Buonasorte G., Cappetti G. & Fiordelisi A. (2000). Recent deep exploration results at the margins of the Larderello–Travale geothermal system. In: Proceedings World Geothermal Congress 2000, pp. 965–970.

Batini F., Bertini G., Gianelli G., Pandeli, E. & Puxeddu M. (1983). Deep structure of the Larderello field: contribution from recent geophysical and geological data. Mem. Soc. Geol. Ital., 25, 219–235.

Batini F., Brogi A., Lazzarotto A., Lotta D. & Pandeli E. (2003). Geological features of the Larderello-Travale and Mt. Amiata geothermal areas (southern Tuscany, Italy). Episodes, 26, 239–244.

Bernard-Romero R.A., Taran Y.A. & Pennisi M. (2010). Geochemistry of boron in fluids of Los Humeros and Los Azufres hydrothermal systems, Mexico, in Birkle and Torres-Alvarado (eds), Water-Rock Interaction 2010, Taylor and Francis Group, London, pp. 145-148.

Bertini G., Casini M., Gianelli G. & Pandeli E. (2006). Geological structure of a long-living geothermal system, Larderello, Italy. Terra Nova, 18, 163–169.

Brogi A., Lazzarotto A., Liotta D. & Ranalli G. (2005). Crustal structures in the geothermal areas of southern Tuscany (Italy): Insights from the CROP 18 deep seismic reflection lines. Journal of Volcanology and Geothermal Research, 148, 60–80.

Capecchiacci F. (2012). Geochimica dei fluidi vulcanici e idrotermali: Origine delle componenti organiche e loro impatto ambientale. Tesi Dottorato di ricerca in Scienze Della Terra, XXIII ciclo. Settore scientifico disciplinare: GEO-08. Università degli Studi di Firenze.

Cathelineau M., Marignac C., Boiron M.C., Gianelli G. & Puxeddu M. (1994). Evidence for Li-rich brines and early magmatic fluid rock interaction in the Larderello geothermal system. Geochim. Cosmochim. Acta, 58, 1083–1099.

Cavarretta G. & Puxeddu M. (1990). Schorl – dravite - ferridravite tourmalines deposited by hydrothermal magmatic fluids during early evolution of the Larderello geothermal field, Italy. Economic Geology, 85, 1236-1251.

Craig H. (1963). The isotope geochemistry of water and carbon in geothermal areas. In: Nuclear Geology on Geothermal Areas, E. Tongiorgi (Ed.), Pisa, Lab. di Geol. Nucl., CNR, Pisa.

D'Amore F. & Pruess K. (1986). Correlations between steam saturation, fluid composition and well decline in vapor-dominated reservoirs. Geothermics 15, 167–183.

D'Amore F. & Celati R. (1983). Methodology for calculating steam quality in geothermal reservoirs. Geothermics 12, 129–140.

D'Amore F. & Panichi C. (1980). Evaluation of deep temperatures of hydrothermal systems by a new gasgeothermometer. Geochim. Cosmochim. Acta 44, 549–556.

D'Amore F. & Truesdell A.H. (1979). Models for steam chemistry at Larderello and The Geysers. In: Proceedings of the 5th Workshop on Geothermal Reservoir Engineering, Stanford, CA, pp. 283–297.

Debye P. & Huckel E. (1923). Zur Theorie der Elektrolyte. Phys. Z.; 24, 185-206.

Ding K. & Seyfried W. (1992). Determination of Fe-Cl complexing in the low pressure supercritical region (NaCl fluid): Iron solubility constraints on pH of subseafloor hydrothermal fluids. Geochimica et Cosmochimica Acta, 56(10), 3681–3692. doi:10.1016/0016-7037(92)90161-B.

Dini A., Mazzarini F., Musumeci G. & Rocchi, S. (2008). Multiple hydro-fracturing by boron-rich fluids in the Late Miocene contact aureole of eastern Elba Island (Tuscany, Italy). Terra Nova. doi:10.1111/j.1365-3121.2008.00823.x.

Duchi V. & Minissale A. (1993). A new hypothesis on the production of Cl-bearing steam in the Larderello geothermal field, Italy. Chem. Erde, 53, 259-271.

Dutrow B.L. & Henry D.J. (2011). Tourmaline. A geological DVD. Elements, 7, 301-306.

Ferrara G.C., Gonfiantini R. & Panichi C. (1965). La composizione isotopica del vapore di alcuni soffioni di Larderello e dell'acqua di alcune sorgenti e mofete della Toscana. Atti Soc. Tosc. Sc. Nat., 72, 3–21.

Gherardi F., Panichi C., Gonfiantini R., Magro G. & Scandiffio G. (2005): Isotope systematics of C-bearing gas compounds in the geothermal fluids of Larderello, Italy. Geothermics, 34, 442–470.

Gianelli G., Manzella A. & Puxeddu M. (1997). Crustal models of the geothermal areas of southern Tuscany (Italy). Tectonophysics, 281, 221–239.

Hawthorne F.C. & Dirlam D.M (2011). Tourmaline the indicator mineral: From atomic arrangement to Viking navigation. Elements, 7, 307-312.

Helgeson H.C., Delany J.M., Nesbitt H.W. & Bird D.K. (1978). Summary and critique of the thermodynamic properties of rock-forming minerals. Amer. J. Sci., 278a, 229 pp.

Holland T.J.B. and Powell R. (2004). An internally consistent thermodynamic data set for phases of petrological interest. J. metamorphic Geol., 1998, 16, 309–343.

Holland T.J.B. and Powell R. (2011). An improved and extended internally consistent thermodynamic dataset for phases of petrological interest, involving a new equation of state for solids. J. metamorphic Geol., 29, 333–383.

Johnson J.W., Oelkers E.H., & Helgeson H.C. (1992). SUPCRT92: A Software Package For Calculating The Standard Molal Thermodynamic Properties Of Minerals, Gases, Aqueous Species, And Reactions From 1 To 5000 Bar And 0 To 1000°C. Computers & Geosciences, 18, 899-947.

Knight C.L. & Bodnar R.J. (1989). Synthetic fluid inclusions: IX. Critical PVTX properties of NaCl-H_2O solutions. Geochimica et Cosmochimica Acta, 53, 3-8.

London D. (2008). Pegmatites. Canadian Mineralogist Special Publication 10, 347 pp.

Lutterotti L, Bortolotti M., Ischia G., Lonardelli I. & Wenk H.-R. (2007). Rietveld texture analysis from diffraction images, Z. Kristallogr., Suppl. 26, 125-130.

Maier C.G. & Kelly K.K. (1932). An equation for the representation of high temperature heat content data. Am. Chemical Soc. Jour., 54, no. 8, 3243-3246.

Marini L. & Manzella A. (2005). Possible seismic signature of the α–β quartz transition in the lithosphere of Southern Tuscany (Italy). Journal of Volcanology and Geothermal Research, 148, 81–97.

Minissale A. (1991). The Larderello geothermal field: a review. Earth-Science Reviews, 31, 133-151.

Ogorodovaa L.P., Melchakova L.V., Kiseleva I.A. & Peretyazhko I.S. (2012). Thermodynamics of natural tourmalines—Dravite and schorl. Thermochimica Acta, 539, 1– 6.

Panichi C., Scandiffio G. & Baccarin F. (1995). Variation of geochemical parameters induced by reinjection in the Larderello area. In: Proceedings of the Geothermal Congress 1995, 18–31 May, Florence, Italy (E. Barbier et al. eds.), 1845–1849.

Pennisi M., Magro G. & Adorni-Braccesi A. (2001). Boron and Helium isotopes in geothermal fluids from Larderello (Italy), in Cidu (ed), Water-Rock Intarction 2001, Swets & Zeitlinger, Lisse, pp. 899-902.

Pitzer K.S. (1973). Thermodynamics of electrolytes - I. Theoretical basis and general equations. Journal of Physical Chemistry, 77, 268-277.

Pokrovskii V.A., (1999). Calculation of the standard partial molal thermodynamic properties and dissociation constants of aqueous HCl0 and HBr0 at temperatures to 1000°C and pressures to 5 kbar - Revised equations of state for the standard partial molal properties of ions and electrolytes. Geochimica et Cosmochimica Acta, 63, 1107-1115.

Puxeddu M., Saupè F., Dechomets R., Gianelli G., & Moine B. (1984). Geochemistry and Stratigraphic correlations - Applications to the investigation of geothermal and mineral resources of Tuscany, Italy. Chemical Geology, 43, 77–113.

Ruaya J.R. & Seward T.M. (1987). The ion-pair constant and other thermodynamic properties of HCl up to 350°C. Geochimica et Cosmochimica Acta, 51, 21–130.

Ruggieri G., Cathelineau M., Boiron M.C. & Marignac C. (1999). Boiling and fluid mixing in the chlorite zone of the Larderello geothermal field. Chem. Geol., 154, 237–256.

Scandiffio G., Panichi C., Valenti M. (1995). Geochemical evolution of fluids in the Larderello geothermal field. In: Proceedings of the World Geothermal Congress 1995, Florence, 18–31 May 1995, pp. 1839–1843.

Seward T.M., Barnes H.L. (1997) Metal Transport by Hydrothermal Ore Solutions: in "Geochemistry of Hydrothermal Ore Deposits", Third Edition, HL Barnes, editor, Wiley-Interscience, Inc., New York, pp. 435-486.

Tassi F., Montegrossi G, Capecchiacci F. & Vaselli O. (2010): Origin and Distribution of Thiophenes and Furans in Gas Discharges from Active Volcanoes and Geothermal Systems. Int. J. Mol. Sci. 2010, 11.

Wolery T. J. (1992). EQ3NR, a computer program for geochemical aqueous speciation-solubility calculations:theoretical manual, User's Guide, and related documentation (version 7.0). Lawrence Livermore National Lab, Berkeley, CA.

FIGURES

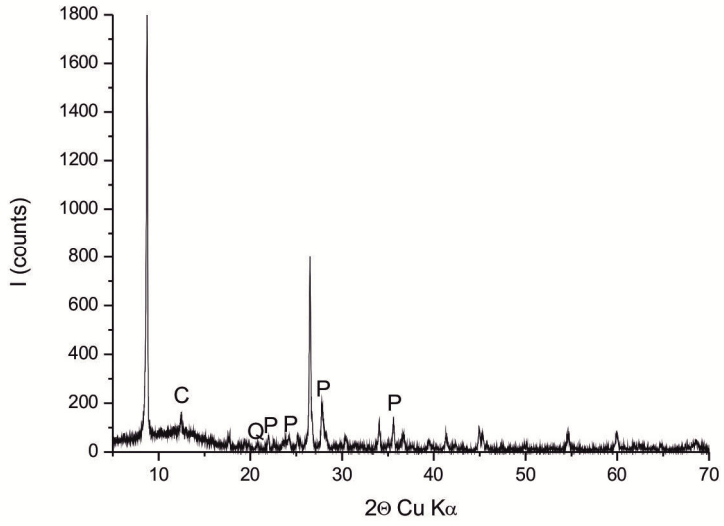

Figure 1.1.1.: XRD spectrum of GN1B sep. Peaks are attributable to plagioclase (P), quartz (Q) and chlorite (C), unlabelled peaks refer to biotite.

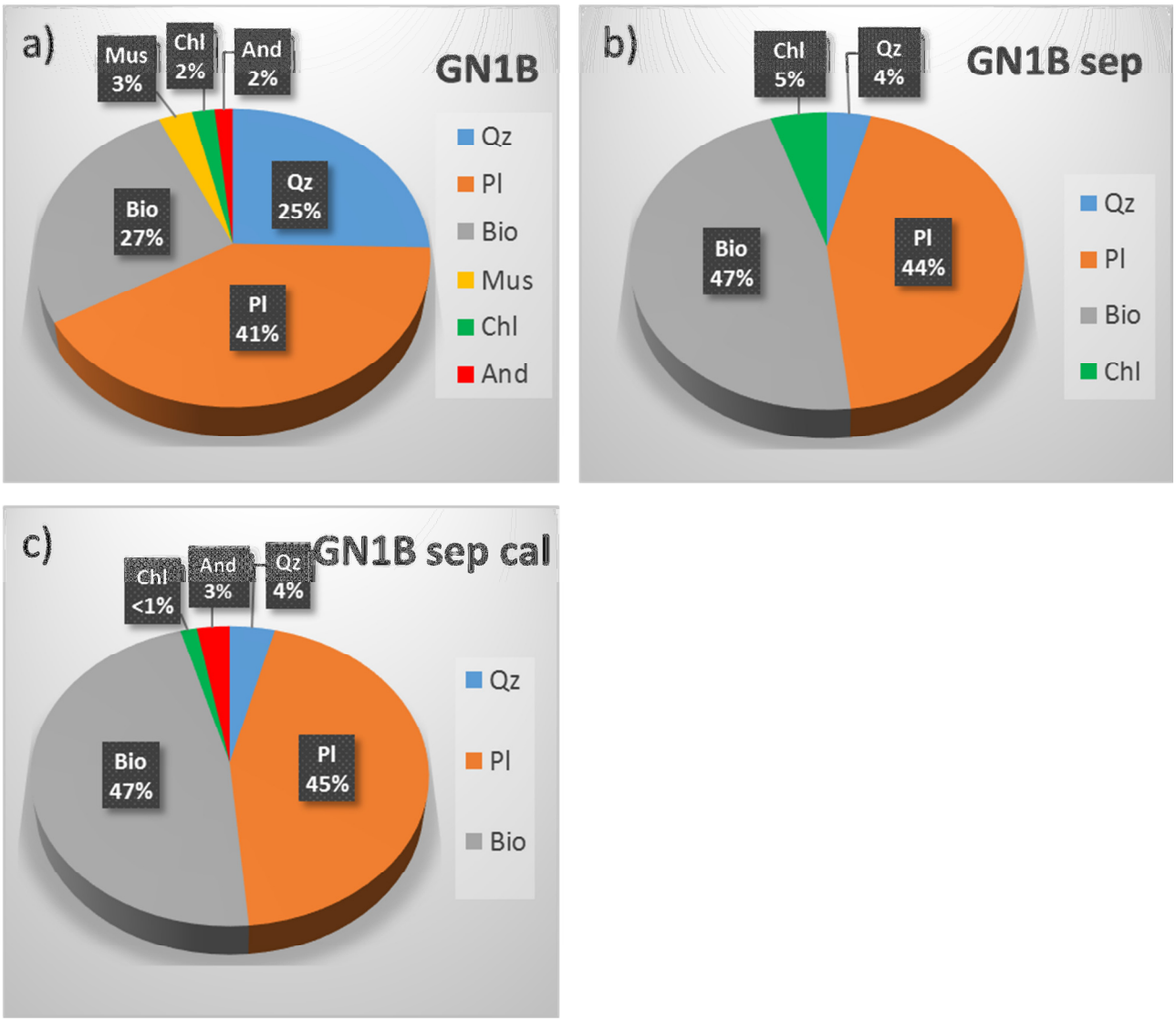

Fig. 1.1.2.: Pie charts representing modal mineralogy (wt%) of the starting materials; Qz = quartz; Pl = plagioclase; Bio = biotite; Mus = muscovite; Chl = chlorite; And = andalusite.

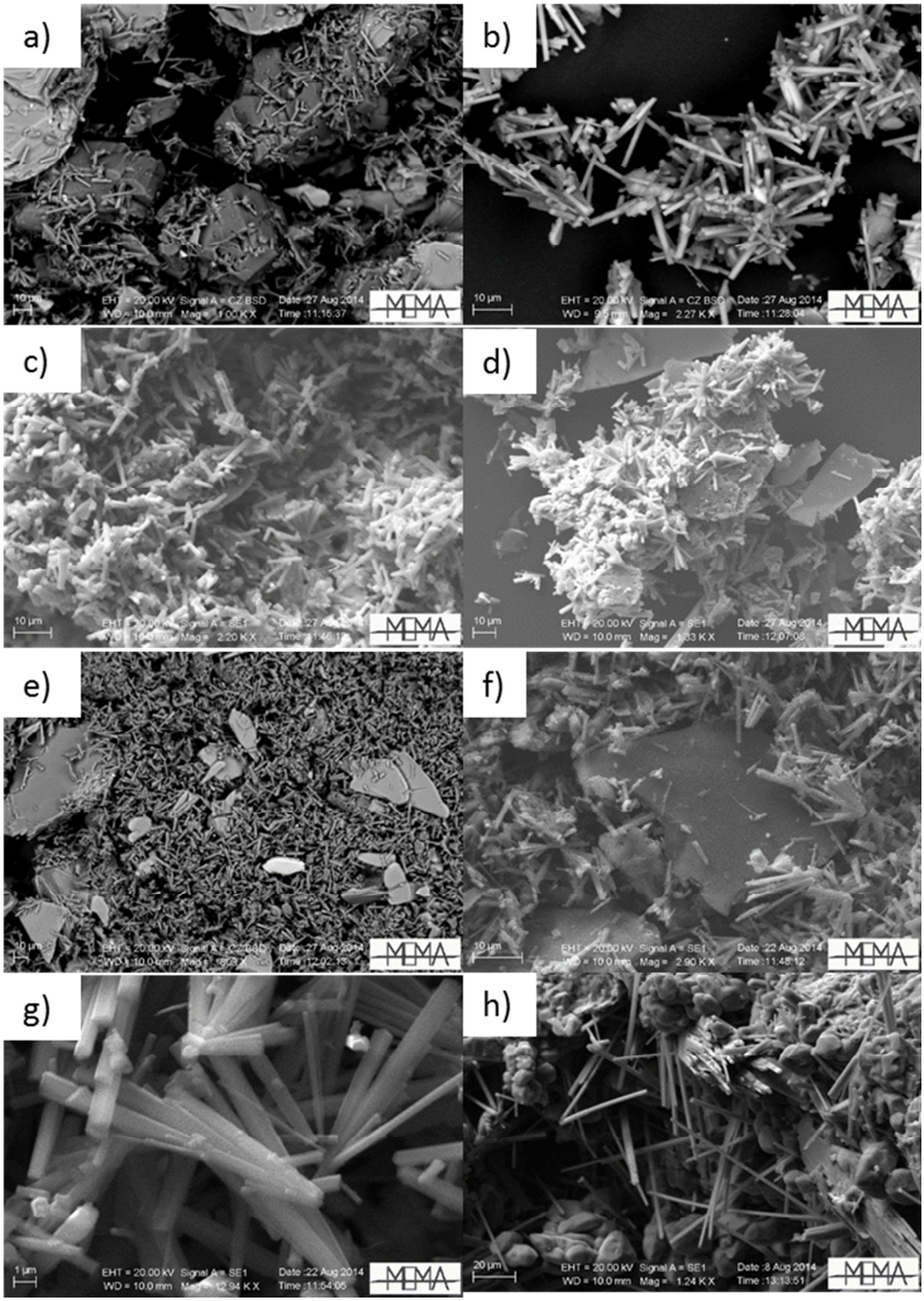

Figure 1.1.3.: SEM images of experimental products showing acicular tourmaline crystals and biotite plates. a) , b): Experiment 2, Backscattered electron (BSE) images; c) , d): Experiment 5, SE images; e: Experiment 5, BSE image; f) , g): Experiment 4, BSE images; h: tourmaline crystals in a natural sample (Stagnone, Elba Island), BSE image. The appearance of crystals is similar to those synthesized but they are longer.

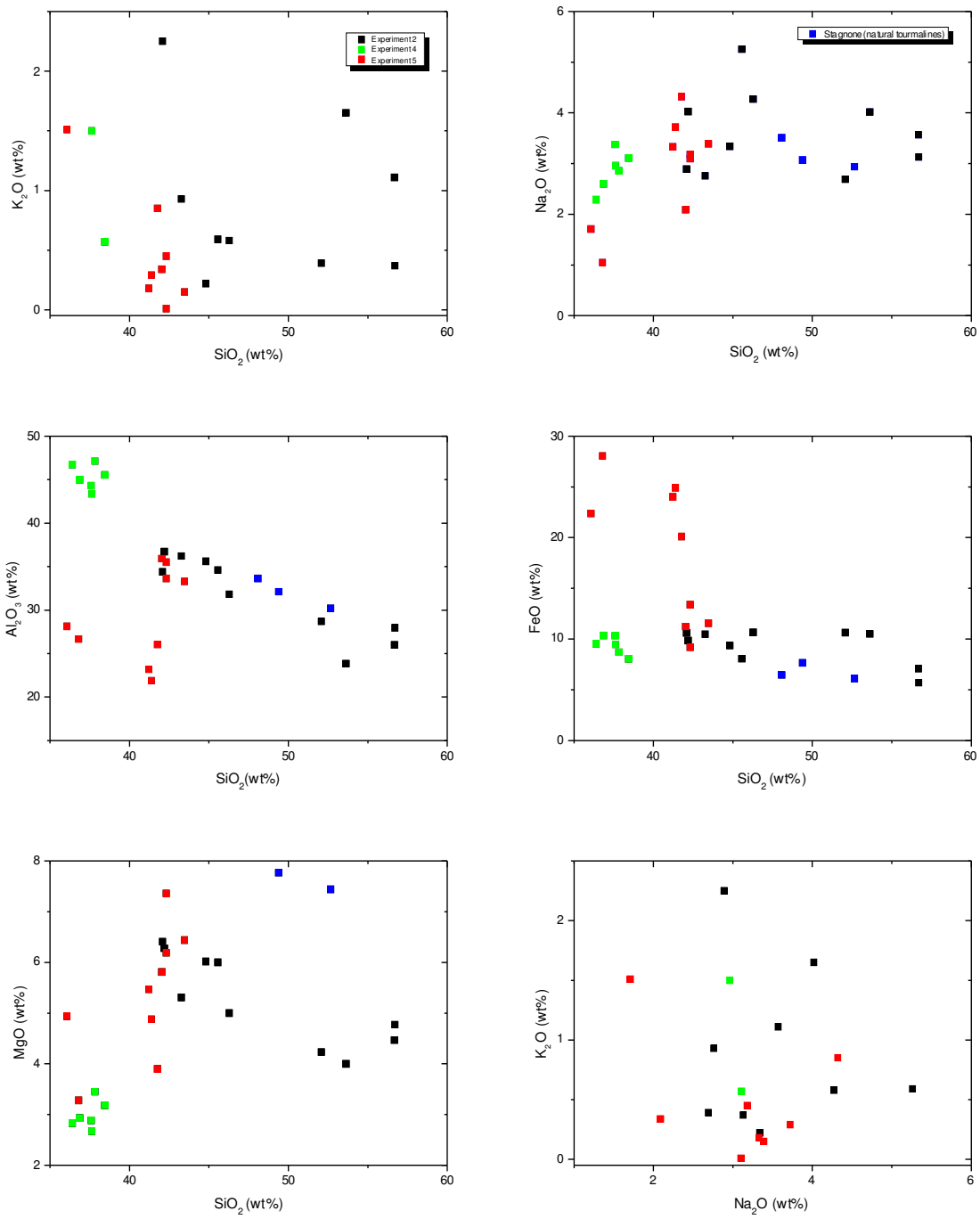

Figure 1.1.4.: Graphs displaying SEM-EDS analyses of tourmaline from experiments 2 (black squares), 4 (green squares) and 5 (red squares). Analyses from some natural tourmaline sampled in Stagnone are also reported for comparison (blue squares).

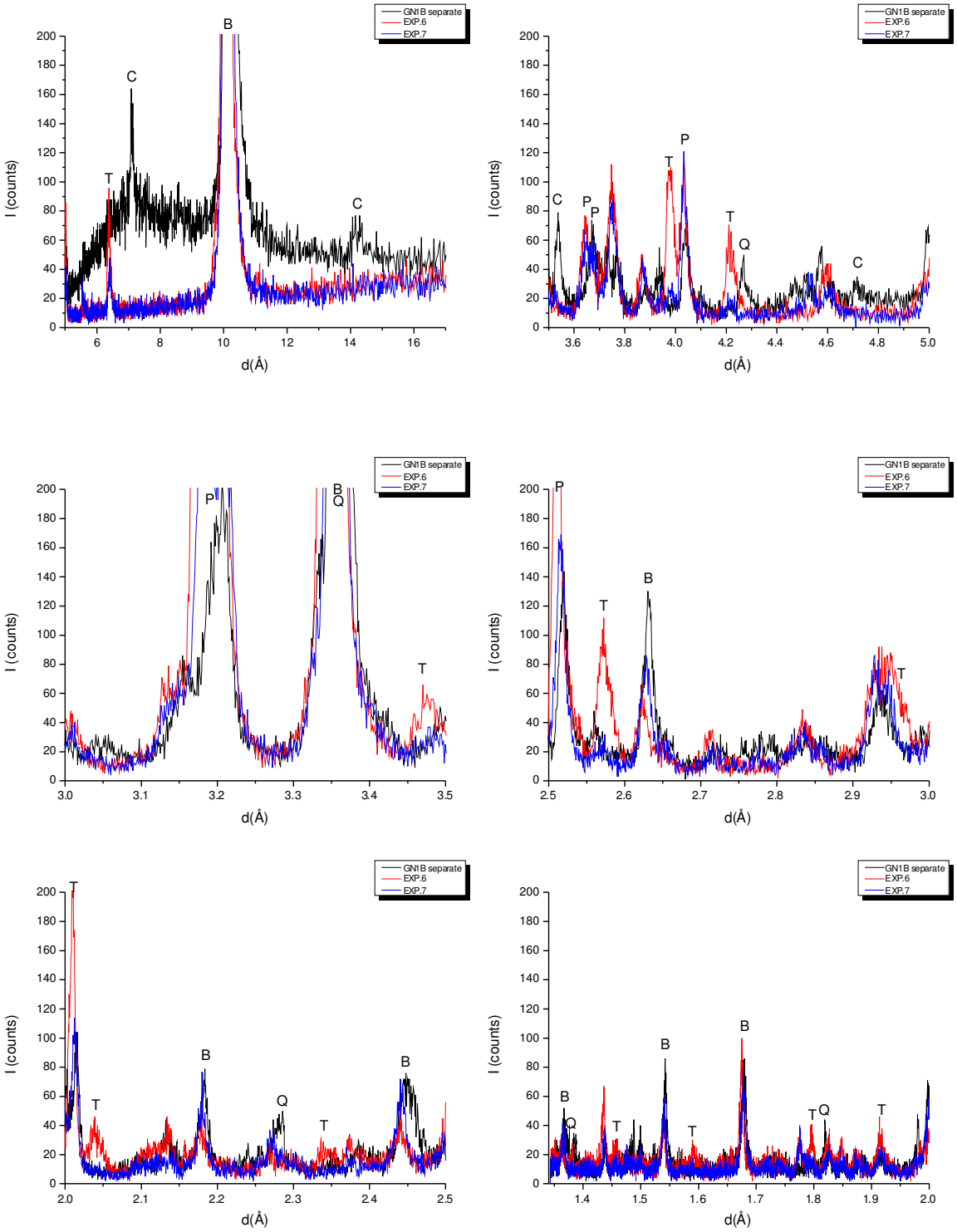

Figure 1.1.5.: XRD spectra of Experiments 6 (red) and 7 (blue) and GN1B sep (black). Peaks are attributed to biotite (B), plagioclase (P), quartz (Q), chlorite (C) and tourmaline (T).

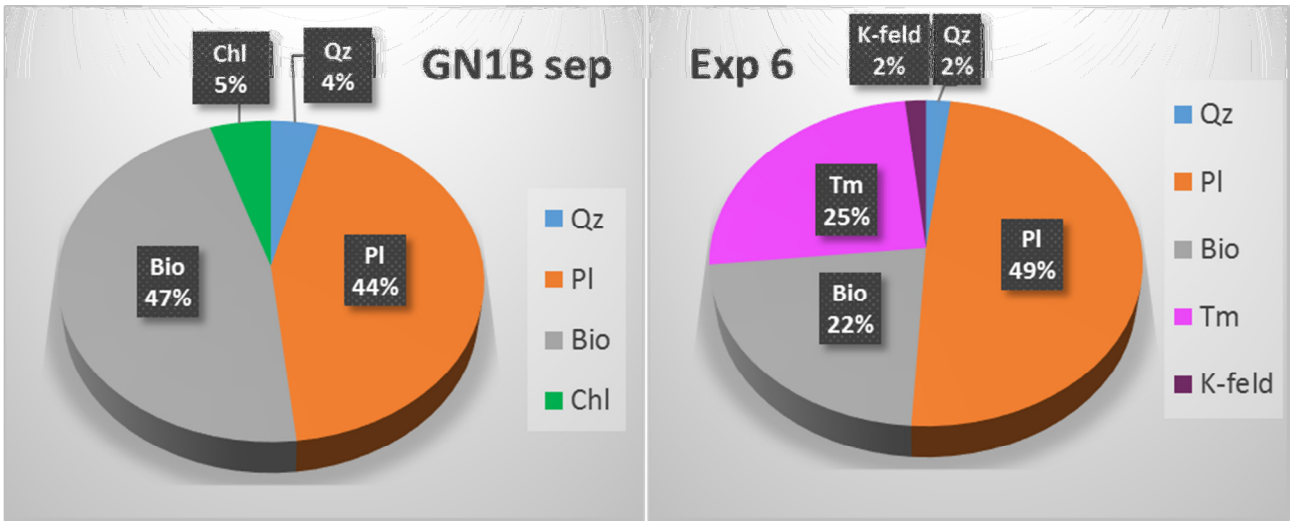

Figure 1.1.6.: Pie charts representing a comparison between modal mineralogy (wt%) of starting material (GN1B sep.) and experiment 6; Qz = quartz; Pl = plagioclase; Bio = biotite; Chl = chlorite; Tm = tourmaline; K-feld = K-feldspar.

a)

Dravite	Na	Mg_3	Al_6	Si_6O_{18}	$(BO_3)_3$	$(OH)_3$	(OH)
Schorl	Na	$Fe^{2+}{}_3$	Al_6	Si_6O_{18}	$(BO_3)_3$	$(OH)_3$	(OH)

b)

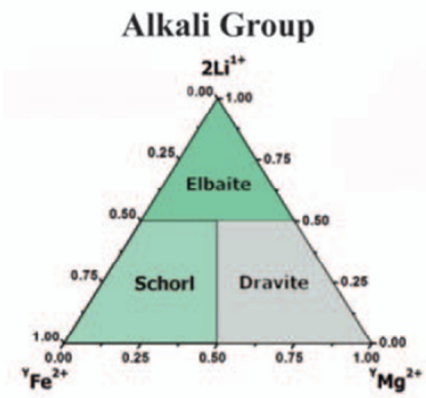

Figure 1.1.7.: a) Dravite and schorl end-member compositions in tourmaline (general formula: $XY_3Z_6[T_6O_{18}][BO_3]_3V_3W$); b) Triangular graph reporting the classification of alkali group of tourmaline (from Hawthorne & Dirlam, 2011).

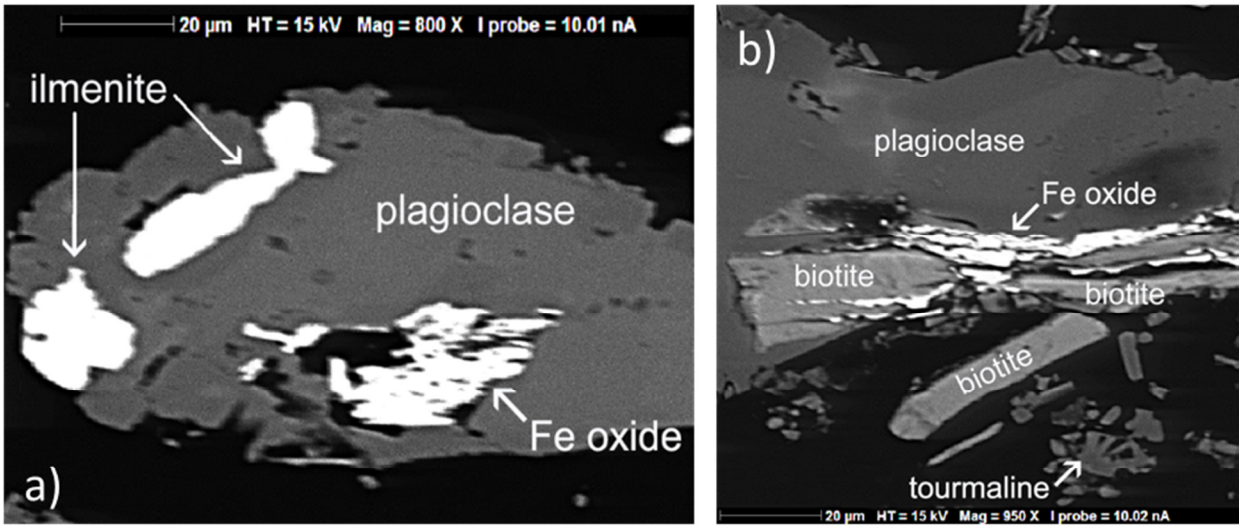

Figure 1.1.8.: Backscattered electron image of neo-formed Fe--oxides in experiment 6. a) Ilmenite and Fe-oxide on plagioclase; b) neo-formed Fe--oxides close to plagioclase and biotite crystals.

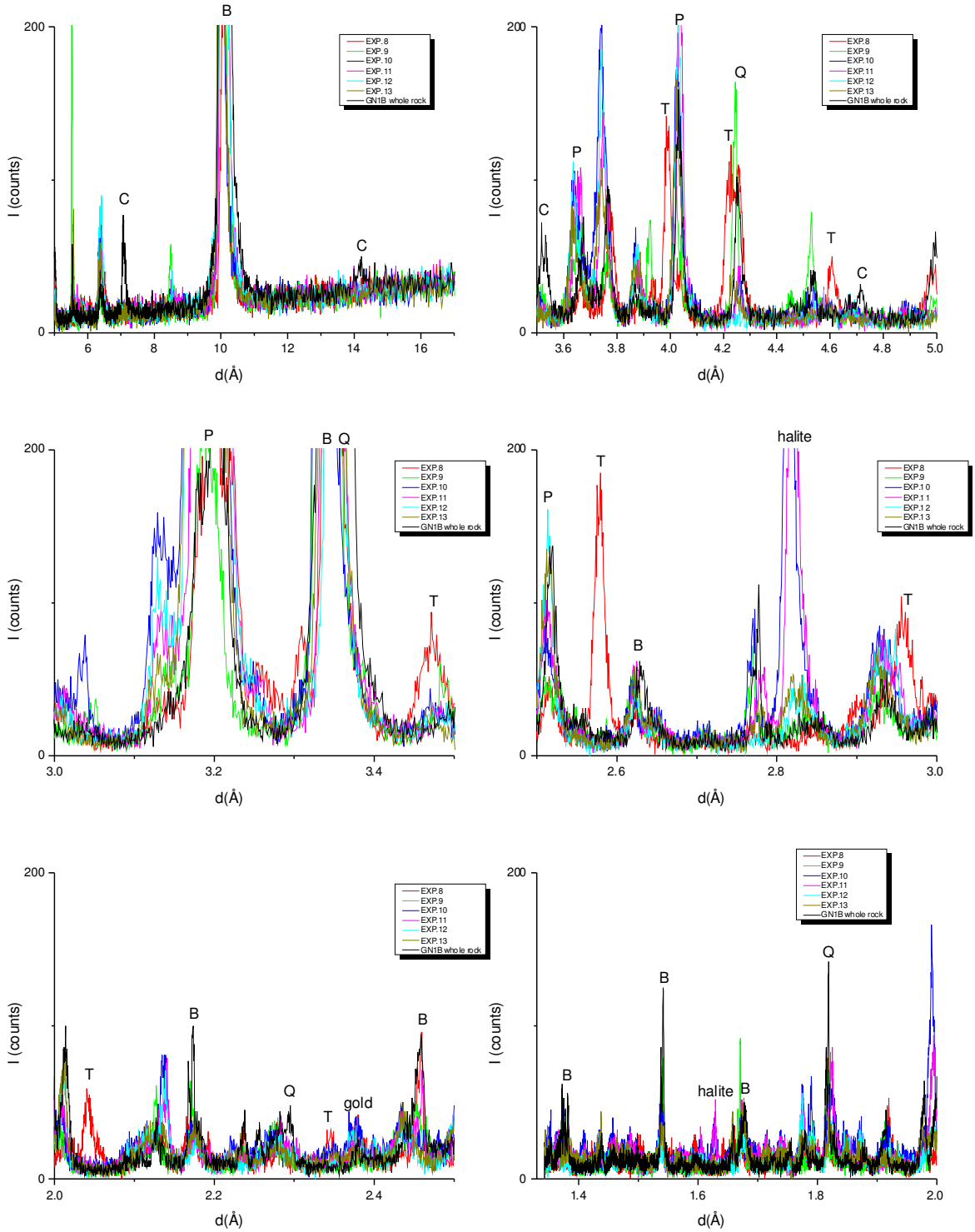

Figure 1.1.9.: Comparison of XRD spectra of GN1B (black) and of experiments 8 (red), 9 (green), 10 (blue), 11 (purple), 12 (light blue), 13(dark green). Peaks are attributed to biotite (B), plagioclase (P), quartz (Q), chlorite (C) and tourmaline (T). Note that tourmaline peaks present only in experiment 8 (red spectra), while chlorite is present only in the starting material GN1B (black spectra).

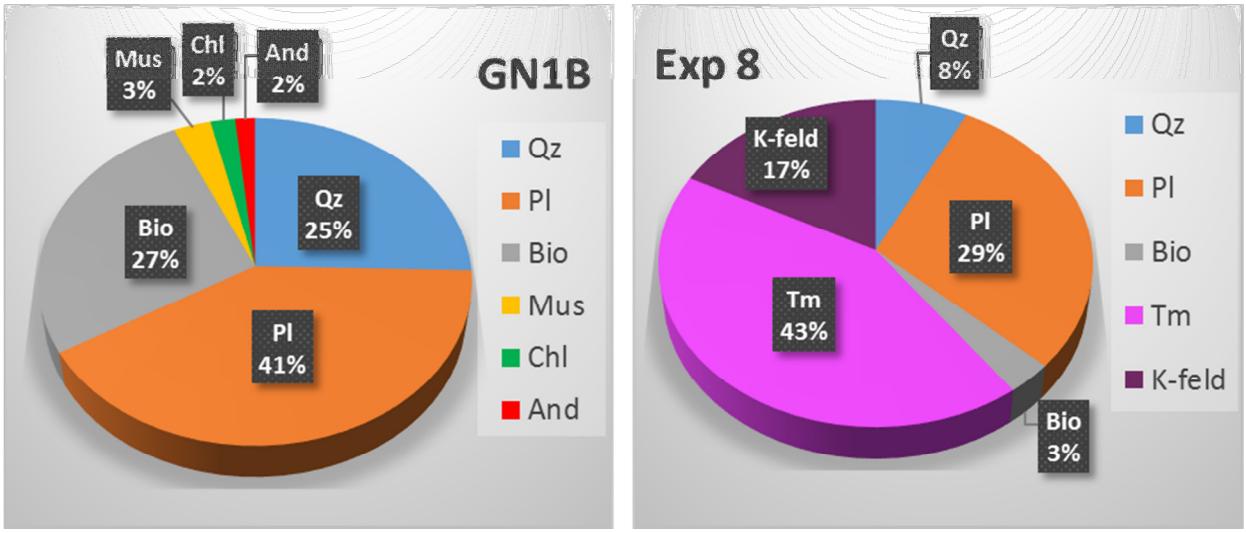

Figure 1.1.10.: Pie charts representing a comparison between modal mineralogy (wt%) of starting material (GN1B) and Experiment 8; Qz = quartz; Pl = plagioclase; Bio = biotite; Mus = muscovire; Chl = chlorite; And = andalusite; Tm = tourmaline; K-feld = K-feldspar.

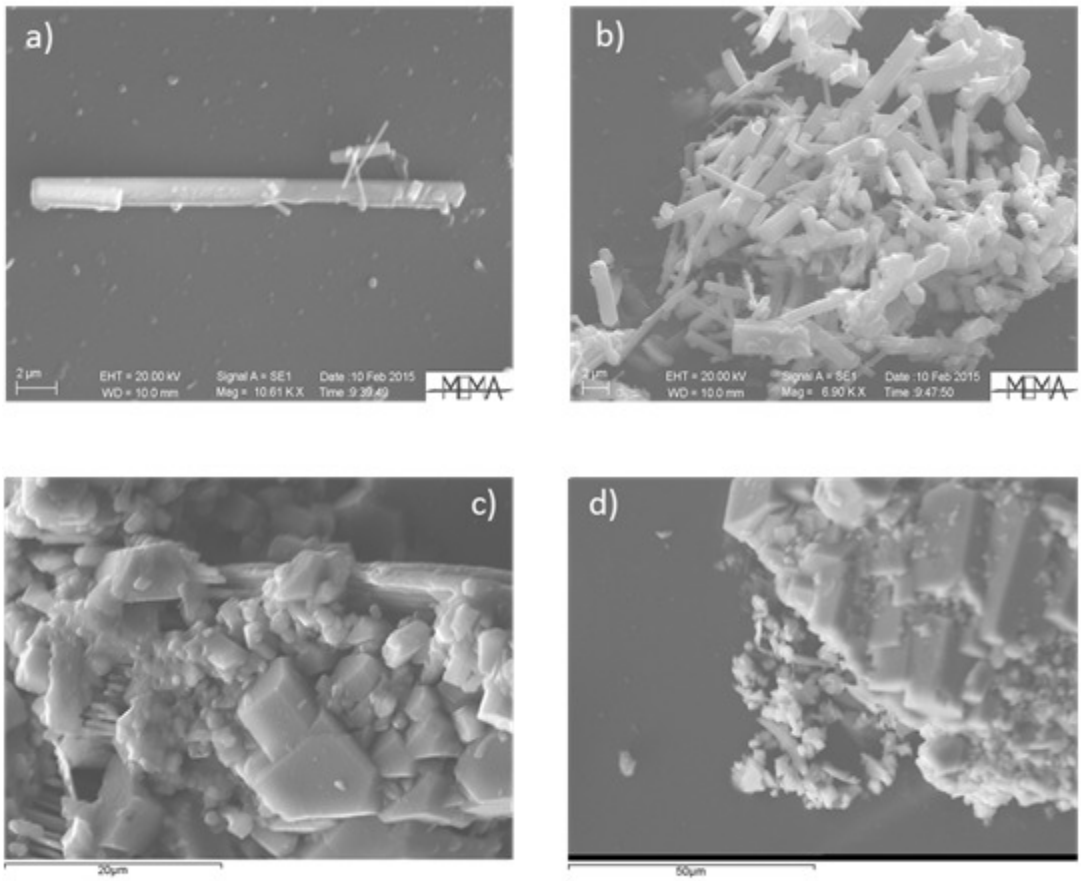

Figure 1.1.11.: Secondary electrons images: a) and b) of tourmaline of experiment 8; c) biotite and plagioclase of experiment 10; d) and biotite and plagioclase of experiment 11.

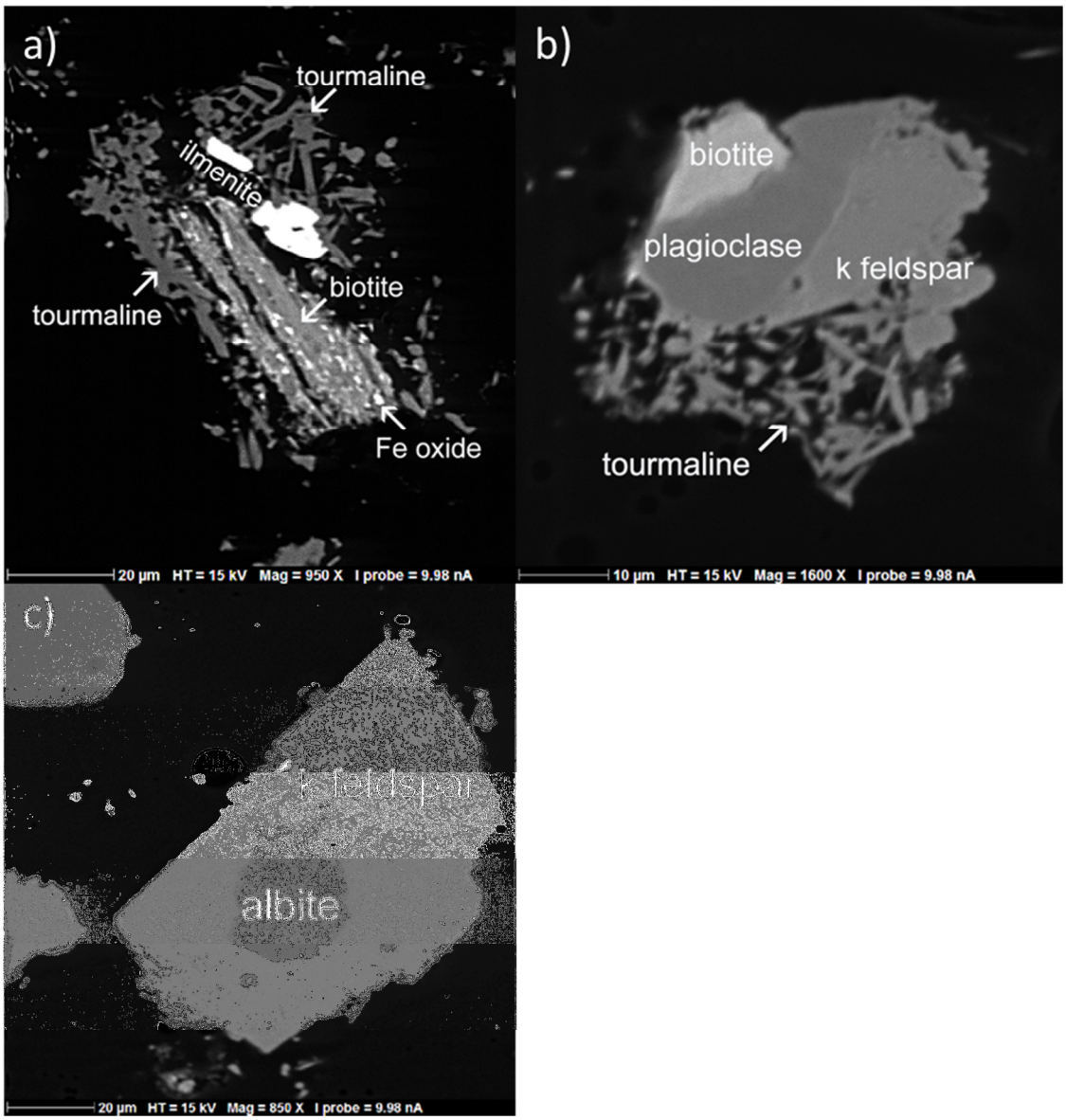

Figure 1.1.12.: Backscattered electron image of experiment 8: a) neo formed Fe--oxides on biotite and tourmaline; b) neo-formed K-feldspar on a plagioclase relict and tourmaline; c) neo formed K-feldspar grown on an albite relict from the starting material.

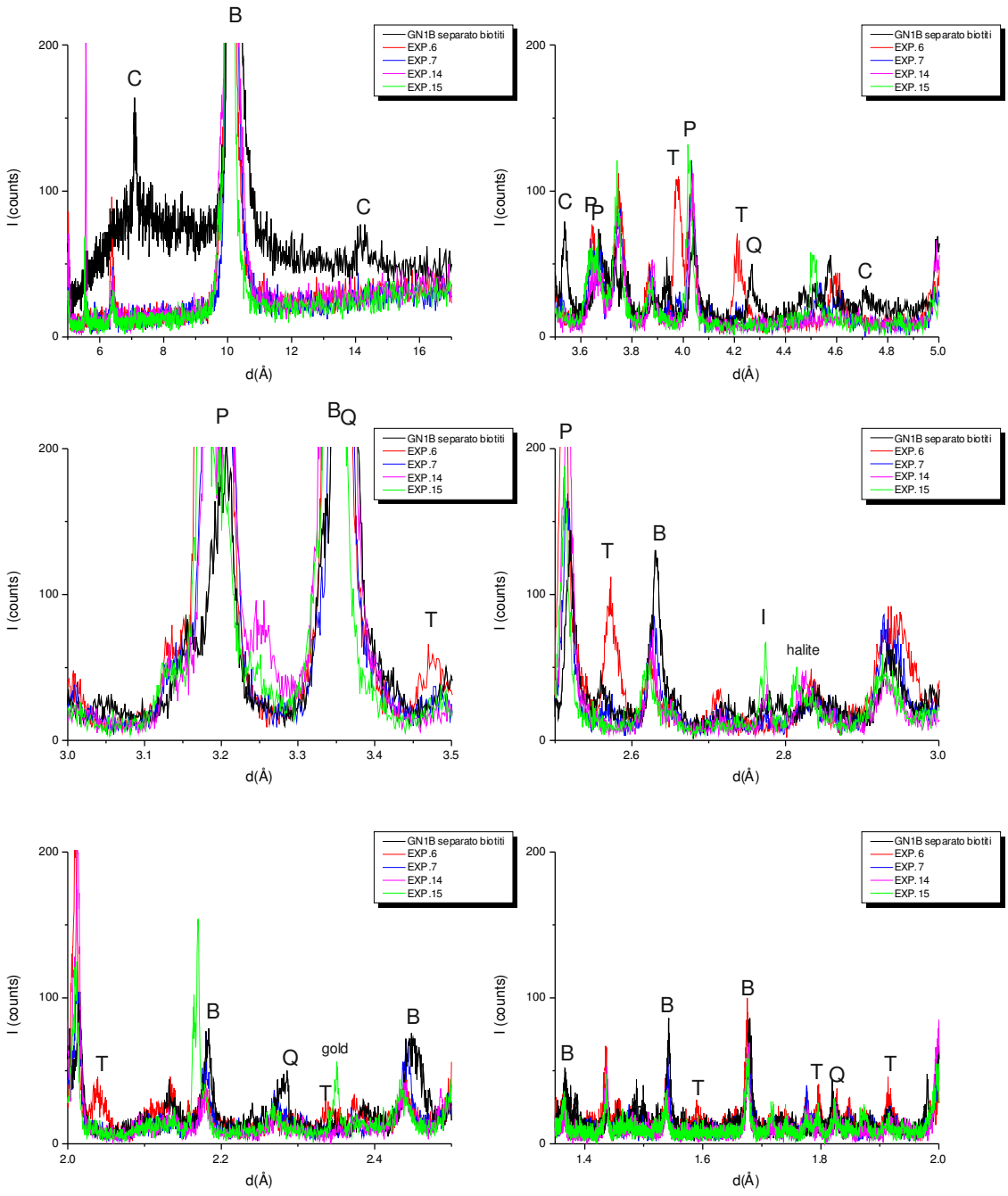

Figure 1.1.13.: comparison of XRD spectra of GN1B sep. (black) and of Experiments 6 (red), 7 (blue), 14 (purple), 15 (green). Peaks are attributed to biotite (B), plagioclase (P), quartz (Q), chlorite (C) and tourmaline (T) and, probably, ilmenite (I). Note that tourmaline peaks are only in Experiment 6, while chlorite is present only in the starting material. Halite was found in some experiments, Gold (from the capsule) was only detected in Experiment 15.

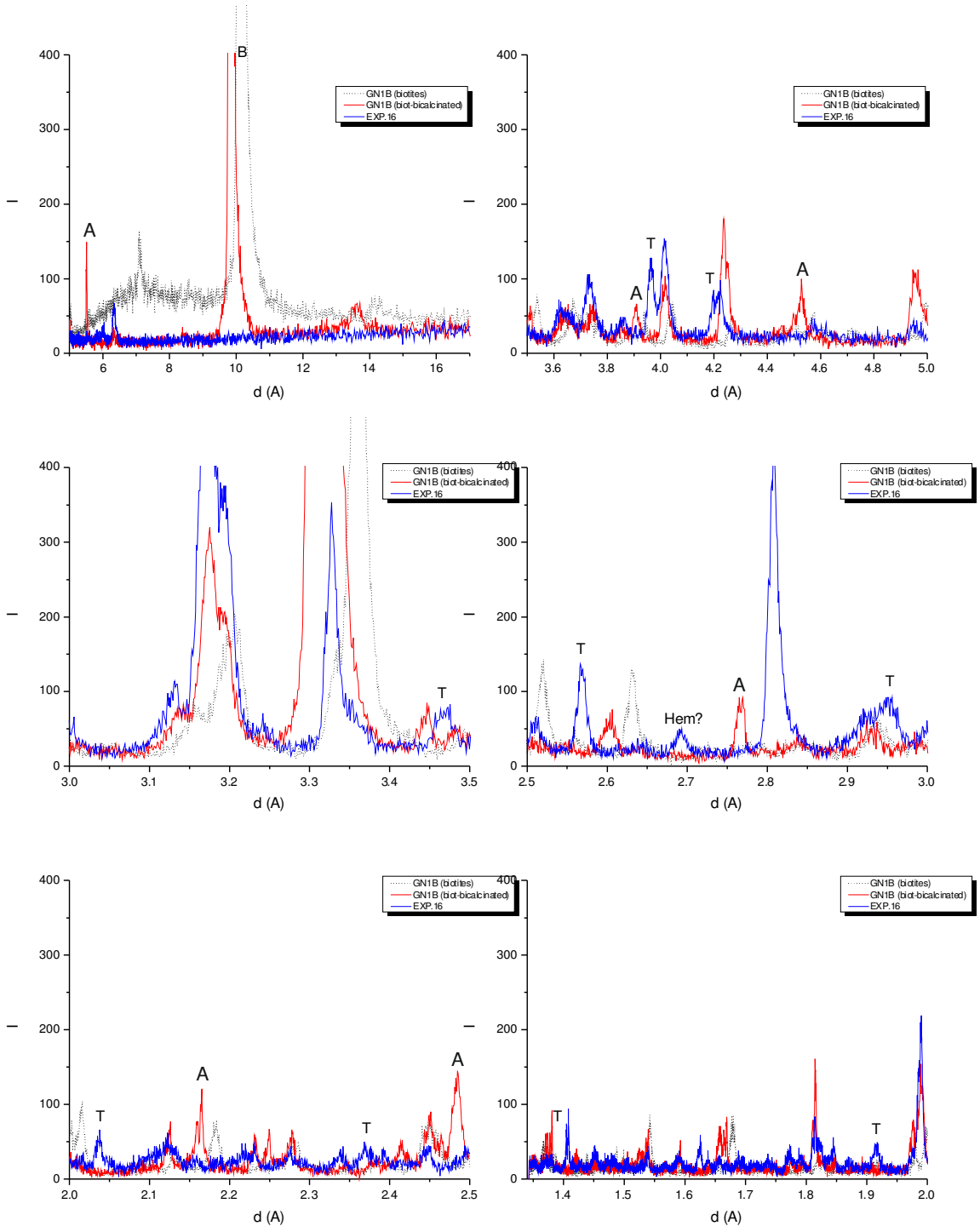

Figure 1.1.14.: Comparison of XRD spectra of GN1B sep. (dotted black), GN1B sep. cal. (red) with experiment 16 (blue). Peaks are attributed to biotite (B), Hem = hematite (?) chlorite (C) and tourmaline (T). Note that chlorite peaks disappeared in GN1B sep. cal. and tourmaline is present in experiment 16.

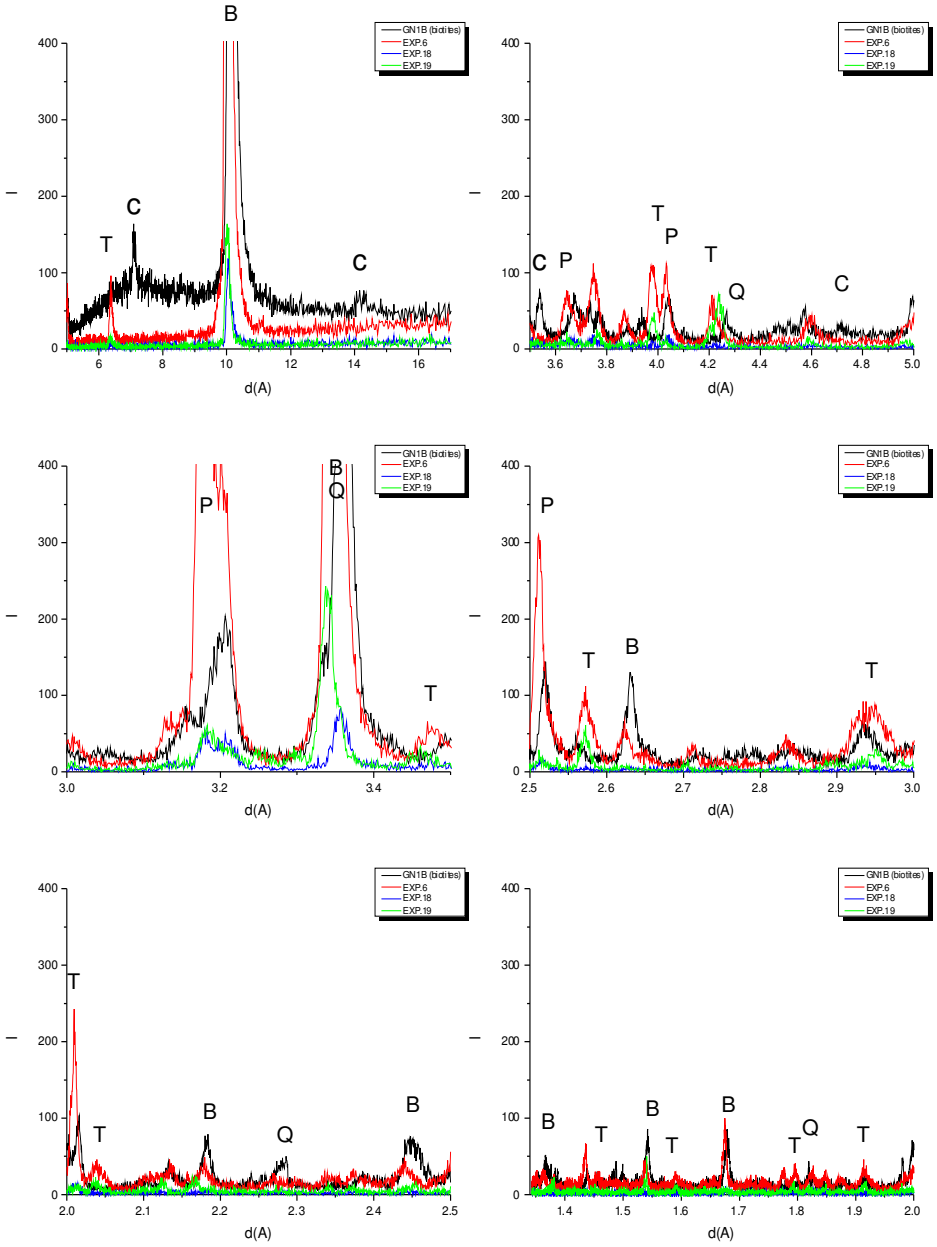

Figure 1.1.15.: Comparison of XRD spectra of GN1B sep. (black), experiment 6 (red) with experiment 18 (blue) and 19 (green). Peaks are attributed to biotite (B), plagioclase (P), quartz (Q), chlorite (C) and tourmaline (T).

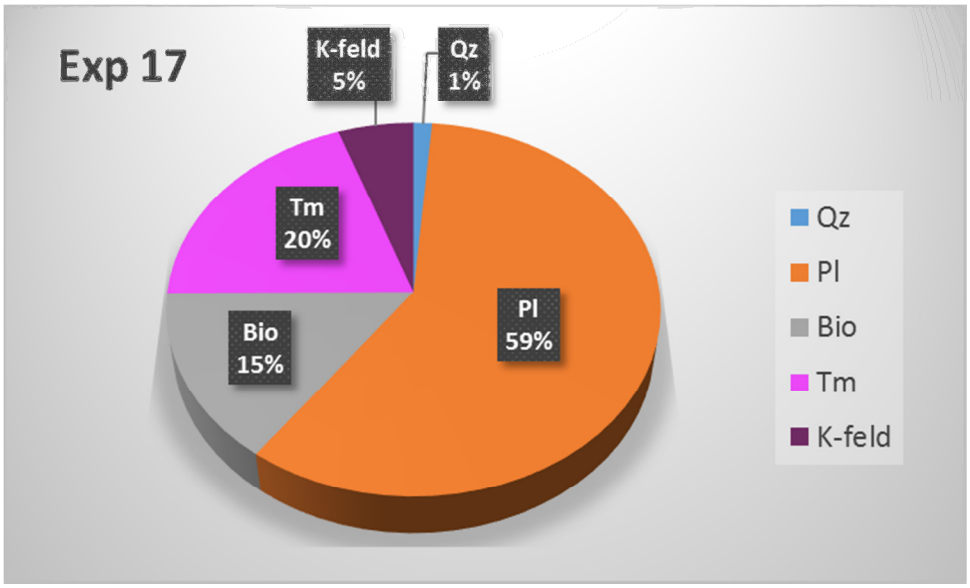

Figure 1.1.16.: Pie chart representing Rietveld refinement of experiment 17. The following phases are represented (in wt%): Qz = quartz; Pl = plagioclase; Bio = biotite; Tm= tourmaline; K-feld = K-feldspar.

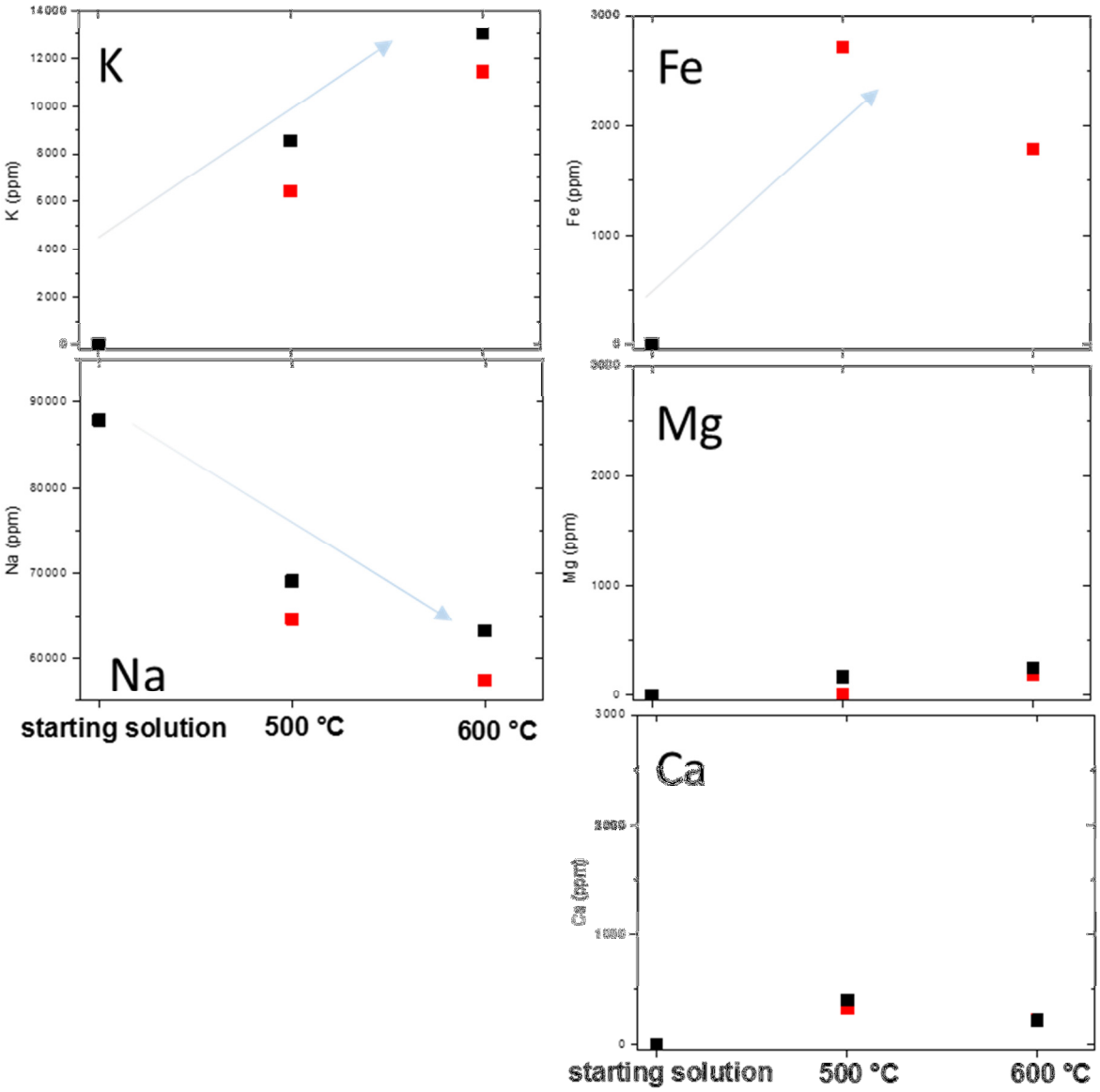

Figure 1.1.17.: K, Na, Fe, Mg and Ca contents measured in fluids of the starting solution (20wt% NaCl), experiment 17 (500°C, 1000 bar) and experiment 6 (600°C, 1000 bar). Analyses were performed through LC (black squares) and ICP-OES (red squares).

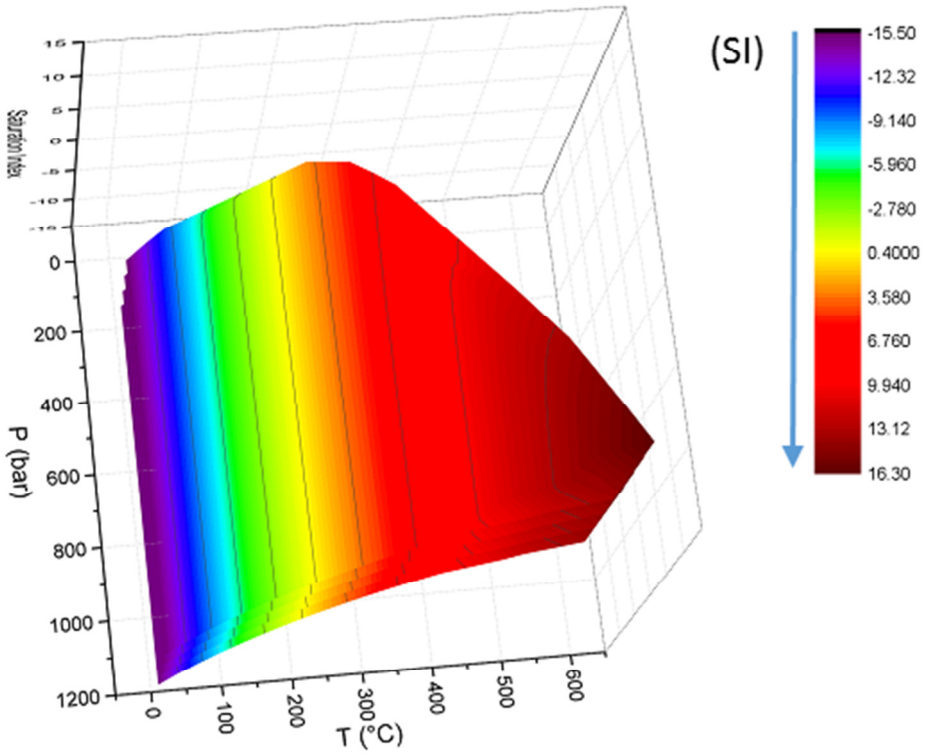

Figure 1.2.1.: Saturation Index (SI) of tourmaline, versus pressure and temperature: NaCl 20 wt%; pH 3 and activities set equal to 1 except for $B(OH)_3$.

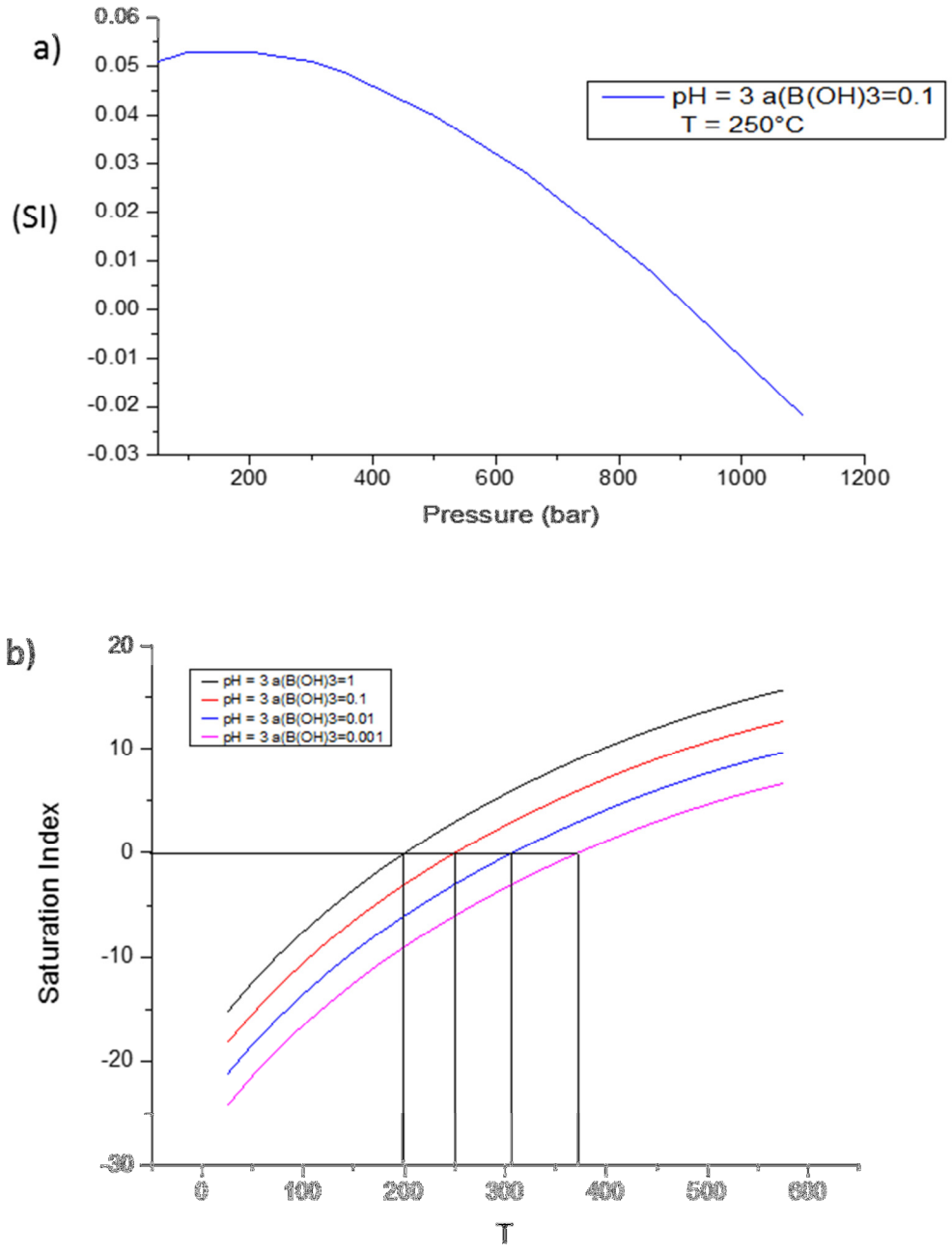

Figure 1.2.2.: a) Tourmaline SI as function of pressure; b) SI dependence with temperature considering different Boron activities in the fluid.

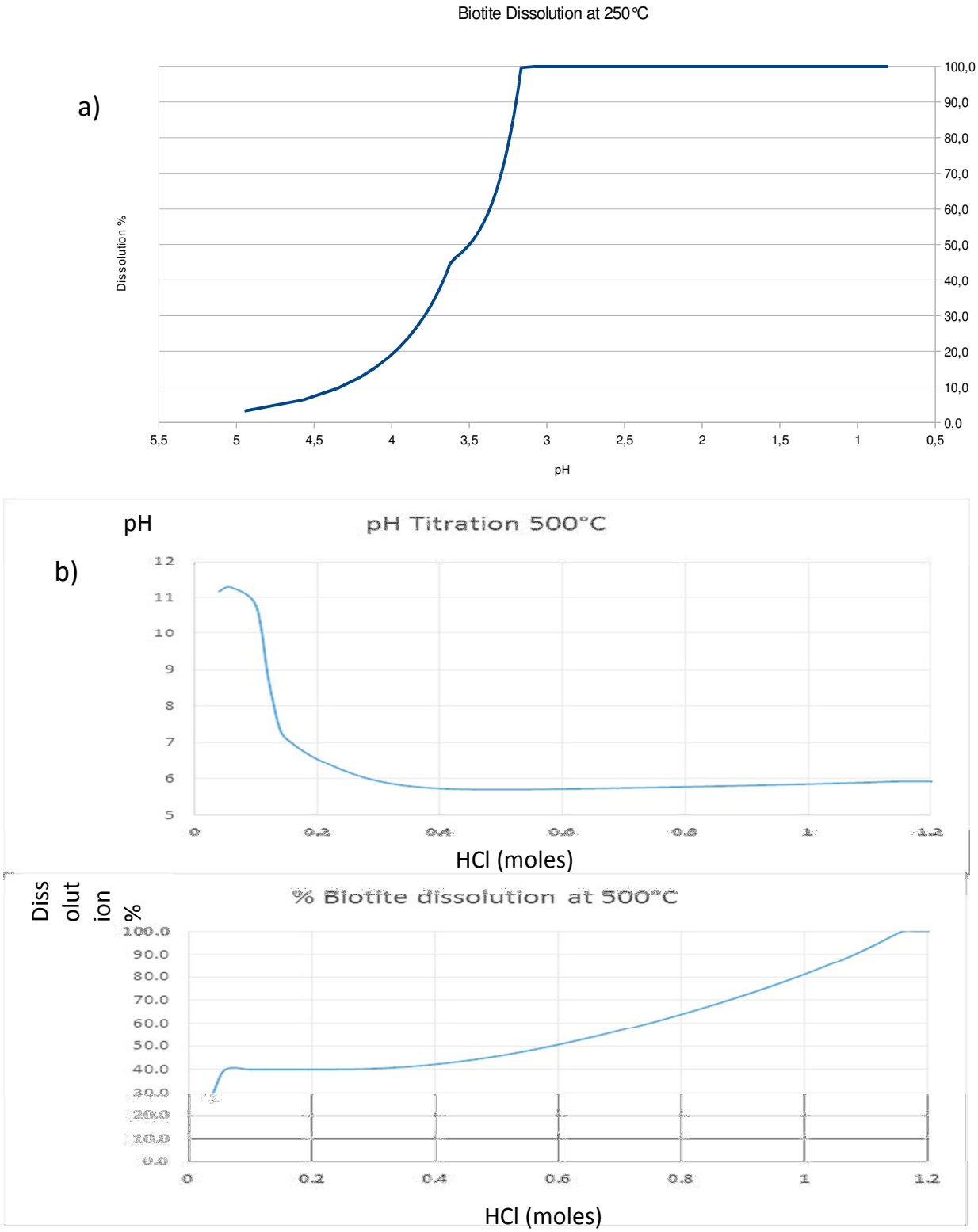

Figure 1.2.3.: a) Biotite dissolution in a batch reaction model obtained by using pure water and titrating 0.1 mole of biotite with HCl. a)Titration at 250°C, b) titration at 500°C; variation of pH in function of HCl contents (up) and biotite dissolution in function of HCl contents (bottom).

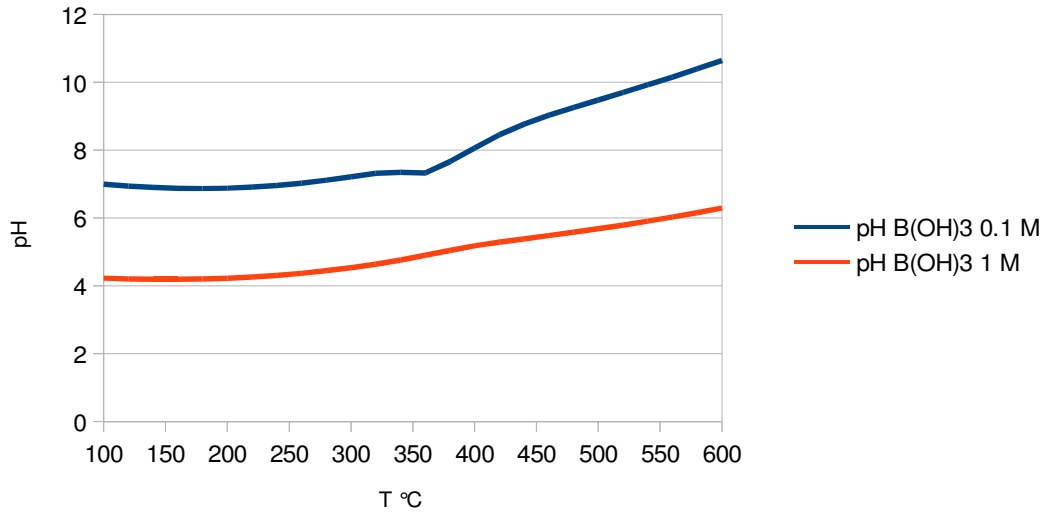

Figure 1.2.4.: pH obtained from boric acid 1M and 0.1M as function of temperature.

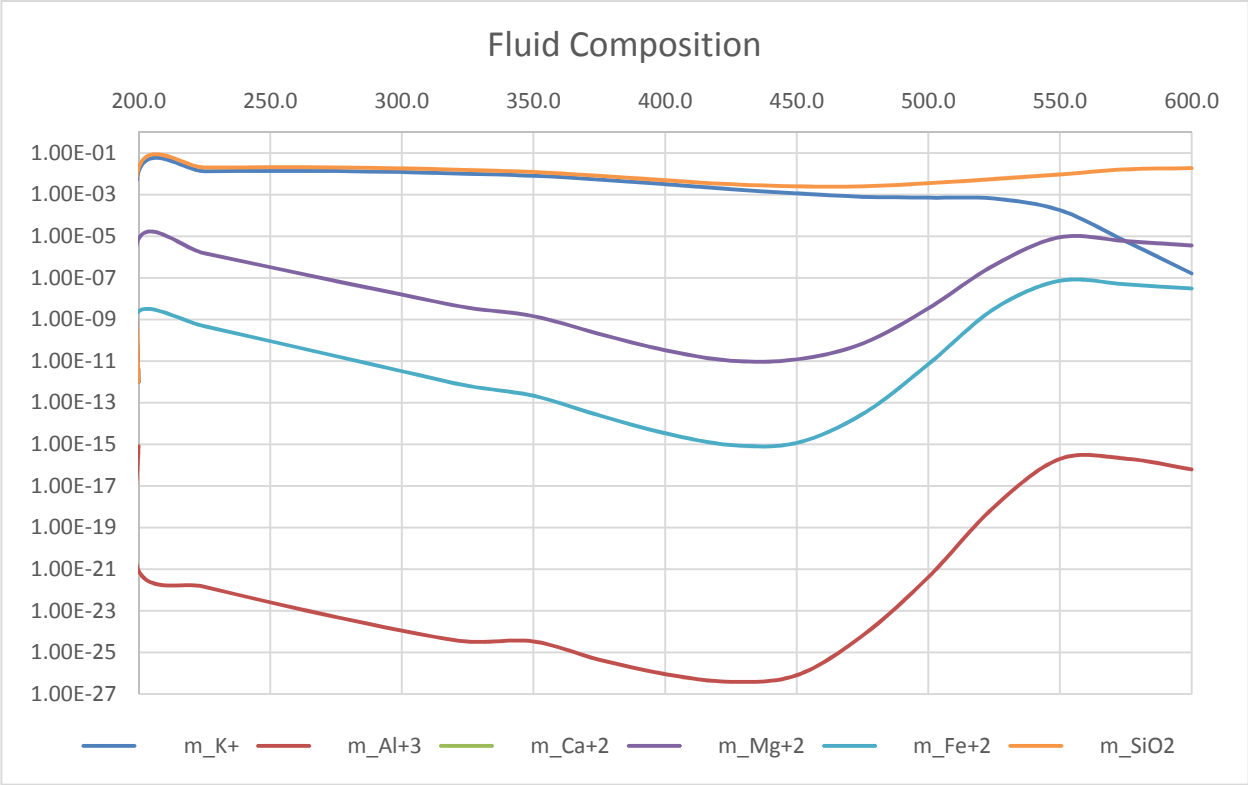

Figure 1.2.5.: Variation of species molarity vs Temperature (°C). The concentration of aqueous species follow the pH behaviour, i.e. it is lowering as pH increase and increasing as pH lower, in particular it increase at temperature higher than 450° when pH lower down to 3 (figure 1.2.6).

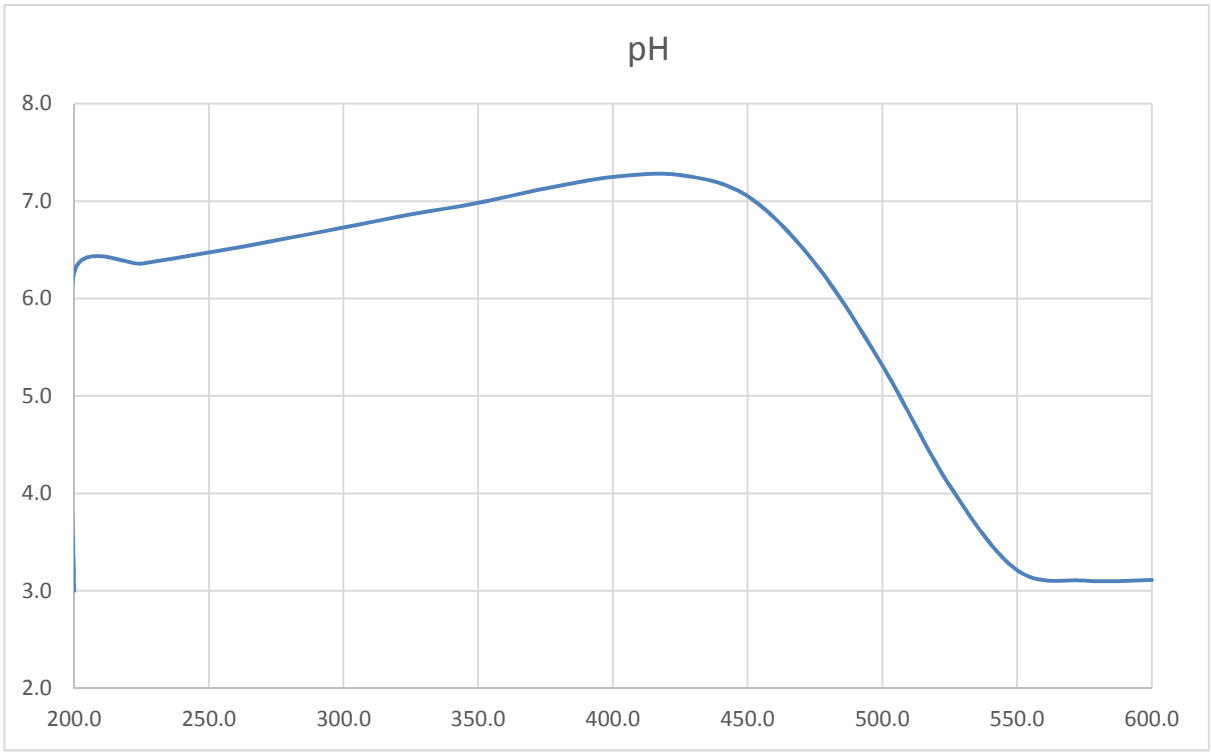

Figure 1.2.6.: pH variation with temperature (°C).

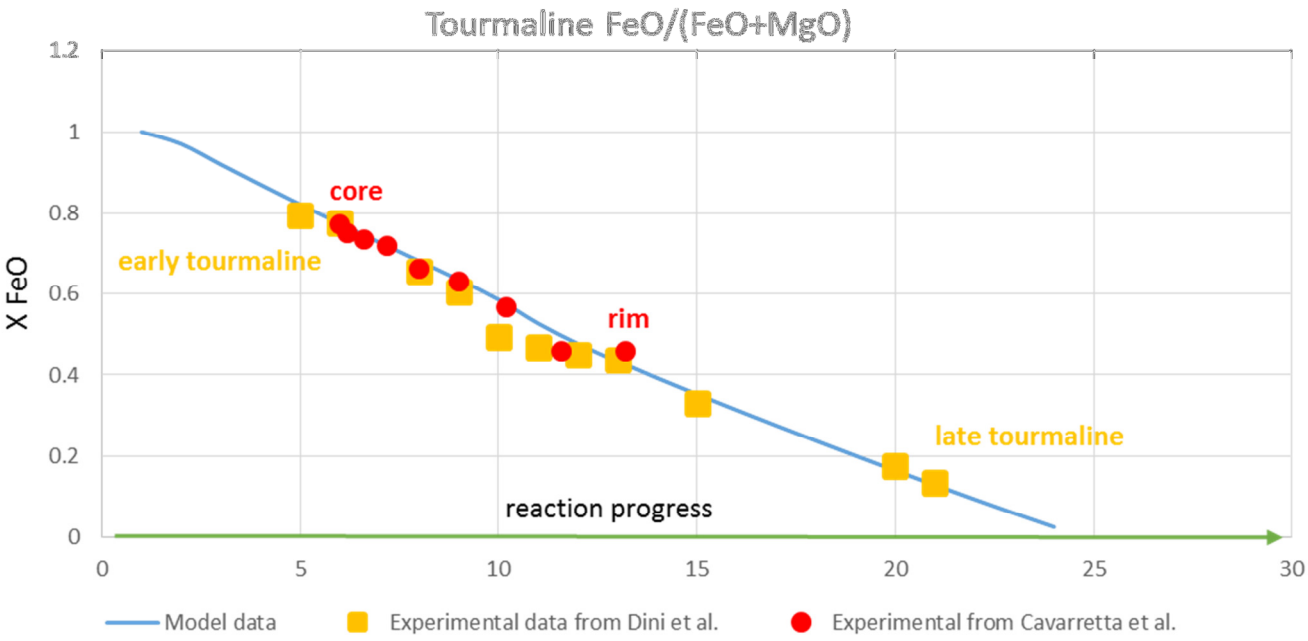

Figure 1.2.7.: Reaction progress vs XFeO in Elba (Dini et al., 2008) and Larderello (Cavarretta & Puxeddu, 1990) schorl-dravite tourmaline data compared with modelled data.

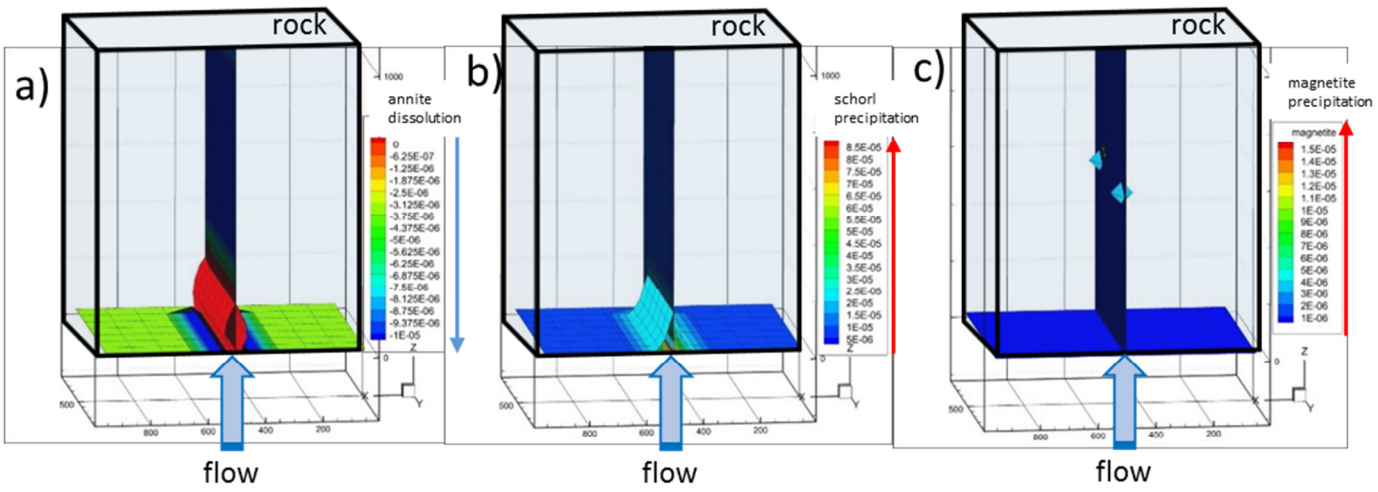

Figure 1.2.8.: 3D first model of the system; coordinates x,y, z represent the dimensions of micachist block . a) The annite solid Volume Fraction variation (dissolution) for a 0.3 years step after 40 years, b) The schorl Solid Volume Fraction variation (precipitation) for a 0.3 years step after 40 years, c) The magnetite Solid Volume Fraction variation (precipitation) for a 0.3 years step after 40 years.

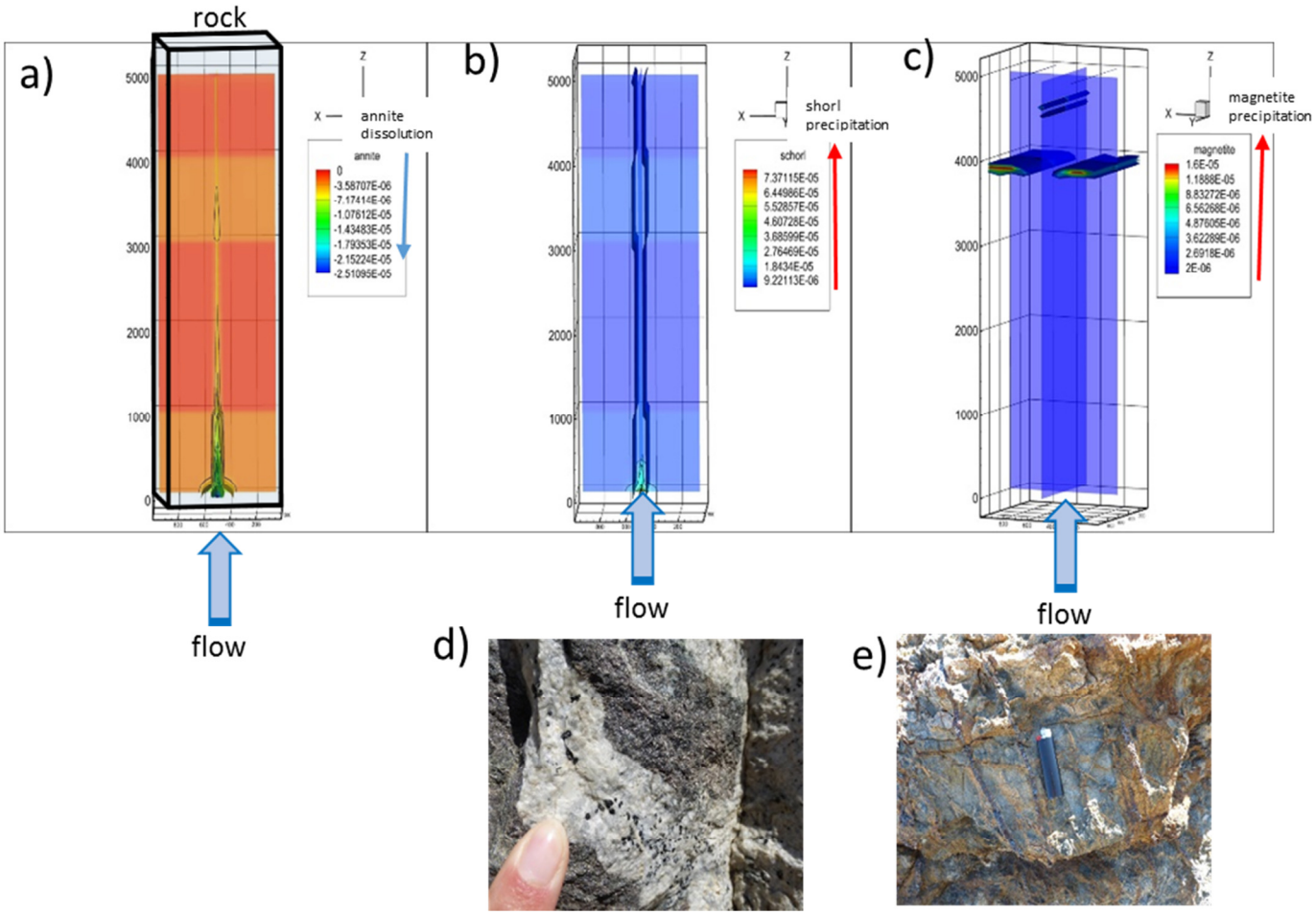

Figure 1.2.9.: 3D second model of the system; coordinates x,y, z represent the dimensions of micachist block. a) The annite Solid Volume Fraction variation (dissolution) after 50 years, b) The schorl Solid Volume Fraction variation (precipitation) after 50 years , c) The magnetite Solid Volume Fraction variation (precipitation) after 50 years, d) Picture of a granite vein with tourmaline, e) vein filled with Iron Oxide in Elba Island.

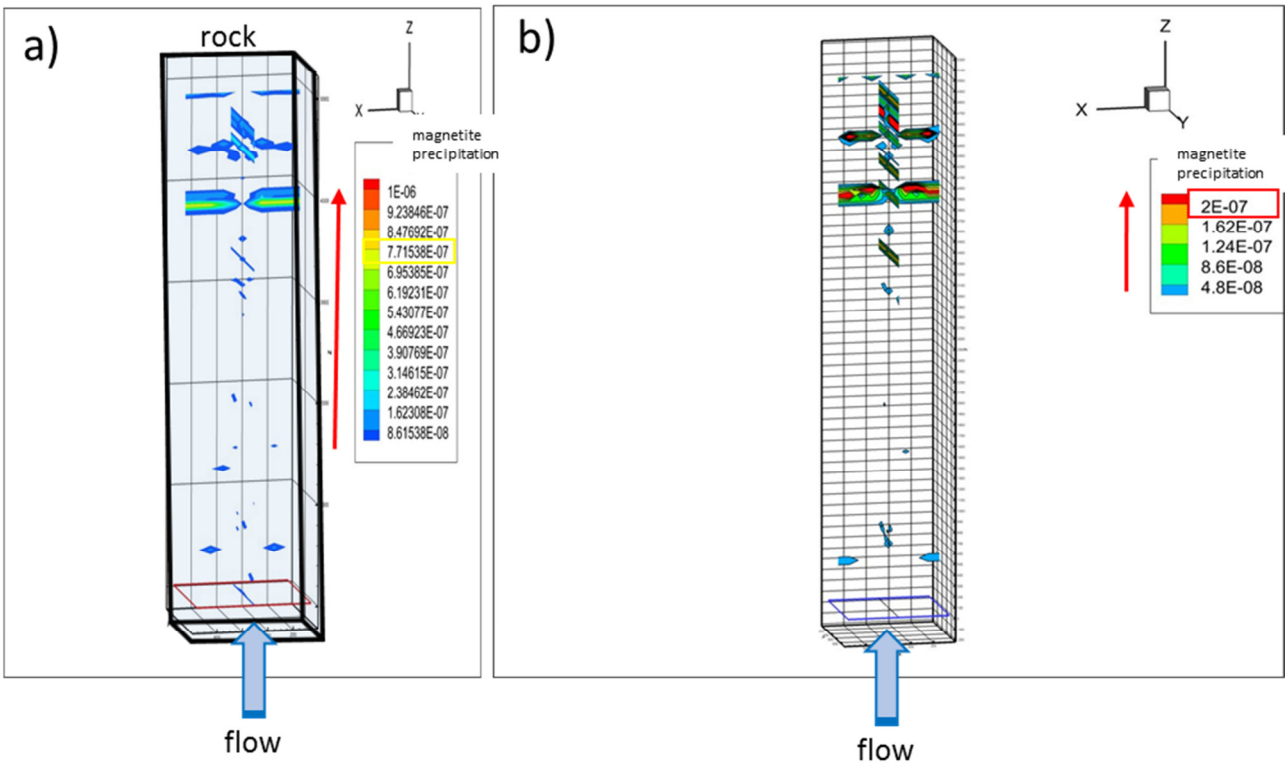

Figure 1.2.10.: 3D third model of the system; coordinates x,y,z represent the dimensions of micaschist block . a) The magnetite Solid Volume Fraction variation (precipitation) after 90 days with 1 Kg/s Inflow reach the maximum value of about 7.7 E-7; b) magnetite Solid Volume Fraction variation (precipitation) after 90 days with 5 Kg/s Inflow reach the maximum value of about 2 E-7.

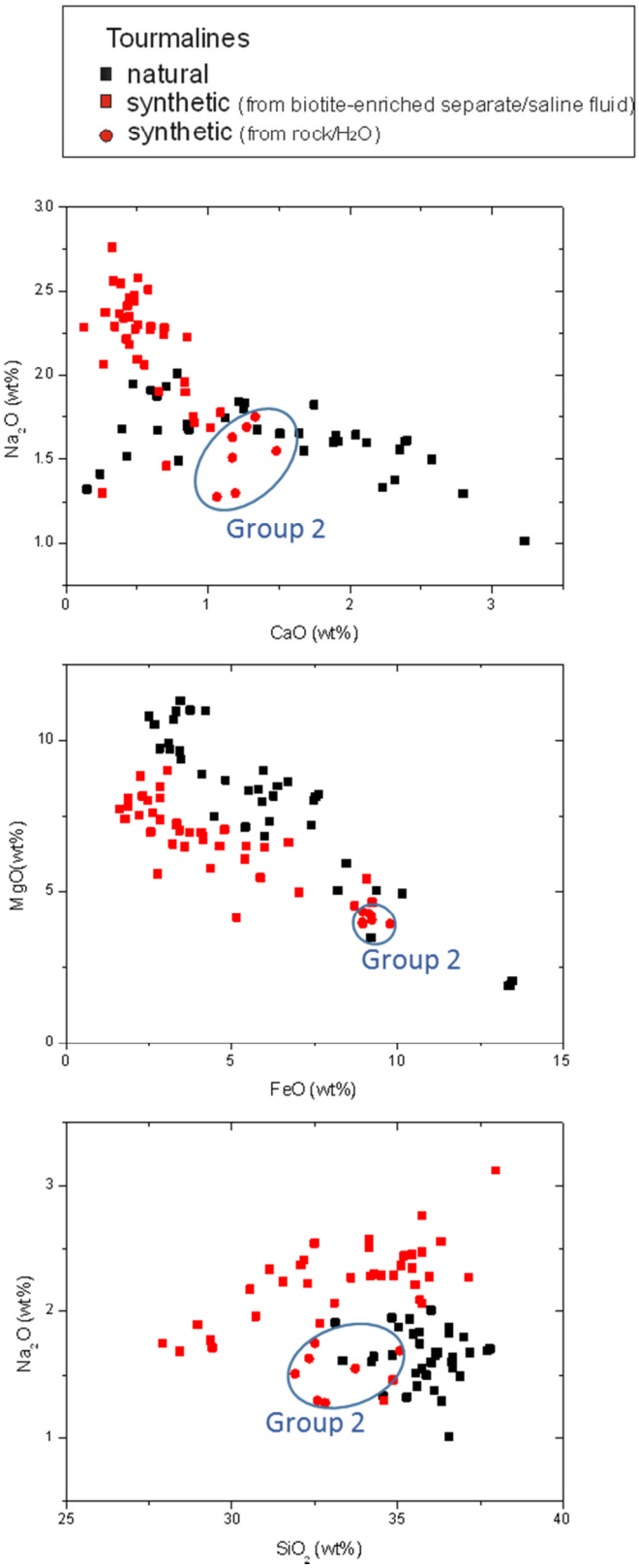

Figure 1.3.1.: Graphs showing some major oxides in both synthetic and natural tourmaline. Synthetic crystals (in red) are split in Group 1 (biotite enriched separate + saline fluid) and Group 2 (rock + pure water).

TABLES

Table 1.1.1: Mineral chemistry in GN1B sample. (continued…)

	chlo	chlo		biot	biot	biot	biot	biot	biot	biot	biot	biot		plag	plag	plag
Sample	GN1B	GN1B		GN1B	GN1B	GN1B	GN1B	GN1B	GN1B	GN1B	GN1B	GN1B		GN1B	GN1B	GN1B
analyses	bio1	1		11	20	26	28	31	33	35	36	37		10	23	38
SiO2	23.55	24.08		33.80	33.11	33.47	33.33	33.79	33.42	33.66	32.87	33.37		64.73	66.82	66.43
TiO2	0.14	0.28		2.29	3.65	2.77	2.75	2.95	3.37	3.10	3.49	2.93		0.03	0.06	0.23
Al2O3	20.85	20.88		20.36	19.27	20.14	19.70	19.34	19.19	19.51	19.03	19.80		18.79	19.10	19.21
Cr2O3	0.26	0.08		0.00	0.32	0.74	0.23	0.25	0.58	0.47	0.07	0.35		0.42	0.92	0.00
FeO	31.96	30.66		23.21	24.68	23.61	22.50	23.65	22.90	23.74	24.26	23.24		0.78	0.75	0.17
MnO	0.46	0.74		1.19	1.31	1.35	0.96	0.88	0.68	1.05	1.10	0.91		1.40	0.78	0.70
MgO	9.87	10.38		6.89	5.29	5.93	6.90	6.89	6.65	6.17	5.84	6.70		0.00	0.00	0.02
CaO	0.07	0.02		0.07	0.18	0.00	0.20	0.00	0.00	0.15	0.01	0.00		0.45	0.44	0.39
Na2O	0.06	0.00		0.13	0.24	0.27	0.20	0.30	0.14	0.26	0.29	0.23		12.16	11.69	11.49
K2O	0.28	0.60		9.85	9.69	9.88	10.10	9.69	10.42	10.07	10.04	9.62		0.13	0.21	0.37
Sum	87.51	87.74		97.77	97.74	98.16	96.86	97.74	97.35	98.19	96.99	97.17		98.89	100.76	99.01
Cations per 28 O:			***Cations per 22 O:***										***Cations per 8 O:***			
Si	5.219	5.281	Si	5.157	5.114	5.117	5.139	5.170	5.143	5.148	5.116	5.129	Si	2.942	2.965	2.972
Al IV	2.781	2.719	Al IV	2.843	2.886	2.883	2.861	2.830	2.857	2.852	2.884	2.871	Al	1.007	0.999	1.013
sum	8.000	8.000	sum	8.000	8.000	8.000	8.000	8.000	8.000	8.000	8.000	8.000	Fe3+	0.033	0.031	0.007
													sum T	3.981	3.995	3.992
Al VI	2.665	2.677	Al VI	0.817	0.622	0.745	0.718	0.658	0.622	0.665	0.607	0.715				
Ti	0.023	0.047	Ti	0.262	0.424	0.318	0.319	0.340	0.391	0.357	0.408	0.339	Ca	0.022	0.021	0.019
Mg	3.262	3.394	Fe2+	2.963	3.192	3.022	2.904	3.029	2.950	3.039	3.160	2.989	Na	1.072	1.006	0.996
Fe2+	5.928	5.629	Mn	0.153	0.171	0.175	0.125	0.113	0.088	0.136	0.145	0.119	K	0.008	0.012	0.021
Mn	0.087	0.138	Mg	1.567	1.219	1.352	1.587	1.572	1.525	1.407	1.356	1.535	sum Y	1.101	1.039	1.036
Ca	0.017	0.005	Cr	0.000	0.039	0.089	0.029	0.030	0.071	0.057	0.009	0.042				
Na	0.025	0.000	sum	5.763	5.667	5.702	5.683	5.741	5.647	5.662	5.684	5.740	sum T+Y	5.083	5.033	5.028
K	0.080	0.167														
sum	12.087	12.057	Ca	0.011	0.031	0.000	0.032	0.000	0.000	0.024	0.001	0.000	An	2.0	2.0	1.8
			Na	0.037	0.073	0.081	0.060	0.088	0.042	0.078	0.086	0.070	Ab	97.3	96.8	96.2
Mg #	35.5	37.6	K	1.917	1.910	1.928	1.987	1.892	2.046	1.966	1.993	1.887	Or	0.7	1.2	2.1
			sum	1.965	2.013	2.008	2.079	1.979	2.088	2.068	2.081	1.957				
vacancies	0.018	0.110	Tot.	15.728	15.680	15.710	15.762	15.721	15.735	15.730	15.766	15.697				
Mg+Fe	9.190	9.023														
Al+vac.	2.683	2.787	Mg #	34.6	27.6	30.9	35.3	34.2	34.1	31.6	30.0	33.9				
Type	I	I	H2O calc	3.93	3.89	3.93	3.89	3.92	3.91	3.93	3.85	3.91				
	Fe-chl	Fe-chl	Sum calc	101.7	101.6	102.1	100.8	101.7	101.3	102.1	100.8	101.1				
Variety	chamosite	chamosite														
			XMg	0.346	0.276	0.309	0.353	0.342	0.341	0.316	0.300	0.339				
			XFe	0.654	0.724	0.691	0.647	0.658	0.659	0.684	0.700	0.661				
			annite	0.38	0.40	0.39	0.37	0.39	0.38	0.39	0.39	0.37				
			siderophyllite	0.28	0.32	0.30	0.28	0.27	0.28	0.29	0.31	0.29				
			phlog	0.20	0.15	0.17	0.20	0.20	0.19	0.18	0.17	0.19				
			eastonite	0.15	0.12	0.14	0.15	0.14	0.15	0.13	0.13	0.15				

Table 1.1.1: Mineral chemistry in GN1B sample.

	cord	cord	cord			musc	musc	musc		and	and	and	and		ilm	ilm
Sample	GN1B	GN1B	GN1B			GN1B	GN1B	GN1B		GN1B	GN1B	GN1B	GN1B		GN1B	GN1B
analyses	14	18	21			4	6	39		15	16	25	30		13	34
SiO2	46.48	46.62	47.00			45.18	44.69	45.30		35.47	35.98	36.36	35.66		0.00	0.01
TiO2	0.05	0.00	0.00			0.11	0.41	0.24		0.02	0.05	0.00	0.33		51.52	51.69
Al2O3	31.55	31.21	31.28			33.27	34.74	35.52		61.88	61.18	61.22	61.11		0.05	0.00
Cr2O3	0.38	0.57	0.34			0.47	0.43	0.00		0.68	0.54	0.00	0.28		0.00	0.30
FeO	11.22	12.60	11.35			3.63	1.09	1.63		1.00	0.87	1.28	1.34		47.39	49.23
MnO	1.20	0.87	0.68			0.67	0.66	0.59		0.74	0.47	0.53	0.60		3.95	2.50
MgO	5.33	5.26	5.02			1.35	0.33	0.48		0.00	0.00	0.01	0.02		0.03	0.07
CaO	0.09	0.10	0.13			0.00	0.03	0.05		0.00	0.07	0.06	0.03		0.02	0.02
Na2O	1.99	1.06	1.72			0.46	0.51	0.58		0.00	0.03	0.02	0.00		0.05	0.11
K2O	0.30	0.14	0.26			7.46	8.18	7.79		0.00	0.09	0.15	0.07		0.03	0.20
Sum	98.59	98.43	97.78			92.59	91.08	92.18		99.79	99.28	99.62	99.44		103.04	104.14
:Cations per 18 O. Fe2+/3+ calc. on the basis of for charge balance					*Cations per 22 O:*				*Cations per 5 O:*					*Molar proportions of cations normalized to a formula unit of 2 sites (Stormer, 1983).*		
Si	4.792	4.869	4.900		Si	6.185	6.158	6.155	Si	0.970	0.987	0.994	0.979			
Al	3.833	3.841	3.844		Al IV	1.815	1.842	1.845	Ti	0.000	0.001	0.000	0.007	Si	0.000	0.000
Ti	0.004	0.000	0.000		sum	8.000	8.000	8.000	Al	1.998	1.981	1.976	1.981	Ti	0.947	0.942
Fe3+	0.982	0.606	0.710						Fe2+	0.023	0.020	0.029	0.031	Al	0.001	0.000
Cr	0.031	0.047	0.028		Al VI	3.551	3.801	3.843	Mn	0.017	0.011	0.012	0.014	Fe2+	0.969	0.998
Mg	0.820	0.820	0.781		Ti	0.011	0.042	0.024	Mg	0.000	0.000	0.000	0.001	Mn	0.082	0.051
Fe2+	0.000	0.496	0.281		Fe2+	0.415	0.126	0.186	Ca	0.000	0.002	0.002	0.001	Mg	0.001	0.003
Mn	0.105	0.077	0.060		Mn	0.077	0.077	0.068	Na	0.000	0.002	0.001	0.000	Ca	0.000	0.001
Ca	0.010	0.011	0.014		Mg	0.277	0.069	0.097	K	0.000	0.003	0.005	0.002	Cr	0.000	0.006
Na	0.398	0.214	0.347		Cr	0.051	0.047	0.000	Cr	0.015	0.012	0.000	0.006			
K	0.039	0.019	0.035		sum	4.383	4.162	4.218	sum	3.023	3.018	3.021	3.022	Fe3+ calc.	0.105	0.110
sum	11.014	11.000	11.000											Fe2+ calc.	0.863	0.888
					Ca	0.000	0.004	0.007						FeOcalc	42.25	43.81
Mg#	88.7	58.9	69.6		Na	0.121	0.138	0.153						Fe2O3calc.	5.72	6.02
					K	1.304	1.439	1.350								
					sum	1.425	1.580	1.510						X(Fe2+,S2+)	0.91	0.94
														X(Fe3+, S3+)	0.99	0.95
					Tot.	13.807	13.743	13.728								
														X' Ilm	0.95	0.94
					Mg #	39.96	35.33	34.32								
					H2O calc	4.38	4.35	4.41								
					Sum calc	97.0	95.4	96.6								

Table 1.1.2: List of experiments.

PREPARATION and EXPERIMENTS																		
Experimental run	**2**	**4**	**5**	**6**	**7**	**8**	**9**	**10**	**11**	**12**	**13**	**14**	**15**	**16**	**17**	**18**	**19**	**20**
Start. Mat. type*	1	2	1	1	1	3	3	3	3	3	3	4	4	5	1	4	3	1
Start. Mat. (g)	0.0389	0.0330	0.0510	0.3955	0.5264	0.0421	0.0523	0.0539	0.0486	0.0492	0.0362	0.0540	0.0276	0.0310	0.3284	0.0451	0.0486	0.3130
H3BO3 (g)						0.0114				0.0059	0.0104			0.0073		0.0134	0.0115	
Fluid type**	20wt%NaCl	20wt%NaCl	20wt%NaCl	20wt%NaCl	20wt%NaCl	pure H2O	pure 0.1M	0.01M	0.1M	20wt%NaCl	20wt%NaCl	0.1M	0.01M	20wt%NaCl	20wt%NaCl	20wt%NaCl	pure H2O	pure H2O
Fluid (g)	0.0786	0.0394	0.0514	0.6593	0.6520	0.0831	0.0839	0.0836	0.0854	0.0803	0.0839	0.0859	0.0404	0.0759	0.6487	0.0919	0.0867	0.5215
Length capsule (mm)	18	19	17	97	97	25	25	25	25	20	20	20	15	20	92	25	25	95
Solid/fluid	0.49	0.84	0.99	0.60	0.81	0.64	0.62	0.64	0.57	0.69	0.56	0.63	0.68	0.50	0.51	0.64	0.69	0.60
H3BO3 calc (M)	1.6	2.3	3.2	1.9	2.6	2.2	0.1	0.0	0.1	1.2	2.0	0.1	0.0	1.6	1.6	2.4	2.1	1.94
T(°C)	**500**	**500**	**500**	**600**	**540**	**600**	**600**	**600**	**600**	**600**	**600**	**600**	**600**	**500**	**500**	**600**	**600**	**500**
P(bar)	**1300**	**1300**	**1300**	**1000**	**1000**	**1000**	**1000**	**1000**	**1000**	**1000**	**1000**	**1000**	**1000**	**1000**	**1000**	**1000**	**1000**	**1000**
Duration experiment (h)	**168**	**168**	**168**	**167**	**164.5**	**168**	**168**	**168**	**168**	**167**	**167**	**167**	**167**	**165**	**165**	**167**	**167**	**168**
Result	OK	OK	OK	OK	FAILED	OK	OK	OK	OK	FAILED	FAILED	FAILED	OK	OK	OK	OK	OK	OK
*Starting material																		
1: GN1B sep. – H3BO3 (4:1 in weight)																		
2: GN1B sep. – H3BO3 - Al2O3 (4:1:1 in weight)																		
3: GN1B whole rock																		
4: GN1B sep.																		
5: GN1B sep. cal.																		
**Fluid type																		
20wt%NaCl aqueous solution prepared using suprapur NaCl and milliQ water																		
0.1M: aqueous solution (20wt%NaCl) 0.1M H3BO3																		
0.01M: aqueous solution (20wt%NaCl) 0.01M H3BO3																		
pure 0.1M: milliQ water 0.1M H3BO3																		
pure H2O: milliQ water																		

Table 1.1.3.: SEM-EDS analyses of experimental products.

Phase	tourmaline	tourmaline	tourmaline	tourmaline	tourmaline	tourmaline	tourmaline	tourmaline	tourmaline	tourmaline	tourmaline	tourmaline	tourmaline	tourmaline	tourmaline	tourmaline	tourmaline	tourmaline	tourmaline	tourmaline	tourmaline	tourmaline	tourmaline	tourmaline
Experiment	2	2	2	2	2	4	4	4	4	4	5	5	5	5	5	8	8	8	8	8	8	8	8	8
analysis	2,1	2,4	3,2	7,2	7,4	1,1	1,3	1,5	1,6	1,7	1,1	3,1	3,2	3,4	4,2	1,1	1,2	2,1	3,1	6,1	6,2	7,1	8,1	8,2
SiO2	42.19	45.56	42.07	43.26	44.81	37.83	37.62	36.86	36.40	37.59	42.03	42.31	41.22	41.38	41.76	39.59	35.50	43.38	34.80	43.10	43.68	45.15	44.30	44.21
TiO2	0.53		1.15				0.62				1.37	1.02	1.98	2.46	2.07	1.60	2.19	0.00	0.00	0.80	0.70	0.00	0.92	0.62
Al2O3	36.73	34.61	34.40	36.22	35.61	47.15	43.38	45.01	46.75	44.33	35.92	33.64	23.20	21.89	26.04	33.01	31.06	36.85	31.73	37.49	36.66	33.29	36.22	36.83
FeO	9.85	8.07	10.60	10.49	9.36	8.71	9.46	10.36	9.54	10.35	11.24	13.41	24.02	24.91	20.11	18.75	24.35	11.27	26.59	11.26	10.60	12.49	10.28	8.81
MnO																								
CaO	0.38		0.24	0.91	0.61		1.29	1.67	1.59	1.47	1.19	0.32	0.60	0.46	0.95	2.06	2.55	1.01	2.77	1.69	1.29	1.69	1.18	1.40
MgO	6.28	6.00	6.41	5.31	6.02	3.45	2.67	2.93	2.83	2.88	5.81	6.19	5.47	4.88	3.90	3.76	3.45	4.84	3.32	3.93	5.21	4.29	5.04	5.37
Na2O	4.03	5.26	2.89	2.76	3.34	2.86	2.96	2.60	2.29	3.38	2.09	3.10	3.33	3.72	4.32	1.23	0.90	2.67	0.78	1.74	1.86	1.63	2.08	2.04
K2O		0.59	2.25	0.93	0.22		1.50				0.34	0.01	0.18	0.29	0.85	0.00	0.00	0.00	0.00	0.00	0.00	1.46	0.00	0.00
Cl							0.49	0.56	0.60															

Table 1.1.4.: EPM analyses of experimental products. (continued…)

Phase	tourmaline	tourmaline	tourmaline	tourmaline	tourmaline	tourmaline	tourmaline	tourmaline	tourmaline	tourmaline	tourmaline	tourmaline	tourmaline	tourmaline	tourmaline	tourmaline	tourmaline	tourmaline
Sample	Exp 2	Exp 2	Exp 2	Exp 2	Exp 2	Exp 2	Exp 5	Exp 5	Exp 5	Exp 5	Exp 6	Exp 6	Exp 6	Exp 6	Exp 8	Exp 8	Exp 8	Exp 8
analysis	0d	6	11	16	18	19	17	18	19	20	6	7	9	15	4	9	10	13
SiO_2	30.55	35.54	35.75	35.44	35.10	34.52	34.86	30.72	32.28	37.95	34.16	34.28	34.18	32.09	33.72	32.82	35.07	32.33
TiO_2	0.93	0.39	0.48	0.50	0.41	0.56	0.94	0.90	0.67	0.83	1.06	1.32	0.98	1.16	0.65	0.67	0.87	0.63
Al_2O_3	30.32	34.66	35.51	34.89	34.76	34.49	32.23	32.91	31.97	29.47	34.86	33.51	35.09	35.89	33.91	31.38	33.95	30.78
Cr_2O_3	0.17	0.02	0.00	0.16	0.31	0.00	0.09	0.00	0.27	0.02	0.13	0.09	0.01	0.09	0.00	0.04	0.14	0.20
FeO	9.23	3.72	1.87	3.33	2.30	4.77	8.71	5.43	3.41	4.35	2.24	3.05	4.13	2.83	9.22	8.96	9.15	9.78
MnO	0.07	0.08	0.04	0.03	0.00	0.07	0.04	0.00	0.01	0.01	0.03	0.00	0.00	0.01	0.03	0.00	0.00	0.25
MgO	4.66	6.97	8.10	7.28	8.17	7.07	4.55	6.52	7.03	5.80	8.85	9.04	6.82	8.10	4.06	4.33	4.29	3.94
CaO	0.45	0.42	0.55	0.45	0.37	0.60	0.71	0.83	0.85	1.02	0.58	0.51	0.12	0.27	1.48	1.06	1.27	1.17
Na_2O	2.18	2.22	2.06	2.46	2.37	2.29	1.46	1.96	2.23	3.12	2.51	2.30	2.29	2.37	1.55	1.28	1.69	1.63
K_2O	0.04	0.00	0.03	0.07	0.10	0.00	0.07	0.00	0.14	0.20	0.06	0.03	0.07	0.00	0.00	0.20	0.00	0.00
H_2O*	3.27	3.65	3.70	3.67	3.66	3.63	3.54	3.378	3.400	3.569	3.67	3.64	3.62	3.59	3.55	3.39	3.64	3.36
B_2O_3*	9.48	10.58	10.73	10.65	10.60	10.52	10.25	9.79	9.85	10.34	10.63	10.55	10.49	10.39	10.30	9.83	10.55	9.74
Li_2O*	0.00	0.00	0.00	0.00	0.00	0.00	0.00	0.00	0.00	0.00	0.00	0.00	0.00	0.00	0.00	0.00	0.00	0.00
Total*	91.36	98.24	98.84	98.92	98.15	98.52	97.46	92.45	92.11	96.69	98.77	98.32	97.79	96.78	98.48	93.96	100.62	93.82
Structural formula based on 31 anions (O, OH, F)																		
T: Si	5.60	5.84	5.79	5.79	5.75	5.70	5.91	5.45	5.69	6.38	5.58	5.65	5.66	5.37	5.69	5.80	5.78	5.77
Al	0.40	0.16	0.21	0.21	0.25	0.30	0.09	0.55	0.31	0.00	0.42	0.35	0.34	0.63	0.31	0.20	0.22	0.23
sum T	6.00	6.00	6.00	6.00	6.00	6.00	6.00	6.00	6.00	6.38	6.00	6.00	6.00	6.00	6.00	6.00	6.00	6.00
B	3.00	3.00	3.00	3.00	3.00	3.00	3.00	3.00	3.00	3.00	3.00	3.00	3.00	3.00	3.00	3.00	3.00	3.00
Z: Al	6.00	6.00	6.00	6.00	6.00	6.00	6.00	6.00	6.00	5.84	6.00	6.00	6.00	6.00	6.00	6.00	6.00	6.00
Mg	0.00	0.00	0.00	0.00	0.00	0.00	0.00	0.00	0.00	0.16	0.00	0.00	0.00	0.00	0.00	0.00	0.00	0.00
sum Z	6.00	6.00	6.00	6.00	6.00	6.00	6.00	6.00	6.00	6.00	6.00	6.00	6.00	6.00	6.00	6.00	6.00	6.00
Y: Al	0.15	0.55	0.57	0.50	0.47	0.42	0.35	0.34	0.34	0.00	0.30	0.15	0.51	0.44	0.43	0.34	0.37	0.24
Ti	0.13	0.05	0.06	0.06	0.05	0.07	0.12	0.12	0.09	0.11	0.13	0.16	0.12	0.15	0.08	0.09	0.11	0.08
Cr	0.02	0.00	0.00	0.02	0.04	0.00	0.01	0.00	0.04	0.00	0.02	0.01	0.00	0.01	0.00	0.01	0.02	0.03
Mg	1.27	1.71	1.96	1.77	2.00	1.74	1.15	1.73	1.85	1.29	2.16	2.22	1.69	2.02	1.02	1.14	1.05	1.05
Mn	0.01	0.01	0.01	0.00	0.00	0.01	0.01	0.00	0.00	0.00	0.00	0.00	0.00	0.00	0.00	0.00	0.00	0.04
Fe2+	1.42	0.51	0.25	0.45	0.32	0.66	1.24	0.81	0.50	0.61	0.31	0.42	0.57	0.40	1.30	1.32	1.26	1.46
sum Y	3.00	2.83	2.84	2.81	2.87	2.90	2.87	2.99	2.82	2.01	2.91	2.97	2.89	3.01	2.84	2.90	2.81	2.89
X: Ca	0.09	0.07	0.10	0.08	0.07	0.11	0.13	0.16	0.16	0.18	0.10	0.09	0.02	0.05	0.27	0.20	0.22	0.22
Ba	0.00	0.00	0.00	0.00	0.00	0.00	0.00	0.00	0.00	0.00	0.00	0.00	0.00	0.00	0.00	0.00	0.00	0.00
Na	0.78	0.71	0.65	0.78	0.75	0.73	0.48	0.67	0.76	1.02	0.80	0.73	0.73	0.77	0.51	0.44	0.54	0.56
K	0.01	0.00	0.01	0.01	0.02	0.00	0.02	0.00	0.03	0.04	0.01	0.01	0.01	0.00	0.00	0.04	0.00	0.00
vacancy	0.13	0.22	0.25	0.13	0.16	0.16	0.38	0.17	0.05	0.00	0.09	0.17	0.23	0.18	0.23	0.32	0.23	0.21
OH	4.00	4.00	4.00	4.00	4.00	4.00	4.00	4.00	4.00	4.00	4.00	4.00	4.00	4.00	4.00	4.00	4.00	4.00
Mineral Name	Schorl	Dravite	Dravite	Dravite	Dravite	Dravite	Schorl	Dravite	Dravite	Dravite	Dravite	Dravite	Dravite	Dravite	Schorl	Schorl	Schorl	Schorl
Tourmaline Recalculation: Developed by Julie Selway & Jian Xiong																		
**** B2O3, H2O and Li2O = calculated by stoichiometry; B = 3 apfu, OH+F = 4 apfu & Li = 15-total(T+Z+Y).***																		

Table 1.1.4.: EPM analyses of experimental products.

Phase	K-feldspar	K-feldspar	K-feldspar		biot	biot	biot	biot	biot	biot	biot	biot	biot		ilm	ox	ox	ox	ox
Sample	Exp 8	Exp 8	Exp 8		Exp 2	Exp 2	Exp 5	Exp 5	Exp 6	Exp 6	Exp 9	Exp 11	Exp 11	Exp 15	Exp 6	Exp 6	Exp 6	Exp 6	Exp 6
analysis	8bis-1	8bis-3	8bis-4		5	12	2	13	10	16	4	2	3	2	3	1b1	1b2	1b3	1b4
SiO_2	62.28	63.49	63.85		33.76	33.78	33.27	33.49	33.88	33.68	35.34	34.32	34.12	32.75	0.61	2.93	2.51	2.02	4.08
TiO_2	0.12	0.02	0.00		2.98	2.16	3.45	3.17	2.89	2.67	2.81	2.25	3.11	2.69	50.83	1.06	1.01	0.99	1.27
Al_2O_3	18.67	18.43	19.95		19.43	18.28	18.26	17.86	19.26	19.70	19.97	19.99	19.30	19.79	0.02	1.10	1.05	0.89	2.16
Cr_2O_3	0.00	0.00	0.00		0.00	0.14	0.07	0.11	0.00	0.11	0.03	0.05	0.21	0.00	0.01	0.00	0.01	0.93	0.35
FeO	1.23	0.53	1.54		21.99	22.14	22.52	22.88	22.74	21.07	21.98	21.68	20.69	20.88	44.89	93.24	95.60	93.57	86.25
MnO	0.22	0.38	0.23		0.23	0.01	0.14	0.16	0.25	0.15	0.16	0.27	0.14	0.28	0.53	0.06	0.26	0.30	0.55
MgO	0.04	0.17	0.23		6.02	8.14	6.20	7.39	5.60	7.09	6.51	6.54	7.49	5.81	1.10	0.71	0.68	0.23	0.80
CaO	0.62	0.35	0.13		0.00	0.00	0.00	0.10	0.00	0.04	0.11	0.24	0.00	0.07	0.13	0.00	0.38	0.17	0.07
Na_2O	3.11	2.48	2.54		0.25	0.19	0.33	0.14	0.23	0.37	0.11	0.18	0.27	0.56	0.17	0.28	0.27	0.29	0.25
K_2O	11.77	13.30	12.82		9.01	9.50	9.34	9.71	9.16	9.55	8.83	8.96	8.90	8.43	0.00	0.19	0.00	0.20	0.35
Sum	98.06	99.15	101.30		93.67	94.34	93.60	95.01	93.99	94.44	95.86	94.48	94.23	91.27	98.29	99.58	101.76	99.59	96.12
															Fe (wt%)	72.48	74.31	72.73	67.04
Numbers of ions on the basis of 8 O:				Numbers of ions on the basis of 22 oxygens:												Fe3O4?	Fe3O4?	Fe3O4?	Fe3O4?
Si	2.93	2.96	2.91																
Al	1.03	1.01	1.07	Si	5.31	5.30	5.28	5.26	5.33	5.25	5.39	5.33	5.29	5.26					
Fe	0.05	0.02	0.07	Al IV	2.69	2.70	2.72	2.74	2.67	2.75	2.61	2.67	2.71	2.74					
sum T	4.01	4.00	4.04	sum Z	8.00	8.00	8.00	8.00	8.00	8.00	8.00	8.00	8.00	8.00					
Ca	0.03	0.02	0.01	Al VI	0.91	0.68	0.70	0.56	0.90	0.87	0.97	0.99	0.82	1.01					
Na	0.28	0.22	0.22	Ti	0.35	0.25	0.41	0.37	0.34	0.31	0.32	0.26	0.36	0.33					
K	0.71	0.79	0.75	Fe2+	2.89	2.91	2.99	3.00	2.99	2.75	2.80	2.82	2.69	2.81					
Sr	0.00	0.00	0.00	Mn	0.03	0.00	0.02	0.02	0.03	0.02	0.02	0.04	0.02	0.04					
Ba	0.00	0.00	0.00	Mg	1.41	1.90	1.47	1.73	1.31	1.65	1.48	1.51	1.73	1.39					
sum Y	1.02	1.03	0.98	Cr	0.00	0.02	0.01	0.01	0.00	0.01	0.00	0.01	0.03	0.00					
				sum Y	5.60	5.77	5.60	5.70	5.59	5.61	5.60	5.62	5.65	5.58					
sum T+Y	5.03	5.03	5.02																
				Ca	0.00	0.00	0.00	0.02	0.00	0.01	0.02	0.04	0.00	0.01					
An	3.05	1.68	0.65	Na	0.08	0.06	0.10	0.04	0.07	0.11	0.03	0.05	0.08	0.17					
Ab	27.80	21.69	22.97	K	1.81	1.90	1.89	1.94	1.84	1.90	1.72	1.78	1.76	1.73					
Or	69.15	76.62	76.38	sum X	1.88	1.96	1.99	2.00	1.91	2.02	1.77	1.87	1.84	1.91					
				Tot.	15.48	15.73	15.59	15.71	15.49	15.63	15.37	15.49	15.49	15.49					
				Mg #	32.78	39.57	32.92	36.54	30.48	37.50	34.54	34.95	39.20	33.16					

Table 1.1.5.: Analyses performed through Liquid Chromatography on aqueous solution used as in experiments and on Solution 6. -=below detection limit. NH4, Br and PO4 were below detection limit for both solutions. Error%=100*(cations-anions)/(cations+anions) in meq/l. Acceptable analyses should have it < 5%. Data relative to Solution in Exp.6 (in red) are calculated according to 1:93 dilution and considering Cl as a tracer (see text). Note that the effective salinity of the solution utilised in experiments is 21.67 wt%.

	NaCl 20%	**Solution 6**	**Solution in Exp. 6**	
ppm			(dilution 1:93)	Cl as a tracer
Na	87856	680	63240	74518
Cl	128872	1176	109368	128872
Li	-	1.24	115	136
K	-	140	13020	15342
Mg	-	2.7	251	296
Ca	-	2.33	217	255
F	-	1.29	120	141
SO_4	-	1.02	95	112
True salin.(%)	21.67			
meq/l				
Na	3821.49	29.58		
Cl	3635.32	33.17		
Li		0.18		
K		3.58		
Mg		0.22		
Ca		0.12		
F		0.07		
SO_4		0.02		
error%	*2.5*	*0.62*		

Table 1.1.6.: Analyses of fluids extracted from experiments 6, 17 and 20 performed through ICP-OES and LC. Dilution for liquid extraction were 1:93 (experiment 6), 1:79 (experiment 17), and 1:94 (experiment 20). na= not analysed, bdl= below detection limit.

Experiment	**6**		**17**		**20**	
T (°C)	600		500		500	
	ICP	LC	ICP	LC	ICP	LC
Na	57446	63240	64636	69046	bdl	398
Li	131	115	85	84	19	9.7
K	11439	13020	6438	8548	529	312
Mg	185	251	8	169	104	29
Ca	229	217	326	403	85	140
Fe	1786		2709		312	
Mn	237		164		1.9	
Si	na		274		1994	
Ni	na		1.7		bdl	
Cl		109368		119527		479
F		120		77		128
SO4		95		442		95
NO3		bdl		17		39
NH4		bdl		28		52

Table 1.2.1.: Average XFeO obtained from SEM data of synthetic tourmaline compared with modeled XFeO at the end of reaction.

	Average	Dev Std
Exp4	0.637524	0.036471
Exp2	0.497011	0.060852
Exp5	0.63594	0.133766
Model	0.65	

Table 1.2.2.: Volume fraction of minerals in the micaschist at the beginning of the simulation.

Mineral	Volume Fraction of Solid
Albite	0.4
k-feldspar	0.001
Annite	0.3
Quartz	0.09
Phlogopite	0.2
Dravite	0.0000
Schorl	0.0000
Magnetite	0.0000

2. Fluid-rock interaction in basalt of Iceland

Main features of the Geitafell fossil hydrothermal system

The extinct Geitafell central volcano, located in East Iceland, provides the opportunity to study the evolution of volcano-hydrothermal systems analogous to those currently active in rifting neovolcanic zone, like the Krafla geothermal system.
In the geothermal area of Geitafell several secondary alteration minerals formed as a reaction between host rock and hydrothermal fluids (Table 2.1., after Fridleifsson, 1983). Within the central volcano, evidence for up to seven periods of hydrothermal activity is preserved in the crosscutting relationships of alteration veins. The earliest veins predate contact-metamorphic activity and are composed of limonite and clays. Upon the emplacement of a central gabbros, a high-temperature system was active and produced a contact metamorphic aureola consisting of an inner aureola of sanidinite facies basaltic lava hornfels (formed by secondary augite-andesine-ore) enveloped by an outer aureole of skarn deposits, moreover an actinolite-sphene assemblage occurs within the gabbro and also replace wall-rock zones of contact aureola (Fridleifsson, 1984) (see report of Task 3.1 for further details). Later hydrothermal events superimposed the high-temperature assemblage in the vein centre, producing the precipitation quartz, feldspar, epidote, albite, prehnite etc.
Fridleifsson (1984) suggested that the skarn minerals were produced from supercritical fluid (T≥400°C, P≤0.3 kbar), whereas, the actinolite-sphene assemblage developed from super-heated steam (T≥300°C, P≤0.1 kbar). Extensive high-temperature hydrothermal circulation also produced a widespread mineral alteration that includes: actinolite, epidote, chlorite, quartz, calcite and sulfides. Andradite garnet is also a common mineral in amygdale fillings.
The study of fluid inclusions trapped within hydrothermal alteration minerals of Geitafell indicated that the characteristics of the fluids of this paleo-geothermal system, are comparable with those of the "Krafla-like" geothermal systems, supporting the hypothesis that this fossil system is a proxy of these active systems (see report of Task 3.1). The main features of Krafla are reported below. Moreover, as numerical modelling of fluid-rock interaction processes was also extended to "Reykjanes-like" geothermal fields we also report below a description of the main features of the Reykjanes geothermal field.
In particular, supercritical conditions were tentatively hypothesized on the basis of fluid inclusion data in garnet assuming a pressure of at least 350 bars.

Main features of the *Krafla* geothermal system

The Krafla geothermal system is located within the active Krafla caldera of the Northern Volcanic Zone (Figure 2.1a). The Krafla volcano has a 300,000 year long history of predominately basaltic volcanic activity, with significant presence of rhyolitic rocks. Most recently activity was during 1975–1984, the so-called Krafla Fires (Sæmundsson, 1991).
Three distinct well fields within the system can be distinguished on the base of different subsurface temperature and permeability (Arnórsson, 1995). As far as the two most productive well fields are concerned (shown in Figure 2.1c), Suðurhlíðar shows a classical two-phase system in which temperatures follow the boiling point

curve with depth. On the contrary, the Leirbotnar well field shows a constant temperature-depth profile at ~205 °C down to 1 km depth, whereas in the deepest portion follows the boiling point of water. This evidence can be interpreted as the result of an inferred aquiclude that occurs at approximately 1,000–1,500 m depth, which separates an upper and lower fluid circulation zone (Ármannsson et al., 1987; Darling & Ármannsson, 1989). High downhole temperatures of Hvíthólar, a third, smaller well field, located to the south (not shown in Figure 2.1c), are ascribed to hot fluids uprising along the Krafla caldera rim.

The Krafla geothermal fluids have low total dissolved solid content (~700 ppm; Arnórsson, 1995), bicarbonate is the major anion (Ármannsson et al. 1987), whereas oxygen and hydrogen isotopes have a meteoric signature (Figure 2.2), although both $\delta^{18}O$ and δD values of fluids discharged from individual wellheads are in a large range: −13.4 to −10.3‰ and −95 to −85‰, respectively (Darling & Ármannsson, 1989; Sveinbjörnsdóttir et al., 1986). Attempts to simulate the geothermal fluid composition by titrating Krafla rock with local groundwater suggested that the geothermal fluid composition cannot derive from water and rock interactions alone, but volcanic gas must have been added too (Ármannsson, 2001).

The chemistry and physical properties of individual wells reveals several additional anomalies:

1) in the upper zone of Leirbotnar temperatures are lower than expected if fluids were a product of boiling from the lower zone. Instead, there must be mixing with cold groundwater recharged from another source.

2) Although the water recharge to the deep aquifer in Leirbotnar field has a likely source in a level plateau stretching to the north and west of the field (Arnórsson, 1995; Darling & Ármannsson, 1989), there is no similarly obvious source for the Suðurhlíðar field. Krafla Mountain, located to the northeast of Hveragil, forms a hydrologic barrier between the Suðurhlíðar well field and high-elevation regions to the north that recharge the Leirbotnar field. Darling & Ármannsson (1989) suggested that recharge to Suðurhlíðar is coming from a more distant southern region, but a specific source is not clear, nor is the process by which groundwater cross the hydrologic barriers created by faults along the southern caldera rim. Pope et al 2015, suggests that meteoric waters derived from a single source in the northwest are separated into the shallow sub-boiling reservoir, and deeper two-phase reservoir. Interaction between these reservoirs occurs by channelized vertical flow of vapor along fractures, and input of magmatic volatiles further alters fluid chemistry in some wells. Isotopic compositions of hydrothermal epidote reflect local equilibrium with fluids formed by mixtures of shallow water, deep vapor condensates and magmatic volatiles, whose ionic strength is subsequently derived from dissolution of basalt host-rock.

In the recent past, due to unrest of volcanic activity in the Krafla region, some wells suffered large inputs of CO_2 and other magmatic gases, resulting in fluid pH as low as 2 and contaminated two upflow zones causing deposition and corrosion in wells (Ármannsson et al., 1987, 1989; Arnórsson, 1995; Bird & Spieler, 2004). Geochemical monitoring of main gas concentrations in geothermal fluids, started when fissure eruptions occurred within the Krafla caldera between 1975 and 1984, showed a systematic decrease in the gas contents of Leirbotnar wells as magmatism has subsided (Ármannsson et al., 1989). The fumarole composition in the area was relatively stable from 1871 to 1975 when the Krafla Fires started. Their effects were apparently twofold: 1) a large amount of volcanic gas swamped parts of the system, sending the gas composition out of equilibrium but gradually to a new equilibrium

(Ármannsson et al., 1989) and 2) other parts seem to have become hotter due to the proximity of magma, and the gas composition changed accordingly.
The gas concentrations of the affected fluids have declined markedly in later years, although they are still high in the northeastern part of the area. Currently, the gas likely flows from a "pool" reservoir formed some years ago during magmatic gas influx. The conceptual geochemical model of Krafla finds confirmation and insights in recent geophysical models (Gasperikova et al., 2015; Rosenkjaera et al., 2015)
In June 2009,the exploratory borehole IDDP-01 at Krafla, the first deep well designed to explore a super-critical geothermal reservoir, failed to reach its target as drilling had to be terminate at a depth of only 2.1 km when magma unexpectedly entered the borehole (Hólmgeirsson et al.,2010; Pálsson et al.,2014).

Main features of the *Reykjanes* geothermal system
The Reykjanes geothermal system is located on the southwestern tip of the Reykjanes Peninsula, on the landward extension of the Mid-Atlantic Ridge (Figure 2.3.). It is composed of highly fractured basalt lavas and hyaloclastites that have been intruded by shallow dikes and sills, with mafic intrusions more abundant with increasing depth (Franzson et al., 2002; Kristmannsdóttir, 1983). The Reykjanes volcanic system is the subaerial continuation of the submarine Reykjanes Ridge. The volcanic system is hosted in an oblique extensional tectonic setting, resulting in episodic fissure eruptions (Clifton & Kattenhorn, 2006). Fracturing and faulting in the region is due to extension along a NE–SW trending graben zone, marking the sub-aerial continuation of the Reykjanes Ridge (see Arnórsson, 1995 for summary). Surface geothermal manifestations at Reykjanes include steam vents, fractures emanating steam, steam heated mud pools, and warm ground.
No boiling springs, except Gunnuvher, are currently present at Reykjanes, but a seawater geyser was active between 1906 and 1930 (Sapper, 1908; Bàrdarson, 1931). Steam vents and steam heated mud pools are located in the two most active and intensely altered parts of the geothermal area (Figure 2.1b).
Reykjanes is a two-phase geothermal system to ~1500 m depth, in which temperatures follow the boiling point curve with depth and both liquid and vapor are present. Below ~1500 m, temperatures are approximately constant, with the highest recorded down-hole temperature at about 320°C. The Reykjanes geothermal system was considered to be dominated by seawater-derived hydrothermal fluids due to the elevated chloride content and total dissolved solids observed in this region relative to other high-temperature fields in Iceland, which apparently have a meteoric source (e.g. Krafla), or a mixed meteoric-seawater source, such as the nearby Svartsengi geothermal system (Arnórsson, 1995). Total chloride content, in fact, closely approximates seawater values, although other major elements including SiO_2, Ca, and K indicate that fluids have undergone substantial chemical modification through boiling, water– rock interaction, and perhaps evaporation (Figure 2.4.; Lonker et al., 1993; Arnórsson, 1995; Pope et al., 2009). However, hydrogen isotope values of Reykjanes fluids are inconsistent with an exclusively seawater-sourced geothermal fluid, which should have a δD_{FLUID} ≈0‰ (low as −23.1‰) (Figure 2.2), but is comparable to the isotopic composition of Svartsengi fluids (~−24‰), which are considered to be a mixture of ~70% seawater and 30% local meteoric water (ıD is approximately− 48‰) given their total dissolved solids content and salinity (Pope et al., 2014; Lonker et al., 1993; Ragnarsdóttir & Walther, 1984). Fluid inclusion studies of hydrothermal alteration minerals indicate a range of salinities from fresh to

seawater values (<1000 to 35,000 ppm) (Fowler et al., 2015; Franzson et al., 2002). The CO_2 concentrations range from about 500 to 2,500 mg/kg and variations in concentration for individual wells are generally small. Although CO_2 concentration seems to be buffered by minerals to some extent, there are some wells that do not follow the predicted relationship between CO_2 concentration and temperature, e.g. well RN-15, which has a reference temperature of 285°C but nonetheless has fairly high CO_2 concentrations (Óskarsson et al., 2015).
N_2 and Ar concentrations in the deep liquid are not controlled by mineral buffers, but rather by the inflow (from magma or fresh water) and outflow (in steam) of these gases to and from the reservoir. Studies of gas isotopes at Reykjanes indicate that Ar is largely derived from air and that the same applies to N_2 in recent years, but at the onset of production more magmatic N_2 was present in the system (Óskarsson et al., 2015).
Host rocks of the Reykjanes geothermal includes hyaloclastite, breccia, tuff, extrusive basalt, diabase, as well as a marine sedimentary sequence. The progressive hydrothermal alteration sequence observed with increasing depth results from reaction of geothermal fluids with the basaltic host rock, and was used to classify hydrothermal alteration into temperature- and depth- related zones (e.g. Franzson et al., 2002; Freedman et al., 2009; Fridleifsson et al., 2005). An assemblage of greenschist facies alteration minerals, including actinolite, prehnite, epidote and garnet, occurs at depths as shallow as 350 m. These minerals are commonly found in Icelandic geothermal systems at temperatures above 250°C (Bird & Spieler, 2004). This requires hydrostatic pressures that exceed the present-day depth to boiling point curve, and therefore must record alteration at higher fluid pressures, perhaps as a result of Pleistocene glaciation.

2.1. Fluids geochemistry and Volatile Organic Compounds (VOCs) of Krafla and Reykjanes geothermal systems, (Iceland)

As part of the IMAGE project, a sampling campaign for the gas collection from boreholes and fumaroles was carried in two different geothermal fields: Krafla and Reykjanes, respectively North-East and South-West Iceland. In addition the compositions of the liquid phase (brines) produced by the boreholes sampled for gas collection and the steam/liquid ratio of the discharged fluids were derived from samples taken during routine geochemical monitoring of the geothermal fields

The aims of this work was:

1) To obtain the composition of the reservoir fluids of two geothermal systems that will be used to validate the results of thermodynamic modelling
2) To study the VOCs composition, as well as the main gas composition and isotopic signatures, in order to compare different geothermal systems and to investigate the variation between the deep and the shallow part of the reservoirs. A special focus was devoted to the use of VOCs as geochemical tracers for the study of chemical-physical processes that control the volcanic/hydrothermal reservoir, with the aim to contribute to the study of indicators that can reveal the presence of fluid in supercritical conditions.

Sampling was carried out by Capecchiacci Francesco (CNR-IGG) and Ester Inga Eyjólfsdóttir (ISOR Iceland Geosurvey) between 19 and 23 May 2014.

Sampling strategy

The Krafla high-temperature geothermal system lies in the northern part of the neo-volcanic zone in Iceland. The Reykjanes geothermal field is located in the southwestern tip of the Reykjnes peninsula, 55 km southwest of Reykjavík. The Reykjanes peninsula is characterized by extensive postglacial lava fields.
During 19 - 21 May the sampling team carried out a fieldtrip in the Krafla geothermal system to collect gas samples from 3 different natural manifestation (fumaroles) and 3 boreholes characterized by different deep, as shown in Figure 2.1.1.
Fumaroles: *KRA FUM 1*(T 100°C), *KRA FUM 2* (T 98°C), *KRA FUM 3* (T 99°C).
Boreholes: *KJ 20* (well depth 1822m; T 186°C; P n.d.), *KJ 31* (deep 1400; T 184.6°C; P 10.3 bar at the well-head), *KJ 13* (800m; T 172.4 °C; P 8.1 bar at the well-head).
For each sampling point were collected different gas aliquots, as follows:

a) 1 Giggenbach bottle (evacuated doubleport gas bottle containing 40% NaOH) for main gas composition analysis;
b) 1 Glass Vial for VOCs analysis ;
c) 1 Glass Vial for $\delta^{13}C$ of CO_2 analysis ;
d) 1 condensate in plastic bottle for acidic gas analysis;

During 22-23 May, the sampling team carried out a fieldtrip at the Reykjanes geothermal system, where gas samples from 3 different fumaroles and from 3 boreholes were also collected (Figure 2.1.2.).
Fumaroles: *REY FUM 1*(T 103°C), *REY FUM 2* (T 102.6°C), *REY FUM 3* (T 101.5°C)
Boreholes: *H21* (well depth 1713m; T 220.9°C; P 22.4 bar), *H 27* (well depth 1503m; T 210.5°C; P 22.4 bar), *H 11* (well depth 2248m; T 238.5 °C; P 31.6 bar)
As Krafla, for each sampling point were taken:

e) 1 Giggenbach bottle for main gas composition analysis;
f) 1 Glass Vial for VOCs analysis ;
g) 1 Glass Vial for $\delta^{13}C$ of CO_2 analysis ;
h) 1 Plastic Bottles for condensate;

Total of 24 samples.
Gas samples for the analysis of the main gas components of the fumaroles were collected by using a 0.7 m long titanium tube inserted into the vent and connected, through a sampling line consisting of dewared glass tubes (Vaselli et al., 2006), to pre-evacuated 60 mL glass flasks equipped with a Thorion® valve and filled with a 5M NaOH solution (Giggenbach, 1975; Montegrossi et al., 2001) (Figure 2.1.3.). Gas samples for the analysis of VOC´s in the fumaroles were collected into the 12 mL glass vials after water vapor condensation carried out using water/ice-cooled glass device (Graham type condenser) connected to the dewared glass tubes (Figure 2.1.4.). Gas samples for the analysis of the main gas components of the boreholes were collected by using of ISOR equipment for the separation of the gas from the liquid phase and for the pressure removal (Figure 2.1.5.).
More detailed description of the fluid sampling and analytical methods are reported in Appendix 2

Main gas compositions

Outlet temperatures (in °C), depth and pressure of the wells, concentrations of the inorganic gases (CO_2, H_2S, N_2, Ar, O_2, H_2 and He, He), CH_4, (expressed in mmol/mol) in the dry gas fraction and $\delta^{13}C–CO_2$ (in ‰ V-PDB) are reported in Table 2.1.1a,b.
In agreement with the chemical inorganic main gas composition reported in literature (e.g. Christenson et al., 2010; Marks et al., 2010; Ármannsson et al., 2013; Ármannsson et al., 2014), besides steam (H_20 > 96%), the main gas compounds are CO_2, ranging from 765 to 885 mmol/mol, H_2S (from 22 to 143 mmol/mol), N_2 and H_2 (from 38 to 83 mmol/mol and from 13 to 89 mmol/mol respectively). Significant concentrations of CH_4 (from 0.23 to 2.75 mmol/mol), Ar (from 0.65 to 1.44 mmol/mol), and minor concentrations of O_2 and He (<0.6 mmol/mol) were also measured, with minor differences in terms of absolute concentrations between two different systems and from boreholes to fumaroles. The $\delta^{13}C$-CO_2 values, ranging from -0.57 to -4.15‰ V-PDB (Table 2.1.1.).
Relative He, N_2 and Ar contents in gases from the Krafla and Reykjanes wells point to a strong mantle source signatures (Figure 2.1.6.). Two component mixing between MORB and atmospheric end members is evident in both systems, consistent with Iceland's position on the mid-Atlantic Ridge.
Acidic gases (SO_2, HCl and HF) were not detected, suggesting that the deep magmatic input in the two systems was efficiently buffered by the hydrothermal reservoir (Ármannsson & Jeffrey, 1989**)**.

Brines
The geochemical d ata of the liquid phase in the geothermal wells of Krafla and Reykjanes (Tables 2.1.2. and 2.1.3., respectively) were derived from samples taken during routine geochemical monitoring of the geothermal fields .
In agreement with literature data (e.g. Pope et al., 2009; Pope et al., 2014), the Reykjanes brines are characterized by high salinity, whereas the Krafla brines show a relatively low salinity. The Reykjanes geothermal system is a seawater-dominated system that has been active since the Pleistocene and has undergone extensive hydrothermal alteration. Hence, modern fluids are chemically modified through diffusional exchange with relict hydrous alteration minerals. On the contrary, the Krafla geothermal system is hosted within an actively forming caldera, where magmatic fluids and local precipitation are mixed and variably separated into liquid and vapor phases by boiling processes affected by the heterogeneous permeability of the caldera's extrusive fill and subsequent intrusion of dikes and sills of both mafic and silicic origins.

VOCs
Up to 16 different VOCs, pertaining to the alkane (7 compounds), alkene (2 compounds), aromatic (4 compounds), sulfonated (3 compounds) groups, were identified and quantified (Table 2.1.4.).
The total amount of light hydrocarbons in Krafla (up to 0.007 mmol/mol) is one order of magnitude lower than Reykjanes (up to 0.02 mmol/mol). Significant concentrations of C_2–C_3 alkanes (e.g. C_2H_6 up to 0.01 mmol/mol), aromatics (e.g C_6H_6 up to 0.0018 mmol/mol) and S-substituted (C_4H_4S up to 0.0016 mmol/mol) are present, whereas alkenes are < 0.0000031 mmol/mol (Figure 2.1.7.).
According to the alkanes-alkenes-aromatics ternary diagram (Figure 2.1.8.), samples show a dominant hydrothermal-type composition and there were no indications of

strong cracking processes related to the presence of a magmatic component (Capaccioni et al., 2001; Tassi et al., 2005).

Heteroaromatics

Heteroaromatics compounds are indicative of medium-high temperature processes(60 < T < 350 °C), in particular thiophenes typically characterise hydrothermal fluids. In fact, according to Tassi et al. (2010) these S-bearing compounds are efficiently produced at hydrothermal conditions, whereas tend to be destroyed in presence of hot (T > 400°C), highly oxidizing fluids from a magma source. On the contrary, magmatic fluids are characterised by enrichments in furans (O-bearing compounds). Therefore, the "total S vs. thiophenes" correlation (Figure 2.1.9.) and the absence of furans, indicates that the Krafla and Reykjanes fluids are characterised by a dominant hydrothermal component, clearly distinguishable from both the typical magmatic fluids and low-temperature emissions. The correlation between C_4H_4S, 3-C_5H_6S and C_6H_6 (Figure 2.1.10a,b) can be explained by 2 hypotheses:
1) at hydrothermal conditions mono-aromatics and thiophenes are efficiently produced by similar genetic processes;
2) mono-aromatics and thiophenes have a similar behavior in response to changes of chemical-physical conditions caused by presence of oxidizing and high temperature (>400°C) magmatic fluids.

Summarizing, the study of Krafla and Reykjanes systems has the following scientific implications:
- Thiophenes can be utilized to evaluate contributions of fluids produced in different "natural sources", i.e., hydrothermal and magmatic. These results may have useful applications in geothermal prospection but also in in volcanic monitoring;
- C_6H_6, coupled with S-bearing heteroaromatics, can be considered a good tracer of the hydrothermal component in natural systems.

In the near future, we will try to use light alkane and alkene compounds for geothermometric evaluations and for determination of redox conditions of the deep fluid source.
The chemical and isotopic data show that the magmatic component in these gases is strongly modified by scrubbing due to hydrothermal water at temperatures up to 350°C (primary scrubbing) and shallow meteoric water (secondary scrubbing). The effects of scrubbing are stronger for gas discharges from bubbling pools than for the fumarolic gases.
The chemical-physical behavior of heterocyclic compounds (i.e. thiophenes and furans) represents a potential source of information that can be used for geochemical monitoring during future deep drilling, in order to detect any changes in the conditions related to the arrival of deep magmatic fluids.

2.2 Water-rock experiments by hydrothermal autoclave

Fluid-rock interaction experiments were performed in order to test the mineralogical transformations experienced by a typical Icelandic basalt when reacting with a fluid in super-critical conditions (400-600°C, 500 bar). Different fluid compositions were considered, as reported below.
The analytical methods used for experiments are described in Appendix I.

2.2.1 Starting material

Solids

A representative fresh basalt (sample EJ29A) was chosen as solid reactant for the experiments. The sample is a basaltic lava erupted from Eyjafjallajökull volcano during 2010. It is constituted by olivine, clinopyroxenes and plagioclase phenocrysts and a groundmass composed by glass and plagioclase, and less abundant olivine and spinel. The whole rock chemical analysis (determined by means of XRF) is reported in Table 2.2.1, whereas in Table 2.2.2 Electron probe micro-analysis (EPMA) of minerals and glass are reported.

The compositions of olivine and plagioclase phenocrysts are Fo_{78-73} and An_{62-57}, respectively, while less forsteritic (Fo_{65-60}) and anorthitic (An_{40}) compositions have been recorded in groundmass crystals. Clinopyroxene phenocrysts show generally diopsidic and augitic composition. Spinels in the groundmass are mainly magnetite-ulvöspinel solid solution.

The glass has SiO_2 contents in the range 53-59 wt% and shows significant variations in all analyzed major oxides (Table 2.2.2).

Fluids

As fluid reactant we initially considered pure water since fluid inclusions studies (Task 3.1) show that salinities of fluid inclusions is very low. Thus, experiments 1-6 were performed with MilliQ water.

After the first set of experiments different types of acidified solutions were chosen in the experiments:

H_2O: milliQ water

H_2O-HCl pH3: aqueous solution prepared with milliQ water and hydrochloric acid in order to achieve pH=3

H_2O-H_2SO_4 pH3: aqueous solution prepared with milliQ water and sulphuric acid in order to achieve pH=3

Experiments 9 and 10 were performed adding $Ag_2C_2O_4$ to the solution so that its decomposition causes a CO_2 molality of about 0.2. $Ag_2C_2O_4$ was prepared by reacting $H_2C_2O_4$ with $AgNO_3$, according to the following reaction:

$$H_2C_2O_4 + 2AgNO_3 = Ag_2C_2O_4 + 2NO_3^- + 2H^+$$

The $Ag_2C_2O_4$ decomposes at T= 140°C, according to the following reaction:

$$Ag_2C_2O_4 = 2CO_2 + 2Ag$$

For the experiments, we arbitrarily selected two different solid/fluid ratios: 1.6 and 0.3-0.4.

2.2.2 P-T conditions of experiments and equipment

Fluid inclusions data indicate that super-critical conditions at Geitafell could occurred at a pressure of at least 350 bar. Our experimental instrument does not allow to precisely control the pressure below 500 bar. Therefore, we chose to perform

experiments at pressure of 500 bar. We selected three temperatures, just to spanning from liquid-like (400-500°C) to vapour-like (500-600°C) supercritical fluid (Figure 2.2.1). Experiments duration varied from 166 to 213 h.
In Isl1-Isl6 experiments basalt (EJ29A) reacted with pure water at temperatures of 400, 500 and 600°C.
In Isl7 and Isl8 the basalt reacted with an aqueous solution of hydrochloric acid (at 400 and 500°C, respectively) while experiments Isl9 and Isl10 were run in the same conditions in a CO_2-bearing system (CO_2 molality of about 0.2). Finally, in Isl11 an acid (pH=3) aqueous solution with H_2SO_4 was chosen as fluid reactant.
The last three experiments were developed employing "long gold capsules" in order to recover the fluid after the experiment.
Details about reactants and experimental conditions are reported in Table 2.2.3.

2.2.3 Results

The different sets of experiments will be distinctly described.

Experiments Isl1-Isl6

Experimental products indicate that neo-formed minerals barely crystallized, as evidenced in the XRD spectra (Figure 2.2.2.) in which peaks are mainly attributable to plagioclases and, secondarily, to clinopyroxenes of the starting material.
We would have expected to find abundant alteration phases among the experimental products, since they could be stable in the experimental conditions (Figure 2.2.3.).
In fact, considering a basaltic protholit, the phases stable in the albite-epidote and hornblende hornfels facies are mainly actinolite, epidote, chlorite, talc, biotite, albite, quartz, almandine, anthophyllite, cordierite.
Moreover, in the XRD spectra none of the skarn minerals or late hydrothermal minerals observed at Geitafell were found.
Note that spectra of experiments performed at the same P-T conditions are very similar and thus the variation of solid/fluid ratios used in the experiments seems to be ineffective to the alteration of the basalt.
Considering the XRD spectra, the peaks at low 2 theta (6-7°), and possibly interpreted as saponite, appear only in experiments run at 400°C (Isl2, Isl4).
The findings of the latter mineralogical phase only in experiments at 400°C is congruent with observations from Cohen et al. (1980) that described "the synthesis of saponite from naturally occurring igneous rocks of intermediate to ultrabasic composition". In that paper, rocks were treated with water at 350-450°C and pressures as high as 350 bar and olivine and other ferromagnesian minerals along with cryptocrystalline and glassy material were believed to be the main reactive materials. As a result of the hydrothermal treatment, a number of chemical and physical changes occurred that resulted in a mineral mixture with saponite-like properties.
Scanning Electron Microscopy (SEM) investigations in our experiments (Figure 2.2.4.-2.2.5.) did not highlight extensive modification of the original phases. In experiments run at 400°C (Isl4) original plagioclase (bytwonite) seems to transform in Na-rich plagioclase (labradorite/andesine) and a Ca-rich phase, possibly epidote (Figure 2.2.4.a,b).

At higher temperatures (500-600°C) observations show very small crystals (<5 μm) growing on original phases (Figure 2.2.5.) that could be represented by actinolite.
EMP analyses of possible saponite are reported in Table 2.2.4. Analyses also detected olivine (Fo_{84}), and clinopyroxene (augite) similar to those found in the starting material (see Table 2.2.2); rare ilmenite and glass were also found.
As evidenced also by SEM-EDS investigations, plagioclase are richer in Na respect to phenocrysts in the starting material. In particular, we found An_{54-47} and An_{27} in Isl4 and Isl5 experiments, respectively.
In addition, neo-formed phases, ascribable to allumino/titanian- edenite (ISl4), and ferric subsilicic kaersutite (Isl5), were detected in the two experiments run at 400 and 500°C.
Summarizing, basalt- pure water experiments in the range 400-600 °C (at P=500 bar) show modest spilitization and scarce amphibole formation, not easily identifiable through XRD investigation and barely visible to SEM and EMP. The most evident alteration process is the saponite formation at 400°C, mainly due to the alteration of the glass occurring in the groundmass of the basalt.

Experiments Isl7-Isl10
Experiments using HCl solutions employed a solid/fluid ratio of about 0.3 and lasted longer than previous experiments (213 vs 166 hours).
XRD spectra of experiments are reported in Figures 2.2.6. and 2.2.7., in which experiments completed at the same temperature are compared (only peaks not present in the starting material are labelled).
XRD spectra at T=400°C (Isl7 and Isl9) shows a peak at low 2 theta referable to saponite (Figure 2.2.6.). Moreover, they show peaks attributable to halite (NaCl) and chlorargyrite (AgCl), besides to Ag, derived from the decomposition of $Ag_2C_2O_4$. These phases could be precipitated during the cooling of the experiment; however, their presence implies a Cl-rich system derived both by glass dissolution (Cl is contained in glass matrix of EJ29A, Table 2.2.2.) and HCl decomposition.
XRD spectra at 500°C (Isl8 and Isl10) show a peak referable to scapolite (scapolite series formula: $Na_4Al_3Si_9O_{24}Cl$ - $Ca_4Al_6Si_6O_{24}CO_3$), and this phase was probably present also in the experiment performed (at 500 °C) using pure water as a fluid reactant (Isl6 green line in Figure 2.2.2.).
This implies that Cl, necessary to form scapolite may come from the glass of the basalt starting material. Scapolite likely resulted from the alteration of the abundant plagioclase micro-phenocrysts found in the starting material.
Peaks referred to chlorargyrite are lacking and halite main peak (2theta= 21.7°) is less intense than in experiments run at 400°C. This suggests a reduced Cl activity in experiments at 500°C in respect to those run at 400°C. Actinolite main peak (2theta= 28.6°) is present mainly in the experiment in which $Ag_2C_2O_4$ was used to produce CO_2.
SEM and EPMA investigations do not disclose the presence of other neo-formed phases, undetectable to XRD. Overall, even if this set of experiments shows similar results to those performed considering pure water as fluid reactant, they display that basalt alteration is more effective by using low pH fluid (through the addition of HCl and/or CO_2).
The use of long capsules in CO_2-bearing experiments (Isl9 and Isl10) allowed the extraction of the fluid at the end of the runs, adopting the same procedure described in appendix I. Unfortunately, the weight change recorded in Isl10 at the end of the

experiment (Table 2.2.2.) hindered the use of fluid from this capsule for experimental calculation. Concurrently, a "blank reagents" solution was prepared using the same HCl aqueous solution, the prepared $Ag_2C_2O_4$ and the milliQ water employed in experiment Isl9 and using the same dilution factor.
This solution ("blank reagents") was analysed together with solution extracted from Isl9 capsule in order to verify the possibility of any contaminants during the experiment.
Analyses, performed through LC and ICP-OES, are reported in Table 2.2.5.
Analyses of the blank reagents solution indicate that contamination from reactants used in the preparation of the starting solution is negligible, since the total amount of analysed species is less than 15 ppm. In Isl9 fluid, apart Cl used in the starting fluid, it is remarkable the high SO_4 content, whereas Na and Ca are the most abundant cations.
Glass from the basalt groundmass represents the more likely SO_4 source (Tables 2.2.1 and 2.2.2) and the importance of its dissolution also arise from data obtained previously. Na and Ca, besides to be originated by glass, may derive from plagioclases in addition.
Despite the concentration of sulphur in glass of EJ29A is quite variable, EPMA did not reveal the presence of any S-bearing phases, thus suggesting it is mostly enclosed in the glass phase. Considering the bulk composition of starting material (Table 2.2.1), the Loss On Ignition (LOI) in EJ29A is about 0.4 wt%; if about 93% of LOI (0.37 wt%) is attributable to S, this is enough to explain the detected SO_4 in the fluid.

Experiment Isl11
XRD spectrum of this experiment (Figure 2.2.8.) reveals the presence of neo-formed anhydrite ($CaSO_4$), quartz and possibly, hematite. The latter phases are commonly found in Geitafell, as a result of alteration of primary phases in basalt (Table 2.2.1.). The occurrence of anhydrite indicates Ca availability in the system at P-T conditions of experiment; nevertheless, the SO_4 availability in the system (due to the introduction of sulphuric acid into the capsule) allowed the formation of this phase, hindering the precipitation of other Ca-bearing phases such as epidote and actinolite.
In the same Figure, Isl11 spectrum is compared with Isl8 and EJ29A spectra. Interestingly, it can be noted in Isl11 the disappearance of peaks pertaining to augite (e.g. peak at $2\Theta=29.8°$, corresponding to the most intense peak of this phase). On the contrary, peaks relating to this phase are present in Isl10 spectrum.
The analysis of fluid phase extracted from the capsule of this experiment is reported in Table 2.2.5. Congruently to what deduced from the characterisation of solid through XRD, the fluid has high Mg and Ca contents derived from augite dissolution. It is likely that silica produced from augite dissolution strongly contributed to quartz crystallization, a phase commonly found among alteration products of basalts in Geitafell area (Table 2.2.1.).

Outline of experimental results
Experiments concerning basalt- pure water interaction in the range 400-600°C (at P=500 bar) show modest spilitization and possibly low amphibole formation. On the contrary, saponite formation at 400°C is an evident process that probably interested the glass of the groundmass of the basalt.
The obtained results suggest that glass palagonitization (palagonite representing the first stable product of volcanic glass alteration, Stroncik & Schmincke, 2002) is the

main alteration process suffered by the basalt during the experiments. In details, palagonite is actually composed of a variety of smectites (such as saponite) and very minor amounts, if any, of zeolites and oxides. Such alteration process is in agreement with observation by Stefànsson & Gìslason (2001) at lower T forchemical weathering of basalts in Southwest Iceland: here, with increasing reaction (basaltic glass + meteoric water) progress, Ca-Fe-Mg smectite becomes the primary secondary minerals, limiting the mobility of Ca, Fe, Mg, Si, and Al. Experimental results indicate that saponite is found at 400°C, in contrast to observations on active geothermal system in which this phase is only found at lower temperatures. This discrepancy can be possibly imputed to the slow kinetic of the reaction which should transform saponite in other higher temperature minerals at 400°C.
Experiments concerning interaction processes between basalt and low pH fluid (through the addition of HCl and/or CO_2) in the same range of temperature and pressure evidenced that basalt alteration is slightly more effective but do not contribute to the formation of typical alteration phases found in geothermal systems. On the contrary, the use of sulphuric acid in an experiment resulted in a strong Ca, Fe, Mg, Si mobilization, mainly due to clinopyroxene dissolution (as evidenced by XRD spectra) and, secondarily, also by plagioclase and olivine dissolution. This process, besides to allow anhydrite, quartz and hematite crystallization (feasibly during the cooling of the experiment), produced a fluid strongly enriched in Mg and Ca, respect to the fluids obtained when sulphuric acid was not utilized.

2.3 Thermodynamic modelling

High temperature gas phase model
Given the thermodynamic database reported in Appendix 2, the first step was to model an ideal gas phase as often encountered in geothermal and volcanic system. As supercritical water is strongly oxidizing, formation of SO_2 and CO_2 preferentially occur in such conditions. However, this do not correspond to the conditions encountered in volcanic and geothermal systems. This important difference is due to the dominant redox buffer usually occurring in high temperature natural system, that could be a NNO, $FeO_{1.5}$ or sulfur buffers; these three main buffers have an overlapping region, around Eh=0.10443 (volt) (0.1045 for $FeO_{1.5}$ buffer and 0.1037 for the equilibrium H_2S/SO_2 sulfur buffer). In this case, if we use iron and sulfur in the rocks as dominant buffers, we could compute the gas speciation reported in Table 2.3.1. at 600°C, that is representative of water/ sulfur /carbon/chlorine interaction.

Mineral alteration model
The hydrothermal alteration of an Icelandic Basalt was modeled by means of PHREEQC 3.1.2, using the chemical composition of an unaltered basalt sample (EJ29A). This is the basalt lava erupted from Eyjafjallajökull volcano during 2010 also used for fluid-rock experiments. Normative mineral composition was computed on the basis of the whole rock chemical analysis reported in Table 2.2.1. The relative amount of moles of normative minerals per 1 L of reacting H_2O are reported in Table 2.3.2.
Since hydrothermal alteration is pH sensitive, we carried out several models using different initial pH, whose extreme values referred to pure water (pH 9 at 250°C; Tab.

2.3.3.) and acidic water (pH nearly 5 obtained adding sulfur, readily hydrolized to H_2S and SO_2; Tab. 2.3.4.) and an intermediate pH (pH= 7, Tab. 2.3.5.). Furthermore, gas phases (CO_2, sulfur species) and chlorine were varied as well. For the Geitafell ("Karfla-like") alteration model we used very-low salinity water, whereas for the "Reykjanes-like" model we use a fluid with the composition of sea-water as reacting fluid.

2.3.1 Results of water-rock interaction for the Geitafell ("Krafla-like") systems

As the "Krafla-like" systems are characterised by very low-salinity we used as initial fluid pure water. Figures 2.3.1., 2.3.2. and 2.3.3. show that the only constant of water-rock interaction at the three different pH values is the transformation K-feldspar/microcline. The behavior of the other phases are usually different at different pH. However, some processes can be highlighted. The main common processes observed are amphiboles (tremolite) disappearing at nearly 460°C, with a transient presence of diopside and garnet (andradite and grossular) appearance at higher temperature. Epidote shows a behavior similar to amphibole. Prehnite is sensitive to pH, disappearing at lower temperature with pH increase, while albite appears at lower temperature with pH increase.
Considering the phases detected by Fridleifsson (1983, 1984) at Geitafell and also in the samples investigated during this project (see report task 3.1) in which high quantity of garnets (in particular andradite) containing wollastonite and hedendergite relicts, albite, abundant epidote, can be observed, as evidence of a retro-metamorphic path, the best fitting model is possibly that at pH 6 in the 450-550°C range. Those samples where high quantity of Fe-actinolite, tremolite and prehnite, are observed are in agreement with the same model but at lower temperature (< 400°C, see Figure 2.3.3.).
The main discrepancy between natural samples and the proposed model is related to a high amount of Fe-bearing phases in Geitafell samples. This can be imputed to the low Fe(II) concentration resulting in our model, which gives a low amount of iron bearing alteration minerals. In the natural system, therefore, Fe concentration is likely higher. This difference may be related to the occurrence of Iron complexants in the natural fluid, not included in this model, that enhance Fe solubility. Another hypothesis is that the iron dissolution does not occur simultaneously to the precipitation of alteration minerals.

2.3.2 Fluid composition

Acidic Environment fluid composition (pH5)
In this case the alteration of basalt EJ29A was modeled adding volatile species, as reported in Table 2.3.4, to water in order to buffer the pH at about 5 at 200°C.The added sulphur species will be re-equilibrated according to the redox buffer, and the composition added is convenient from a numerical point of view. CO_2 and HCl do not show any relevant changes vs temperature in the model, apart from the partitioning between gas and liquid phases, while the sulphur species evolve from a reduced state at low temperature (high H_2S) to an oxidized state at high temperature (high SO_2) in the gas phase (Figure 2.3.4b).

The resulting fluid composition in Figure 2.3.4a shows the general behavior of diminution of the species concentrations as temperature increase along the water boiling curve (salt needed to keep liquid water is not shown). The pH evolution shows two main changes in buffer, at 300 and 425°C (Figure 2.3.5.); in particular the latter is related to the major mineralogical changes occurring in the alteration mineral shown in the solid phase evolution (Figure 2.3.2.). In fact, above 460°C epidote and prehnite disappear, whereas fosterite, diopside and grossular appear. Tremolite is stable between 360 and 475°C.

Basic Environment fluid composition (pH9)

The basic environment alteration (Figure 2.3.6.) considers the equilibrium of the rock minerals with water with a minor volatile content, as reported in Table 2.3.5, which occur at about pH 9 at 200°C. The pH evolution shows many buffer, the main of which is at nearly 380°C (Figure 2.3.7.) and is related to the first main change in to the mineralogical composition (Figure 2.3.1.) and it can be observed in the fluid phase as well (Figure 2.3.6a).

The gas composition behavior is very similar as described in the acidic environment alteration, but the abundance of gas components are very low and dominated by CO_2. (Figure 2.3.6b).

Calibrated acidity fluid composition

The calibrated acidity model (Figures 2.3.8.-2.3.9.) is, among many other buffers (computed or possible), the most realistic fluid computed model comparable to the fluid of KJ-13 and KJ-31 wells. The calibrated acidity model considers the equilibrium between the normative minerals of the reference basalt with water containing volatile species with a concentration (reported in Table 2.3.5.) calibrated to obtain a pH equal to that KJ-13 deep fluid at 260°C. The pH evolution (Figure 2.3.9.) shows several buffers, the main of which is at nearly 475°C and is related to the main change in the mineralogical composition, that is observed also in the mineralogical evolution at pH 7 of basalt alteration model that is considered as the most realistic to the field observation (Figure 2.3.3.). At 475°C there are changes in redox conditions of the gas components (Figure 2.3.8b), with the H_2S/SO_2 ratio getting closer to 0, and a high amount of hydrogen is found in the whole temperature range modeled.

This point is to be related also to a strong diminution of sulfur species in solution and also general solute abundances, in particular magnesium, due to the appearing of new stable mineral phases, with the only exception of aqueous SO_2 (Figure 2.3.8a). It should be pointed out that aqueous SO_2 hydrolyze to H_2SO_3 and not to H_2SO_4, so that H_2SO_4 is reducing its concentration at high temperatures.

2.3.3 Alteration model validation

Model validation was performed by comparing the composition of the fluid obtained by our model with those of natural geothermal fluids. The first step to validate the thermodynamic model was to reconstruct the deep (reservoir) fluid composition of the geothermal wells of Krafla sampled during this project (KJ-13, KJ-31 and KJ-20The composition of the reservoir fluid has been reconstructed by means of WATCH 2.4 (Arnosson et al., 1982) on the basis of water and gas compositions, sampling temperature and pressure, steam/gas ratio at the well-head and a reference temperature (Table 2.3.6.). The fluid from KJ-20 well, however, was not considered

for modellization as it is characterised by relatively low pH and very low ions contents that make unreliable any attempt in evaluating possible chemical equilibria.
The reference temperature was evaluated by using Na/K geothermometer. For a more accurate reconstruction of the fluid equilibria, we also provided the computation of simultaneous equilibrium curves of minerals as function of temperature, according to Spycher & Reed (1984) (Figures 2.3.10. and 2.3.11.). The first point of convergence is at 260°C +- 20°C for fluids of both wells (KJ-13, KJ-31), and include also the Na/K geothermometer mineral equilibrium; the latter give 237°C and 288°C for KJ-13 and KJ-31, respectively. The higher temperature at 490°C +-20 found for KJ-31 is related to albite and garnets, while at 380°C +-20 for KJ-31 is related to actinolite. For KJ-13 instead we found a high temperature equilibrium related to epidote-albite at 440°C +-20, but the possible point related to actinolite at 340°C could only be guessed.
Given the above considerations, the 260°C equilibrium temperature were used for modeling the deep fluid composition. The results obtained were very similar, thus only the KJ-13 will be used as representative of the deep fluid composition.
The deep fluid composition gives a pH 7.7; thus this composition could be compared with the basalt alteration model at pH 7 (effective pH at 260°C is 7.2), at the temperature of 260°C.
In Table 2.3.6. and Figure 2.3.12. the compositions of the fluid obtained by our model and that of the deep geothermal fluids are compared. The composition of the fluid obtained from the basalt alteration model is generally in good agreement with that of the deep fluid of the KJ-13 well. The main discrepancies are given by iron and magnesium. The Mg inconsistency can be explained considering that Mg is not directly controlled by Mg-minerals, as in many cases it could be a substituent for Ca or Fe in solid solutions (which are not considered in our model), thus an higher content of Mg in the natural fluids was expected.
The discrepancy of Fe was evidenced also in the description of mineral abundances; Fe-bearing minerals should be more abundant than what we have obtained in the model, and this aspect can have consequences in the iron content in the liquid phase. This problem have a deepest rooting: the Fe-bearing phases, like Fe-oxides, are greatly oversaturated by using the sampled water composition.

2.3.4 Results of water-rock interaction for the "Reykjanes-like" systems

In order to model the hydrothermal alteration of Reykjanes basalts, we consider the presence of a reacting fluid with the composition of sea water (Table 2.3.7.) and the results obtained for the Geitafell ("Krafla-like") alteration model order to model the acidic conditions of the geothermal fluids found typical and we consider presence of seawater instead of pure (meteoric) water.
The main effect of seawater on the alteration model of the reference basalt (Table 2.3.2.) could be resumed as: 1) sulphate deposition, generally anhydrite, 2) sulphate reduction into sulphur or sulphides, due to the low redox condition of the basalt, and 3) production of an acidic aggressive environment that induce a low-grade serpentinization on the basalts.
The anhydrite deposition is not taken in to account in the present model, but it could be described as two distinct processes; i) gypsum-bassanite-anhydrite deposition due to progressive seawater boiling, ii) anhydrite deposition at high temperature due to interaction of sulphate in the hydrothermal fluid with calcium in the rock forming minerals.

The sulphate reduction is included in the model, and it is responsible for the presence of pyrite at low temperature (see Figure 2.3.13.).
The hydrothermal alteration of peridotite and basalts produces serpentinites in both submarine and terrestrial environments. Serpentinization is an exothermic, hydration reaction whereby water reacts with mafic minerals such as olivine and pyroxene, to produce lizardite, antigorite, and/or chrysotile. The thermal transformation, stability field, and reaction kinetics of serpentine minerals antigorite, chrysotile, and lizardite have been studied to draw a comprehensive model for their dehydroxylation and recrystallization reactions. It was found that the three serpentine polymorphs decompose at different temperatures. Chrysotile is stable up to 750°C, lizardite up to 775°C and antigorite decomposes at 800°C. During dehydroxylation, a metastable transition phase was observed in antigorite and, to a minor extent, in lizardite (Gualtieri et al., 2012).
The reaction sequences of chrysotile, lizardite, and antigorite leading to the formation of stable high-temperature products (i.e. forsterite and enstatite) are considered in our model, however in order to simplify the, we assume amesite as representative a low grade metamorphism as Mg-endmember for the serpentinization (chlinochlore could be another proxy but only for low temperature). Figure 2.3.13. shows that this process could occur in a wide range of temperature, ending in the forsterite stability. Fosterite endmember of olivine is also a component considered in the composition of reference basalt, but in our numerical model it could be produced also by metamorphism of serpentinite assemblage and successive dehydration at high temperature, with a sporadic chamosite occurrence at low temperature. Figure 3.3.13. also shows that pyrite is present at relatively low temperature, whereas magnetite and Fe-Actinolite at higher temperature. The assemblage albite-epidote-tremolite is observed also in this alteration model, and albite is occurring in the whole temperature range while epidote-tremolite is found in the range 400-500°C.

2.3.5 Fluid composition

The aqueous phase composition reflect the behavior already observed for Krafla (acid model), and the same is observed in the gas phase. The main change is observed in the gas phase, in which appear Cl_2, S_8 and an high H_2 content, due to the redox interaction of seawater with Fe(II) in the basaltic rock. The volatile added in order to obtain the acid environment are reported in Table 2.3.7., and are very similar to the composition used for the acid model in Krafla but with higher HCl content, due to the seawater effect. As side effect, in order to match the resulting fluid salinity after phase partitioning (e.g. chlorine) and water rock interaction we used a concentrated seawater (concentration factor 1.8) solution for sodium, magnesium and chlorine, reported in table 2.3.14a,b.

2.3.6 Alteration model validation

Model validation was performed by comparing the composition of the fluid obtained by our model with those of natural geothermal fluids. The fluid composition of three wells (RN11, RN21 and RN27) were considered for the model validation. The deep fluid were provided by ISOR and were reconstructed by means of watch 2.4 (Arnosson et al. 1982) using reference temperatures of 270°C for RN27, 285°C for RN21 and

295°C for RN11 fluids, on the basis of water and gas compositions, sampling temperature and pressure, steam/gas ratio at the well-head (Table 2.3.8.).
The three wells have a similar chemical composition, and could be evaluated together with the computed fluid for the validation of the model.
The pH of three wells (between 4.6 and 4.8) is in good agreement with computed pH for the model (4.9). In Figure 2.3.15. composition of the deep fluids are compared with the fluid composition modeled at 340°C. In general, there is a good agreement between the modelled fluid and the deep fluids, with the exception of sulphate and magnesium. The excess of sulphate is related to the construction of our model that did not consider anhydrite precipitation. The discrepancy of Mg concentration can be related to the fact that the fluid is close to the high solubility zone, evidenced in the high concentration in the water phase composition (figure 2.36.14a,b) and in the changes in mineral stability. Any discrepancy in our thermodynamic model is here increased and in this case it affect Mg.

2.4. Discussion

Water-rock interaction experiments and a numerical model were performed with the aim to better understand the alteration of basalt reacting with pure water or pure water + acidic gasses at supercritical conditions in hydrothermal system similar to the fossil system of Geitafell (i.e. "Krafla-like system"). Water-rock experiments between pure water and basalt at 500 bar showed a significant formation of saponite at 400°C likely coming from the dissolution of the glass of the basalt's groundmass. On the contrary, the formation of other secondary phases in the range 400-600°C is modest, and limited to the formation of secondary plagioclase (labradorite/andesine) and a Ca-phase (presumably epidote) at 400°C, and possibly actinolite at higher temperature (500-600°C). In addition, amphibole (allumino/titanian- edenite, and ferric subsilicic kaersutite) was detected in experiments run at 400-500°C. Thermodynamic modelling indicates that amphibole (in this case tremolite) can be present as alteration product of the basalt at temperature up to 460°C. The occurrence of amphiboles at higher temperature in the experiments can be imputed to different stability conditions of the neo-formed amphiboles with respect to tremolite.
Other high-temperature minerals found in the Geitafell fossil hydrothermal system (e.g. garnet, hedenbergite etc.; Fridleifsson, 1984) and also present in numerical modelling at temperature of 400-600°C were not detected. Moreover phases stable in the albite-epidote hornfels (actinolite, epidote, chlorite, talc, biotite, albite quartz) and in hornblende hornfels (biotite, almandine, quartz, anthophyllite, cordierite) facies, typical of the alteration of basaltic protholit, are scarce or absent in our experiment. This may be imputed to kinetic reason or also to variations due to the cooling of the capsules.
Experiments concerning interaction processes between basalt and relatively low pH fluid (through the addition of HCl and/or CO_2) in the same range of temperature and pressure evidenced that basalt is slightly more reactive, but alteration products are the same, with the exception of scapolite which was found in the experiments performed at 500°C. Experiment with H_2O+HCl+CO_2 produce significant concentration of Na, Ca (>1000 ppm) and SO_4^{2-} (c.a. 3500 ppm) in the fluid. The sulfur in the fluid was likely introduced by the alteration of the glass which contain up 0.46 wt.% of S

(Table 2.2.2). On the contrary, the use of sulphuric acid in an experiment resulted in a strong Ca, Fe, Mg, Si mobilization, mainly due to clinopyroxene and minor plagioclase and olivine dissolution. This process, besides to allow anhydrite, quartz and hematite crystallization (feasibly during the cooling of the experiment), produced a fluid strongly enriched in Mg and Ca, respect to the fluids obtained when sulphuric acid was not utilized. Strong Ca mobilization was already reported for Geitafell fossil hydrothermal system by Fridleifsson (1984) who suggested, on the basis of the alteration minerals a massive Ca^{2+} leaching from the contact metamorphic aureole rocks. This observation suggests that Ca mobilization in basalts may be related to the significant input of SO_2 in very-high temperature hydrothermal system. As shown by cations concentration in the fluids modelled at different pH of the "Krafla-like" system cations are more leached at lower pH (Figs. 2.3.6, 2.3.8, 2.3.8.), especially if fluids contain high SO_2 contents.

The numerical model for "Reykjanes-like" systems shows that epidote-tremolite may occur to up 500°C, whereas Fe-actinolite and forsterite can be present at higher temperature. Marks et al. (2010) report the presence of amphibole of variable composition in alteration minerals of the Reykjanes geothermal fields. In particular, the higher temperature conditions led to the formation of magnesio-hornblendic amphibole, which is rimmed by lower temperature actinolite. Our modelling suggests that Mg-amphibole (i.e. tremolite) could form between 460 and 500°C. This in agreement with the occurrence of magnesio-hornblende in mafic rocks metamorphosed above 425°C, at pressures above 0.5 kbar, with oxygen fugacity in the range of the hematite-magnetite buffer (Liou et al., 1974; Moody et al., 1983). We, therefore, suggest that Mg-amphibole at Reykjanes is indicative of temperature >450°C.

The numerical models for the "Krafla like" and Reykjanes-type" systems were validated comparing the composition of the fluid obtained from the basalt alteration model with that of the reconstructed deep fluids. For "Krafla-like systems in general the composition of the two fluids are comparable with the exception of Mg and Fe, whose concentration in the geothermal fluid may not be equilibrated with the expected mineralogical phases. Also the validation of numerical model of the "Reykjanes-like" was positive with the exception of the Mg content.

An important aspect of validations, is that the modelled fluids require the presence of SO_2 in order to be comparable with the geothermal fluids. A similar model was done by Ármannsson (2001), but limited at 205 and 295°C, using a basalt as solid phase and a titration process with a gas phase made mainly by CO_2, SO_2 and H_2S. The work, as well as our, suggested that gas needs to be added to approach the Krafla wells fluid composition.

In general, the occurrence of sulfur species in Icelandic geothermal fluids is considered essentially to be related to the direct input of magmatic gasses in the geothermal fluids. However, our experiment with fluids containing only HCl or $HCl+CO_2$ showed that some S is released during basalt leaching. We, therefore, suggest that fluid-rock interaction can enhance the presence of sulfur species in the fluid.

The results of geochemical analyses (VOCs) and of the gas phase from Krafla and Reykjanes geothermal wells and fumaroles show a dominant hydrothermal-type composition and there are no indications of strong cracking processes related to the presence of a magmatic component. The magmatic component in these gases were likely heavily modified by scrubbing due to hydrothermal water at temperatures up to

350°C (primary scrubbing) and shallow meteoric water (secondary scrubbing). The effects of scrubbing are stronger for gas discharges from bubbling pools than for the fumarolic gases. However, as heterocyclic compounds (i.e. thiophenes and furans) are tracer of different source contributions (i.e. hydrothermal and magmatic) such compounds can be used for geochemical monitoring during future deep drilling, in order to detect any changes in the conditions related to the arrival of deep magmatic fluids.

2.5 Final remarks

The results of experimental data and thermodynamic modelling of fluid-rock interaction in the Geitafell fossil hydrothermal systems ("Krafla-like" geothermal system) highlight the following conclusions:

- The formation of secondary minerals during autoclave experiment was modest possibly because of kinetic effect, with the exception of saponite formation which could be also formed during the cooling of the capsules.
- The scarce secondary phases, formed in the range 400-600°C, are: plagioclase (labradorite/andesine), a Ca-phase (presumably epidote), amphibole (allumino/titanian- edenite, and ferric subsilicic kaersutite, and possibly actinolite), scapolite and anhydrite+hematite+quartz (when H_2SO_4 is present in reacting fluid).
- The presence of CO_2, HCl and H_2SO_4 appears to enhance fluid-rock interaction. In particular, when H_2SO_4 is present in the reacting fluid Ca^{2+} is significantly mobilized as also suggested by thermodynamic modelling at relatively low pH.

The consequence of the above points concern the possible exploration/exploitation of the super-critical geothermal reservoir that likely occur below the Icelandic geothermal fields: i) secondary amphibole, without evidence of retrograde alteration minerals, are expected to found at temperature up to 600°C, in particular Mg-amphibole at Reykjanes is indicative of temperature >450°C, ii) the recognition of an alteration assemblage dominated by anhydrite+hematite+quartz can be indicative of a Ca^{2+} leaching process related to the presence of SO_2 in the fluid, suggesting a close source of this component (magma degassing). Geochemical monitoring of heterocyclic compounds during future deep drilling can also allow to the identification of a magmatic source.

References

Ármannsson H. & Jeffrey W.A. (1989). Gas changes in the Krafla geothermal system, Iceland. Chemical Geology, 76, 175-196.

Ármannsson H., Fridriksson T., Benjamínsson J. & Hauksson T. (2013). History of gas in geothermal fluids, Krafla, northeast Iceland. Procedia Earth and Planetary Science 7, 23-26.

Armannsson H., Fridriksson T., Gudfinnsson G.H., Olafsson M., Oskarsson F. & Thorbjornsson D. (2014): IDDP—The chemistry of the IDDP-01 well fluids in relation to the geochemistry of the Krafla geothermal system. Geothermics 49 (2014) 66–75.

Ármannsson, H. (2001: Reaction of groundwater with rock from the Krafla area, N-E Iceland and volcanic gas. In R. Cidu (editor). Water-Rock Interaction, Balkema, Swets & Zeitlinger, Lisse, The Netherlands, 779-82.

Ármannsson, H., Gudmundsson Á. & Steingrímsson B.S. (1987). Exploration and development of the Krafla geothermal area. Jökull 31, 13–29.

Arnórsson S. (1995). Geothermal systems in Iceland: structure and conceptual models-I. High-temperature areas. Geothermics 24, 561–602.

Arnórsson S., Sigurdsson S. & Svavarsson H. (1982). The chemistry of geothermal waters in Iceland. I. Calculation of aqueous speciation from 0°C to 370°C. Geochimica et Cosmochimica Acta, 46, 1513 - 1532.

Bàrdarson G.G. (1931). The warm sea water pool at Reykjanes. Nàttu´rufreadingurinn 1, 78–80 (in Icelandic).

Bird D.K. & Spieler A.R. (2004). Epidote in geothermal systems. Reviews in Mineralogy & Geochemistry, 56, 235-300.

Capecchiacci F. (2012) Geochimica dei fluidi vulcanici e idrotermali: Origine delle componenti organiche e loro impatto ambientale. Tesi Dottorato di ricerca in Scienze Della Terra, XXIII ciclo. Settore scientifico disciplinare: GEO-08. Università degli Studi di Firenze. PhD Thesis, in Italian.

Capaccioni B., Tassi F. & Vaselli O. (2001). Organic and inorganic geochemistry of low temperature gas discharges at the Baia di Levante beach, Vulcano Island, Italy. J. Volcanol. Geotherm. Res. 108, 173-185.

Christenson B.W., Halldor A., Mack Kennedy B. & van Soest T.J. (2010). Geochemical Reconnaissance of Fluids from the Krafla and Nesjavellir Thermal Areas, Iceland: Baseline Studies in Support of the IDDP. Proceedings World Geothermal Congress 2010 Bali, Indonesia, 25-29 April 2010.

Clifton A.E. & Kattenhorn S.A. (2006). Structural architecture of a highly oblique divergent plate boundary segment. Tectonophysics, 419, 27–40.

Cohen E., Dudeney A.W.L. & Shaw R. (1980). Synthesis of clay-like materials. UK Patent 1,560,504. Date Issue: 6 February.

Darling W.G. & Ármannsson H. (1989). Stable isotopic aspects of fluid flow in the Krafla, Namafjall and Theistareykir geothermal systems of northeast Iceland. Chemical Geology, 76, 197-213.

Fowler, A. P.G., Zierenberg, R. A., Schiffman, P., Marks, N. and Friðleifsson, G. Ó. (2015). Evolution of fluid–rock interaction in the Reykjanes geothermal system, Iceland: Evidence from Iceland Deep Drilling Project core RN-17B. Journal of Volcanology and Geothermal Research, 302, 47-63, 2015.

Franzson H., Thordarson S., Bjornsson G., Gudlaugsson S.Th., Richter B., Fridleifsson G.O. & Thorhallsson S. (2002). Reykjanes high-temperature field, SW-Iceland: geology and hydrothermal alteration of well RN-10. In: Twenty-seventh Workshop on Geothermal Reservoir Engineering. Stanford University, Stanford, CA.

Freedman A.J.E., Bird D.K., Arnórsson S., Fridriksson T., Elders W.A. & Fridleifsson G.Ó. (2009). Hydrothermal minerals record variations in CO_2 partial pressures in the Reykjanes geothermal system, Iceland. American Journal of Science 309, 788–833.

Fridleifsson G.O. (1983). Mineralogical evolution of a hydrothermal system. Geothermal Resources Council. Transactions 7, 147–152.

Fridleifsson G.O. (1984). Mineralogical evolution of hydrothermal system II: Heat sources - Fluid interactions, Geothermal Resources Council Transactions, 8, 119-123.

Fridleifsson G.O., Blischke A., Kristjánsson B.R., Richter B., Einarsson G.M., Jónasson H., Franzson H., Sigurdsson O., Danielsen P.E., Jónsson S.S., Thórdarson S., Thórhallsson S., Hardardóttir V. & Egilson T. (2005). Reykjanes Well Report RN-17 & RN-17ST, Iceland GeoSurvey.

Gasperikova E., Rosenkjaer G.K., Arnason K., Newmana G.A. & Lindsey N.J. (2015). Resistivity characterization of the Krafla and Hengill geothermal fieldsthrough 3D MT inverse modeling. Geothermics, in press.

Giggenbach W.F., 1975: A simple method for the collection and analysis of volcanic gas samples. Bull. Vulcanol., 34, 132-145.

Gualtieri A.F., Giacobbe C. & Viti C. (2012). The dehydroxylation of serpentine group minerals. American Mineralogist, 97, 666-680.

Hólmgeirsson S., Guðmunsdsson Á., Pálsson B., Bóasson H.Á., Ingason K. & Þórhallsson S. (2010). Drilling operations of the first Iceland Deep Drilling well (IDDP). In: Proceedings of the World Geothermal Congress 2010, Bali, Indonesia, 25–39 April, 2010. Paper 2129, pp.1–10.

Liou, J., Kim, H., Maruyama, S. (1983). Prehnite–epidote equilibria and their petrologic applications. J. Petrol. 24, 321–342.

Moody, J., Meyer, D., Jenkins, J. (1983). Experimental characterization of the greenschist/ amphibolite boundary in mafic systems. Am. J. Sci. 283, 48–92.

Kristmannsdóttir H. (1983). Chemical evidence from Icelandic geothermal systems as compared to submarine geothermal systems. In: Rona, P., Bostrom, K., Laubier, L., Smith Jr., K.L. (Eds.), Hydrothermal Processes at Seafloor Spreading Centers. Plenum Press, New York, pp. 291–320.

Lonker S.W., Franzson H. & Kristmannsdóttir H. (1993). Mineral-fluid interactions in the Reykjanes and Svartsengi geothermal systems, Iceland. America Journal of Science 293, 127–150.

Marks N., Schiffman P., Zierenberg R.A., Franzson H. & Fridleifsson G.Ó. (2010). Hydrothermal alteration in the Reykjanes geothermal system: Insights from Iceland deep drilling program well RN-17. Journal of Volcanology and Geothermal Research 189, 172-190.

Montegrossi G., Tassi F., Vaselli O., Buccianti A. & Garofalo K., (2001), Sulfur Species in Volcanic Gases. Anal. Chem., 73, 3709-3715.

Óskarsson F., Fridriksson T. & Thorbjörnsson D. (2015). Geochemical Monitoring of the Reykjanes Geothermal Reservoir 2003 to 2013. Proceedings World Geothermal Congress 2015 Melbourne, Australia, 19-25 April 2015.

Pálsson B., Hólmgeirsson S., Guðmundsson Á., Bóassson H.Á., Ingason K., & Þórhallsson S. (2014). Drilling Well IDDP-1. Geothermics 49, 23–30.

Pope E. C., D. K. Bird, S. Arnórsson and N. Giroud, (2015). Hydrogeology of the Krafla geothermal system, northeast Iceland. Geofluids, doi: 10.1111/gfl.12142

Pope E.C., Bird D.K. & Arnórsson S. (2014). Stable isotopes of hydrothermal minerals as tracers for geothermal fluids in Iceland. Geothermics 49, 99-110.

Pope E.C., Bird D.K., Arnórsson S., Fridriksson T., Elders W.A. & Fridleifsson G.Ó. (2009). Isotopic constraints on ice age fluids in active geothermal systems: Reykjanes, Iceland. Geochimica et Cosmochimica Acta, 73, 4468–4488.

Ragnarsdóttir K.V., Walther J.V. & Arnórsson S. (1984). Description and interpretation of the composition of fluid and alteration mineralogy in the geothermal system, at Svartsengi, Iceland. Geochimica et Cosmochimica Acta, 48, 1535–1553.

Reed M.H. & Spycher N.F. (1984). Calculation of pH and mineral equilibria in hydrothermal waters with application to geothermometry and studies of boiling and dilution. Geochim. Cosmochim. Acta, 48, 1479-1492.

Rosenkjaera G.K., Gasperikova E., Newman G.A., Arnason K. & Lindsey N.J. (2015). Comparison of 3D MT inversions for geothermal exploration: Casestudies for Krafla and Hengill geothermal systems in Iceland. Geothermics , in press.

Sæmundsson K. (1991). ´ Jarðfræði Kröflukerfisins(ThegeologyoftheKraflasystem). In: Garðarsson, A., Einarsson,Á.(Eds.), NáttúrraM´ yvatns. HIN, pp.24–95.

Sapper K. (1908). On some Icelandic volcanic fissures and crater rows. Neu. Jahrb. Min. Geol. Pala¨ontol., 26 (in German).

Stefànsson A. & Gìslason S.R. (2001): Chemical weathering of basalts, southwest Iceland: effect of rock crystallinity and secondary minerals on chemical fluxes to the ocean. American Journal of Science, 301, 513-556.

Sveinbjörnsdóttir A.E., Coleman M.L. & Yardley B.W.D. (1986). Origin and history of hydrothermal fluids of the Reykjanes and Krafla geothermal fields, Iceland: a stable isotope study. Contributions to Mineralogy and Petrology 94, 99–109.

Tassi F., Vaselli O., Capaccioni B., Giolito C., Duarte E., Fernandez E., Minissale A. & Magro G. (2005). The hydrothermal-volcanic system of Rincon de la Vieja volcano (Costa Rica): A combined (inorganic and organic) geochemical approach to understanding the origin of the fluid discharges and its possible application to volcanic surveillance. Journal of Volcanology and Geothermal Research 148, 315-333.

Tassi F., Montegrossi G., Capecchiacci F. & Vaselli O. (2010). Origin and Distribution of Thiophenes and Furans in Gas Discharges from Active Volcanoes and Geothermal Systems. Int. J. Mol. Sci. 2010, 11.

Vaselli O., Tassi F., Montegrossi G., Capaccioni B. & Giannini L. (2006). Sampling and analysis of fumarolic gases. Acta Vulcanol., 1-2, 65-76.

FIGURES

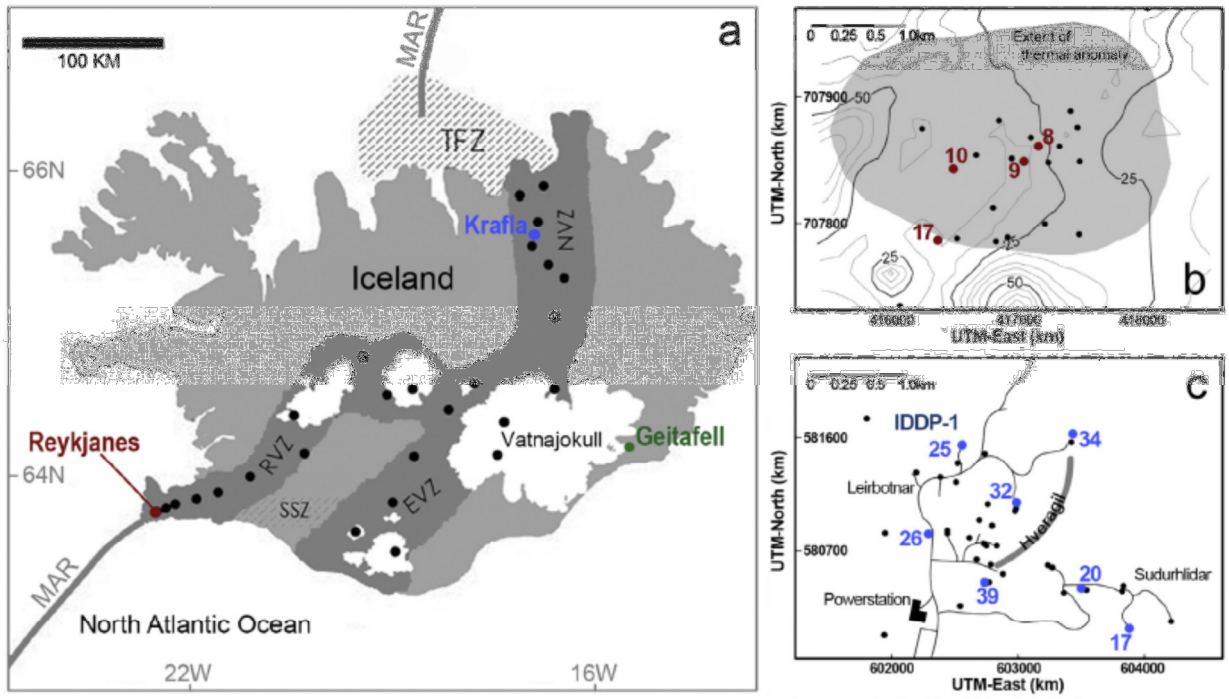

Figure 2.1.: (a) Geologic map of Iceland, from Pope et al. (2009). Filled circles: high-temperature geothermal fields. MAR: Mid-Atlantic Ridge; RVZ: Reykjanes volcanic zone; EVZ: Eastern volcanic zone; NVZ: Northern volcanic zone; TFZ: Tjörnes fault zone; SSZ: South Iceland Seismic Zone. (b) Reykjanes geothermal field. Filled circles represent wells; topographic contours=5m. Adapted from Pope et al. (2009). (c) Krafla geothermal field. Filled circles represent wells; lines represent roads. Well maps for both geothermal fields courtesy of Iceland GeoSurvey.

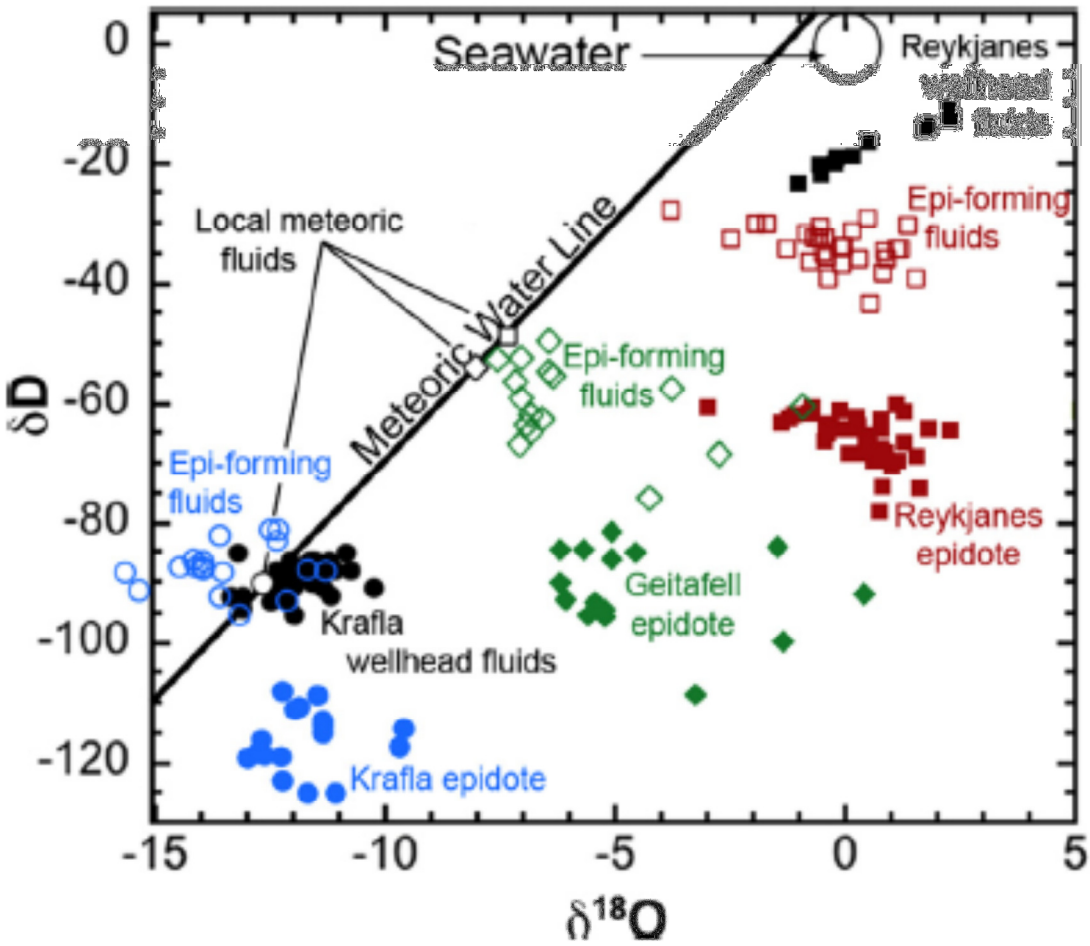

Figure 2.2.: Hydrogen and oxygen isotopic composition of epidote from the Reykjanes (shaded squares), Krafla (shaded circles) and Geitafell geothermal systems (shaded diamonds) and the fluids that are in isotopic equilibrium with these minerals (open symbols of complementary shape) (Pope, 2011; Pope et al., 2009; this study). Compositions of geothermal fluids in equilibrium with epidote (Epi-forming fluids) were calculated using the temperature-isotope fractionation curves of Chacko et al. (1999) for hydrogen and the combined equations of Kohn and Valley (1998), Matsuhisa et al. (1979) and Matthews et al. (1983) for oxygen. Compared to the isotopic composition of wellhead discharge fluids and local groundwater from the two active wells, the meteoric water line, and seawater (Craig, 1961; Darling and Ármannsson, 1989; Pope et al., 2009; Sveinbjörnsdóttir et al., 1986). (For interpretation of the references to color in the main text, the reader is referred to the web version of the article.) (From Pope et al., 2014).

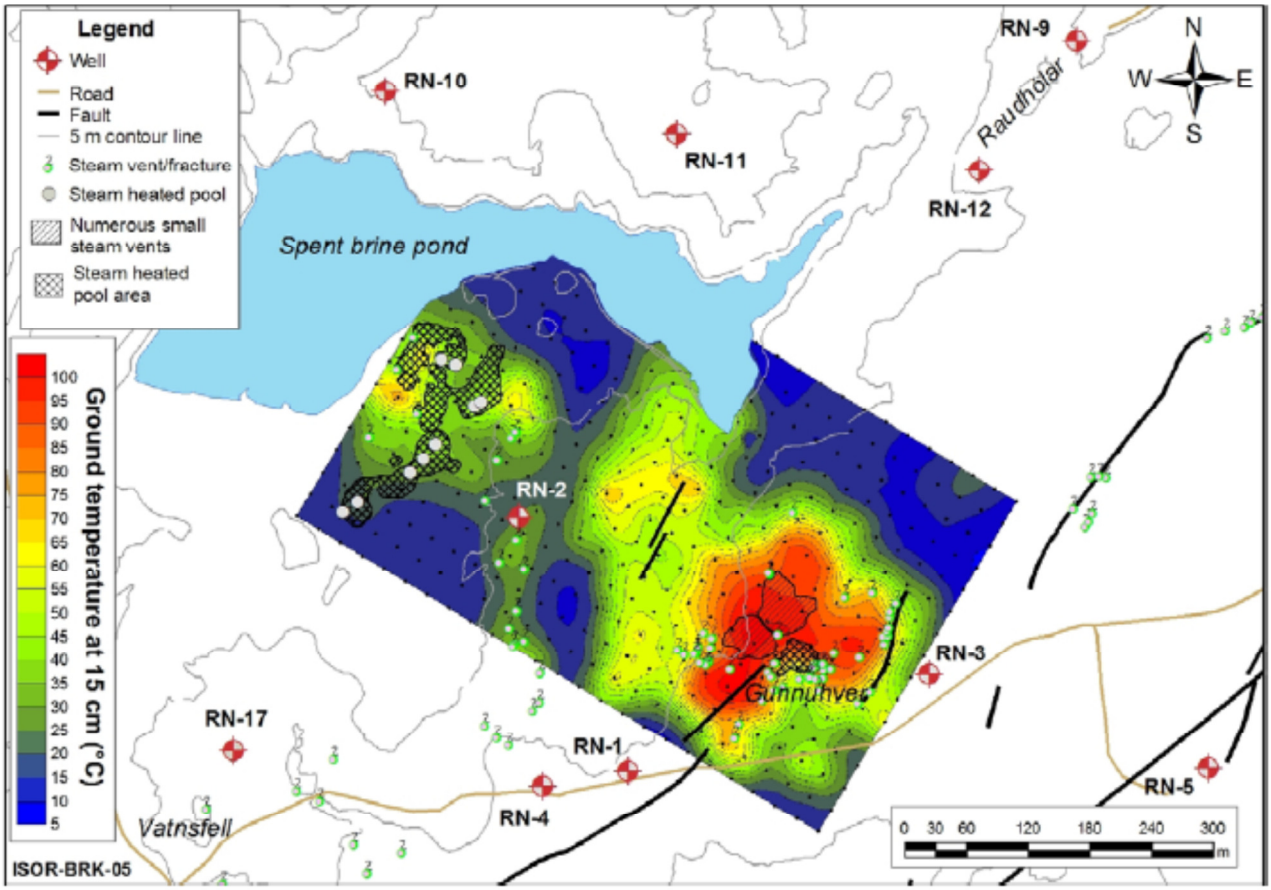

Figure 2.3.: Map of the Reykjanes geothermal area showing surface geothermal manifestations, including steam vents, steam fractures and steam heated pools. Soil temperature at 15 cm depth is shown by filled contour lines in the present study area (Fridriksson et al., 2006).

Concentrations in ppm	RN-8[a]	Krafla[a]	MARK-1[b]	NGS[c]	Seawater[d]
Temp °C	267	300	350	273	2
pH	5.3*	6.5*	4.6*	4.7*,[e]	7.8
SiO_2	543	500	1093	1172	6.4
B	7.5	0.6	5.6	4.7[f]	4.45
Na	9594	105	11,724	11,724	10,800
K	1480	20.9	923	1009	392
Ca	1467	1.07	397	834	411
Mg	1.24	0.011	0[g]	0[g]	1290
Fe	0.238	0.048	122	49	3.4
Al	0.06	–	0.14	0.11	0.001
$\sum CO_2$	781	4267	0[g]	0[g]	114
SO_4	24.4	67.6	0[g]	0[g]	2712
H_2S	26.1	65.3	201	224	0
Cl	19648	223.4	19,818	20,527	19,800
δD	−23.1‰[h]	−88‰[i]	+3‰[j]	1‰[j]	+1.5‰[h]
$\delta^{18}O$	−1.1‰[h]	−12.4‰[i]	+2.37‰	−1.4‰[j]	+0.2‰h

*The values are the calculated pH of the reservoir water at the reported temperature.

[a] Arnórsson, 1995.
[b] Campbell et al., 1988.
[c] Von Damm et al., 1985.
[d] Quinby-Hunt and Turekian, 1983.
[e] Bowers et al., 1988.
[f] Spivack and Edmond, 1987.
[g] Endmember values extrapolated to 0 Mg, SO^4 and Alalkinity <0.
[h] Ólafsson and Riley, 1978.
[i] Darling and Ármannsson, 1989; Krafla isotopic values reflect fluctuations in meteoric water values.
[j] Shanks et al., 1995.

Figure 2.4.: Comparison of end-member fluid compositions from Reykjanes, Krafla, seawater, and mid-ocean ridge vents (From Marks et al., 2010).

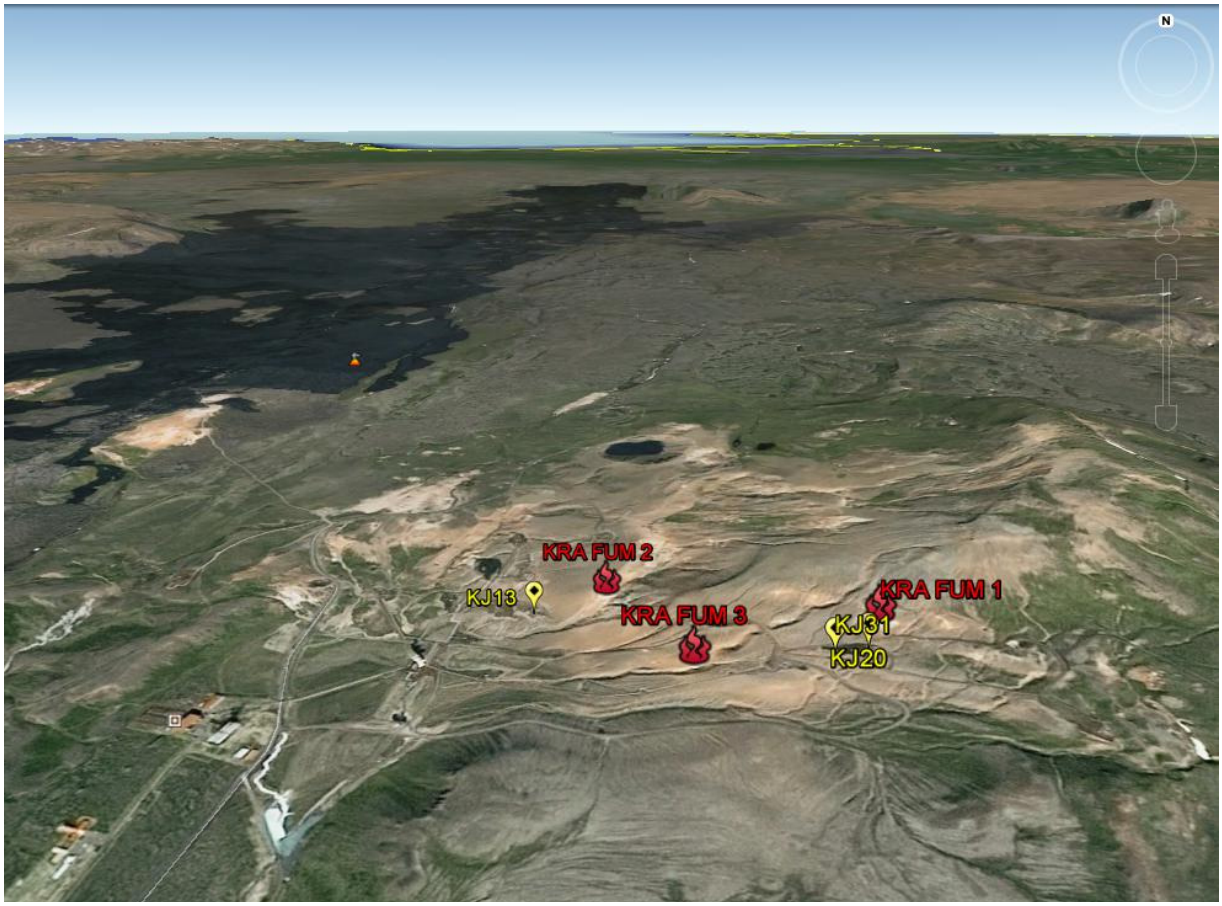

Figure 2.1.1.: Krafla geothermal field, map of sampled fumaroles (red) and boreholes (yellow).

Figure 2.1.2.: Reykjanes geothermal field, map of sampled fumaroles (red) and boreholes (yellow).

Figure 2.1.3.: Gas sampling line for fumaroles.

Figure 2.1.4.: Sampling line for VOCs using water/ice-cooled glass device (Graham type condenser).

Figure 2.1.5.: Boreholes sampling equipment.

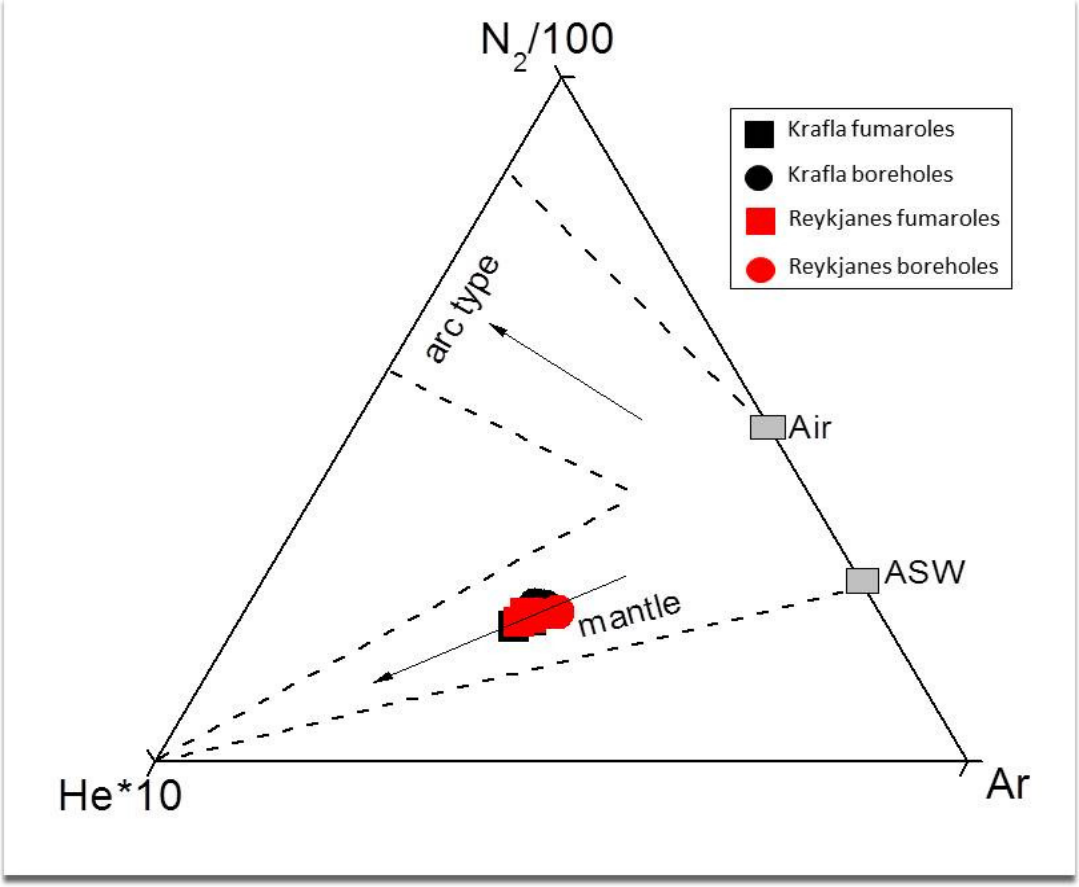

Figure 2.1.6.: Relative compositions of Ar, N_2 and He for Krafla and Reykjanes fluids.

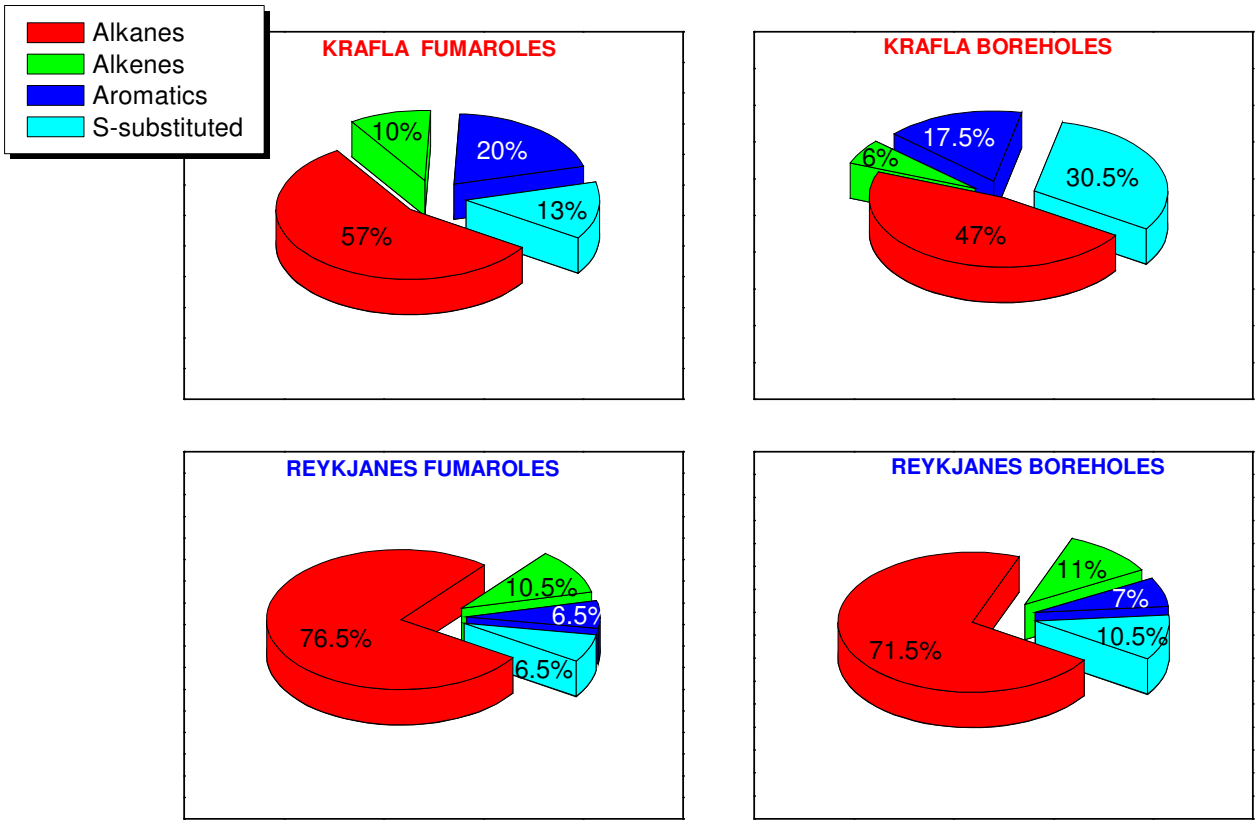

Figure 2.1.7.: Relative abundances of VOC compositional groups.

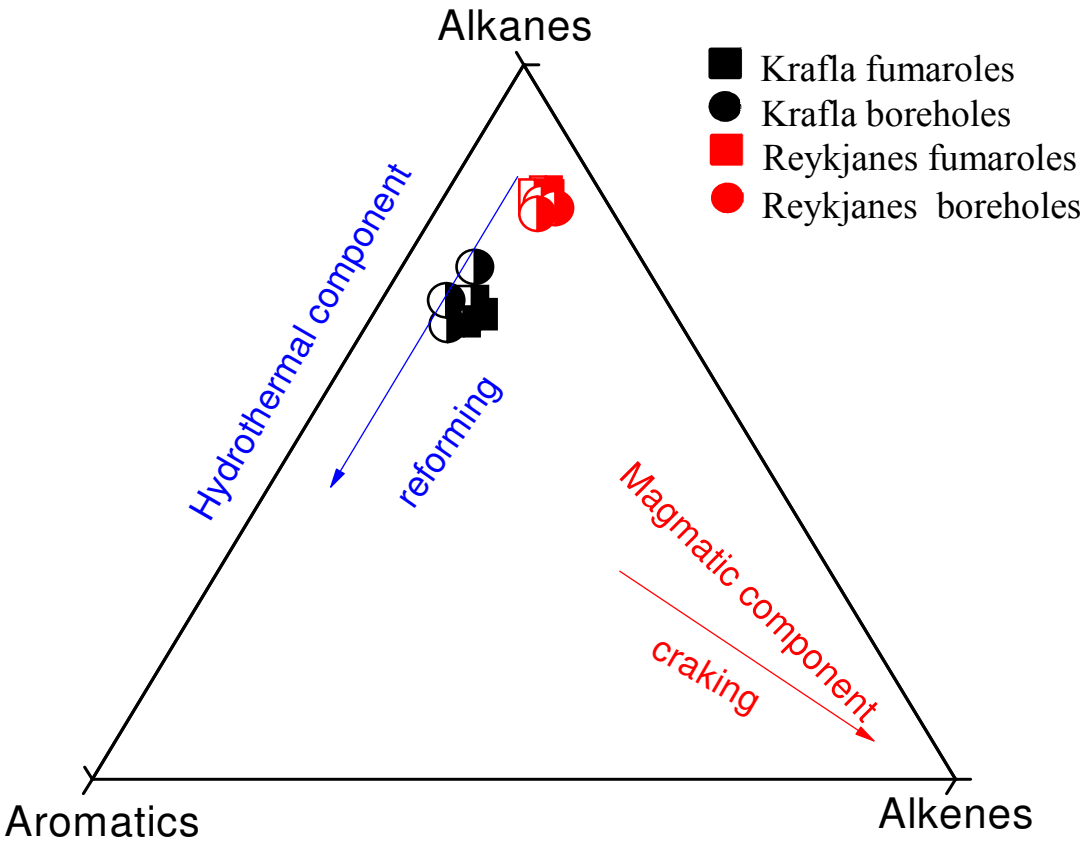

Figure 2.1.8.: Alkanes-alkenes-aromatics ternary diagram.

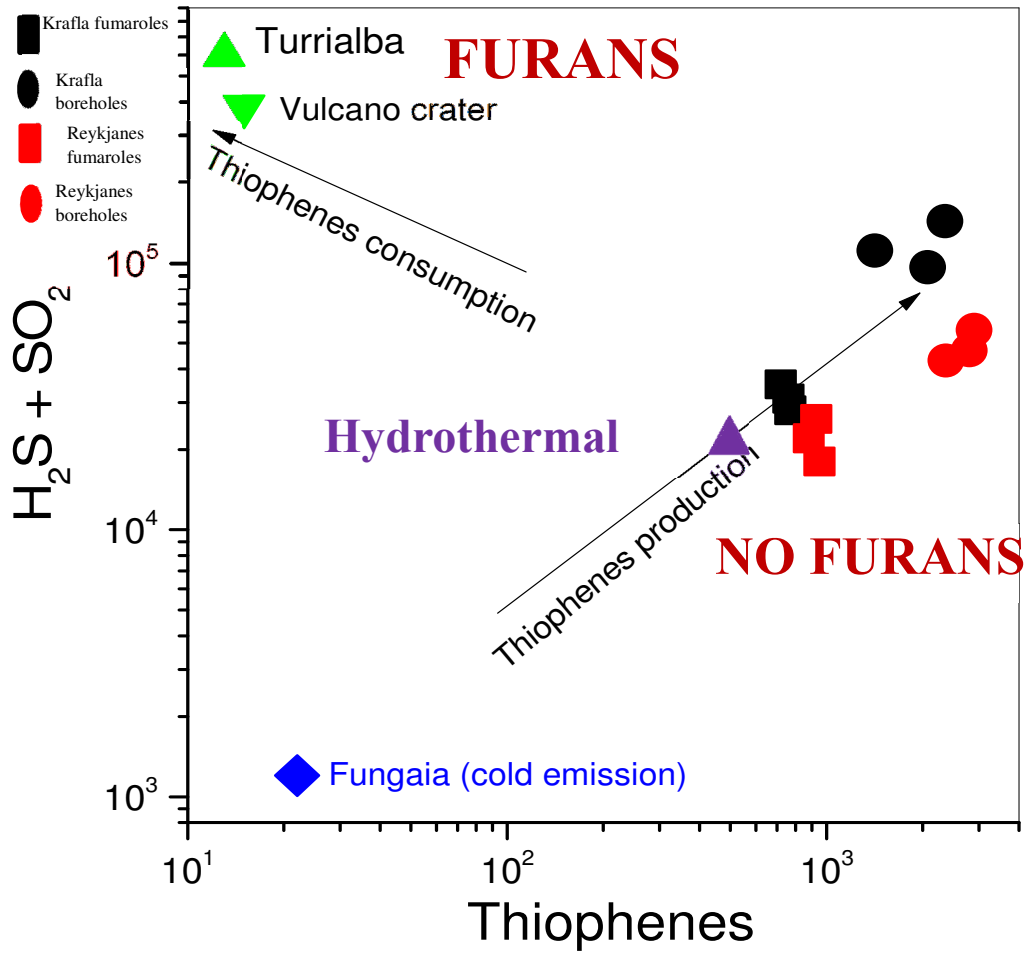

Figure 2.1.9.: Total S Vs thiophenes binary diagram (conc. in ppb on logarithmic scale) , data from Tassi et al. (2010) and Capecchiacci (2012).

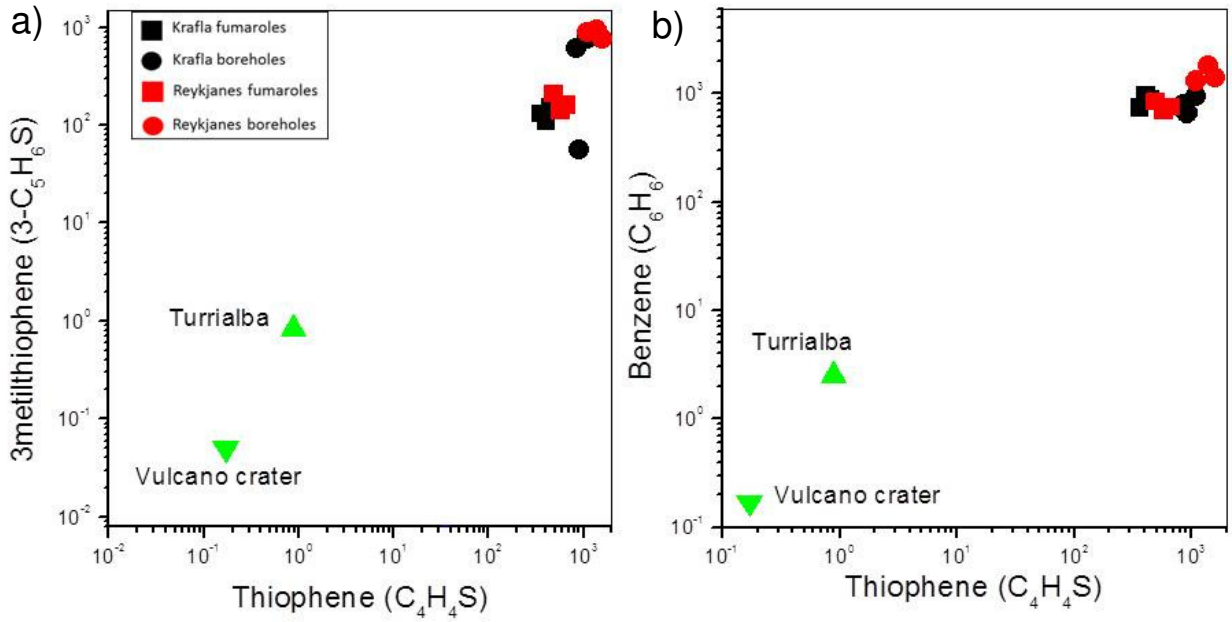

Figure 2.1.10.a-b: Aromatics Vs thiophene binary diagram (conc. in ppb on logarithmic scale), data from Tassi et al. (2010) and Capecchiacci (2012).

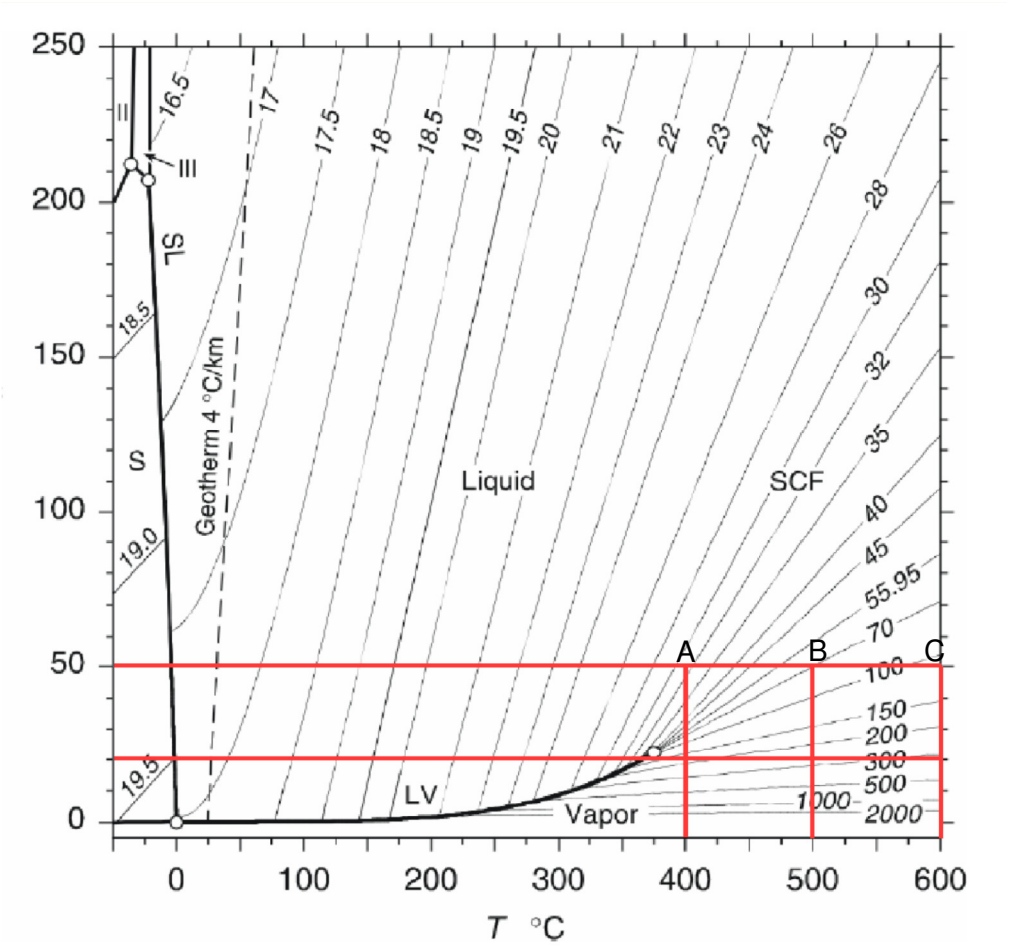

Figure 2.2.1.: The three intersecting points (A,B,C) in the upper red line (50 MPa) refers to the P-T experimental conditions selected for the experiments.

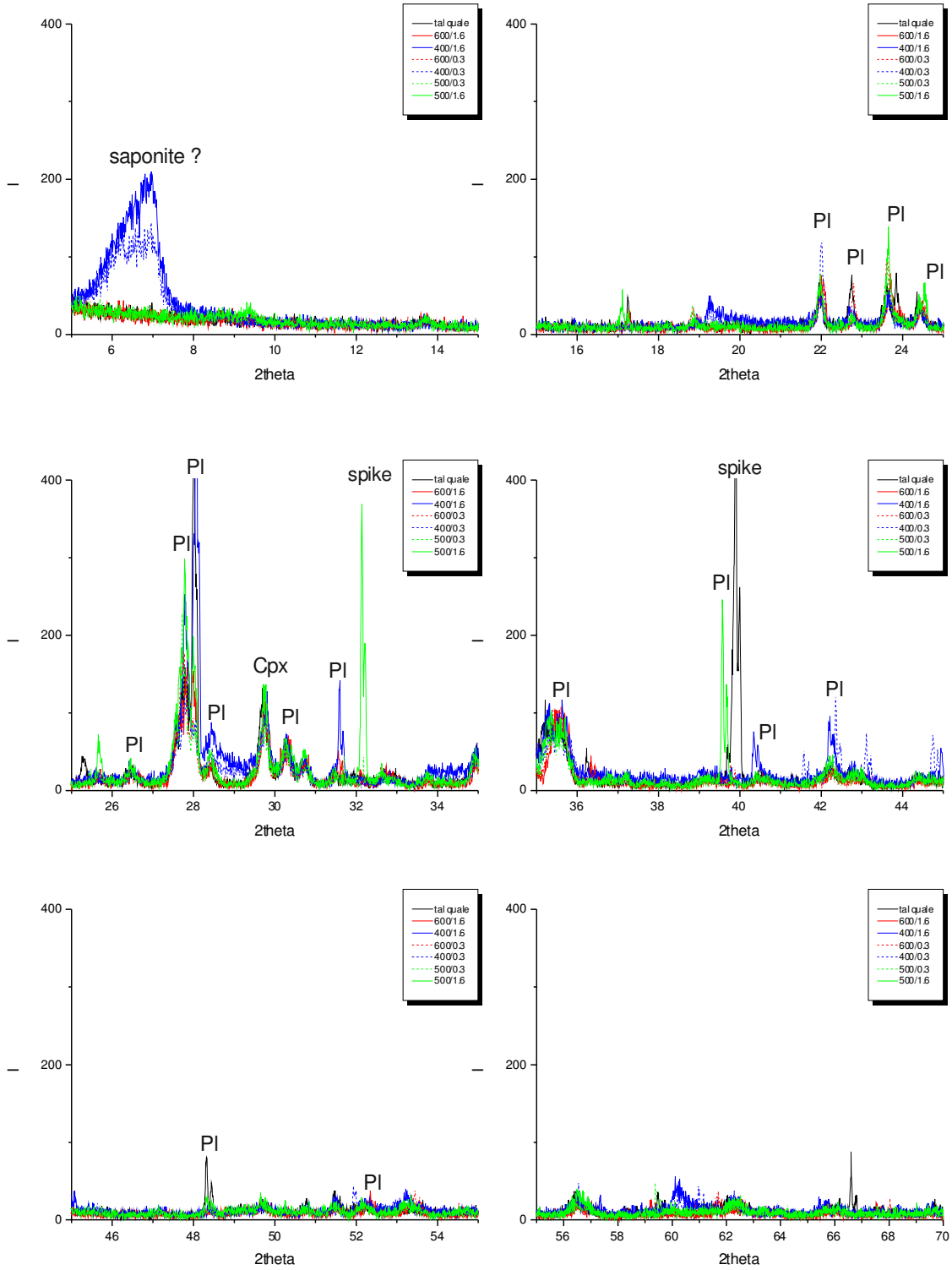

Figure 2.2.2.: XRD spectra of experimental products of Experiments Isl1-Isl6 and starting material EJ29A (black line). Isl1 (red line), Isl2 (blue line), Isl3 (red dotted line), Isl4 (blue dotted line) Isl5 (green dotted line), Isl6 (green line). Peaks are attributed to plagioclase (Pl), clinopyroxene (Cpx). Note some anomalous peaks labelled spike, due to instrumental instability.

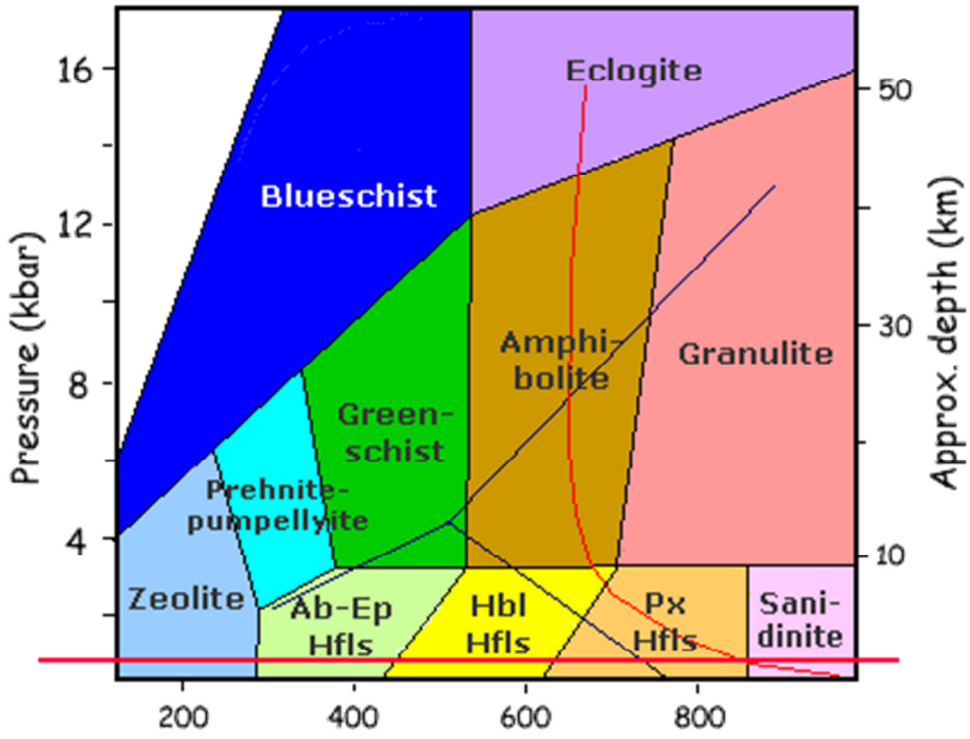

Figure 2.2.3.: P-T diagram of metamorphic facies. The red line represents the 500 bar isobar. Experiments interest the albite+epidote and hornblende hornfels facies.

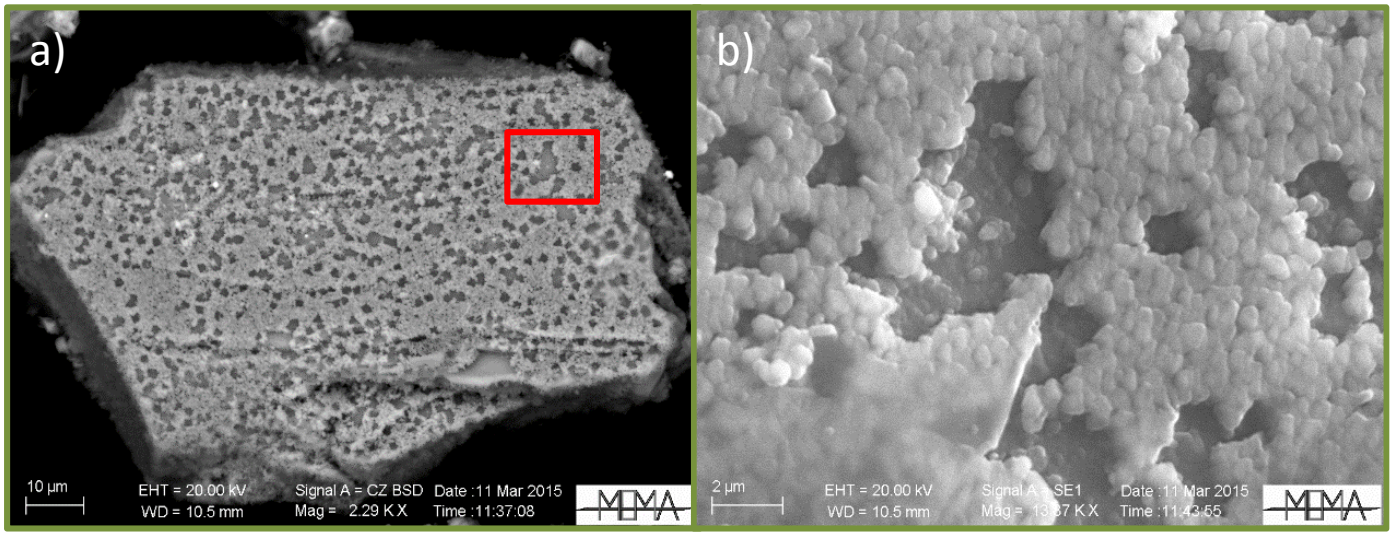

Figure 2.2.4.: a) Secondary electron images of products in Isl4 experiment (400°C, 500 bar). b) The image is an enlargement of the image on the left and corresponds to the red rectangle area. Neo-formed Na-rich plagioclase (white) growth on original plagioclase (dark grey).

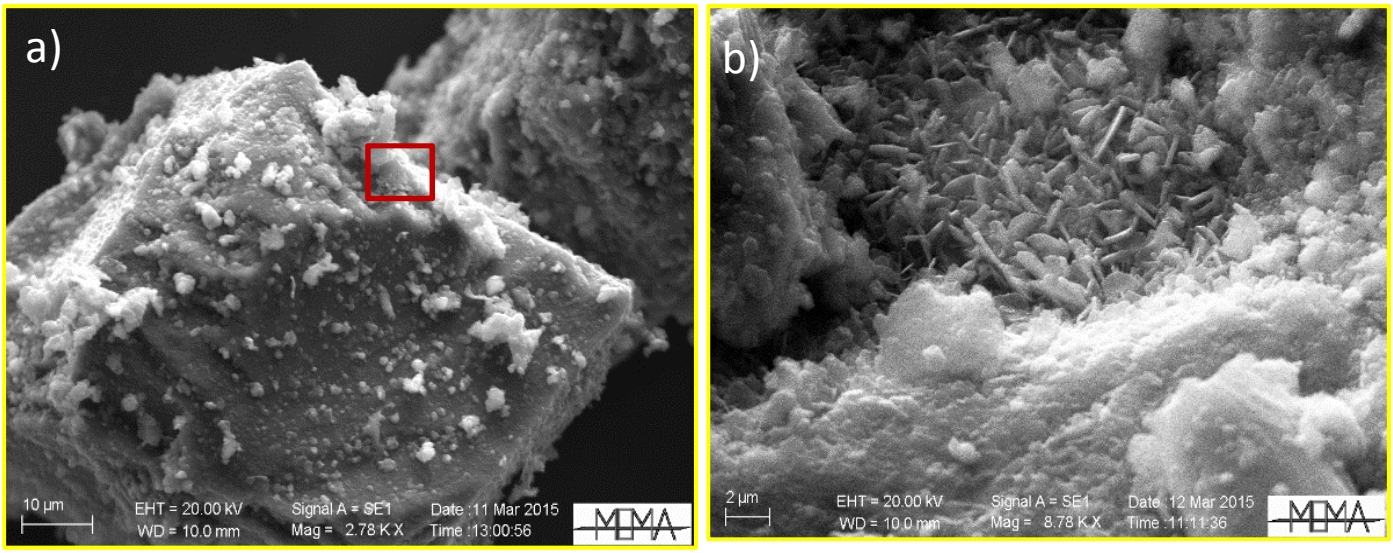

Figure 2.2.5.: a) Secondary electron images of products in Isl3 experiment (600°C, 500 bar). b) In the image (enlargement of image on the left) some small lamellar crystals are observable that could be interpreted as actinolite.

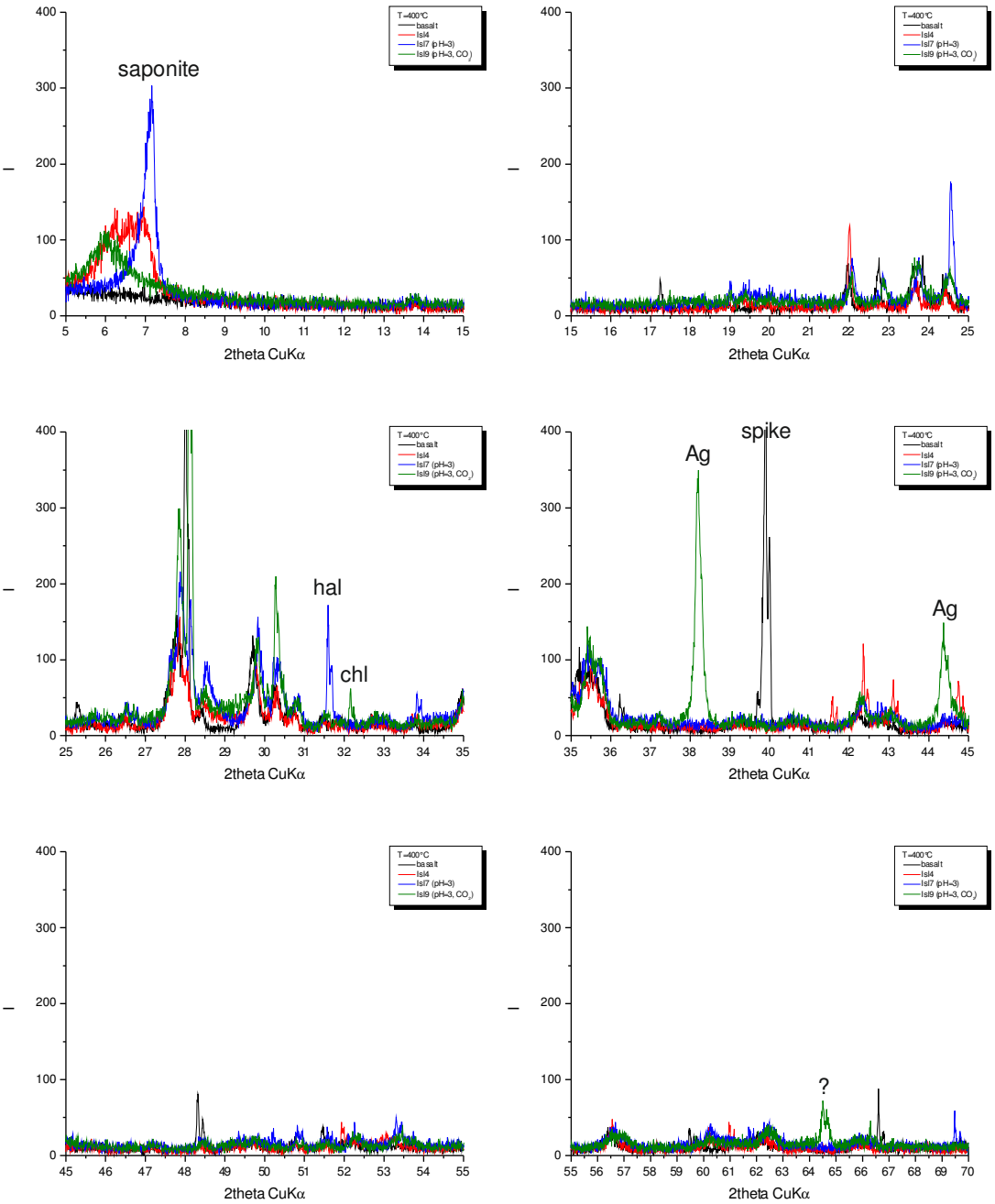

Figure 2.2.6.: XRD spectra of experimental products obtained at T= 400 °C. The spectra of Isl7 (blue line) and Isl9 (green line) are compared with starting material EJ29A (black line) and Isl4 experiment (red line), Chl= chlorargyrite (AgCl), hal= halite (NaCl).

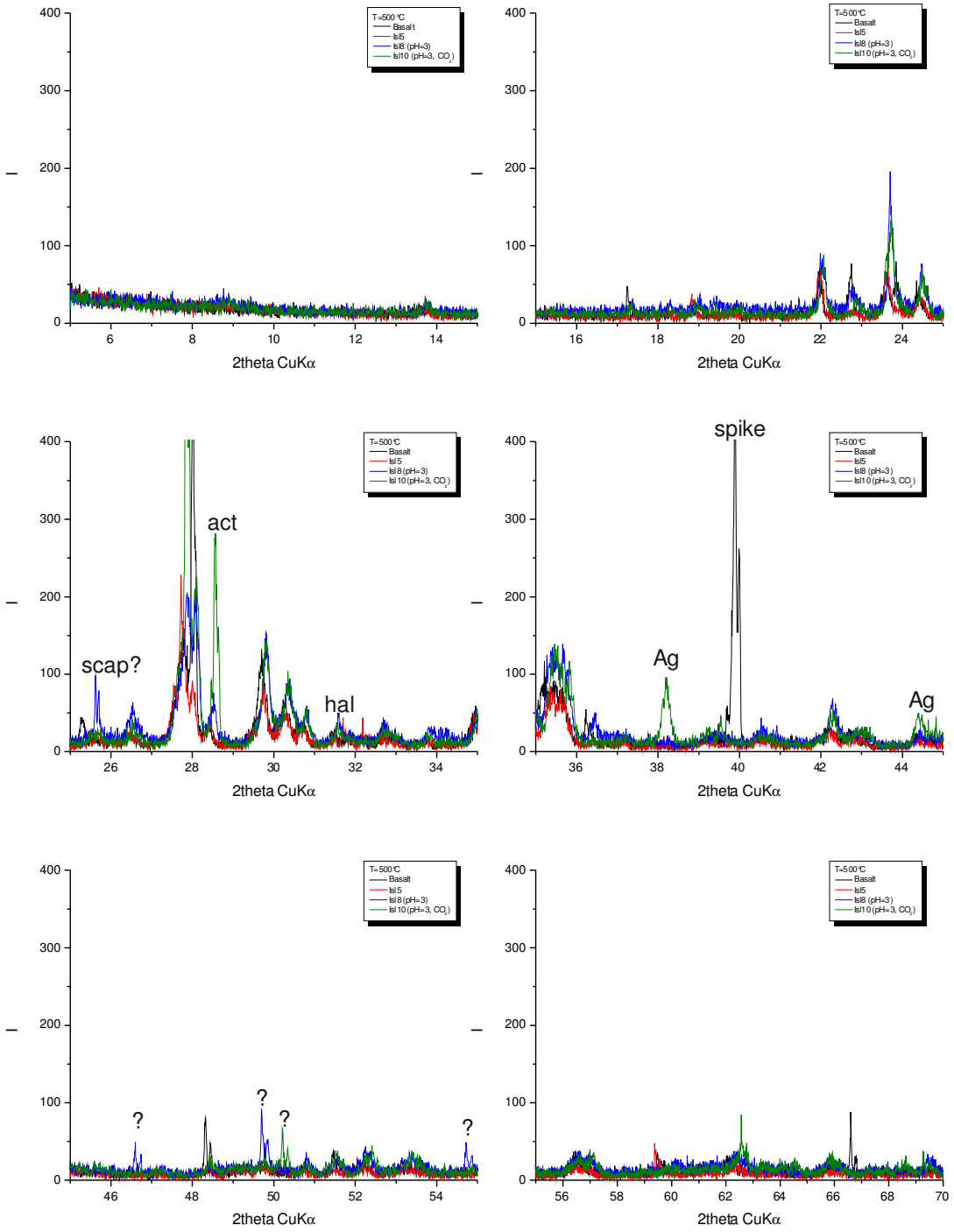

Figure 2.2.7.: XRD spectra of experimental products obtained at T = 500 °C. The spectra of Isl8 (blue line) and Isl10 (green line) are compared with starting material EJ29A (black line) and Isl5 experiment (red line). hal= halite (NaCl), act= actinolite, scap= scapolite, Ag = metallic silver.

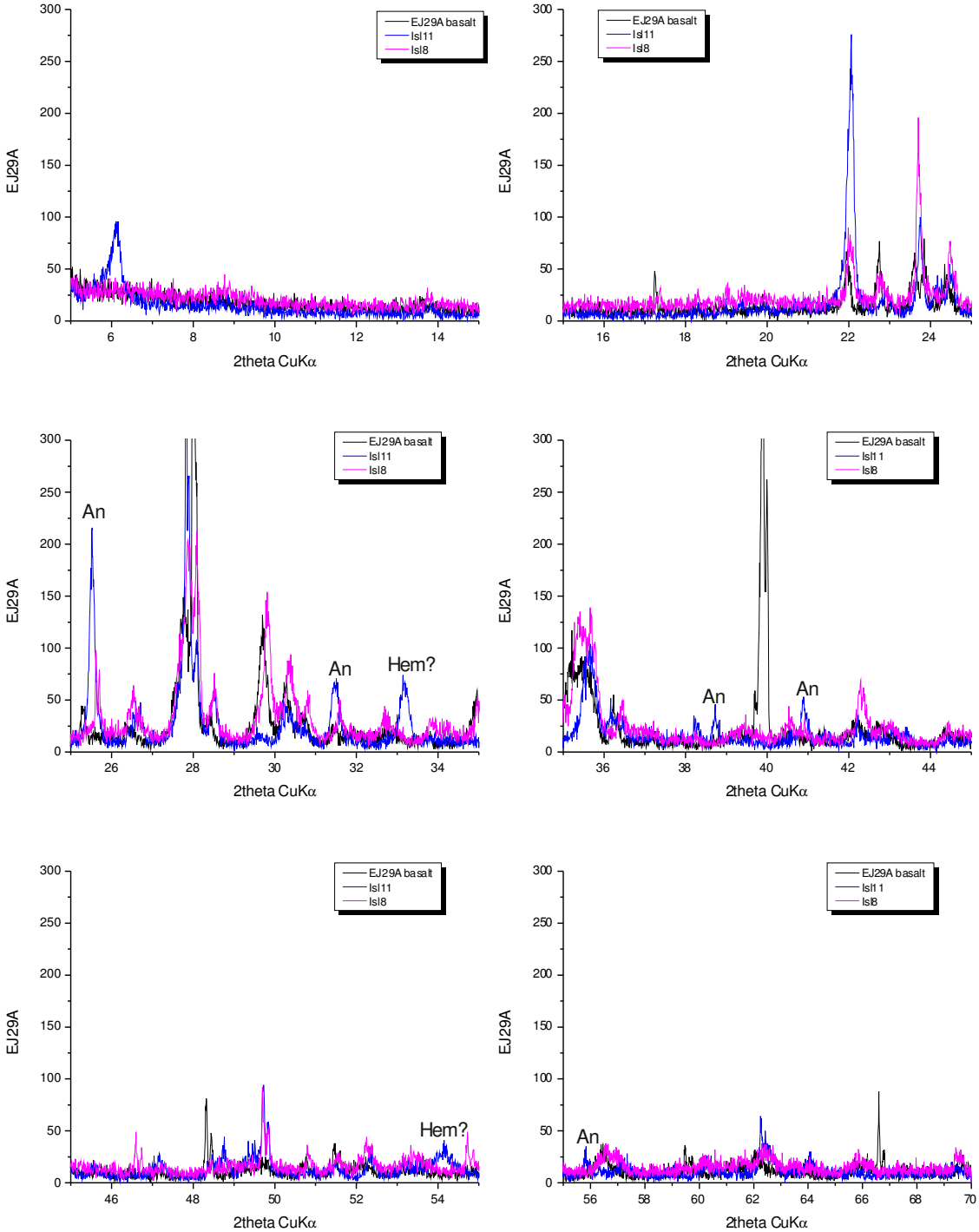

Figure 2.2.8.: XRD spectrum of Isl11 experiment. The spectra of Isl8 and EJ29A are also reported for comparison. Labels (An= anhydrite; Hem= hematite; Qz=quartz) are reported only for peaks present in Isl11.

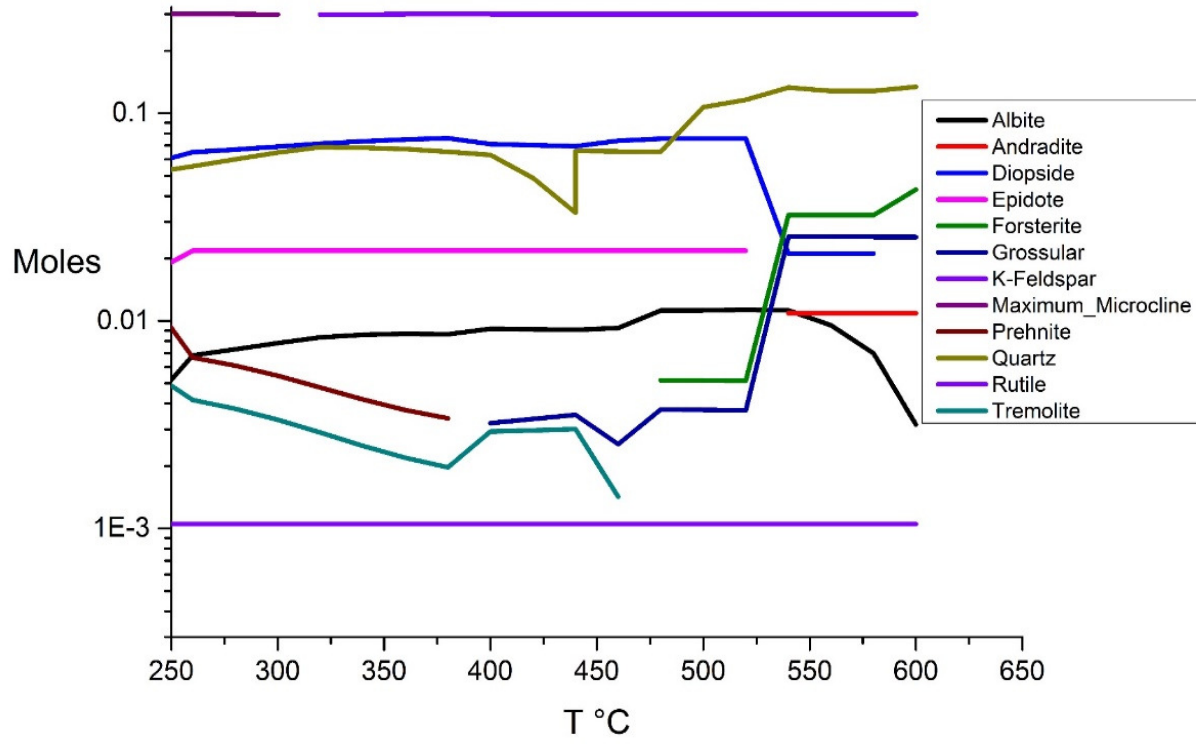

Figure 2.3.1.: Abundance in moles of secondary mineral phases obtained by alteration of the normative minerals of the reference basalt at pH 9. The normative minerals are not reported in the diagram as they are characterized by significantly higher amounts. However, some of secondary minerals could be in the normative composition; in this case only the newly formed amount of such minerals is reported.

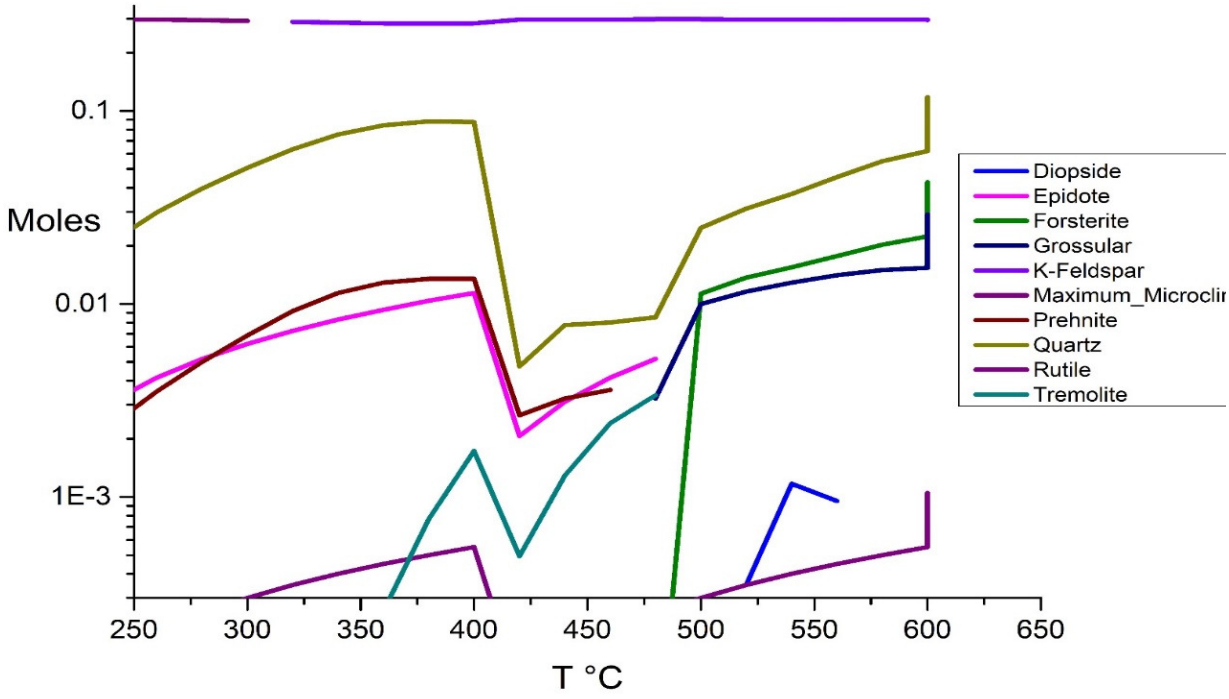

Figure 2.3.2.: Abundance in moles of secondary mineral phases obtained by alteration of the normative minerals of the reference basalt at pH 5. The normative minerals are not reported in the diagram as they are characterized by significantly higher amounts. However, some of secondary minerals could be in the normative composition; in this case only the newly formed amount of such minerals is reported.

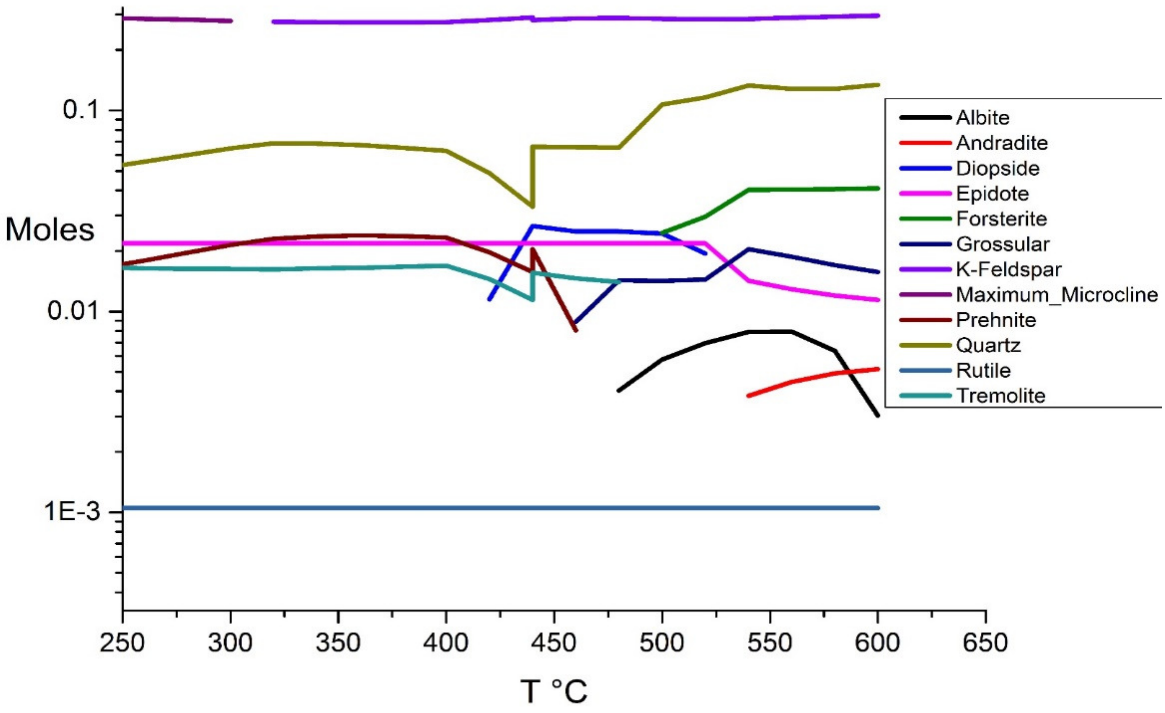

Figure 2.3.3.: Abundance in moles of secondary mineral phases obtained by alteration of the normative minerals of the reference basalt at pH 7. The normative minerals are not reported in the diagram as they are characterized by significantly higher amounts. However, some of secondary minerals could be in the normative composition; in this case only the newly formed amount of such minerals is reported.

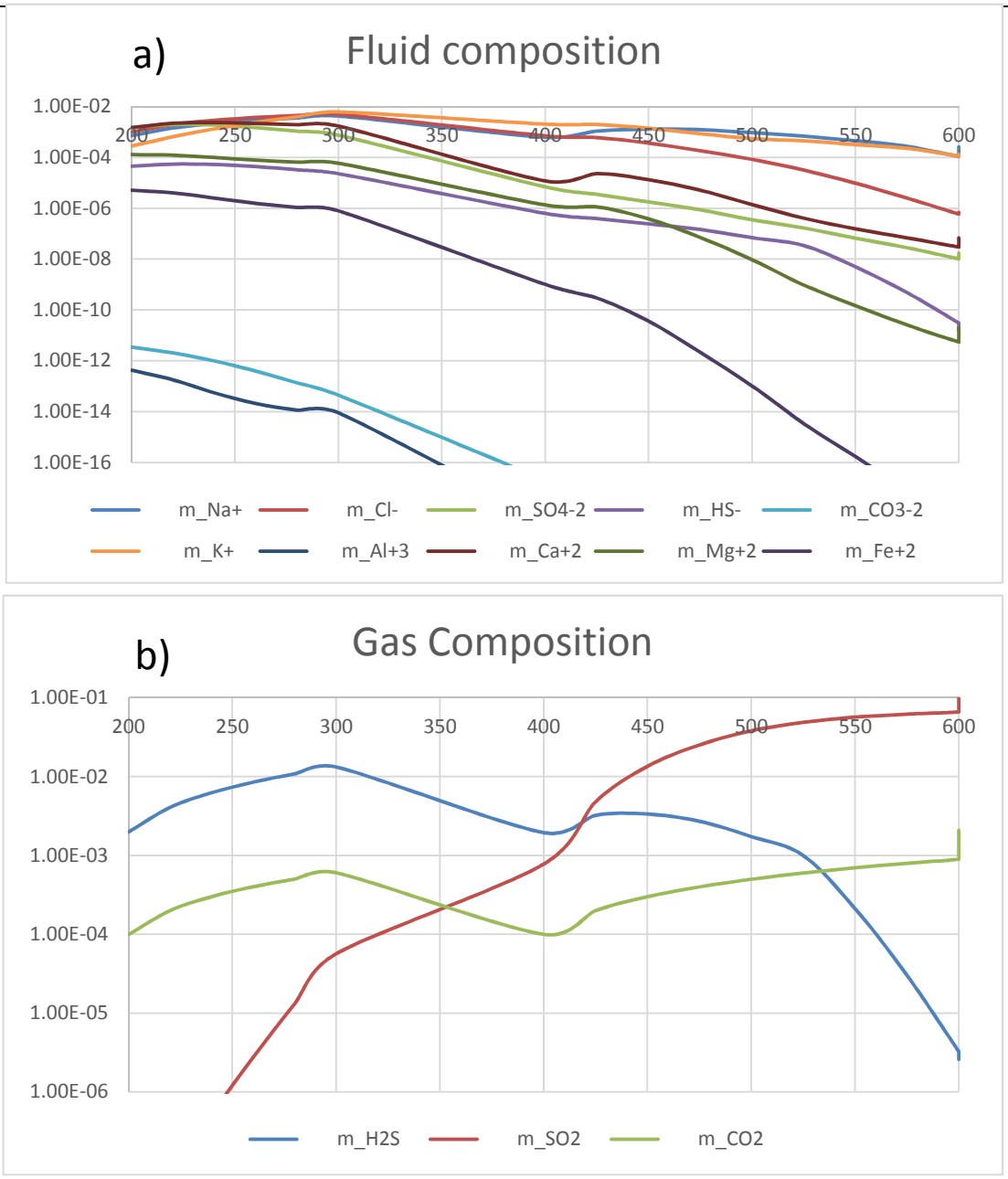

Figure 2.3.4.: Variation of chemical components vs temperature in liquid (mol/l) (a) and gas (partial pressure in bar) (b) phases in the model performed at pH=5.

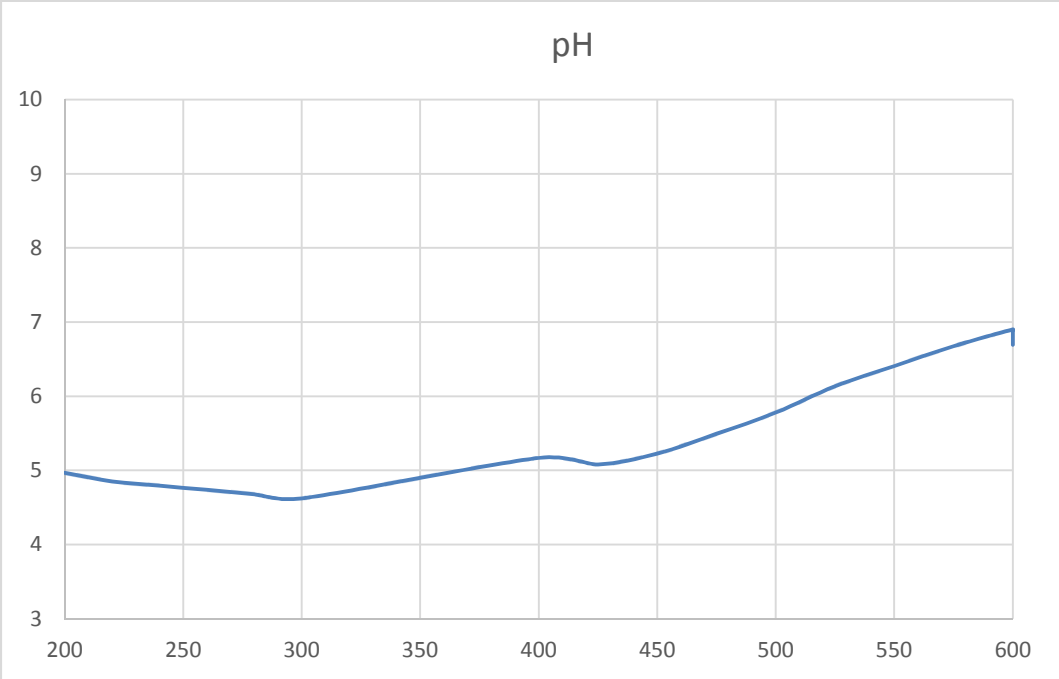

Figure 2.3.5.: pH vs temperature (°C).

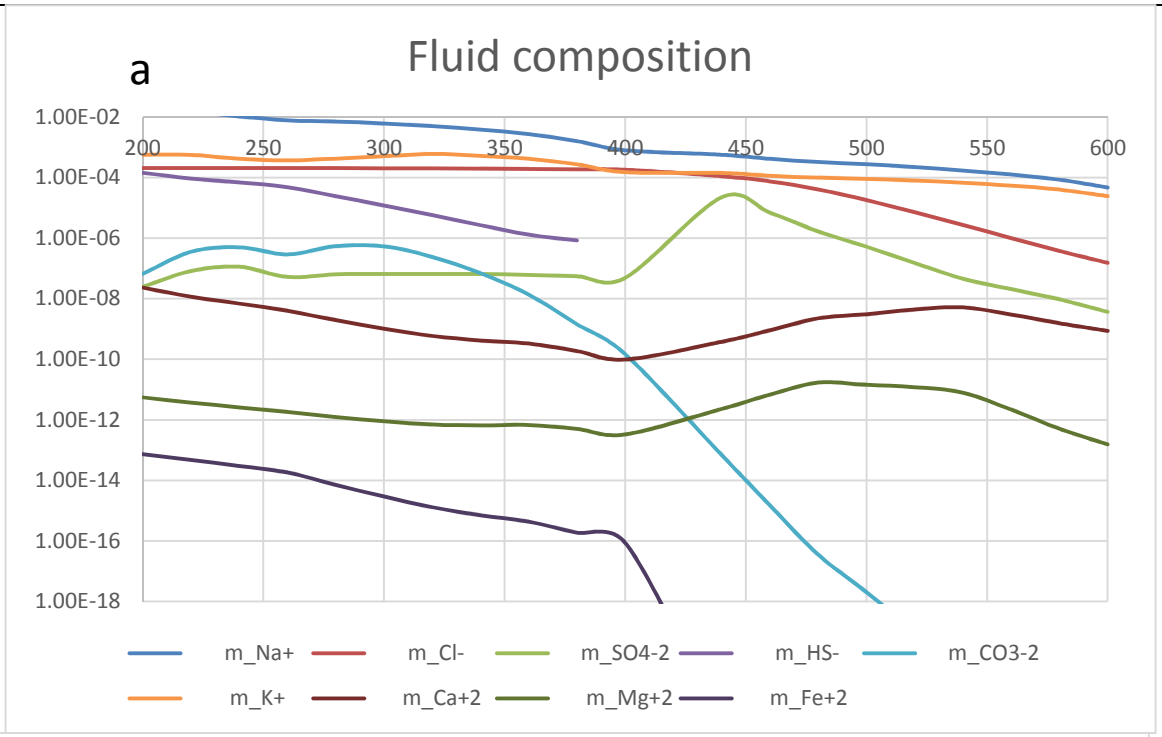

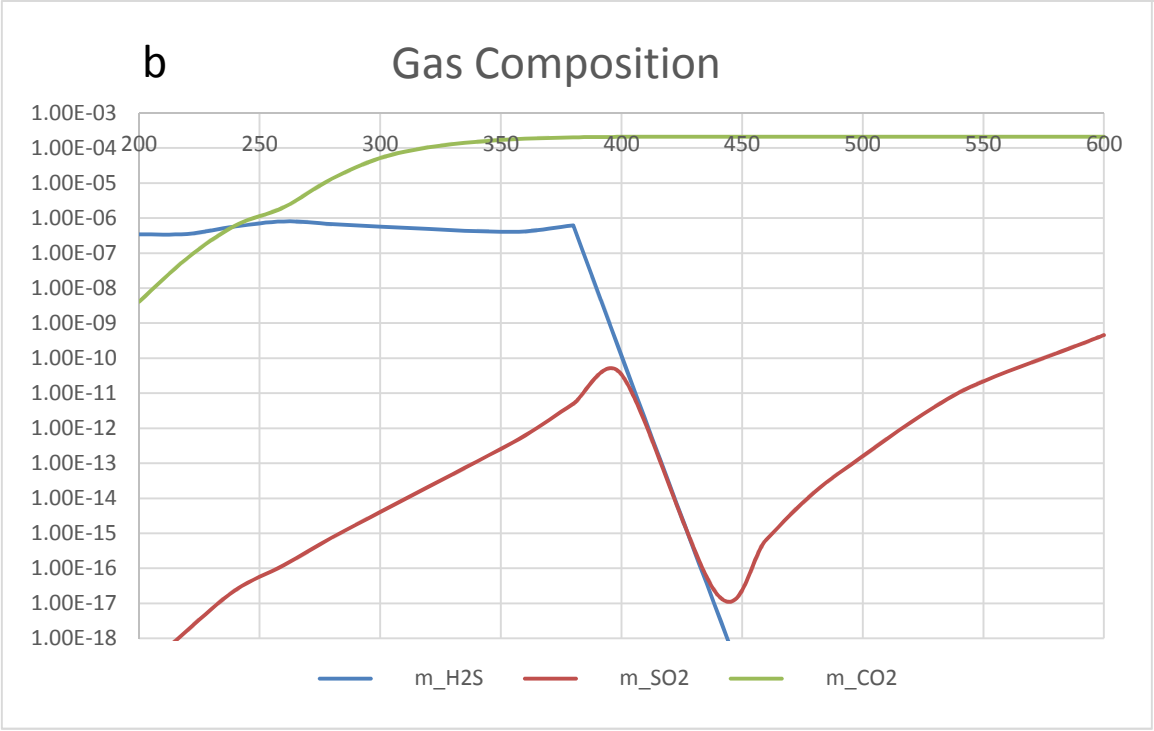

Figure 2.3.6.: Variation of chemical components vs temperature in liquid (mol/l) (a) and gas (partial pressure in bar) (b) phases in the model performed at pH=9.

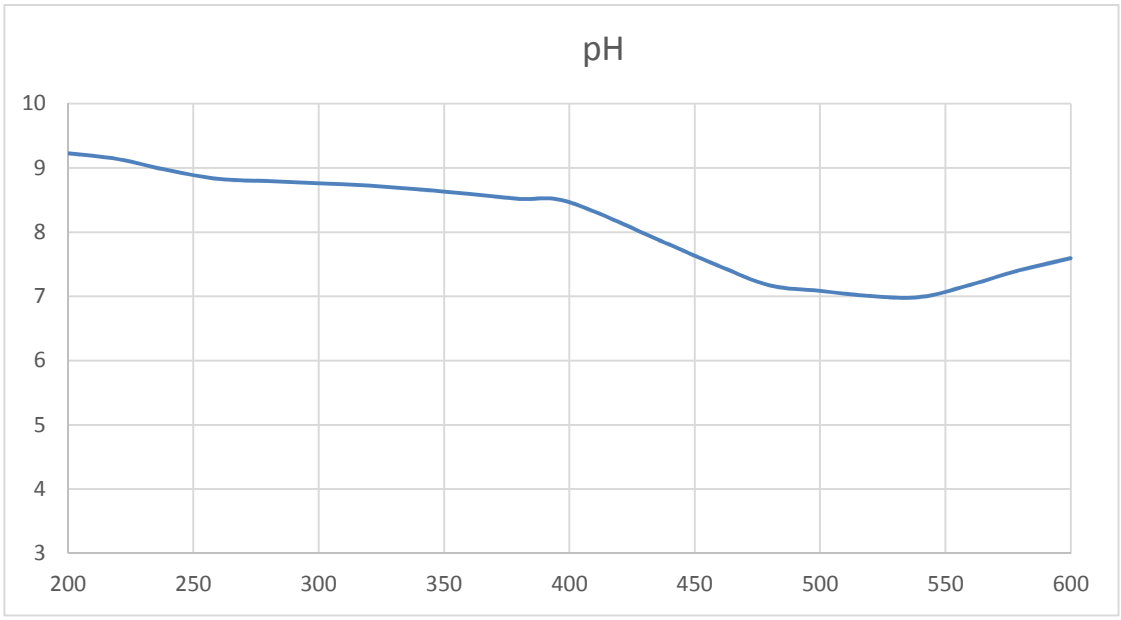

Figure 2.3.7.: pH vs temperature (°C).

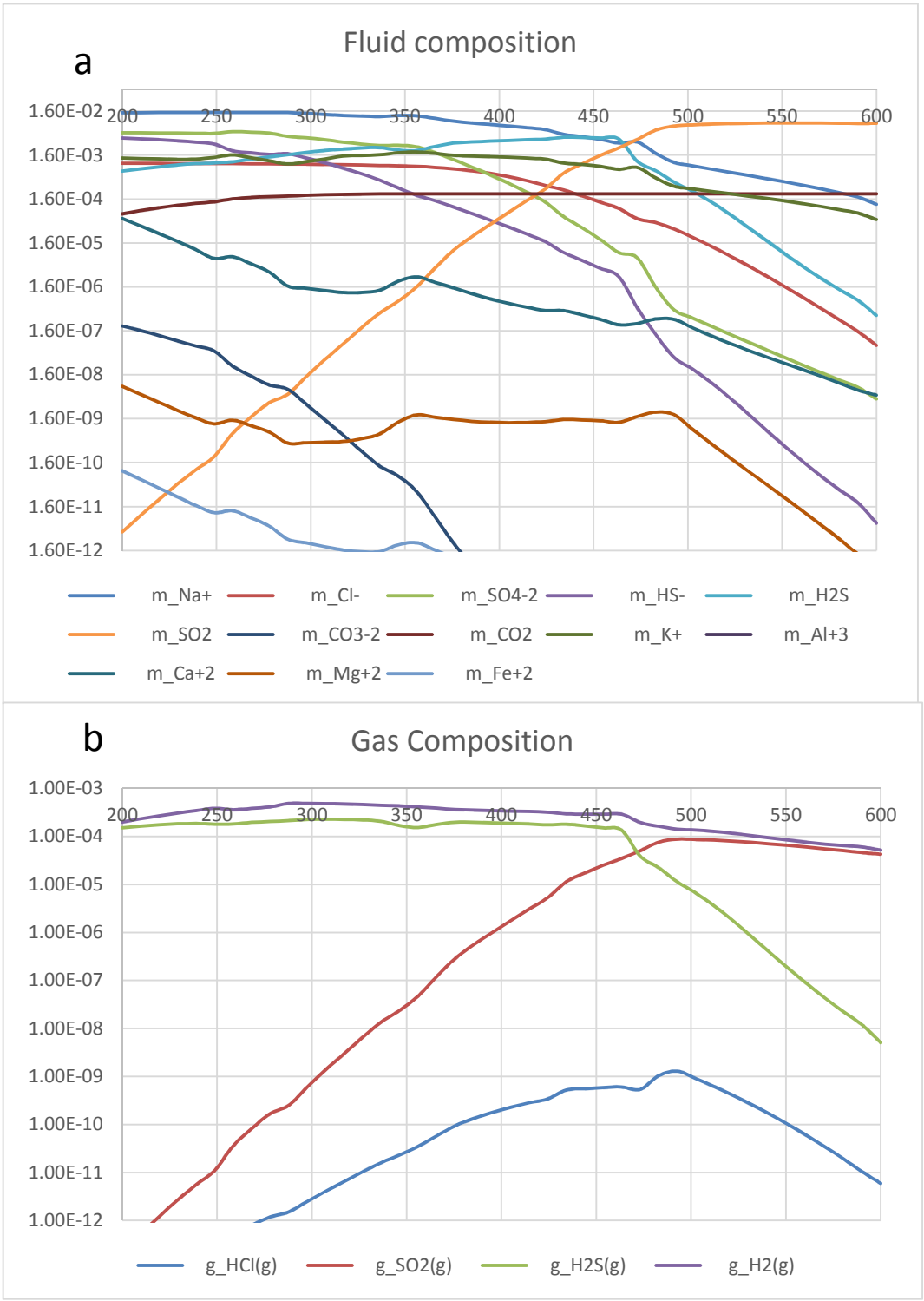

Figure 2.3.8.: Variation of chemical components vs temperature in liquid (mol/l) (a) and gas (partial pressure in bar) (b) phases in the model performed at pH=7.

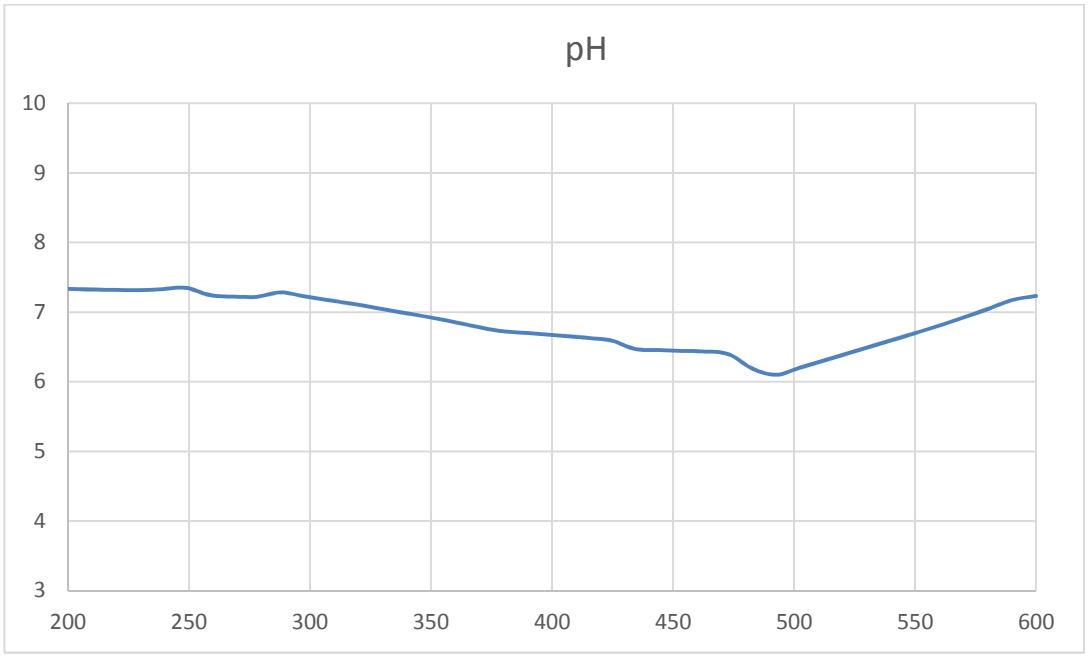

Figure 2.3.9.: pH vs temperature (°C).

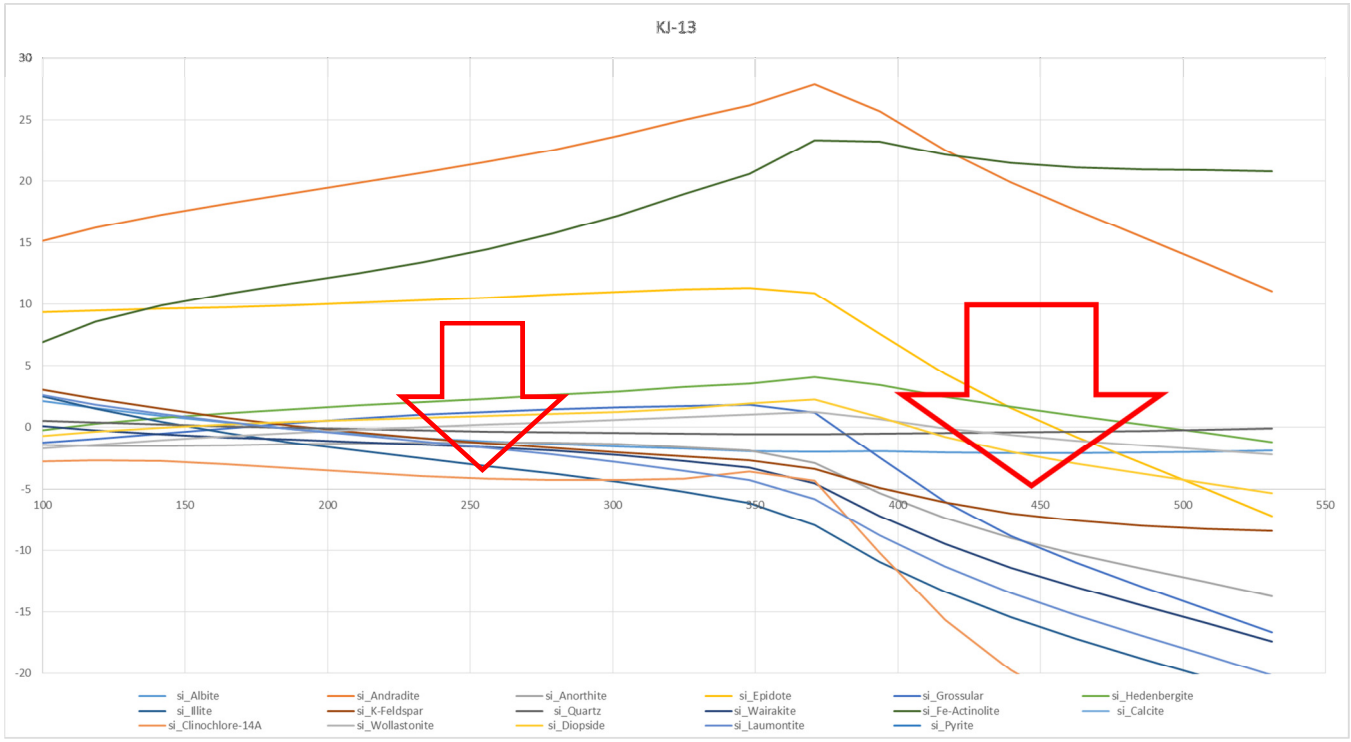

Figure 2.3.10.: Simultaneous equilibrium model for KJ-13 well, Saturation Index (SI) of different mineralogical species is reported in function of temperature.

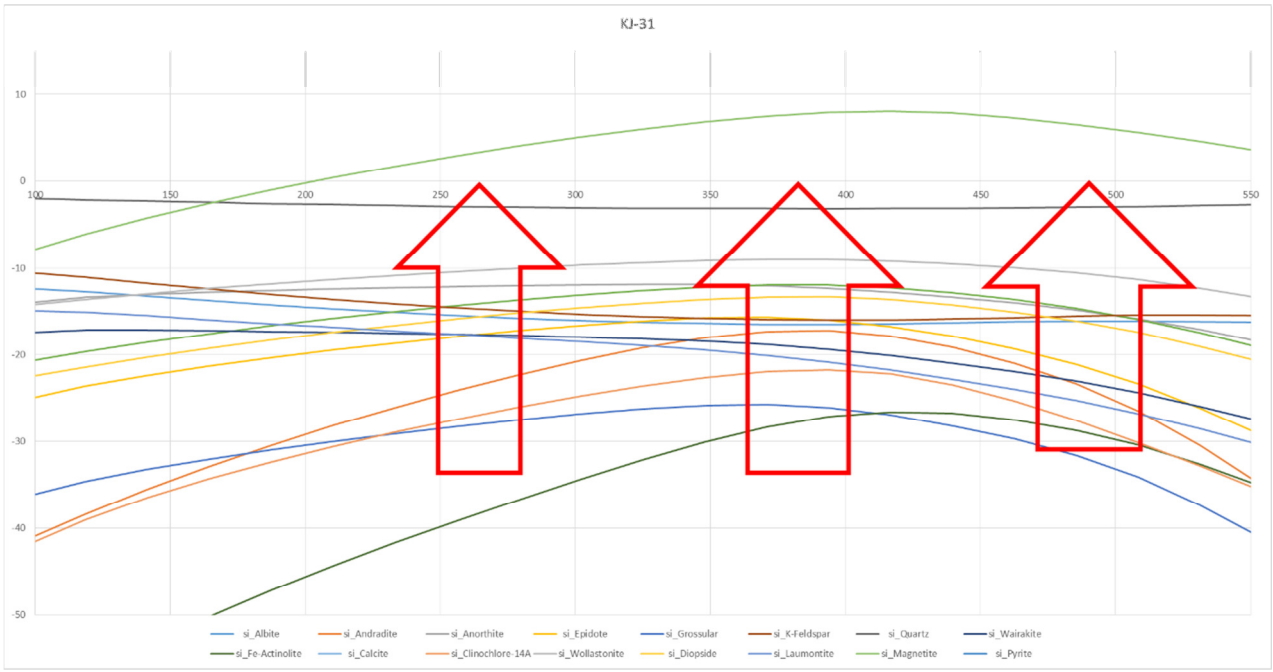

Figure 2.3.11.: Simultaneous equilibrium model for KJ-31 well; Saturation Index (SI) of different mineralogical species is reported in function of temperature.

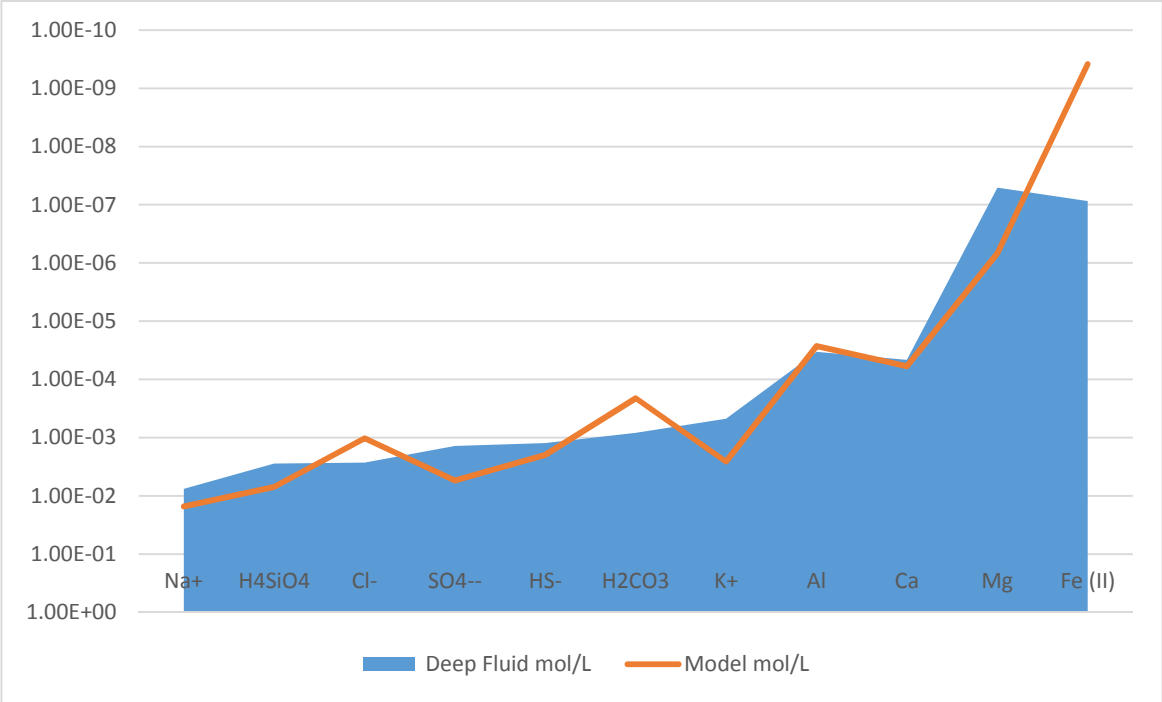

Figure 2.3.12.: Comparison of deep Krafla fluid and modeled fluid composition (mol/l).

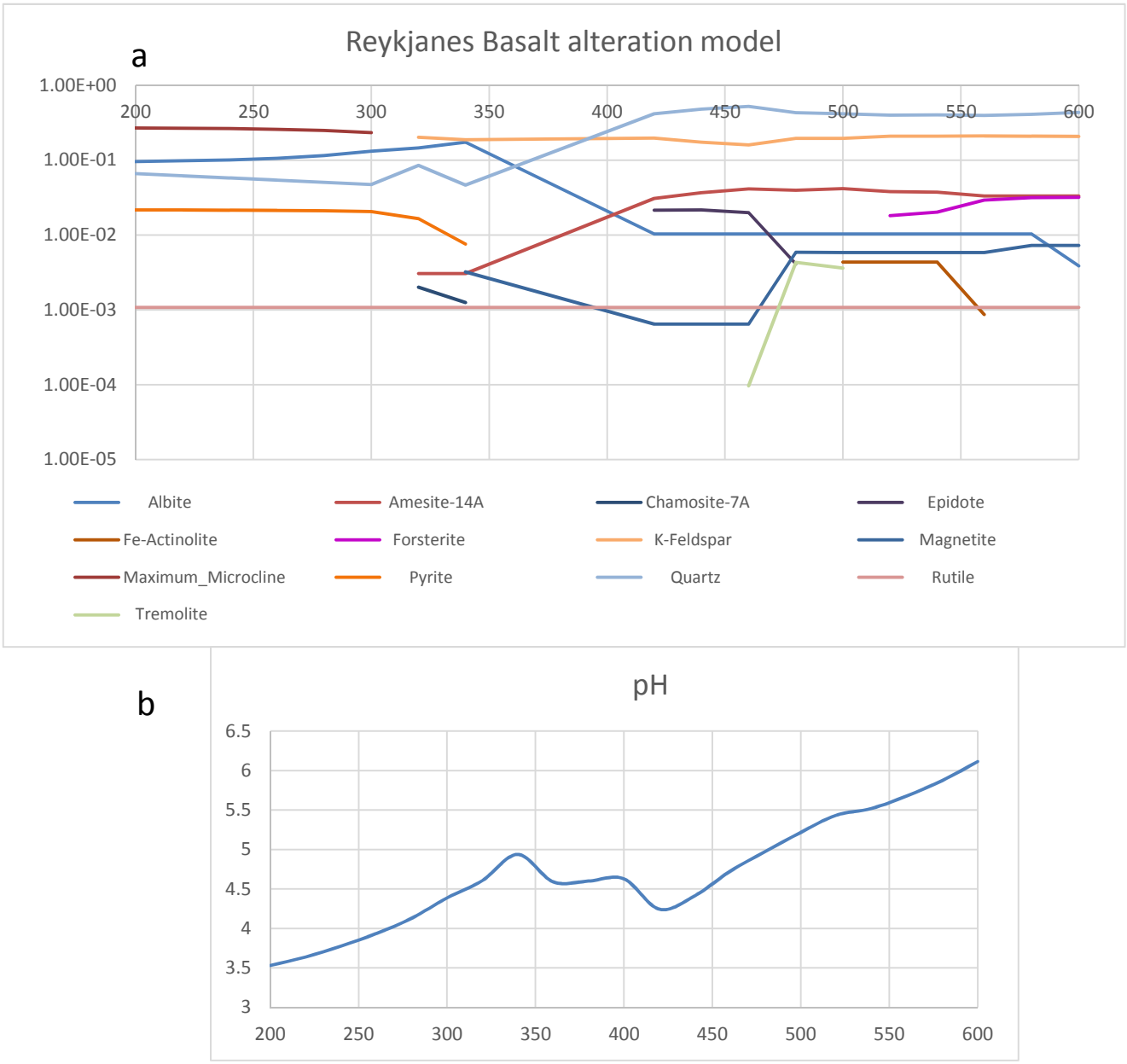

Figure 2.3.13: (a) Abundance in moles of the mineral phases (moles) versus temperature obtained by alteration of the reference basalt at pH 3.5; (b) variation of pH vs temperature (°C).

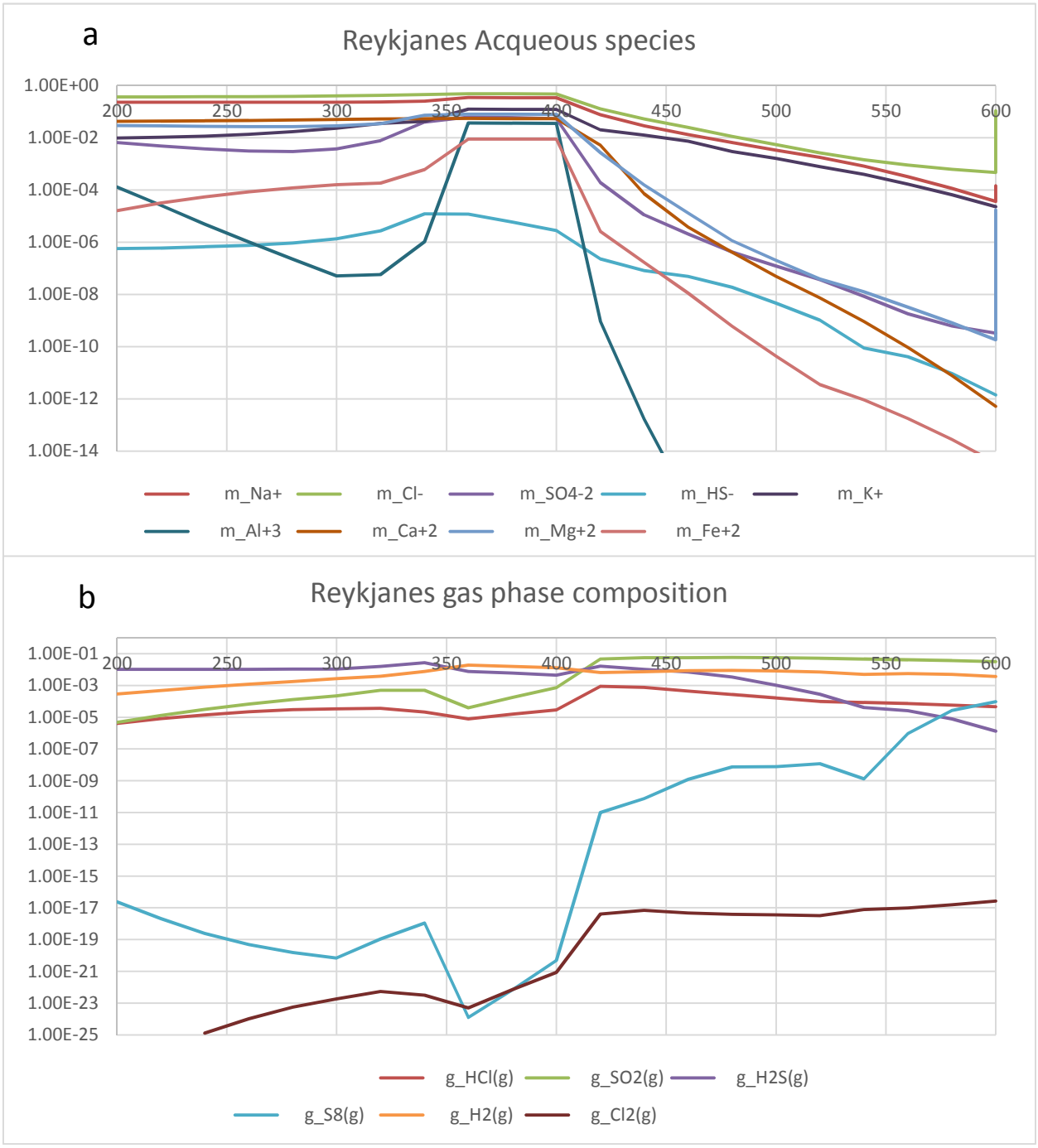

Figure 2.3.14.: Variation of chemical components vs temperature in liquid (mol/l) (a) and gas (partial pressure in bar) (b) phases in the model performed at pH 3.5

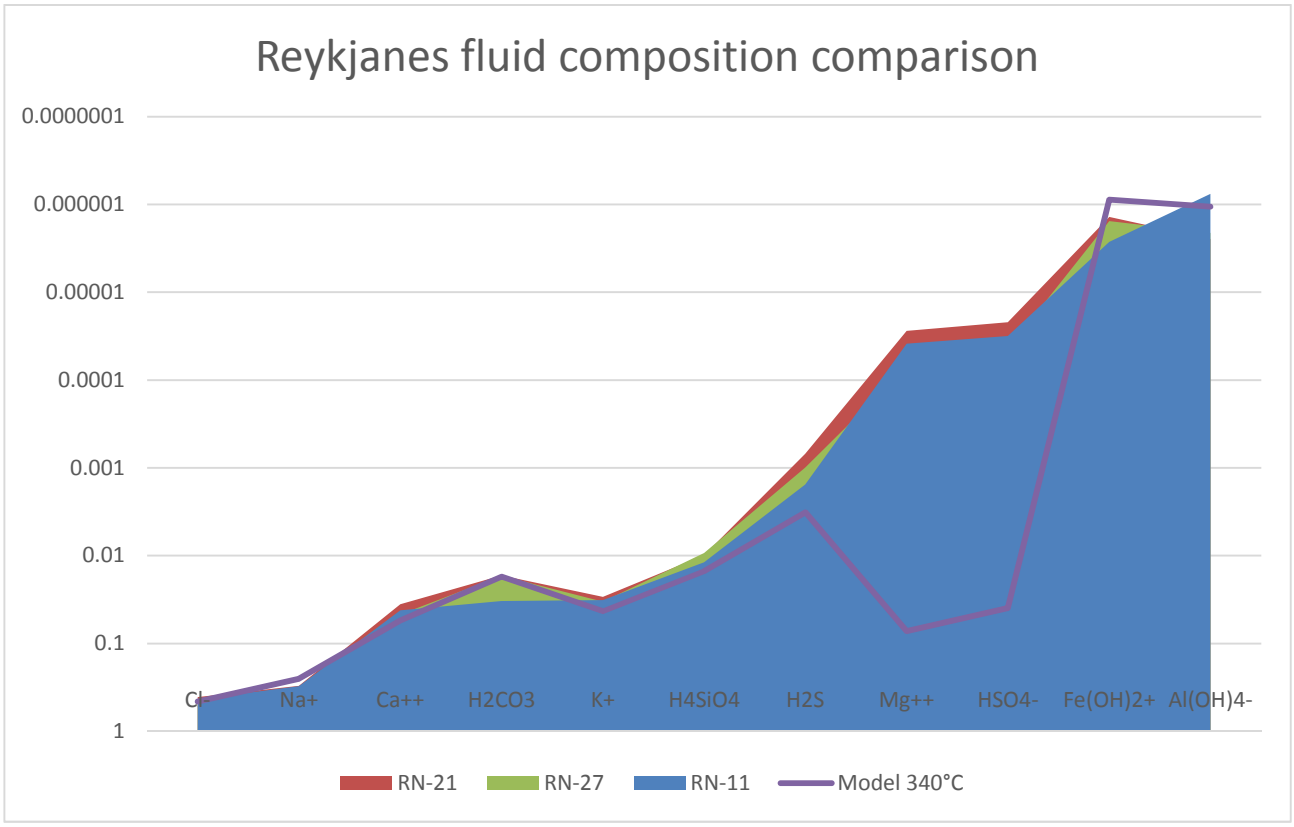

Figure 2.3.15: Comparison of deep Reykianes fluids and modeled fluid composition (mol/l).

TABLES

Table 2.1 Phases commonly found in Geitafell as a result of alteration of primary phases in basalts (after Fridleifsson, 1983).

	Geitafell primary phases			
	Pyroxene	Plagioclase	Olivine	ilmenite
	Geitafell secondary alteration phases			
	Chlorite zone	**Epidote zone**	**Andradite zone**	**Actinolite zone**
Quartz	x	X	X	X
Calcite	x	X	X	X
Smectite	x	x		
Talc	x			
Chlorite	**X**	X	X	X
Albite/K feld	X	X	X	X
Epidoto		**X**	X	X
Garnet			**X**	X
Actinolite			X	**X**
Hedenbergite			x	x
Limonite	x	X	x	x
Fe-oxides		x	X	X
Sphene	x	x	X	X
Pyrite	x	X	X	X
Zeolites*	X	X	X	X
X = index mineral				
X = abundant				
X = scarce				
* related to regional low-temperature hydrothermal alteration overprinting				

Table 2.1.1 a-b: Outlet temperatures, depth and pressure of wells, chemical composition of the (a) dry gas fraction (in mmol/mol) and $\delta^{13}C–CO_2$ (in ‰ V-PDB), of samples collected in Krafla and Reykjanes geothermal systems, (b) condensate (in mg/L).

a)

	ICELAND		Depth	T °C	P bar	CO_2	H_2S	N_2	CH_4	Ar	O_2	H_2	He	$\delta^{13}C–CO_2$
KRAFLA	KRA FUM 1	fumarol		100		810	31	83	2.75	1.44	0.56	71	0.16	-4.15
	KRA FUM 2	fumarol		98		826	28	77	2.51	1.35	0.51	65	0.18	-3.72
	KRA FUM 3	fumarol		99		802	35	71	1.74	1.25	0.42	89	0.15	-3.85
	KJ13	well	800	186	8.1	815	111	38	0.23	0.65	0.15	35	0.081	-0.57
	KJ20	well	1822	184.6		765	143	47	0.27	0.73	0.22	44	0.086	-2.11
	KJ31	well	1400	172.4	10.3	794	96	53	0.35	0.86	0.18	56	0.095	-0.6
REYKJANES	REY FUM 1	fumarol		103		862	26	68	1.35	1.16	0.44	41	0.14	-3.05
	REY FUM 2	fumarol		102.6		847	22	75	1.16	1.21	0.11	54	0.15	-3.05
	REY FUM 3	fumarol		101.5		866	18	77	1.28	1.32	0.35	36	0.17	-2.68
	RN-11	well	2248	238.5	31.6	882	43	56	0.84	0.95	0.19	17	0.11	-2.54
	RN-21	well	1713	220.9	22.4	875	47	61	0.91	1.08	0.27	15	0.11	-2.45
	RN-27	well	1503	210.5	22.4	885	56	44	0.94	0.75	0.13	13	0.087	-2.68

b)

ISLANDA	mg/L	Condensate	F^-	Cl^-	Br^-	NO_3^{2-}	SO_4^{2-}	Na^+	NH_4^+
	KRA FUM 1		0.15	2.01	0.001	0.13	5.87	n.d.	n.d.
	KRA FUM 2		0.10	1.90	n.d.	0.11	4.23	n.d.	n.d.
KRAFLA	KRA FUM 3		0.17	2.43	0.005	0.10	6.38	n.d.	n.d.
	KJ13		0.15	2.00	0.012	0.05	9.14	n.d.	n.d.
	KJ20		0.47	2.44	0.006	0.05	10.86	2.50	n.d.
	KJ31		0.51	2.48	0.003	0.06	9.34	n.d.	n.d.
	REY FUM 1		0.05	1.95	0.001	0.18	3.43	n.d.	2.07
	REY FUM 2		0.14	2.03	0.001	0.12	3.22	n.d.	1.35
REYKJANES	REY FUM 3		0.10	2.15	0.001	0.08	3.18	n.d.	n.d.
	RN-11		0.46	2.93	0.006	0.05	18.21	n.d.	5.75
	RN-21		0.62	3.02	0.005	0.08	16.34	n.d.	4.97
	RN-27		0.54	2.68	0.035	0.09	22.26	n.d.	3.98

Table 2.1.2.: Chemical composition of the liquid phase from the Krafla boreholes (Steam fraction at collection: KJ-13 =1.0001, KJ-31= 0.3783).

Krafla				
Name		KJ-13	KJ-20	KJ-31
Number		15060	15065	15068
Pressure	bar	8.9	9.9	11
Enthalpy	kJ/kg	1512	2705	2783
Flow	kg/s	18.6	4.5	0.7
pH		8.84	8.18	4.2
T-pH	°C	19	15.8	30.3
Conductivity	µS/cm	1132	1550	320
Cl		44.1	308.4	21.8
SO4		303.9	11.1	4.6
F		1.13	2.51	0.01
SS	mg/kg	0	0	
CO2	mg/kg	40.3	158.6	
H2S	mg/kg	63.49	89.32	
B	mg/kg	0.954	4.02	0.351
Na	mg/kg	221	263	-0.1
Mg	mg/kg	0.003	0.003	0.007
Al	mg/kg	1.13	0.349	0.041
Si	mg/kg	217	414	0.565
P	mg/kg	-0.001	0.002	-0.001
K	mg/kg	27.2	48.9	-0.4
Ca	mg/kg	3.05	1.25	-0.1
V	µg/kg	1.68	3.63	0.07
Cr	µg/kg	0.029	0.043	0.207
Mn	mg/kg	0	0.001	0.001
Fe	mg/kg	0.006	0.006	0.09
Co	µg/kg	0.006	0.008	0.011
Ni	µg/kg	-0.05	0.058	0.096
Cu	µg/kg	-0.1	-0.1	-0.1
Zn	µg/kg	0.373	2.62	9.25
As	µg/kg	3.24	41.6	0.379
Sr	mg/kg	0.019	0.006	0
Mo	µg/kg	-0.05	0.632	-0.05
Cd	µg/kg	-0.002	-0.002	-0.002
Ba	µg/kg	1.23	0.53	0.089
Hg	µg/kg	-0.002	0.002	0.011
Pb	µg/kg	-0.01	-0.01	0.01
Ion Balance	%	99.9	68.3	
Gas Ratio	l/kg	0.391	0.781	0.62

Table 2.1.3.: Chemical composition of the liquid phase from the Reykjanes boreholes: enthalpy (kJ/kg) : RN-11 =1317, RN-21=1263, RN-27 =1185; Steam fraction at collection: RN-11 =0.1526, RN-21= 0.1793, RN-27 = 0.1125; Gas ratio (l/kg): RN-11 =0.08, RN-21= 0.06, RN-27 = 0.14.

Well	RN-11
Sample ID	20140242
Date	21.07.2014
P (bar-g)	34.0
T (°C)	241.6
LIQUID PHASE	
pH (/°C)	5.37 / 22.2
CO_2	49.8
H_2S	2.82
NH_3	1.71
B	9.09
SiO_2	836
Na	11770
K	1720
Mg	1.10
Ca	1960
F	0.26
Cl	23530
Br	84.0
SO_4	11.4
Al	0.0426
As	0.114
Ba	12.8
Cd	<0.00005
Co	<0.00005
Cr	0.000784
Cu	0.00139
Fe	0.267
Hg	<0.000002
Mn	3.80
Mo	0.0111
Ni	0.00624
Pb	<0.0003
Sr	10.5
Zn	0.121
TDS	40180

Well	RN-21
Sample ID	20140279
Date	20.08.2014
P (bar-g)	20.7
T (°C)	217.3
LIQUID PHASE	
pH (/°C)	5.99 / 22.5
CO_2	18.4
H_2S	0.38
NH_3	1.17
B	8.95
SiO_2	715
Na	11000
K	1580
Mg	0.81
Ca	1730
F	0.22
Cl	21610
Br	76.0
SO_4	13.6
Al	0.121
As	0.126
Ba	9.01
Cd	<0.00005
Co	<0.00005
Cr	0.000149
Cu	0.00146
Fe	0.175
Hg	0.000004
Mn	1.40
Mo	0.0173
Ni	0.00646
Pb	0.00170
Sr	9.30
Zn	0.0299
TDS	38372

Well	RN-27
Sample ID	20140377
Date	27.10.2014
P (bar-g)	25.9
T (°C)	226.2
LIQUID PHASE	
pH (/°C)	5.46 / 21.8
CO_2	27.3
H_2S	1.40
NH_3	1.39
B	9.46
SiO_2	624
Na	11630
K	1630
Mg	1.93
Ca	2090
F	0.22
Cl	23280
Br	81.1
SO_4	23.8
Al	0.120
As	0.0844
Ba	12.2
Cd	<0.00005
Co	<0.00005
Cr	<0.0001
Cu	<0.0005
Fe	0.322
Hg	<0.000002
Mn	1.33
Mo	0.0195
Ni	<0.0003
Pb	<0.0003
Sr	11.1
Zn	0.0544
TDS	41438

Table 2.1.4.: Chemical composition of C_2-C_6 VOCs (in mmol/mol) in the dry gas fraction of samples from the Krafla and Reykjanes geothermal systems.

ICELAND	ethane C_2H_6	propane C_3H_8	propene C_3H_6	iso-butane i-C_4H_{10}	n-butane n-C_4H_{10}	iso-butene i-C_4H_8	iso-pentane i-C_5H_{12}	n-pentane n-C_5H_{12}	n-hexane n-C_6H_{14}	Dimetil-S Dimetil-S	benzene C_6H_6	thiophene C_4H_4S	toluene C_7H_8	ethyllbenzene etil-C_6H_6	3metylthiophene C_5H_6S	m.p xylene m-p-C_8H_{10}
KRA FUM 1	0.0015	0.00035	0.0000003	0.00025	0.00035	0.00066	0.00021	0.00033	0.00045	0.00016	0.00087	0.00045	0.00011	0.00012	0.00015	0.000084
KRA FUM 2	0.0016	0.00038	0.0000004	0.00026	0.00033	0.00057	0.00026	0.00031	0.00046	0.00025	0.00095	0.00041	0.00012	0.000095	0.00011	0.000046
KRA FUM 3	0.0011	0.00027	0.0000002	0.00017	0.00019	0.00046	0.00015	0.00029	0.00051	0.00023	0.00074	0.00036	0.00013	0.000098	0.00013	0.000073
KJ13	0.00088	0.00026	0.0000002	0.00016	0.00018	0.00031	0.00014	0.00016	0.00032	0.00045	0.00066	0.00091	0.000088	0.000078	0.000056	0.000065
KJ20	0.0013	0.00034	0.0000004	0.00024	0.00032	0.00036	0.00026	0.00036	0.00039	0.00048	0.00094	0.0011	0.00011	0.000074	0.00077	0.000094
KJ31	0.0015	0.00038	0.0000004	0.00026	0.00033	0.00042	0.00028	0.00035	0.00047	0.00061	0.00078	0.00085	0.000075	0.000079	0.00061	0.000055
REY FUM 1	0.0071	0.0013	0.0000014	0.00087	0.00095	0.0017	0.00044	0.00048	0.00056	0.00011	0.00075	0.00066	0.000071	0.000066	0.00016	0.000026
REY FUM 2	0.0065	0.0012	0.0000012	0.00071	0.00083	0.0015	0.00039	0.00055	0.00061	0.00016	0.00069	0.00058	0.000055	0.000059	0.00014	0.000028
REY FUM 3	0.0062	0.0012	0.0000013	0.00066	0.00069	0.0013	0.00027	0.00036	0.00087	0.00025	0.00084	0.00049	0.000056	0.000044	0.00021	0.000031
H11	0.0088	0.0018	0.0000021	0.0011	0.0013	0.0024	0.00084	0.00098	0.0016	0.00038	0.0013	0.0011	0.00011	0.000081	0.00088	0.000047
H21	0.011	0.0028	0.0000031	0.0012	0.0018	0.0035	0.00095	0.0012	0.0015	0.00044	0.0014	0.0016	0.000089	0.000086	0.00076	0.000056
H27	0.0095	0.0021	0.0000025	0.0013	0.0017	0.0028	0.00094	0.0011	0.0018	0.00057	0.0018	0.0014	0.000097	0.000088	0.00093	0.000074

Table 2.2.1: Whole rock analysis (wt%) of basalt EJ29A.

SiO_2	47.1
TiO_2	3.1
Al_2O_3	15.0
FeOtot	12.5
MnO	0.2
MgO	8.0
CaO	10.0
Na_2O	2.9
K_2O	0.7
P_2O_5	0.4
LOI	0.4
Total	100.24

Table 2.2.2. : Mineral chemistry (in wt%) in basalt EJ29A. (cont.)

Phase	glass	glass	glass	glass		olivine	olivine	olivine	olivine		plagioclase	plagioclase	plagioclase	plagioclase	plagioclase
Sample	EJ29A	EJ29A	EJ29A	EJ29A		EJ29A	EJ29A	EJ29A	EJ29A		EJ29A	EJ29A	EJ29A	EJ29A	EJ29A
analysis	gl2	gl4	gl5	gl6		1	2	6	23		15	16	19	20	29bis
note						phenocr.	phenocr.	phenocr.	gdmass		phenocr.	phenocr.	phenocr.	phenocr.	gdmass
SiO2	54.74	53.71	57.57	58.94		37.78	39.48	37.70	36.63		52.57	53.22	52.63	51.65	55.64
TiO2	1.22	3.13	0.17	2.23		0.22	0.17	0.00	0.23		0.38	0.15	0.20	0.40	0.62
Al2O3	20.30	14.05	24.90	16.00		0.04	0.09	0.00	0.41		30.03	29.29	28.57	29.19	25.50
Cr2O3	0.01	0.00	0.02	0.05		0.00	0.09	0.02	0.00		0.00	0.00	0.00	0.00	0.00
FeO	4.85	12.28	1.55	9.34		23.62	21.70	20.24	31.11		0.74	0.93	1.10	1.01	nd
MnO	0.16	0.31	0.00	0.13		0.39	0.23	0.30	0.58		0.00	0.00	0.00	0.00	0.03
MgO	2.80	1.74	0.22	1.12		37.33	41.10	40.19	30.80		0.16	0.21	0.25	0.13	0.22
CaO	10.03	4.92	8.22	2.96		0.17	0.13	0.03	0.58		13.09	12.33	12.48	13.15	8.68
Na2O	5.80	3.71	7.04	3.02		0.00	0.00	0.00	0.00		4.28	4.91	4.72	4.91	6.76
K2O	0.73	3.15	0.80	2.97		0.00	0.00	0.00	0.00		0.16	0.32	0.26	0.32	0.57
P	0.16	2.21	0.43	1.81											
S	0.26	0.49	0.00	0.00											
Cl	0.12	0.26	0.00	0.23											
Sum	101.19	99.96	100.94	98.82		99.55	102.98	98.50	100.33		101.41	101.36	100.22	100.76	98.03
					Numbers of ions on the basis of 4 oxygens					*Cations per 8 O:*					
					Si	1.00	0.99	0.99	1.00	Si	2.37	2.40	2.40	2.36	2.58
					Fe	0.52	0.46	0.44	0.71	Al	1.60	1.56	1.54	1.57	1.39
					Mn	0.01	0.00	0.01	0.01	Fe	0.03	0.04	0.05	0.04	0.00
					Mg	1.47	1.54	1.57	1.26	sum T	4.00	3.99	3.99	3.97	3.97
					Ca	0.00	0.00	0.00	0.02						
					Ni	0.00	0.00	0.00	0.00	Ca	0.63	0.60	0.61	0.64	0.43
					sum M	2.01	2.01	2.02	2.00	Na	0.37	0.43	0.42	0.43	0.61
										K	0.01	0.02	0.02	0.02	0.03
					Fo %	73.79	77.14	77.96	63.82	sum Y	1.02	1.04	1.04	1.10	1.07
					Fa %	26.21	22.86	22.04	36.18						
										sum T+Y	5.01	5.03	5.03	5.07	5.04
										An	62.23	57.11	58.49	58.67	40.19
										Ab	36.86	41.12	40.04	39.63	56.64
										Or	0.91	1.78	1.47	1.70	3.17

Table 2.2.2. : Mineral chemistry (in wt%) in basalt EJ29A.

Phase	clinopyroxene	clinopyroxene	clinopyroxene	clinopyroxene	clinopyroxene	clinopyroxene		spinel	spinel	spinel
Sample	EJ29A	EJ29A	EJ29A	EJ29A	EJ29A	EJ29A		EJ29A	EJ29A	EJ29A
analysis	26	27	28	31bis	32bis	33bis		7	9	10
note										
SiO2	45.73	45.18	44.15	47.82	48.33	48.69		0.00	0.14	0.04
TiO2	3.38	3.53	4.20	2.51	2.53	2.03		7.25	14.92	11.20
Al2O3	5.73	4.36	4.88	3.65	3.52	2.59		16.26	6.76	6.78
Cr2O3	0.19	0.12	0.00	0.00	0.00	0.04		18.63	6.18	12.97
FeO	10.19	13.00	14.53	11.74	12.71	12.12		46.29	65.56	60.50
MnO	0.15	0.34	0.26	0.37	0.29	0.15		0.29	0.53	0.51
MgO	12.01	11.78	9.90	13.17	13.18	12.74		8.94	5.10	4.77
CaO	21.03	19.07	19.85	19.43	18.99	20.05				
Na2O	0.49	0.80	1.03	0.83	0.69	0.45				
K2O	0.00	0.33	0.06	0.12	0.00	0.11				
P										
S										
Cl										
Sum	98.90	98.50	98.86	99.65	100.23	98.98		97.66	99.21	96.79
Number of ions on the basis of 4 cations. Fe2+ and Fe3+ calculated to yield 4 cations.							*Formula on the basis of 24 cations. Fe3+ calculated in order*			
and 6 oxygens.(for details, see Morimoto, Miner. e Petrol., 39, 55, 1988).							*to get 32 oxygens.*			
Si	1.74	1.74	1.71	1.80	1.81	1.86	Si	0.00	0.04	0.01
Al IV	0.26	0.20	0.22	0.16	0.16	0.11	Ti	1.43	3.09	2.38
Fe3+	0.00	0.06	0.07	0.04	0.03	0.03	Al	5.02	2.19	2.26
sum T	2.00	2.00	2.00	2.00	2.00	2.00	Cr	3.86	1.35	2.90
							Fe3+	4.27	6.20	6.06
Al VI	0.00	0.00	0.00	0.00	0.00	0.00	sum B	14.57	12.87	13.61
Fe 3+	0.10	0.11	0.13	0.11	0.09	0.06				
Ti	0.10	0.10	0.12	0.07	0.07	0.06	Fe2+	5.87	8.91	8.26
Mg	0.68	0.68	0.57	0.74	0.74	0.72	Mn	0.06	0.12	0.12
Cr	0.01	0.00	0.00	0.00	0.00	0.00	Mg	3.49	2.09	2.01
Fe2+	0.12	0.11	0.18	0.07	0.10	0.16	sum A	9.43	11.13	10.39
sum M1	1.00	1.00	1.00	1.00	1.00	1.00				
							A+B	24.00	24.00	24.00
Na	0.04	0.06	0.08	0.06	0.05	0.03				
Mn	0.00	0.01	0.01	0.01	0.01	0.00	Fe2O3	21.68	29.89	28.45
Ca	0.86	0.79	0.82	0.78	0.76	0.82	FeO	26.79	38.67	34.91
Fe2+	0.10	0.14	0.09	0.14	0.18	0.14	Oxygens	32.00	32.00	32.00
Mg	0.00	0.00	0.00	0.00	0.00	0.00				
sum M2	1.00	1.00	1.00	1.00	1.00	1.00				
							Fe2TiO4	17.84	38.82	29.80
M1+M2	2.00	2.00	2.00	2.00	2.00	2.00	MgAl2O4	14.44	4.99	4.21
O	6.00	6.00	6.00	6.00	6.00	6.00	MgFe2O4	12.31	14.10	11.29
							MgCr2O4	11.10	3.06	5.40
Q	1.76	1.71	1.67	1.74	1.78	1.84	FeAl2O4	16.64	8.50	9.68
J	0.07	0.12	0.15	0.12	0.10	0.07	FeFe2O4	14.18	24.01	25.93
							FeCr2O4	12.79	5.22	12.41
Wo	45.88	41.57	43.92	41.14	39.99	42.32	MnAl2O4	0.38	0.34	0.35
En	36.48	35.72	30.50	38.82	38.63	37.43	MnFe2O4	0.32	0.96	0.93
Fs	17.64	22.71	25.57	20.04	21.39	20.24				
Mg #	75.53	73.14	67.70	77.46	72.86	70.74				
FeO	6.93	7.70	8.42	6.83	8.74	9.39				
Fe2O3	3.63	5.88	6.79	5.46	4.40	3.04				

Table 2.2.3: List of experiments.

Experiment	Isl1	Isl2	Isl3	Isl4	Isl5	Isl6	Isl7	Isl8	Isl9	Isl10	Isl11
Rock (g)	0.0688	0.0703	0.0334	0.0374	0.0372	0.0669	0.0359	0.0250	0.2051	0.1312	0.1326
Fluid (g)	0.0416	0.0425	0.0978	0.1007	0.0971	0.0413	0.0987	0.0744	0.6456	0.4021	0.4175
Fluid (type)*	H2O	H2O	H2O	H2O	H2O	H2O	H2O-HClpH3	H2O-HClpH3	H2O-HClpH3	H2O-HClpH3	H2O-H2SO4pH3
Ag2C2O4 (g)	-	-	-	-	-	-	-	-	0.0238	0.0141	-
Length capsule (mm)	18	22	25	27	25	23	25	25	97	97	95
solid/liquid	1.65	1.65	0.34	0.37	0.38	1.62	0.36	0.34	0.32	0.33	0.32
CO2 (m)									0.24	0.23	
Result	OK	OK	OK	OK	OK	OK	OK	OK	OK	NO	OK
P (bar)	**500**	**500**	**500**	**500**	**500**	**500**	**500**	**500**	**500**	**500**	**500**
T (°C)	**600**	**400**	**600**	**400**	**500**	**500**	**400**	**500**	**400**	**500**	**500**
duration (h)	**166**	**166**	**166**	**166**	**166**	**166**	**213**	**213**	**213**	**213**	**168**

**H2O = MilliQ; H2O-HClpH3 = HCl aqueous solution, so that pH=3; H2O-H2SO4pH3 =H2SO4 aqueous solution, so that pH=3*

Table 2.2.4: EMP analyses (in wt%) of phases found in experiments.

Phase	saponite ?	saponite ?	saponite ?		olivine		clinopyroxene	clinopyroxene	clinopyroxene		plagioclase	plagioclase	plagioclase	plagioclase	plagioclase	plagioclase	plagioclase		amphibole	amphibole	amphibole
Exp	Isl4	Isl4	Isl4		Isl4		Isl5	Isl5	Isl5		Isl4	Isl4	Isl4	Isl5	Isl5	Isl5	Isl5		Isl5	Isl4	Isl4
analysis	1a	3	9		6		11	12	14		11	13	19	2	5	6	17		3	8	12
SiO_2	47.18	43.35	45.99		40.13		47.74	47.72	44.81		54.66	48.22	56.08	52.86	60.24	47.75	50.95		37.04	49.48	48.66
TiO_2	0.00	0.05	0.01		0.02		0.97	2.12	3.18		0.24	0.06	0.38	0.26	0.27	0.18	0.00		6.94	1.50	3.14
Al_2O_3	5.25	5.95	4.54		0.04		4.03	5.25	4.87		27.02	31.78	26.43	27.35	21.74	30.83	28.98		3.17	14.38	12.69
Cr_2O_3	0.05	0.00	0.01		0.00		0.94	0.32	0.06		0.39	0.06	0.04	0.24	0.00	0.40	0.00		0.00	0.00	0.00
FeO	9.88	10.67	10.03		14.48		6.58	8.55	13.76		1.42	1.80	1.80	1.71	1.44	0.73	1.05		26.92	7.41	9.14
MnO	0.21	0.10	0.07		0.15		0.21	0.36	0.37		0.34	0.18	0.16	0.14	0.07	0.07	0.02		0.62	0.26	0.22
MgO	19.95	18.53	19.95		45.50		15.93	13.75	11.09		0.14	0.14	0.08	0.27	0.12	0.14	0.17		11.26	8.38	7.41
CaO	0.09	0.54	0.80		0.46		19.96	20.65	17.96		10.68	16.06	9.97	11.44	5.90	15.77	13.30		13.92	16.49	16.16
Na_2O	1.80	1.55	0.34		0.01		0.57	0.30	1.39		4.93	2.36	6.12	4.80	8.13	2.45	4.05		0.37	2.04	2.10
K_2O	0.62	0.37	0.48		0.00		0.00	0.20	0.19		0.15	0.06	0.27	0.36	0.67	0.09	0.00		0.11	0.37	0.11
Sum	85.03	81.10	82.22		100.80		96.93	99.21	97.68		99.97	100.71	101.33	99.44	98.59	98.40	98.54		100.33	100.30	99.64
				Cations per of 4 O:		*Cations per 6 O. Fe2+ and Fe3+ calculated to yield 4 cations.*				*Cations per 8 O:*								No. of oxygens	23	23	23
				Si	1.00	Si	1.80	1.79	1.74	Si	2.50	2.21	2.52	2.44	2.75	2.24	2.36	Structural formulae			
				Fe	0.30	Al IV	0.18	0.21	0.22	Al	1.45	1.72	1.40	1.49	1.17	1.71	1.58	Si	5.611	6.880	6.875
				Mn	0.00	Fe3+	0.02	0.00	0.04	Fe	0.06	0.08	0.08	0.07	0.06	0.03	0.05	Al iv	0.565	1.120	1.125
				Mg	1.69	sum T	2.00	2.00	2.00	sum T	4.01	4.01	4.00	4.00	3.98	3.98	3.99				
				Ca	0.01													Al vi	0.000	1.235	0.988
				sum	2.00	Al VI	0.00	0.03	0.00	Ca	0.52	0.79	0.48	0.57	0.29	0.79	0.66	Ti	0.790	0.157	0.334
						Fe 3+	0.16	0.07	0.18	Na	0.44	0.21	0.53	0.43	0.72	0.22	0.36	Cr	0.000	0.000	0.000
				Fo %	84.85	Ti	0.03	0.06	0.09	K	0.01	0.00	0.02	0.02	0.04	0.01	0.00	Fe3+	1.986	0.000	0.000
				Fa %	15.15	Mg	0.79	0.77	0.64	sum Y	0.97	1.00	1.03	1.02	1.05	1.02	1.02	Fe2+	1.424	0.862	1.080
						Cr	0.03	0.01	0.00									Mn	0.079	0.030	0.027
						Fe2+	0.00	0.06	0.08	sum T+Y	4.98	5.01	5.03	5.02	5.03	5.01	5.01	Mg	2.544	1.736	1.560
						sum M1	1.00	1.00	1.00												
										An	54.02	78.69	46.65	55.65	27.55	77.69	64.44	Ca	2.259	2.456	2.447
						Na	0.04	0.02	0.10	Ab	45.10	20.97	51.83	42.28	68.70	21.80	35.55	Na	0.108	0.549	0.576
						Mn	0.01	0.01	0.01	Or	0.88	0.33	1.52	2.07	3.75	0.50	0.01	K	0.020	0.066	0.020
						Ca	0.81	0.83	0.75									OH*	2.000	2.000	2.000
						Fe2+	0.04	0.14	0.14												
						Mg	0.11	0.00	0.00									Total	17.387	17.093	17.033
						sum M2	1.00	1.00	1.00												
																		Calculation scheme	13	13	13
																		Amphibole group	Ca	Ca	Ca
						Wo	42.08	44.17	40.41									(Ca+Na) (B)	2.259	2.456	2.447
						En	46.74	40.93	34.73									Na (B)	0.000	0.000	0.000
						Fs	11.18	14.89	24.86									(Na+K) (A)	0.128	0.615	0.596
																		Mg/(Mg+Fe2)	0.641	0.668	0.591
						Mg #	96.21	79.66	74.24									Fe3/(Fe3+Alvi)	1.000	0.000	0.000
																		Sum of S2	13.000	12.021	11.989
						FeO	1.12	6.25	6.85												
						Fe2O3	6.07	2.55	7.68									Amphibole names	ferri-	alumino	titanian-
																			subsilicic	edenite	edenite
																			kaersutite		

Table 2.2.5.: Analyses (in ppm) of fluid extracted from Isl9 and Isl11 experiments and fluid prepared to verify the presence of contaminants ("blank reagents"). Analyses are performed through ICP-OES and LC; - = below detection limit.

	Isl9		**Isl11**		**"blank reagents"**	
	ICP	LC	ICP	LC	ICP	LC
Na	1752	1600	-	801	-	2.4
Li	6.4	3.9	12		0.08	-
K	617	556	680	648	0.9	-
Mg	267	288	7112	8228	0.1	0.2
Ca	1292	1484	5862	5680	0.4	1
Fe	81		-		-	
Mn	1		146		-	
Si	665		194		0.3	
Ni	5.9		-		-	
P	266		3.6		-	
Cl		4019		443		0.47
F		379		15		0.2-0.5
SO4		3502		47937		3.84
NO3		318		21		1.8
NH4		4.1		38		2.5
Br		-		-		0.01

Table 2.3.1.: Theoretical gas phase composition obtained at 600°C.

		g_SO2(g)	g_H2S(g)	g_H2O(g)	g_S2(g)	g_CO(g)	g_CH4(g)	g_CO2(g)
Dry %	0,42	3,30	3,30		0,00	0,01	0,00	93,39
Dry um/mol	4227,98	33011,01	33011,01		20,18	84,77	0,00	933873,04
Wet %	1,68	0,83	0,83	74,82	0,00	0,00	0,00	23,52
Wet um/mol	16768,96	8313,19	8313,19	746168,17	5,06	21,35	0,00	235178,02

	CO2/CO	H2S/SO2	CH4/CO	CO2/SO2
Model	11016,13	1,00	7,30E-007	28,29

Table 2.3.2.: Relative composition (in moles) of unaltered basalt added to 1L of water.

Minerals	Relative amount moles per liter of water
Albite	6.27
Anorthite	12
Enstatite	12.85
Fayalite	0.83
Ferrosilite	8.18
Forsterite	14
Ilmenite	0.5
Magnetite	0.01
Nepheline	0.9
Wollastonite	9

Table 2.3.3.: Basic environment.

Component	Relative Abundance (moles)
CO2(g)	0.1
HCl(g)	0.1
SO2(g)	0.1
Sulfur	0.1

Table 2.3.4.: Acidic environment.

Component	Relative Abundance (moles)
CO2(g)	1
HCl(g)	10
SO2(g)	95
Sulfur	0.1

Table 2.3.5.: Calibrated acidity environment.

Component	Relative Abundance (moles)
CO2(g)	0.1
HCl(g)	0.5
SO2(g)	5.0
Sulfur	0.0

Table 2.3.6: Ion contents, as results from deep fluid of Krafla recalculated and modeled fluid at 260°C.

Chemical Species	Deep Fluid mol/L	Model mol/L
Na+	7.52E-03	1.51E-02
H4SiO4	2.78E-03	6.98E-03
Cl-	2.69E-03	1.02E-03
SO4--	1.38E-03	5.46E-03
HS-	1.24E-03	1.98E-03
H2CO3	8.24E-04	2.11E-04
K+	4.73E-04	2.58E-03
Al	3.37E-05	2.67E-05
Ca	4.62E-05	5.93E-05
Mg	5.11E-08	6.85E-07
Fe (II)	8.62E-08	3.86E-10

parameters employed for calculation
Reference temperature deg.C : 260.0 (Arbitrary)
Sampling pressure bar abs. : 9.1
Discharge enthalpy kJ/kg : 1512. (Measured)
Discharge kg/s : 18.6
Steam fraction at collection: 0.3783
Measured temperature deg.C : 19.4
Liters gas per kg
condensate/deg.C 1.76/19.0

Table 2.3.7.: Volatile species added in order to obtain the acid environment (pH 3.5) and concentrated seawater employed in the model.

Gas Phase Components	Abundance (mmol)
CO2(g)	1
HCl(g)	50
SO2(g)	95
S(g)	0.1
Water phase Components	Abundance (ppm)
Cl-	35000
Mg+2	2500
Na+	18000

Table 2.3.8: Deep fluids of Reykjanes reconstructed by means of watch 2.4.

Chemicals	RN-11	RN-21	RN-27	Model 340°C
Cl-	0.432	0.408	0.50350061	0.457
Na+	0.3076	0.3034	0.37153523	0.253
Ca++	0.0418	0.03572	0.04666594	0.0547
H2CO3	0.033	0.01686	0.01698244	0.0173
K+	0.032	0.02937	0.03357376	0.0431
H4SiO4	0.0119	0.0099	0.00935406	0.015
H2S	0.00155	0.000691	0.00099083	0.00321
Mg++	0.0000386	0.0000275	7.1121E-05	0.0726
HSO4-	0.0000315	0.000022	4.4361E-05	0.0397
Fe(OH)2+	0.00000266	0.00000139	1.5488E-06	8.80E-07
Al(OH)4-	7.57E-07	0.00000248	2.1038E-06	0.00000106
pH	4.643	4.847	4.601	4.938
parameters employed for calculation				
	RN-11	RN-21	RN-27	
Reference temperature deg.C	295.0 (Arbitrary)	285.0 (Arbitrary)	270.0 (Arbitrary)	
Sampling pressure bar abs.	35	21.7	26.9	
Discharge enthalpy kJ/kg	1317 (Calculated)	1263. (Calculated)	1185. (Calculated)	
Discharge kg/s	0	0	0	
Steam fraction at collection	0.1526	0.1793	0.1125	
Measured temperature deg.C	241.6	217.3	226.2	
Liters gas per kg	condensate/ deg.C 0.08/ 0.0	condensate/ deg.C 0.06/ 0.0	condensate/ deg.C 0.14/ 0.0	

Appendix 1

Analytical methods

Autoclave experiments

Experiments were performed by using a Leco Corp. (model HR-2B-2) cold seal pressure vessel equipment. Solid starting material plus fluid were sealed in Au capsules (4.8 mm external diameter, 4.6 mm internal diameter) and inserted in a René 41 pressure vessel (Figure A1.1.). This is closed in the upper end by a cone-in-cone seal which always remain outside of the furnace (hence cold-seal) and allow the pressure medium (water) to enter/exit vessel. Capsules are kept in the lower end of the vessel by a solid alumina rod and vessel is positioned into a sliding vertical furnace (Figure A1.1.). Pressure is measured by pressure gauges while temperature is controlled and monitored by K-type thermocouples.
XRD analyses on solid phases present before and after the experiments were carried out by using a Philips PW 1050/37 diffractometer (Cu Kα source, 2° 2Θ/minute step size). Rietveld refinement from powder diffraction data were performed using the MAUD software package (Lutterotti et al., 2007). Moreover, SEM/EDS studies on solids products was conducted on a ZEISS EVO MA15 instrument, equipped with an OXFORD INCA 250 EDS detector, 20 kV accelerating voltage, at the Centro di Microscopia Elettronica e Microanalisi of Firenze (M.E.M.A).
Quantitative micro-chemical analyses of minerals on selected samples were performed with a Jeol JXA-8600 electron microprobe using 15 kV accelerating voltage, 10 nA beam current and 15 s counting times for each element (10 s for Na) and data were taken considering the PAP model. Prior to analysis, samples were coated with a thin film of a conducting material (carbon) by means of evaporative deposition. To do that, representative batches of powders were embedded in epoxy resin and flat polished sections were prepared. Once samples were placed in a holder, the coated samples had to be put in electrical contact with the holder in order to dissipate the electrical charging caused by the interaction of the electron beam and the samples.
Long (10 cm) gold capsules have been used for the experiments planned to recover the fluid after fluid-solid interaction runs. The extraction of fluids from long capsule was performed as follows:

- the capsule (Figure A1.2 a) was immersed in milli-Q water into a test tube with a porous stopper (Figure A1.2 b);
- the capsule was crimped (and opened) using a pliers, thus allowing the fluid into the capsule to dilute into the milli-Q water. Knowing the amount of the fluid inserted into the capsule (Table 1.1.2.) the dilution was then calculated;
- the immersion of the test tube in ultrasonic bath for 3 hours favoured the homogenization of the aqueous solution and the powder to be removed from the capsule (Figure A1.2 c);
- after 48h the powder fully sedimented to the bottom of the test tube and the solution was thus recovered through a pipette and subsequently analysed.

Solutions were analysed through Liquid Chromatography by using 861 Advanced Compact IC Metrohm and 761 Compact IC Metrohm for cations (Li, Na, NH_4, K, Mg, Ca) and anions (F, Cl, Br, NO_3, SO_4, PO_4), respectively and by means of ICP-OES (Perkin Elmer Optima 8000).

Geothermal fluid geochemistry

Fumarolic gas sampling

Gas samples for the analysis of the main gas components of the fumaroles were collected by using a 0.7 m long Titanium tube inserted into the vent and connected, through a sampling line consisting of dewared glass tubes (Vaselli et al., 2006), to pre-evacuated 60 mL glass flasks equipped with a Thorion® valve and filled with a 5 M NaOH solution (Giggenbach, 1975; Montegrossi et al., 2001) (Figure 2.12.4).
Gas samples for the analysis of VOCs in the fumaroles were collected into the 12 mL glass vials after water vapor condensation carried out using water/ice-cooled glass device (Graham

type condenser) connected to the dewared glass tubes (Figure 2.12.5). As already highlighted by Tassi et al. (2012b), the dry gas fraction is preferable for VOC analysis since i) H_2S present in the gas phase, which may corrupt the Solid Phase Micro Extraction (SPME) fiber (see details in the following section), is mostly removed during water vapor condensation, and ii) the sensitivity of the analytical method is enhanced by up to one order of magnitude, since removed soluble gases and water vapor constitute up to 90% of the discharged fumarolic fluids.

Boreholes gas sampling

Gas samples for the analysis of the main gas components of the boreholes were collected by using of ISOR equipment for the separation of the gas from the liquid phase and for the pressure removal (Figure 2.12.6).
Also in this case, the sampling bottles for the gas collection consisted of pre-evacuated 60 mL glass flasks equipped with a Thorion® valve and filled with a 5 M NaOH solution.
Gas samples for the analysis of VOCs were collected into the 12 mL glass vials after water vapor condensation using SPME fiber method.

Analysis

Inorganic gases (N_2, H_2, O_2, Ar and CO) and CH_4 stored in the sampling flask headspace were determined with a Shimadzu 15A gas-chromatograph equipped with a Thermal Conductivity Detector (TCD), whereas the concentrations of BTEX were determined with the same GC apparatus used for the analysis of CH_4 and C_6H_6 in the SCC sampling glass vials. Quantification of inorganic gases and CH_4 in the flask headspace was carried out with the same procedure used for FID analysis using a N_2–H_2–O_2–Ar–CO–CH_4 standard mixture. The alkaline solution was used for the analysis of (i) CO2, as CO2_3 , by titration with 0.5 N HCl, and (ii) H_2S by ion-chromatography (Metrohm Compact 761) after oxidation with H_2O_2 (Vaselli et al., 2006). Analytical error was <5%.
In the laboratory, a manual SPME device is inserted through a silicone rubber septum in the 250 mL glass flasks to expose the gaseous mixtures to a DiVinylBenzene (DVB)–Carboxen (Car)–Poly-
DimethylSiloxane (PDMS), 50/30 lm, 2 cm long fiber assembly (Supelco; Bellefonte, PA, USA) for 30 min at 20 °C. This 3-phase fiber is characterized by efficient retentive properties for a wide range of volatile compounds (Shirey, 1999). Organic gases trapped by the SPME fiber are desorbed for 2 min at 230 °C in the column headspace of a Thermo Trace GC Ultra gas chromatograph coupled to a Thermo DSQ Quadrupole Mass Spectrometer. The gas chromatograph is equipped with a split/splitless injection port operating in splitless mode with a dedicated SPME liner (0.75 mm i.d.). The chromatographic column is a 30 m x 0.25 mm i.d. 1.4 lm film thickness TR-V1 fused silica capillary column (Thermo). The carrier gas is He set to a flow-rate of 1.3 mL/min in constant pressure mode. The column oven temperature program is as follows: 35 °C (hold 10 min), ramp at 5.5 °C/min to 180 °C (hold 3 min), ramp at 20 °C/min up to 230 °C (hold 6 min) (Tassi et al., 2008). The mass spectrometer operates in positive electron impact mode (EI) with an ionization energy of 70 eV and a source temperature of 250 °C. The detector is set in full scan mode in the mass range 40–400 m/z. The transfer-line temperature is set at 230 °C.
The $^{13}C/^{12}C$ ratios of CO_2 ($\delta^{13}C$–CO_2) were carried out using a Finnigan Delta S mass spectrometer. CO_2 was analyzed after a two-step extraction and purification procedures of the gas mixtures by using liquid N_2 and a mixture of liquid N_2 and trichloroethylene (e.g. Evans et al., 1998; Vaselli et al., 2006). Internal (Carrara and San Vincenzo marbles) and International (NBS18 and NBS19) standards were used for estimating the external precision. The analytical error and the reproducibility are ±0.05% and ±0.1%, respectively.

Appendix 2

Thermodynamic database review

Solid phases

Geochemical numerical models require comprehensive thermodynamic database. Although today's geochemical database are quite complete, including the most common reaction and reaction constants, some reactions typical of specific environments are not included. Therefore, the thermodynamic properties of some minerals relevant to our model, e.g. Tourmalines, have been added to the THOUGHREACT PITZER default database (data0.ypf). Input data, in a modified format were also added to the provided TOUGHREACT (Thermok.dat) and Phreeqc (llnl.dat) databases, to be used both in Debye-Hückel (Debye and Hückel, 1923) and in the Pitzer (Pitzer, 1973) aqueous models.
In our database we consider only end-member mineral composition. The use of solid solution require the use of end-members and the knowledge of mixing energy, that in the case of ideal solid-solutions is 0. But in general the solid-solutions are not ideal; the mixing energy data for non-ideal solid solution of most of the considered minerals are not available, thus it could not be used in our model.
The data0.ypf database follow the formalism of the EQ3/6 V7.2b code (Wolery, 1992), where solid phase are written as dissolution reactions of mineral in its ionic and aqueous components. In particular several dissolution reactions were added for dravite, schorl, Fe-actinolite, elbaite, Fe-cordierite anhydrous, Fe-sudoite, sudoite, almandine, pyrope, spessartine, Mg-cordierite, Mg-cordierite anhydrous, annite, FeO, grossular, muscovite, paragonite, phlogopite, magnetite, andalusite and sillimanite. As an example here it is reported the dissolution reaction of dravite:

$$NaMg_3Al_6(BO_3)_3Si_6O_{18}(OH)_4 + 25\ H^+ = 6\ Al^{+3} + 3\ B(OH)_3 + 3\ Mg^{+2} + Na^+ + 6\ SiO_2 + 10\ H_2O$$

The chemical equilibrium of above reported reaction is ruled by the logarithm of equilibrium constant (log K) at standard temperature and pressure condition (i.e. 25°C and 1.0132 bar). To calculate the equilibrium constant at a different temperature, TOUGHREACT uses an analytical regression curve calculated on eighth equilibrium constants defined at eighth specific temperature and pressure, from 0°C up to 300°C along the liquid-vapor saturation curve of pure water. LogK grid is organized for temperatures of 0, 25, 60, 100 °C at 1.0132 bar and 150, 200, 250, 300 °C at steam/liquid water pressure. The analytical equation has the following form:

$$LogK = a\log_n(T) + b + cT + \frac{d}{T} + \frac{e}{T^2} \qquad (1)$$

where T is temperature in Kelvin.
For the dissolution reactions of Mg-cordierite, Mg-cordierite anhydrous, annite, FeO, grossular, muscovite, paragonite, phlogopite, magnetite, andalusite and sillimanite no complete thermodynamic data are found in the recent literature. Thus, the logK and the regression coefficients were taken from the EQ3/6 database (data0.dat) by thermodynamic source data of Helgeson et al. (1978). The EQ3/6 database is one of the most complete source of data and constitutes the original source from which most thermodynamic databases were developed. Moreover, EQ3/6 data are consistent with recent literature and small changes only reflect a newer "best fit" to more recent thermodynamic data.
Calculation of log K for dravite, schorl, Fe-actinolite, elbaite, Fe-cordierite anhydrous, Fe-sudoite, sudoite, almandine, pyrope and spessartine were carried out by means of the code SUPCRT92 (Johnson et al. 1992). This code allows to calculate the standard molal thermodynamic properties of a wide variety of minerals, gas and aqueous species and their equilibrium reactions from 1 to 5000 bars and 0 to 1000°C.

The SUPCRT92 package is composed of three programs: i) the MPRONS92 is used to add or modify formation thermodynamic data of each species; ii) the CPRONS92 converts database generated by MPRONS92 in SUPCRT format, and iii) the SUPCRT92 reads and calculates the standard molal Gibbs free energy, enthalpy, entropy, heat capacity, volume and logK for each equilibrium reaction. The SUPCRT original default database (SPRONS92.DAT) contains thermodynamic data for approximately 500 minerals, gases, and aqueous species.

Because of dravite, schorl, Fe-actinolite, elbaite, Fe-cordierite anhydrous, Fe-sudoite, sudoite, almandine, pyrope and spessartine were not included in the SPRONS92.DAT database, they were added by means of MPRONS92 interactive program.
For each solid phases MPRONS92 requires: i) the standard Gibb free energy of formation ($\Delta G°_f$,298) at 298.15K [cal/mol]; ii) the standard enthalpy of formation ($\Delta H°_f$,298) at 298.15K [cal/mol], iii) standard entropy (S°) at 298.15K [cal/mol K]; iv) the volume of minerals [cm^3/mol], v) the standard heat capacity (Cp°)at constant pressure and 298.15K [cal/mol K], iv) temperature-dependent Cp° coefficients (a, b, c; cal/mol K) for use in extrapolating the data to elevated temperatures, using the Maier-Kelly equation (Maier and Kelley 1932):

$$C°_p = a + bT + \frac{c}{T^2} \quad (2)$$

where T is absolute temperature in Kelvin. The heat capacity coefficients *a-c* are expressed as a, b × 10^3, and c × 10^{-5}.
Thermodynamic data representing experimental mineral solubility based on infinite dilution were extracted from the literature after a careful bibliographic research and reported in Table A2.1.
Tourmalines (i.e. elbaite, dravite and schorl) source data are from Ogorodova et al. (2012), whereas granates (i.e. almandine, pyrope, and spessartine), as well as amphiboles (i.e., Fe-actinolite), Fe-cordierite and chlorites (i.e., sudoite and Fe-sudoite) are from Holland and Powel (2004, 2011).

After conversion of modified MPRONS92 in the SUPCRT format, by means of CPRONS92 utility programs, the equilibrium constants at the T-P grid were calculated.
Reactions involved ions, aqueous species (i.e. H_2O and $SiO2_{(aq)}$) and minerals (i.e. quartz), originally reported in the SPRONS92.DAT database were used, after checking the consistency with more recent data. Similarly, quartz (SiO_2) thermodynamic data. Calculated Log K are reported in Table A2.2.
All collected LogK values were adapted to be used as input for TOUGHREACT (Thermok.dat) and PHREEQC databases (llnl.dat), both in Debye-Hückel (Debye and Hückel, 1923) and in the Pitzer (Pitzer, 1973) aqueous models.
Thermok.dat and llnl.dat databases require for each dissolution reaction the logK at EQ3/6 temperature grid and the coefficients for analytic regression curve, to calculate equilibrium constant at different temperatures. On the basis of the log K, the coefficients for analytic regression curve were calculated by means of equation 1 for TOUGHREACT and by equation (3) for PHREEQC:

$$log_{10}K = A_1 + A_2T + \frac{A_3}{T} + A_4 log_{10}T + \frac{A_5}{T^2} + A_6T^2 \quad (3)$$

Where T is temperature in Kelvin.
Regression coefficients for Equation 1 were computed by the utility program Kreg1 provided by TOUGHREACT, whereas for equation 3, a modified versions of Kreg1, accounting for the differences between equations 1 and 3, was used.
To guaranty the inter-comparison among the thermok.dat, llnl.dat and data0.ypf databases, all thermodynamic data were uniformed.

Gas phases

At the present state of the art, the gas phases in both TOUGHREACT and PHREEQC are modeled as being in equilibrium with the liquid phase, and therefore depending on the solution model through eventually dissociation constant and solubility. In the current work the main gas species for carbon, sulphur and chlorine compounds were revised.
The data for graphite, $CH_4(g)$, $CO(g)$ and $CO_2(g)$ were revised and corrected up to very high temperature, being of widespread use also for industrial purpose.
With respect to sulphur components, a solid sulphur phase that take in to account the melting at relatively low temperature (388.36 K) were added, as well as a set of sulphur species gas components commonly referred to geochemical and volcanological works. This components are:
$SO_2(g)$, $H_2S(g)$, $S(g)$, $S_2(g)$, $S_8(g)$;
The thermodynamic data source is NIST (http://webbook.nist.gov/chemistry/) , and the data were available up to more than 1300°C, and this data too are well known and used for industrial purpose, e.g. sulphur conversion in to sulphuric acid.
The main anomaly encountered in the databases were related to HCl(g), that in the default database is given accurate at up to 200°C. By reviewing the log K and the Cl-, HCl(aq), HCl(g) behavior, we can observe a strong inaccuracy for temperature higher than 300°C, in particular with respect to the dissociation in liquid phase. We have found two main papers that have correctly reported solubility and dissociation constant for HCl up to high temperature (Pokrovskii V.A. 1999 and Ruaya and Seward 1987)
Like as for mineral in solid phase, the data for gas phases were computed from the same thermodynamic data in both TOUGHREACT and PHREEQC database format, for having two coherent database.

In spite of the extension of the database data validity with respect to temperature, we are also limited by the code functioning and the implementation of the Equation of State. The PHREEQC code uses an equation of state that provide reference thermodynamic data for liquid phase up to 620°C, given the correct salinity (i.e. 20%), while the TOUGHREACT EOS2 is currently limited at 350°C. In any case, the code won't allow chemical reaction in gas phase.

FIGURES

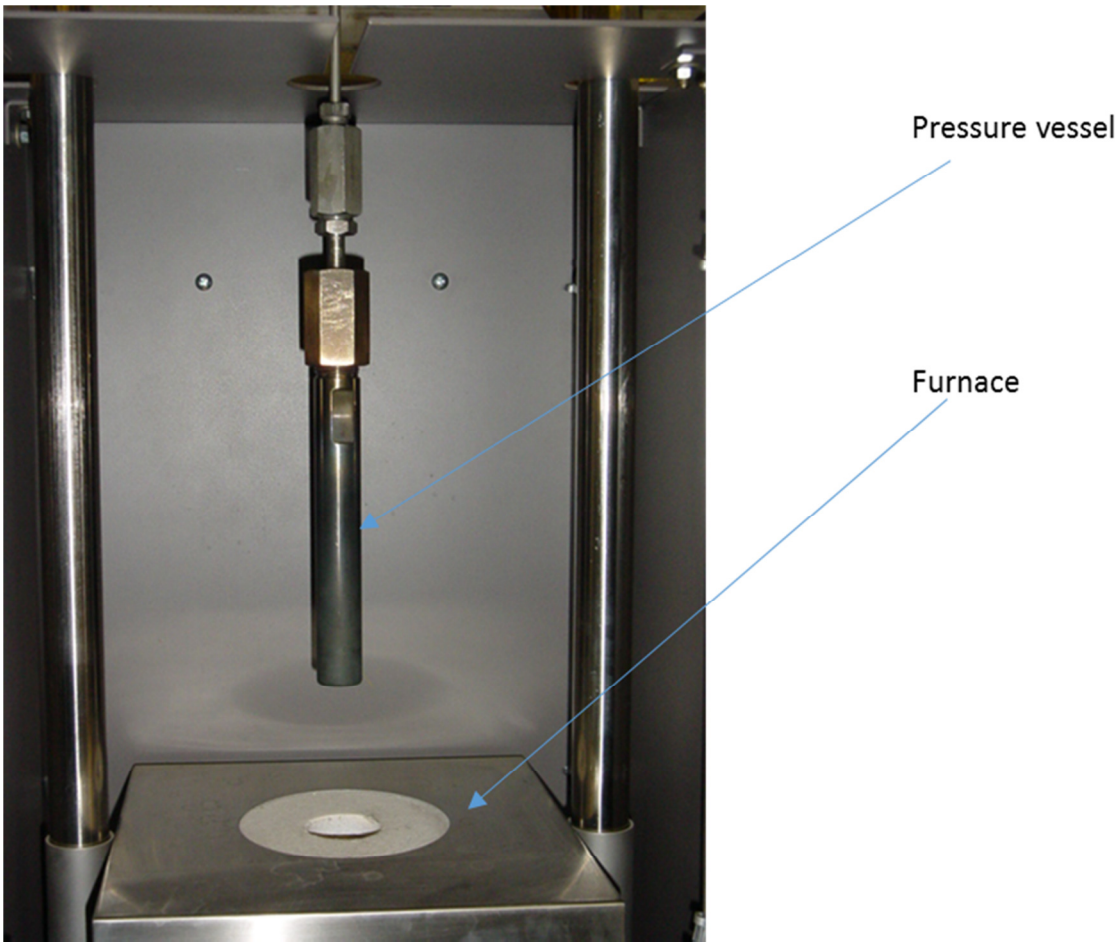

Figure A1.1.: a detail of the cold seal pressure vessel apparatus: a René 41 pressure vessel containing Au capsule(s) is approaching to enter into a sliding furnace.

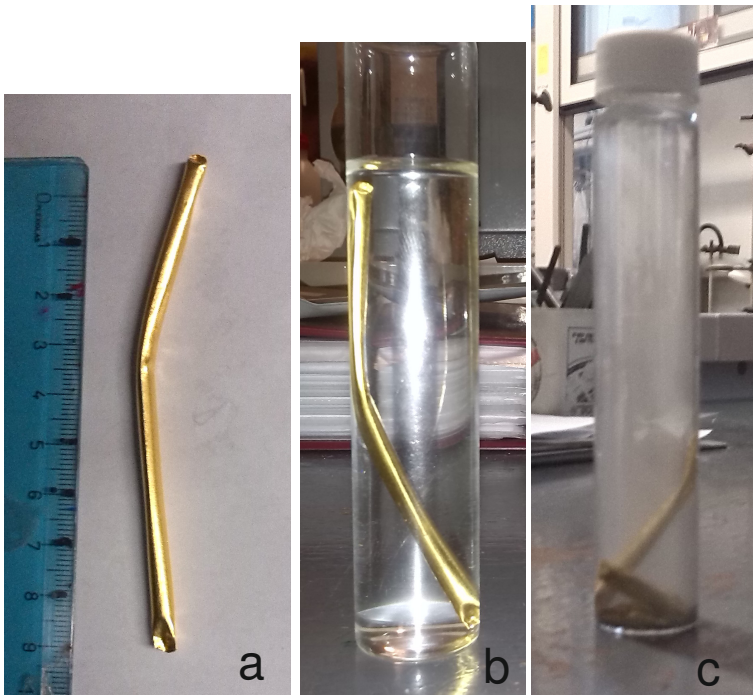

Figure A1.2. a) the capsule of Experiment 6; b) the capsule immersed in milliQ water into a test tube; c) ultrasonic bath let the powder to exit from the capsule.

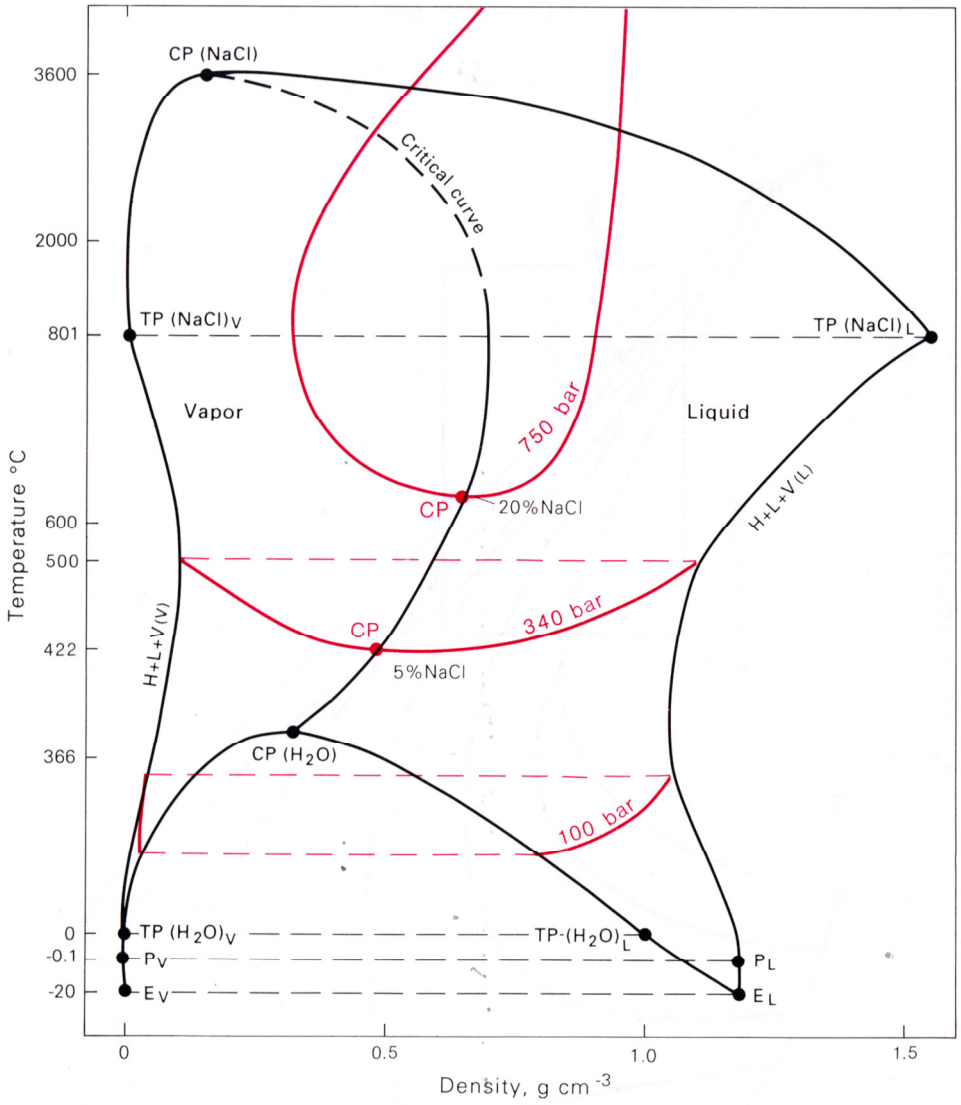

(B) T-V projection showing three isobars (red lines) on the vapor-liquid coexistence surface. The 340 and 750 isobars are above the critical pressure of H_2O (220 bars) and show critical behavior each with a temperature minimum representing the critical point on the NaCl–H_2O critical curve. The 100 bar isobar is below the critical pressure of H_2O and shows no critical behavior, and the minimum temperature is at the boiling curve of pure H_2O. Some example tie-lines (dashed) connect coexisting vapors and liquids.

Figure A2.1.: Water phase diagram.

TABLES

Table A2.1.: Summary of thermodynamic references for the added solid phases.

Name	Formula	Reference
elbaite 2	NaLiAl7.67B3Si6O27(OH)4	Ogorodova et al., 2012
dravite	NaMg3Al6B3Si6O27(OH)4	Ogorodova et al., 2012
schorl	NaFe3Al6B3Si6O27(OH)4	Ogorodova et al., 2012
Mg-amesite	Si2Al4Mg4O10(OH)8	Vidal et al., 2001
daphnite	Si3Al2Fe5O10(OH)8)	Vidal et al., 2001
Mg-sudoite	Mg2Al4Si3O10(OH)8	Vidal et al., 2001
Mg-sudoite 2	Mg2Al4Si3O10(OH)8	Lanari et al., 2014
andalusite eq3/6	Al2SiO5	Waldbaum, 1965
sillimanite eq3/6	Al2SiO5	Waldbaum, 1965
andalusite	Al2SiO5	Salje 1982
sillimanite	Al2SiO5	Salje 1983
albite high	NaAlSi2O8	Holland, 1980
albite low	NaAlSi2O8	Holland, 1980
muscovite eq3/6	KAl3Si3O10(OH)2	Green et al., 1986
albite 2	NaAlSi2O8	Green et al., 1986
paragonite eq3/6	NaAl3Si3O10(OH)2	Green et al., 1986
K-feldspar	KAlSi3O8	Green et al., 1986
chamosite-7a	Fe3Al2Si3O10(OH)8	Saccoccia et al., 1993
Mg-cordierite an. eq3/6	Mg2Al4Si5O18	Newton & Wood, 1979
Mg-cordierite hyd. eq3/6	Mg2Al4Si5O18*1.2H20	Newton & Wood, 1979
Mg-cordierite an. 2	Mg2Al4Si5O18	Dachs & Geiger, 2008
Mg-cordierite hyd.	Mg2Al4Si5O18*1.2H20	Dachs & Geiger, 2008
Fe-cordierite an.	Fe2Al4Si5O18	Dachs & Geiger, 2008
Fe-cordierite hyd	Fe2Al4Si5O18*1.2H2O	Dachs & Geiger, 2008
phengite	K(AlMg0.5Fe0.5)2Si4O10(OH)2	Ogorodova et al., 2006
Fe-celadonite	KFeAlSi4O10(OH)2	Simpson et al., 2000
annite eq3/6	KFe3[Si3AlO10](OH)2	Ogorodova et al., 2009
phlogopite eq3/6	KMg3AlSi3O10(OH)2	Ogorodova et al., 2009
gibbsite	Al(OH)3	Ogordova et al., 2012
nordstrandite	Al(OH)3	Ogordova et al., 2012
gibbsite dehydrated - boehmite	AlOOH	Ogordova et al., 2012
almandino supcrt	Fe3Al2Si3O12	Geiger 1999
pyrope supcrt	Mg3Al2Si3O12	Geiger 1999
grossularia eq3/6	Ca3Al2(SiO4)3	Geiger 1999
spessartine supcrt	Mn3Al2(SiO4)3	Geiger 1999
magnetite eq3/6	Fe3O4	Haavik et al., 2000
FeO eq3/6	FeO	Haavik et al., 2000
hematite	Fe2O3	Haavik et al., 2000
Fe-actinolite		Holland and Powel, 2011
Fe-cordierite anhydrous		Holland and Powel, 2011
Fe-sudoite		Holland and Powel, 2011
sudoite		Holland and Powel, 2011
almandine		Holland and Powel, 2011
pyrope		Holland and Powel, 2011
spessartine		Holland and Powel, 2011

Table A2.2.: Log K following the EQ3/6 grid for added minerals.

Reaction	logK 0.01 °C	logK 25 °C	logK 60 °C	logK 100 °C	logK 150 °C	logK 200 °C	logK 250 °C	logK 300 °C